Development of collagen-like peptide hydrogel biomaterials for soft tissue repair

Alex Ross

Thesis submitted to the University of Ottawa

in partial fulfillment of the requirements

for the Doctorate in Philosophy in Biochemistry

Department of Biochemistry, Microbiology and Immunology

Faculty of Medicine

University of Ottawa

Acknowledgements

I would sincerely like to thank all the members of the BEaTS research group for their help and support during my graduate research. I particularly would like to thank: Xixi Guo, Andres Mercado Salazar, Daniel Nguyen, Aidan MacAdam, and Dr. Marcelo Muñoz for their collaboration and assistance during my studies. I would also like to thank the members of the University of Ottawa Animal Care and Veterinary Services for their help running mouse trials for this project and XiaoLing Zhao for assistance with the histology samples.

I would like to thank the members of my thesis advisory committee: Dr. Benjamin Rotstein, Dr. Katey Rayner, and Dr. Eva Hemmer. I appreciate all the feedback and guidance you have provided me with throughout my graduate research. I am grateful for the support and guidance of my supervisors Dr. Emilio Alarcón and Dr. Erik Suuronen for making this research project possible and enabling my growth as a scientist. Lastly, I would like to thank my family and friends for their uplifting support throughout the course of my studies.

Sources of funding: this work was supported by scholarships from the University of Ottawa, University of Ottawa Heart Institute and the Natural Sciences and Engineering Research Council (NSERC). Operating grants from NSERC, the Canadian Institutes of Health Research (CIHR), Heart and Stroke Canada and a University Research Chair for Dr. Alarcón provided funding for the project. I would like to thank these organizations for making this work possible.

Contribution statement: peptide design, synthesis, purification, and characterization were performed by me with assistance from Daniel Nguyen and Sergio David Garcia Schejtman. Hydrogel formulation, preparation, and characterization was done by me along with Andres Mercado Salazar and Xixi Guo. Molecular dynamics simulations were run by Dr. Horacio Poblete

and Dr. Micaela Gianetti whom I analyzed the data with. 3D printed devices were made by Maxime Comtois-Bona. *Ex vivo* skin experiments were done by me along with Aidan Macadam while cornea testing was done by me and Jinane El-Hage. *In vivo* skin experiments and histology data analysis were done by me and Aidan Macadam. *In vivo* heart experiments were done by Xixi Guo, and we analyzed the echocardiography data together. Cell culture studies were done by Xixi Guo, Jinane El-Hage, and Ramis Ileri. I drafted the manuscript while figure design and statistical analysis were done with the help of Daniel Nguyen, Dr. Emilio Alarcón and Dr. Irene Guzman-Soto.

Disclosure: Alex Ross, Emilio Alarcón, and Erik Suuronen are listed inventors on a patent application for the collagen-like peptide materials presented in this study.

Abstract

Unmet needs in soft tissue repair, such as chronic wounds, scarring, corneal blindness, and heart failure, urgently require new therapies. Hydrogel soft biomaterials offer a promising solution. While traditionally classified as polymers from natural or synthetic sources, advancements in chemical synthesis now enable the synthetic production of natural biofunctional molecules like peptides and proteins. Thus, bioinspired synthetic hydrogels can be designed as reliable, cost-effective and pathogen-free alternatives for soft tissue repair.

Synthetic collagen-like peptides (CLPs) can form natural tissue structures and self-assemble into triple-helix trimers to create 3D hydrogels. In this doctoral dissertation, I developed CLP materials using supramolecular self-assembly and either spontaneous thiol-maleimide Michael addition or photoactivated radical thiol-ene reactivity. A low-volume, rapid combinatory screening approach identified ideal candidates from a library of synthetic peptides. Adjusting peptide concentration or structural properties like junction functionality and reactive group choice allows for hydrogel tuning.

Ex vivo, *in vitro*, and *in vivo* assays assessed the materials' soft tissue repair capabilities. Collagenase degradation and live/dead assays showed suitable biocompatibility and biodegradability. Peptide hydrogels sealed corneal perforations or altered corneal shape. Skin adhesion tests showed strong wound closure strength comparable to commercial adhesives. *In vivo* wound treatment accelerated healing while reducing epithelial thickness and increasing collagen content. In a mouse model of myocardial infarction, CLP hydrogel-treated hearts preserved function at 28 days, while saline control lost function. These results suggest that peptide-based hydrogels are a promising platform for soft tissue repair of the skin, cornea, and heart.

Table of Contents

List of Figures

List of Tables

List of Abbreviations

1,2-Ethanedithiol	EDT
1-Ethyl-3-(-3-Dimethylaminopropyl) Carbodiimide	EDC
2-(N-Morpholino)Ethanesulfonic Acid	MES
2-Methacryloyloxyethyl Phosphorylcholine	MPC
4-(2-Hydroxyethyl)-1-Piperazineethanesulfonic Acid	HEPES
4',6-Diamidino-2-Phenylindole	DAPI
5,5′-Dithiobis-(2-Nitrobenzoic Acid)	DTNB
9-Fluorenylmethyloxycarbonyl	Fmoc
Allyloxycarbonyl	Alloc
American Society for Testing and Materials	ASTM
Analysis of Variance	ANOVA
Angiotensin-Converting Enzyme	ACE
Aortic Valve Closure	AVC
Arginine-Glycine-Aspartate	RGD
Bioengineered Porcine Construct, Double Crosslinked	BPCDX

Cardiovascular Disease	CVD
Circular Dichroism	CD
CLP:PEG-Maleimide Ratio	CM_{ratio}
Collagen-Like Peptides	CLP
Corneal Collagen Crosslinking	CXL
Diabetic Foot Ulcer	DFU
Dichloromethane	DCM
Differential Scanning Calorimetry	DSC
Diisopropylcarbodiimide	DIC
Dimethyl Sulfoxide	DMSO
Dimethylformamide	DMF
Dulbecco's Modified Eagle Medium/Nutrient Mixture F-12	DMEM/F-12
Extracellular Matrix	ECM
Fetal Bovine Serum	FBS
Fourier-Transform Infrared	FTIR
Gelatin Methacryloyl	GelMA

Good Manufacturing Practices	GMP
Hank's Buffer Saline Solution	HBSS
Hematoxylin and Eosin	H&E
Human Cardiac Endothelial Cell	HCEC
Human Skin Fibroblast	HSF
Hyperbaric Oxygen Therapy	HBOT
In Vivo Imaging System	IVIS
Interleukin-4	IL-4
Irgacure-2959	I-2959
Left Ventricular Assist Devices	LVAD
Left Ventricular Ejection Fraction	LVEF
Lithium Phenyl-2,4,6-trimethylbenzoylphosphinate	LAP
Mass Spectrometry	MS
Matrix Metalloprotease	MMP
Melting Temperature	T_m
Methylglyoxal	MG

Microporous Annealed Particle	MAP
Molecular Dynamics	MD
Molecular Weight	MW
Multiple Sequence Alignments	MSA
Myocardial Infarction	MI
Negative Pressure Wound Therapy	NPWT
N-Hydroxysuccinimide	NHS
Optical Coherence Tomography	OCT
Phenylalanine-Phenylalanine	FF
Phenylsilane	PhSiH3
Phosphate Buffered Saline	PBS
Polyethylene Glycol	PEG
Polyvinylpyrrolidone	PVP
Proline-Hydroxyproline-Glycine	POG
Proline-Proline-Glycine	PPG
Ratio of Positive to Negative peak	R_{pn}

Reactive Oxygen Species	ROS
Recombinant Human Collagen	rHC
Reversed-Phase High-Performance Liquid Chromatography	RP-HPLC
Root Mean Square Deviation	RMSD
Root Mean Square Fluctuation	RMSF
Scanning Electron Microscopy	SEM
Solid Phase Peptide Synthesis	SPPS
Tetrakis(triphenylphosphine) Palladium(0)	Pd(PPh3)4
Three-Dimensional	3D
Trifluoroacetic Acid	TFA
Triisopropylsilane	TIS
Tris-(Hydroxymethyl)aminomethane Hydrochloride)	Tris-HCL
Ultraviolet	UV
Ultraviolet A	UVA
Vascular Endothelial Growth Factor	VEGF
Visual Molecular Dynamics	VMD

Some of the text and figures used in this thesis are reproduced with modifications from the following articles: *Ross et al. Advanced Functional Materials 2024, Ross et al. Advanced Functional Materials 2025, and Ross et al. ACS Materials Letters 2026.*

1.0 Introduction

1.1 Current Needs in Cornea Repair

Corneal blindness remains a leading cause of visual impairment, affecting over 12 million people globally. However, it is estimated that only one donor cornea is available for every 70 patients in need.[1] Among the pathologies contributing to this crisis, keratoconus stands out as a prevalent progressive disorder characterized by the thinning and protrusion of the cornea into a conical shape.[2] This structural deformity prevents light from focusing correctly on the retina, leading to distorted vision, myopia, and heightened light sensitivity.[3]

The underlying pathophysiology of keratoconus involves the localized degradation of collagen fibers and a concomitant reduction in the density of specialized fibroblasts in the corneal stroma known as keratocytes.[4] These collagen fibers are essential for maintaining the cornea's shape, strength, and flexibility.[5, 6] However, during disease progression, a significant biochemical imbalance occurs; the depletion of keratocytes is accompanied by an upregulation of matrix metalloproteinases (MMPs). These proteolytic enzymes actively degrade the collagenous framework, resulting in the progressive thinning and mechanical weakening of the stroma.[7, 8]

Current treatments for keratoconus are based on the progression of the disease from early to middle to late stage. In the early stages, treatment typically relies on conservative optical correction through eyeglasses or specialized contact lenses to mitigate refractive errors.[9] As the disease progresses, lenses prove to be insufficient and corneal collagen crosslinking (CXL)[10] is utilized,

where ultraviolet A (UVA) light is used to activate riboflavin and generate reactive oxygen species (ROS), forming additional bonds between collagen and other extracellular matrix (ECM) components such as proteoglycans.[11, 12] While CXL stabilizes the stromal thickness, it is primarily a preservative measure rather than a regenerative one. However, this only provides a temporary relief as end-stage disease progression ultimately demands corneal transplantation.[13] The reliance on donor tissue for end-stage cases highlights an unmet need for alternatives that can restore the cornea's structural integrity and optical clarity without the logistical and immunological complications of transplantation.

1.2 Current Needs in Wound Healing

Functional wound healing is a significant issue as both unhealed chronic wounds (~2% of US population, $20 billion market)[14] and excessive scarring/fibrosis remain prevalent, often without satisfactory treatment.[15] Chronic wound management affects millions of people globally, particularly those with diabetes, obesity, and vascular insufficiencies. Chronic wounds such as diabetic foot ulcers (DFUs) are defined by their failure to progress through the normal, orderly stages of healing.[16] These stages are hemostasis, inflammation, proliferation, and remodelling.[17] Chronic wounds often remain in a prolonged inflammatory phase where a reduction in the functional capacity of fibroblasts and keratinocytes leads to a failure in re-epithelialization.[18] A critical driver of this failure is the overexpression of MMPs; these enzymes cause excessive degradation of the ECM, thereby preventing structural stabilization and effective wound closure.[19]

Current treatments for chronic wounds vary based on the severity and duration of the wound. Early stage management consists of debridement, infection control, and moisture-retentive dressings like foams or hydrocolloids.[20, 21] As wounds fail to heal and become more advanced, therapies such as

negative pressure wound therapy (NPWT)[22] or hyperbaric oxygen therapy (HBOT)[23] can be utilized to stimulate blood flow and oxygenate the tissue. Ultimately, severe non-healing ulcers will require biological skin substitutes or autologous grafts.[24, 25]

Scarring and fibrosis represent the other side of the wound healing response where the persistent activation of myofibroblasts leads to the excessive and disorganized deposition of ECM components, primarily type I collagen.[26, 27] In the skin, this can result in reduced mobility along with physical and psychological discomfort due to patient dissatisfaction with scar appearance.[28, 29] While mature scars are very difficult to treat, current treatments focus on early intervention.[30] These treatments include pressure garments, corticosteroid injections, and laser therapy.[31] However, these approaches remain limited in successfully preventing excessive scarring and fibrosis.

1.3 Current Needs in Heart Repair

Cardiovascular diseases (CVDs) remain the leading cause of global mortality, accounting for approximately 18 million fatalities annually.[32, 33] A primary manifestation of CVD is coronary artery disease, which can culminate in myocardial infarction (MI).[34] The ischemic environment during an MI triggers a cascade of pathological complications, including extensive cardiomyocyte death, adverse cardiac remodeling, and electrical conduction blockages, eventually progressing to end-stage heart failure.[33]

The transition from acute injury to chronic failure is driven by an excessive accumulation of harmful metabolic byproducts, specifically reactive oxygen species (ROS) and methylglyoxal (MG).[35, 36] MG is a highly reactive dicarbonyl compound that has been shown to impair cardiac contractility and accelerate cardiomyocyte apoptosis, thereby exacerbating the loss of functional

tissue.[37] Because adult human cardiomyocytes possess negligible regenerative capacity, the lost muscle is replaced by a non-contractile, fibrotic collagen scar.[38, 39] This scar tissue alters the heart's geometry and mechanical load, initiating a cycle of adverse remodeling characterized by ventricular wall thinning and chamber dilation.[40]

Conventional therapies are primarily palliative, focusing on symptom management and the prevention of subsequent secondary events rather than the restoration of functional myocardium.[41] Pharmacological interventions such as angiotensin-converting enzyme (ACE) inhibitors and beta-blockers can reduce the workload on the heart and minimize further remodeling, but fail to induce regeneration.[42] In severe cases, surgical interventions like the implantation of left ventricular assist devices (LVADs)[43] or heart transplantation[44] are required. While LVADs provide essential mechanical circulatory support, they are associated with high complication rates, including infection and thrombosis.[45] Heart transplantation is severely restricted by a chronic shortage of donor organs as well as the immunological complications of transplantation.[46]

1.4 Biomaterials for Soft Tissue Repair

Significant unmet needs in soft tissue repair, ranging from chronic wounds and pathological fibrosis to corneal blindness and heart failure, demand the development of novel therapeutic strategies. Biomaterials, defined as substances engineered to interact dynamically with biological systems, are uniquely positioned to help address these challenges.[47, 48] Beyond their role as inert medical implants (e.g., stents, prosthetic valves, and dental anchors),[49, 50] modern biomaterials function as bioactive scaffolds that recapitulate the lost ECM and deliver biochemical cues to orchestrate regenerative pathways.[51, 52]

Biomaterials are traditionally categorized by their stiffness (Young's modulus), with hard materials in the MPa to high GPa range and soft materials in the kPa to low GPa range.[53] This classification is biologically critical because of mechanotransduction: the process by which cells sense substrate stiffness to determine their lineage and behavior (e.g., migration, proliferation, and differentiation).[54-56] To avoid mechanical mismatch and chronic irritation, a biomaterial's mechanical properties must be "tuned" to match the target tissue.[57]

Hydrogels, three-dimensional polymeric networks with high water-retention capacity, represent an important and versatile class of soft biomaterials.[58] In dermatological repair, hydrogels function as advanced wound dressings that seal perforations, maintain moisture balance, and provide a protective barrier that accelerates re-epithelialization.[59] Injectable hydrogels can be delivered into the corneal stroma to treat thinning (e.g., keratoconus) by restoring structural thickness and optical clarity.[60] Lastly, injection of hydrogels such as recombinant collagen formulations into the infarcted myocardium can help stop the progression of adverse remodeling and heart failure.[61] Despite their promise, many current hydrogel platforms rely on animal-derived proteins, which present risks of immunogenicity and batch-to-batch variability.[62]

1.5 Natural and Synthetic Materials

Hydrogels are composed of polymers from either natural (derived from living organisms) or synthetic (lab-made) sources.[63] Historically, extracted natural polymers have been widely used as building blocks for the synthesis of materials with therapeutic potential for organ and tissue repair.[64] Natural polymers such as collagen, silk, and alginate originate from animal, plant, or microbial sources and usually offer the advantages of excellent biocompatibility, biodegradability, and inherent cell recognition sites.[65] While some of these materials are already in clinical use,[66-70]

the lack of precise chemical tunability, batch-to-batch variability, generally weak mechanical properties, and potential immunogenicity stemming from biological impurities and pathogen transfer remain barriers to biomedical innovation.[71-73]

The limitations of natural polymers are exacerbated by the fact that a "one size fits all" approach is unrealistic for clinical applications. Organs and tissues possess highly specific physical and mechanical properties, and the extent of tissue damage varies greatly between individuals.[74] Consequently, synthetic materials have gained considerable interest because their properties can be finely tuned to meet specific requirements.[75] Synthetic polymers such as polyethylene glycol (PEG), polycaprolactone, and cyanoacrylates can be precisely chemically synthesized to control both molecular and material properties, offering greater reproducibility, scalability, and customization.[76] While these materials can be engineered for high mechanical strength, they often lack the innate bioactivity of natural polymers and can present challenges regarding long-term biodegradability and biocompatibility.[77]

Among the various synthetic strategies available, short peptide-based materials, typically less than 50 amino acids in length, offer a compelling middle ground.[78] These materials can mimic the biological functions of full-length proteins while providing the flexibility for chemical modification and a relatively low cost of clinical-grade manufacturing.[79, 80] Advancements in chemical synthesis, such as solid-phase peptide synthesis (SPPS),[81] have effectively blurred the line between natural and synthetic classifications.[82] Through chemical production of peptides and proteins, the biofunctional advantages of natural molecules can be retained while capturing the monodispersity and precise structural control of synthetic polymers.[83]

These polypeptide-based materials hold significant potential for applications such as surgical sealants and adhesives, providing an alternative to sutures in delicate tissues where mechanical fastening is difficult or impossible. In these contexts, they can improve healing outcomes and minimize scarring.[84] By utilizing collagen-like peptides (CLPs), it is possible to replicate the hierarchical structure of natural collagen,[85] including the self-assembly into triple-helix trimers that form stable three-dimensional hydrogel networks.[59, 86, 87] Because CLPs elicit a regenerative response similar to that of full-length collagen without the associated risks of animal-derived products, they represent a promising platform for the next generation of soft tissue therapeutics.[88]

1.6 Collagen and Collagen-Like Peptides

Collagen is the most abundant structural protein in the human body, accounting for approximately twenty-five percent of the total protein mass.[89] It serves as the primary architectural component of the extracellular matrix, providing essential tensile strength and structural integrity to tendons, skin, and various internal organs. At the molecular level, collagen is characterized by a sophisticated hierarchical structure beginning with the formation of a right-handed triple helix.[85] This helix is composed of three polypeptide chains, each exceeding 1,400 amino acids in length.[90] The stability of this triple helix is fundamentally dependent on a repeating primary sequence where every third residue is glycine, denoted by the (Gly-X-Y) pattern.[91] In this sequence, the X and Y positions are frequently occupied by proline and 4-hydroxyproline, respectively, which facilitate the tight packing and thermal stability of the helical structure.[92]

The thermal stability of collagenous molecules is determined by the cooperative transition of the triple-helical structure, a process typically quantified by the melting temperature (T_m).[93] In native collagen, this stability is maintained by an extensive network of inter-chain hydrogen bonds,

largely driven by the repeating Proline-Hydroxyproline-Glycine (POG) motifs.[85] Synthetic CLPs successfully replicate this behavior, with stability being thermodynamically favored when the peptides are conjugated to a polymeric backbone or incorporated into a 3D hydrogel network.[94] To remain folded and act as bioactive scaffolds in physiologic conditions, thermal stability at 37 °C is an important design consideration for CLPs.[95] In CLPs, 7-8 POG repeats will generally provide a thermal stability suitable for physiological conditions.[96, 97]

Because of its innate bioactivity, collagen has been extensively utilized as a primary material in tissue engineering.[61, 98, 99] Despite these successes, the use of full-length, animal-derived collagen presents significant technical and clinical challenges. The extraction of collagen from tissues often results in a polydisperse mixture with significant batch-to-batch variability and a risk of transmitting zoonotic diseases or triggering adverse immunological responses.[100] Furthermore, the massive size of the collagen molecule makes it difficult to modify chemically with precision.[101] These limitations have driven the development of CLPs that mimic the essential structural and functional motifs of native collagen. Because they are synthesized chemically, the structure and properties of CLP-based materials can be "tuned" with a level of precision that is impossible to achieve with extracted collagen.[102] This makes CLPs an ideal platform for addressing the "one size fits all" limitation of traditional biomaterials. While native collagen remains a gold standard for bioactivity, CLPs offer a superior balance of safety, reproducibility, and engineerable complexity, bridging the gap between natural biological function and synthetic material precision.

1.7 Structural vs Functional Elements

In the engineering of tissue-instructive scaffolds, a fundamental distinction can be drawn between structural elements and functional elements. Structural elements represent the architectural

features responsible for bulk mechanical integrity and physical support, whereas functional elements comprise the biochemical moieties that directly dictate cellular fate processes.[103] While historically treated as separate design criteria, they are increasingly being recognized as coupled variables where physical forces translate into biological signals through the material-cell interface.[56]

Structural elements are the material features that define mechanical properties, including bulk composition, microstructure, and architecture.[104] These variables determine the elastic modulus, yield strength, toughness, and fatigue life of the scaffold.[105] In the context of soft tissue repair, these elements are engineered to match the target tissue's mechanical environment to avoid stress shielding or implant failure.[106] Through mechanotransduction, cells convert mechanical stimuli from their environment into biochemical signals, thus generating a biological response to the mechanical properties of nearby biomaterials.[107]

Functional elements operate at the surface and near-surface scales to control protein adsorption, integrin binding, and immune recognition.[108] Examples include surface topography,[109] chemical functional groups,[110] immobilized peptides or growth factors,[111] and degradable linkers[112] that release bioactive cues. Unlike structural components, these elements do not primarily carry mechanical load; instead, they instruct cells by affecting adhesion, differentiation, and inflammatory responses through specific signaling pathways. The modification of materials using targeted peptide sequences can provide a diverse array of therapeutic properties, including antihypertensive,[113] antimicrobial,[114] angiogenic,[115] anti-cancer,[116, 117] neuronal growth,[118, 119] anti-apoptotic,[120] drug delivery,[121] and immunomodulatory properties.[122, 123]

Peptide functionalization can be achieved through various chemical methods, such as grafting, oxidation, and aminolysis, or through physical methods including adsorption, entrapment, and layer-by-layer deposition.[124] The selection of an appropriate functionalization strategy is dependent on the chemical composition of the base material and the specific requirements of the peptide sequence.[125] By integrating these functional cues into a mechanically sound structural framework, it is possible to create biomaterials that not only replace lost tissue but actively guide the regenerative process.

1.8 Hydrogel Design

Hydrogels represent the most prevalent class of soft biomaterials due to their high water content (often exceeding 90%), biocompatibility, and mechanical tunability.[126] They can be synthesized using a variety of chemistries that enable the formation of three-dimensional, water-retaining polymer networks with possible features including self-healing, toughness, shear-thinning, and stimuli-responsiveness.[127]

The formation of these networks relies on either physical (non-covalent) or chemical (covalent) crosslinks (Figure 1.1A). Physical interactions, including hydrogen bonding, ionic interactions, and hydrophobic forces, are primarily responsible for the folding and assembly of polypeptides.[128] A prominent example is the self-assembling peptide RADA16, which forms stable scaffolds through ionic-complementary interactions.[129] Physical crosslinking typically results in softer, more dynamic materials formed under mild, cytocompatible conditions, often triggered by subtle shifts in pH or temperature.[130]

In contrast, chemical crosslinking involves covalent bond formation either through spontaneous reactions or those stimulated by light[99], heat[131], or enzymes.[132] Gelatin methacryloyl (GelMA),

which undergoes rapid polymerization upon light exposure, is a widely utilized example of a chemically crosslinked system.[133-135] While chemical crosslinking generally produces stiffer materials, reaction conditions such as the presence of photoinitiators must be carefully optimized to prevent adverse effects on cell viability.[136] Table 1.1 contains a summary of physical vs chemical crosslinking.

The degree and nature of crosslinking dictate the fundamental physicochemical properties of the hydrogel, including stiffness, porosity, swelling capacity, and diffusivity (Figure 1.1B). Stiffness is a critical determinant of cell behavior; through interactions with integrin receptors, the mechanical rigidity of the scaffold influences cellular morphology, proliferation, and migration.[137-138] Generally, as crosslinking density and polymer concentration increase, the elastic modulus rises while the swelling ratio, governed by the balance of osmotic pressure and elastic retractive forces, decreases.[139]

Porosity and diffusivity are also important parameters, as they govern the infiltration of cells, the vascularization of the graft, and the diffusion of nutrients and metabolic waste.[140] However, the optimal parameters for porosity are still not well understood.[141] Diffusivity affects the release of payload from the hydrogel and is typically inversely related to stiffness due to the smaller mesh size in stiff hydrogels.[142] Furthermore, for temporary scaffolds, the biodegradation rate must be synchronized with the deposition of native ECM to ensure seamless tissue integration without the need for surgical removal.[143]

Ultimately, the clinical success of a hydrogel depends on the precise alignment of these properties with the physiological demands of the target tissue. By fine-tuning these parameters, scaffolds can be created that accommodate the high transparency required for the cornea, the mechanical

resilience required by the beating heart, or the rapid cell infiltration essential for wound healing.

	Physical Crosslinking	**Chemical Crosslinking**
Mechanism	Non-covalent interactions such as hydrogen bonds, ionic interactions, and hydrophobic forces.	Covalent bond formation via spontaneous reactions or those activated with light, heat, or enzymes.
Representative examples	Self-assembling peptide hydrogels such as RADA16 or peptide amphiphiles.	Photocrosslinkable GelMA systems; rose bengal collagen photobonding; click chemistry PEG networks.
Tunability	Control via pH, ionic strength, temperature and sequence design with limited maximal stiffness.	Control via functional group density, stoichiometry, light dose, enzyme activity and orthogonal click pairs with larger possible stiffness ranges.
Cytocompatibility	Generally mild formation conditions and reversible bonds; useful for *in situ* gelling.	Dependent on type of reactive group and concentrations used; potentially greater cytotoxicity.

Table 1.1. Crosslinking strategies in hydrogel design. Comparison of mechanism, representative examples, tunability, and cytocompatibility on material properties.

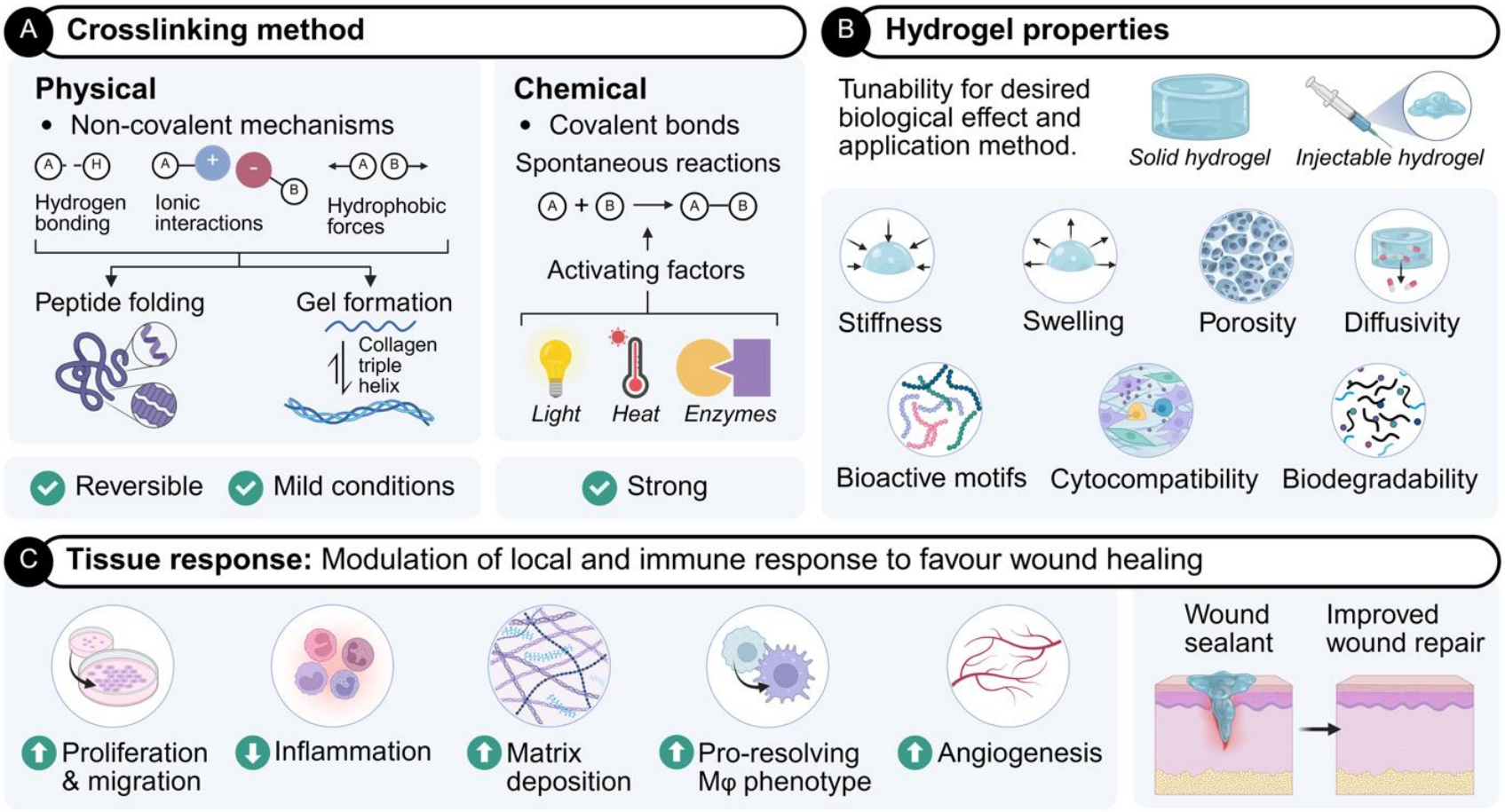

Figure 1.1. Hydrogel design. Network formation: hydrogels are engineered through either physical or chemical crosslinking. These strategies dictate the fundamental architecture of the polymer network. (B) Physicochemical properties: increased crosslinking typically enhances stiffness and mechanical resilience but leads to a reduction in swelling ratio and a decrease in porosity, which in turn limits the diffusivity of nutrients and signaling molecules. (C) Bioactive modulation: beyond mechanical support, functionalization modulates the immune response and provide localized, instructive cues to guide the healing process. Designed in BioRender and edited by Dr. Irene Guzman-Soto.

1.9 Biomaterials for Cornea Repair

An ideal artificial corneal implant must satisfy several stringent benchmarks, including high optical transparency, shape retention under intraocular pressure, ease of surgical application, and long-term immune tolerance (Figure 1.2A). Given that collagen is the predominant structural component of the human corneal stroma, it has served as a logical basis for bioengineered implants.[144] Among the most clinically advanced examples is BPCDX (bioengineered porcine construct, double crosslinked), an animal-derived collagen hydrogel that significantly improved visual acuity and corneal thickness in patients over a 24-month period without adverse effects.[145] Despite these outcomes, animal-derived collagen is inherently heterogenous, source-dependent, and may contain immunogenic or zoonotic contaminants **(**Figure 1.2B).[73] In addition, its extraction and purification require extensive processing to meet clinical safety standards.[88]

To mitigate these risks, recombinant human collagen (rHC) hydrogels with 2-methacryloyloxyethyl phosphorylcholine (MPC) have been developed. rHC-MPC-PEG hydrogels were implanted in high-risk patients, achieving partial vision restoration and stromal integration over 24 months. While recombinant approaches eliminate animal sourcing, they present significant challenges in protein expression, purification, and high-level processing. Furthermore, many of these systems rely on external crosslinkers like 1-ethyl-3-(-3-dimethylaminopropyl) carbodiimide/N-hydroxysuccinimide (EDC/NHS), which can limit *in situ* cell encapsulation due to chemical toxicity.[144] These barriers have shifted interest toward materials where crosslinking and bioactivity are engineered directly into the molecular backbone.

Short CLPs offer a synthetic alternative that mimics the triple-helical folding of native collagen while remaining modular and industrially scalable (Figure 1.2C). Experimental studies have shown

that CLP-based hydrogels achieve regenerative outcomes comparable to rHC implants, including successful epithelial repair and stromal remodeling.[88, 146] A notable application is the LiQD Cornea, a CLP-PEG-fibrinogen conjugate that forms a hydrogel at physiological temperatures within five minutes.[147] Research in feline models demonstrated sustained clarity and tissue integration over 12 months with this system, and subsequent iterations incorporated MPC for anti-inflammatory effects and the GF19 peptide for antiviral protection.[148-150] These multifunctional designs highlight the modularity of CLPs but also demonstrate reliance on multiple components and external crosslinkers. Table 1.2 contains a comparison of different collagen sources.

Photopolymerization is a popular strategy for providing spatiotemporal control over hydrogel formation, as seen with GelCORE, which effectively seals stromal defects in rabbit models via *in situ* light activation.[134] Other proteins such as silk are also used in photopolymerization systems.[151] However, the toxicity of common photoinitiators like riboflavin under UV exposure remains a concern.[152] Visible light can alleviate this issue. For example, a photoresponsive formulation combining CLPs with glycosaminoglycans and PEG used a low energy pulsed blue light to prevent damage to sensitive retinal cells while also regenerating the stroma.[60] Using pulsing to allow time for oxygen diffusion, a low intensity of blue light applied to riboflavin resulted in effective crosslinking with reduced cytotoxicity. Recent findings also suggest that using arginine as a co-initiator can further attenuate riboflavin-induced phototoxicity.[153] Additionally, the incorporation of bioactive molecules like heparin into these formulations can limit cytokine influx, thereby reducing corneal scarring and fibrosis.[154]

Developing effective photopolymerization systems to generate *in situ* biomaterials with minimal toxicity either from chemical additives or use of harsh irradiation along with tuning the biological response will help facilitate cornea repair going forward. Synthetic peptide-based materials such

as CLPs offer a modular, tunable, and light-controllable platform that is clinically scalable. By encoding functionality directly into the peptide sequence while avoiding potential contamination from biological sources, these materials overcome the inherent limitations of animal-derived and recombinant systems and advance the design of next-generation therapies for corneal regeneration.

	Animal-Derived (BPCDX)	**Recombinant (rHC)**	**Synthetic (CLPs)**
Purity	Variable; potential for zoonosis.	High; single protein species.	Absolute; sequence defined.
Scalability	High, but requires rigorous cleaning	Low to Moderate; complex expression.	High; automated peptide synthesis.
Modularity	Limited to post-extraction edits.	High genetic modularity.	Maximum; atomic level control.
Safety	Risk of immune response (telopeptides).	High biocompatibility.	High; low immunogenic footprint.

Table 1.2. Comparison of animal-derived, recombinant, and synthetic collagen systems in cornea repair.

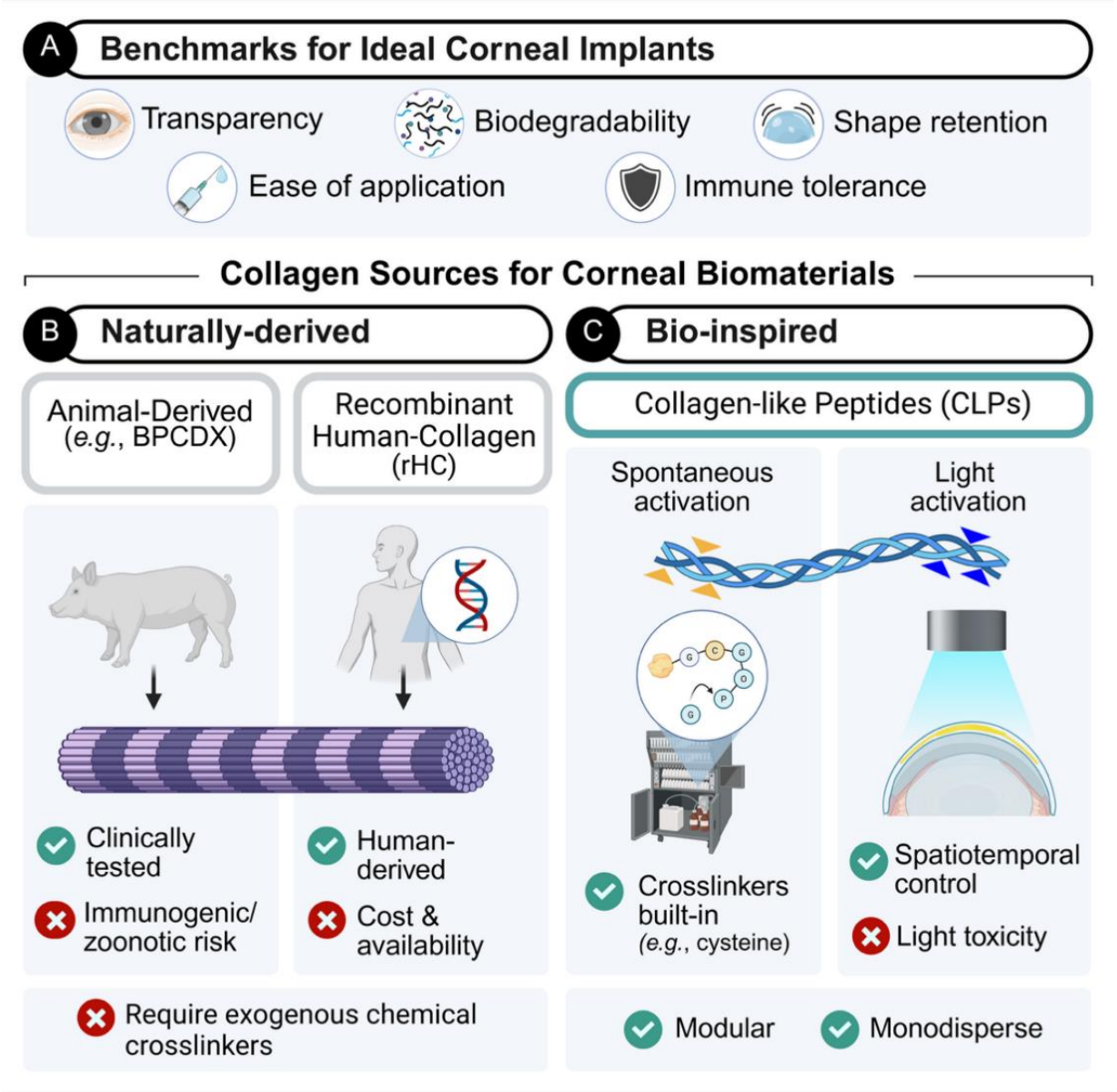

Figure 1.2. Cornea material design. (A) An ideal corneal implant must balance optical transparency, mechanical shape retention, ease of surgical application, controlled biodegradability that matches host tissue turnover, and high immune tolerance to prevent graft rejection.(B) Traditional approaches utilize full-length collagen. While animal-derived sources are abundant, they suffer from batch variability and potential immunogenicity. Recombinant human collagen provides a more uniform alternative but presents significant challenges in large-scale purification.(C) By synthesizing short, sequence-defined peptides that self-assemble into triple helices, crosslinking sites and bioactive motifs can be built into the molecular backbone. Designed in BioRender and edited by Dr. Irene Guzman-Soto.

1.10 Biomaterials for Wound Healing

Hydrogels represent a promising technology for wound management due to their ability to maintain a moist environment, facilitate cell migration, and act as a semi-permeable barrier against external contaminants.[155] Beyond physical protection, advanced wound-healing hydrogels are designed to induce a favorable tissue response by encouraging angiogenesis and matrix deposition while controlling the local inflammatory profile.[156] This is increasingly achieved through peptide biofunctionalization, where specific sequences are integrated to provide biochemical instructions to the wound site. For example, angiopoietin-1 derived Q-peptide accelerated re-epithelialization and granulation in small animals and xenografted human skin, Hsp90α F-5 halted burn progression and promoted keratinocyte-driven re-epithelialization in porcine skin, and a laminin-derived antioxidant dressing with A5G81 enhanced motility, proliferation, and closure in diabetic wounds.[157-161] The physical architecture of the material also plays a role; nanofiber aerogels with precision macrochannels have been shown to amplify these biochemical cues, leading to enhanced neovascularization and tissue infiltration.[162]

Modulating the immune response is another critical function of modern dressings. Experimental work with microporous annealed particle (MAP) hydrogels crosslinked with D-peptides demonstrated the recruitment of myeloid cells and the induction of an antigen-specific adaptive response. This led to regenerative healing, characterized by hair follicle neogenesis and improved tensile strength, even when the material degraded more rapidly than its L-peptide counterparts.[163] Additionally, functionalizing materials with interleukin-4 (IL-4) via collagen-binding domains has been shown to promote M2-like macrophage polarization, shifting the wound environment from a pro-inflammatory to a pro-healing state.[164] However, the complexity of the immune response

necessitates caution, and the development of spatial gradients for these signals remains a major research frontier.[165]

While peptides are often added as functional components, they can also serve as the structural backbone of the hydrogel, potentially acting as tissue sealants that replace traditional sutures.[166] Light-activated tissue sealants composed of methacrylated collagen and rose bengal,[99] as well as formulations with PEG and CLPs that reduce inflammation and scarring in murine wound models provide examples of wound-healing hydrogels.[59, 86] Fibrin is another structural polypeptide that displays inherent immunomodulatory activity by altering cytokine expression.[167, 168] Notably, the crosslinking density and stiffness of these sealants directly shape the repair process: softer, lightly crosslinked gels promote cellular infiltration and minimal scarring, whereas stiffer, heavily crosslinked GelMA hydrogels have been shown to elevate pro-fibrotic signaling.[169]

While many materials have shown successful wound healing in animal models, a deeper understanding of underlying pathophysiology and individual heterogeneity is required as different wounds and sub-regions of the same wound display divergent molecular characteristics.[170] Future wound healing materials will match their properties to specific wound types and subregions through presentation of spatial gradients within the material.

1.11 Biomaterials for Heart Repair

Cardiac biomaterials have two common forms: injectable hydrogels and cardiac patches.[171, 172] While patches offer superior mechanical reinforcement and enhanced retention of therapeutic payloads, injectable hydrogels provide the distinct advantage of minimally invasive delivery, allowing the material to reach deeper into the infarcted myocardium (Figure 1.3B). The design of these materials requires a precise alignment with the physiological and mechanical environment

of the heart. Native myocardium exhibits an elastic modulus of approximately 10–20 kPa and undergoes constant cyclic strain; in contrast, infarcted tissue undergoes fibrotic remodeling, becoming significantly stiffer (>50 kPa).[173-175] Consequently, ideal cardiac materials must mimic the compliance and viscoelasticity of healthy tissue while providing high fatigue resistance to endure millions of contraction cycles.[47] Furthermore, they must be biocompatible, non-immunogenic, and may incorporate bioactive cues such as ECM-derived peptides and growth factors to promote cell adhesion, survival, and angiogenesis, while exhibiting controlled degradation aligned with tissue healing.[176, 177]

Beyond basic mechanical support, advanced cardiac hydrogels must address the complex pathophysiology of MI through multifunctional design. Two critical strategies involve molecular scavenging and immune regulation (Figure 1.3C). Metabolic byproducts, such as MG, can be scavenged to reduce scar size and improve cardiac function.[178] Similarly, ROS-scavenging components or ROS-responsive linkages can mitigate oxidative damage, significantly reducing inflammation and fostering an environment conducive to angiogenesis.[179, 180]

In addition to molecular scavenging, immune response regulation is essential to prevent chronic inflammation and promote a pro-healing phenotype in infiltrating immune cells. Upon contact with myocardial tissue, biomaterials affect the immune response, alter inflammation, and can contribute to macrophage polarization.[181, 182] The inflammatory response is characterized by immune cell recruitment, cytokine expression (e.g. tumour necrosis factor-α, interleukin-1β) and chemokine release, as well as inflammatory pathway activation.[183, 184] Cardiac biomaterials can be engineered to release immunomodulatory agents (e.g. interleukin-10, transforming growth factor-beta) or incorporate bioactive motifs that polarize macrophages toward an M2 reparative phenotype.[185]

A unique requirement for cardiac materials is the restoration of electrical connectivity. The fibrous scars formed after an MI disrupt the heart's natural conduction system, often leading to arrhythmias.[186] To restore synchronized contraction, conductive elements such as gold nanoparticles, carbon nanotubes, or conductive polymers have been integrated into scaffolds.[186, 187] For example, two approaches demonstrated to restore conductivity and improve heart function post-MI are embedded conductive gold nanoparticles within a collagen cardiac patch[188] and peptide-stabilized gold nanoparticle spray.[189] Conductive peptides are an active area of research, where ultrashort peptides modified with 9-fluorenylmethyloxycarbonyl (Fmoc) such as Fmoc-phenylalanine-phenylalanine (FF) are incorporated in materials, resulting in seeded H9C2 cells showing increased elongation and alignment along with treated rat hearts exhibiting increased Connexin 43 expression.[190] However, caution must be applied to not inadvertently cause arrhythmia through biomaterial application.

In summary, both cardiac patches and injectable hydrogels have emerged as promising platforms for cardiac repair due to their multifunctional ability to provide mechanical support, deliver bioactive molecules, scavenge harmful metabolic byproducts, modulate the immune response, and restore electroconductivity. However, several translational challenges hinder their clinical implementation. First, mechanical fragility and mismatch with dynamic myocardial tissue remain major concerns, as materials must withstand cyclic strain without compromising integrity.[47] Second, biological complexity including immune responses, chronic inflammation, fibrosis, and poor vascularization limits long-term integration and functional recovery.[191] Third, scalability and reproducibility of hydrogel synthesis, sterilization, and storage pose manufacturing challenges, while regulatory hurdles complicate approval for clinical use.[192] Finally, limited large-animal and human trial data restricts translation, as most evidence comes from small-animal models, which

do not fully replicate human cardiac physiology.[193] Future approaches aim to overcome these barriers through multifunctional and adaptive hydrogel designs, advanced delivery systems such as image-guided injection, and scalable good manufacturing practices (GMP) compliant production along with validation in large-animal models.

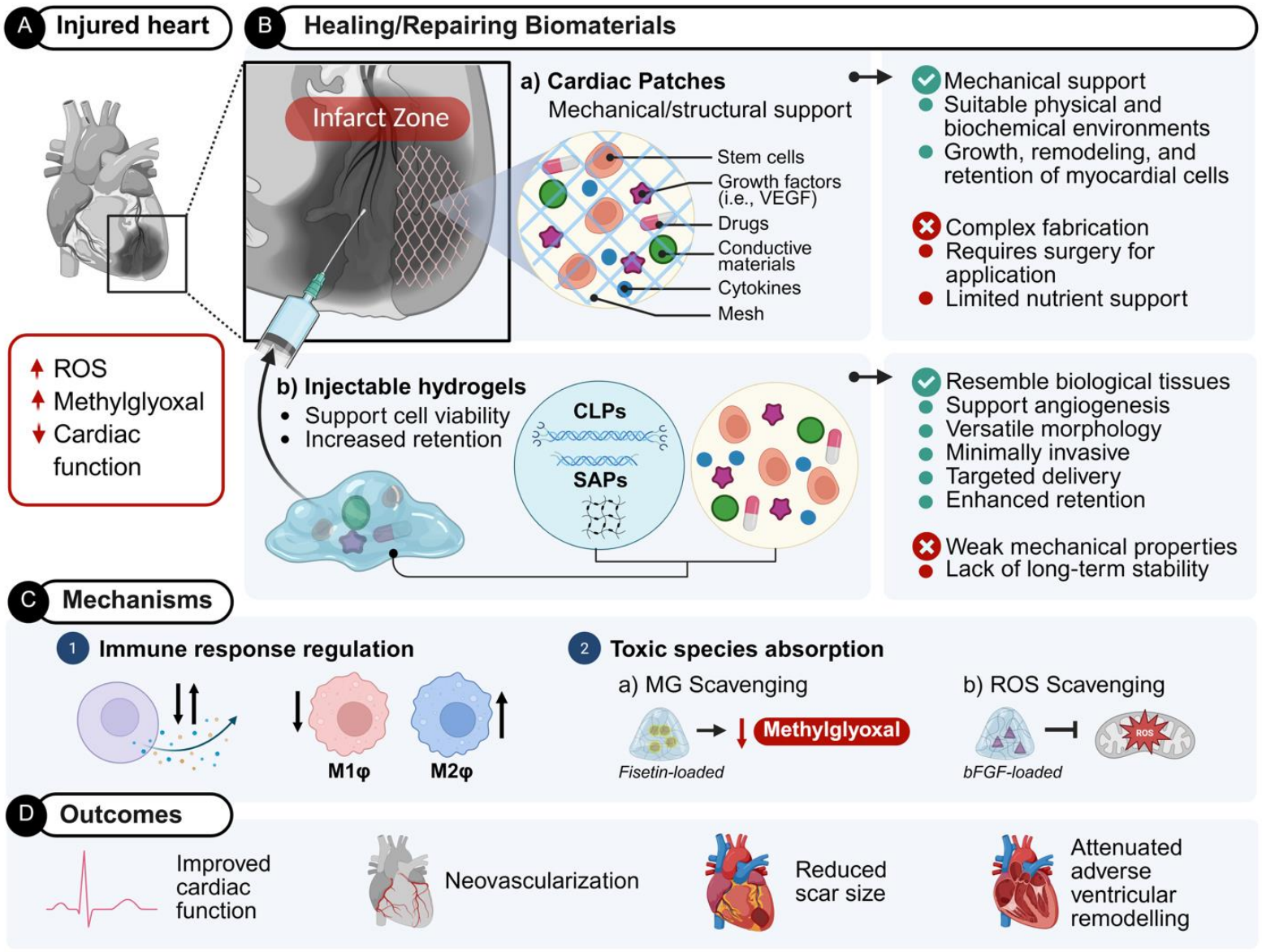
A Injured heart
B Healing/Repairing Biomaterials
Infarct Zone
ROS
Methylglyoxal
Cardiac function
a) Cardiac Patches
Mechanical/structural support
Stem cells
Growth factors (i.e., VEGF)
Drugs
Conductive materials
Cytokines
Mesh
Mechanical support
Suitable physical and biochemical environments
Growth, remodeling, and retention of myocardial cells
Complex fabrication
Requires surgery for application
Limited nutrient support
b) Injectable hydrogels
Support cell viability
Increased retention
CLPs
SAPs
Resemble biological tissues
Support angiogenesis
Versatile morphology
Minimally invasive
Targeted delivery
Enhanced retention
Weak mechanical properties
Lack of long-term stability
C Mechanisms
1 Immune response regulation
M1φ
M2φ
2 Toxic species absorption
a) MG Scavenging
Methylglyoxal
Fisetin-loaded
b) ROS Scavenging
ROS
bFGF-loaded
D Outcomes
Improved cardiac function
Neovascularization
Reduced scar size
Attenuated adverse ventricular remodelling

Figure 1.3. Cardiac material design. (A) Following cardiac injury, the myocardium undergoes a cascade of adverse events, including cardiomyocyte death, intense inflammation, and the formation of a stiff, non-conductive fibrous scar. (B) To address this injury, hydrogels can be injected or cardiac patches may be surgically delivered to provide mechanical reinforcement and a reservoir for cell or drug delivery. (C) These materials function through active pathways including immune response regulation and molecular scavenging. (D) Successful integration of these biomaterials leads to a measurable improvement in cardiac function, stimulated neovascularization to restore blood flow, and a significant reduction in scar size. Designed in BioRender and edited by Dr. Irene Guzman-Soto.

The text and figure below were reproduced with modifications from *Ross et al. Advanced Functional Materials 2024.*

1.12 Multipurpose On-the-Spot Peptide-Based Hydrogels for Skin, Cornea, and Heart Repair

The development of three-dimensional scaffolds for regenerative medicine has historically relied on external chemical crosslinkers to achieve necessary structural integrity. However, many traditional crosslinking agents can be detrimental to cellular health, particularly in sensitive applications such as stem cell delivery. This toxicity often limits the use of such materials to pre-crosslinked implants, where residual reactive side-products must be extensively washed out prior to implantation.[194] To overcome these translational barriers, there is a growing need for materials where the assembly mechanism is inherently cytocompatible and integrated into the molecular design of the peptide sequence itself.

A major challenge in this field is ensuring that the precise design of peptide sequences facilitates robust self-assembly even within a crosslinked state, which is essential for reinforcing the mechanical properties of the resulting hydrogel. Some examples in the literature report bio-orthogonal assembly of peptide-based hydrogels, mainly using cysteine containing peptides.[195-197] However, the application of this chemistry with CLPs remains for the most part underdeveloped.[198] CLPs are unique in their ability to mimic the triple-helical tertiary structure of native collagen, the primary structural protein providing tensile strength to human tissues. These synthetic peptides are typically composed of Proline-Proline-Glycine (PPG) or Proline-Hydroxyproline-Glycine- (POG) amino acid triplets, offering a modular platform for both structural support and biological signaling.[199] By combining bio-orthogonal reactivity through cysteine-maleimide reactivity with

triple-helical assembly, CLPs can be used as structural components that remove the need for external and potentially toxic crosslinkers.

Key to utilizing CLPs as structural building blocks is a fundamental characterization of their molecular structure-function relationships. To date, a thorough investigation into how the specific positioning and identity of each amino acid within a CLP affects the macroscopic properties of a hydrogel remains underdeveloped. Thus, this work will bridge that gap by utilizing the atomic-level control provided by SPPS to engineer a library of CLPs to interrogate structure-function relationships. Factors such as peptide length, position and number of reactive groups along with the contribution of peptide assembly will be assessed to understand the structural role of CLPs on a molecular level. Through a low-volume, rapid combinatory screening approach, an ideal peptide candidate will be developed and used to produce multifunctional materials designed for *in situ* applications across diverse tissue types, including the skin, cornea, and heart. A summary of this integrated design strategy and its multi-organ applications is illustrated in Figure 1.4.

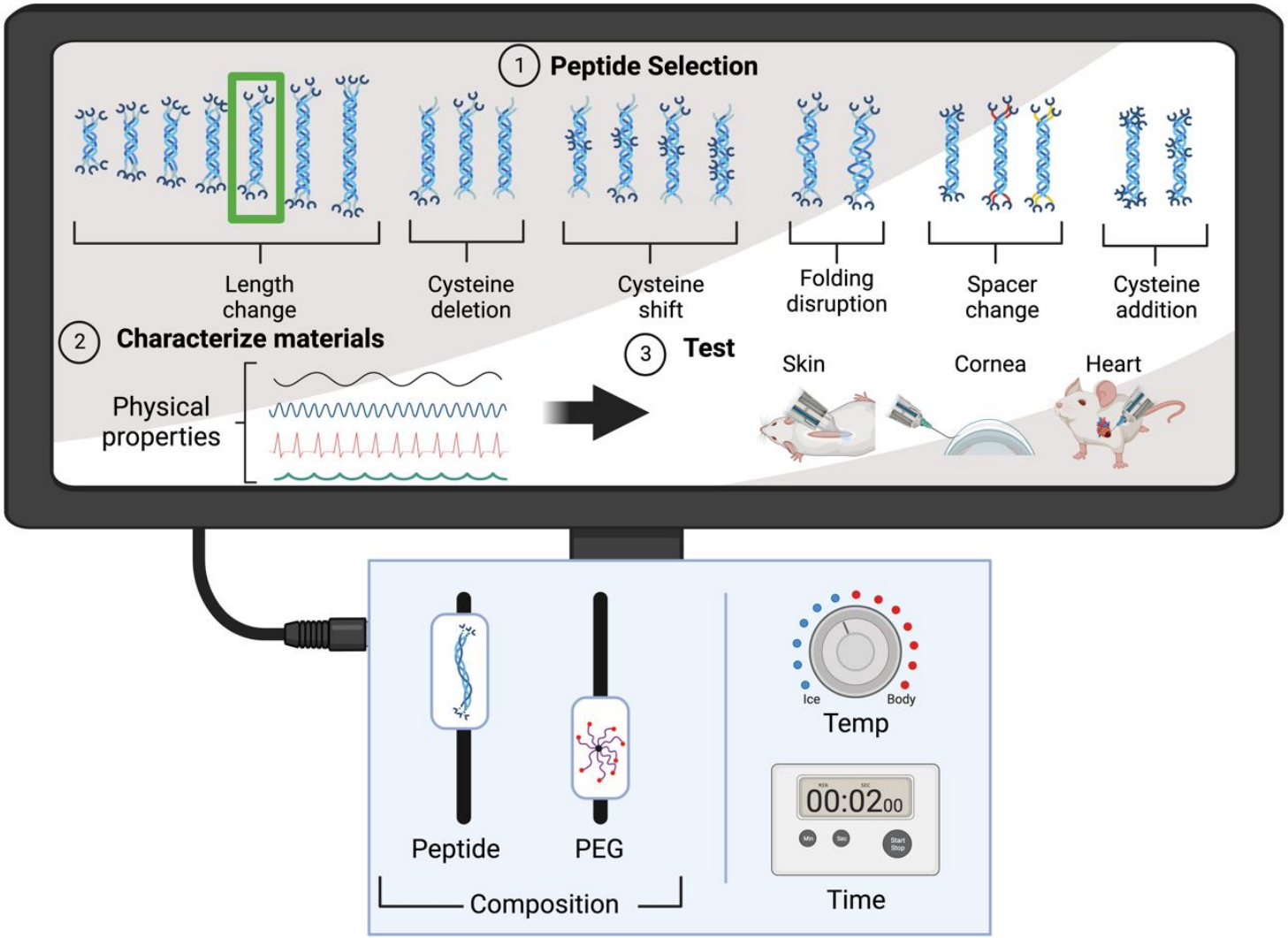

Figure 1.4. Multipurpose peptide-based engineered materials for skin, cornea, and heart repair. Graphical abstract for this work. A library of collagen-like peptides with different molecular structures are screened through a low-volume, rapid combinatory approach. The resulting materials are characterized for their physical properties. As a result of the screening process, a top peptide candidate is identified and used to create *in situ* forming multifunctional hydrogel materials with that can used for skin, cornea, and heart repair.

The text and figures were reproduced with modifications from *Ross et al. Advanced Functional Materials 2025.*

1.13 Mechanically Stable and Tunable Photoactivated Peptide-Based Hydrogels for Soft Tissue Adhesion

Peptide-based materials frequently lack the mechanical robustness required for load-bearing soft tissue applications.[80, 200] To compensate, they are regularly conjugated to synthetic polymers such as PEG to form hybrid scaffolds.[59, 201] While these systems are effective at improving elasticity and toughness, they often sacrifice molecular simplicity and monodispersity. Consequently, the design of "peptide-only" systems that possess both robust and tunable mechanical properties remains a significant challenge in biomaterials science.

A unifying feature of both native collagen fibrils and engineered collagen biomaterials is crosslinking, which provides essential mechanical reinforcement. In native tissues, intermolecular crosslinks introduced by enzymes like lysyl oxidase contribute crucially to tissue stiffness and durability.[202] In engineered collagen systems, crosslinking is commonly achieved using carbodiimide-based chemistries such as EDC/NHS[61] or small-molecule crosslinkers including genipin[203] or glutaraldehyde.[204] Although effective, these traditional methods typically offer limited spatiotemporal control over the crosslinking process.[205] Therefore, a crosslinking strategy for peptide-based biomaterials that could be: (i) encoded directly into the peptide sequence, (ii) executed efficiently in aqueous buffer under mild conditions, (iii) controlled with high spatiotemporal precision, and (iv) designed to minimize cytotoxic byproducts, was selected for.

The radical thiol-ene reaction (Figure 1.5) is one that satisfies these criteria.[206, 207] Thiol-ene chemistry proceeds through step-growth kinetics and reaches the gel point at high monomer

conversion, yielding more homogenous networks and fewer unreacted alkenes than alkene homopolymerization.[208] This is an important consideration given the cytotoxicity of unreactive alkene monomers.[209] Furthermore, thiol-ene chemistry is less sensitive to the presence of oxygen and can be efficiently performed in aqueous solutions exposed to regular atmospheric conditions.[210]

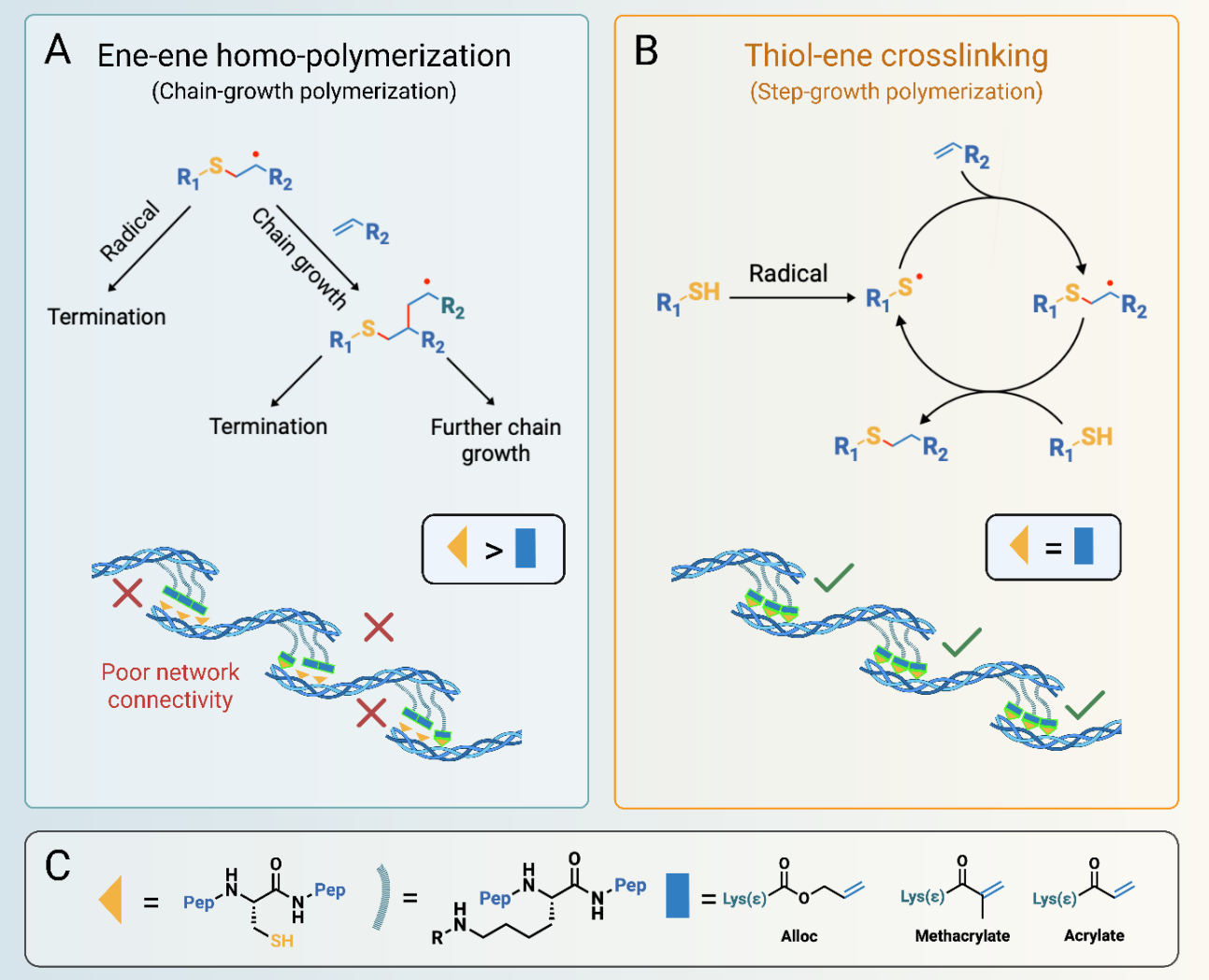

Figure 1.5. Reactivity scheme for photoactivated peptides. Illustration for the (A) ene-ene homopolymerization and (B) thiol-ene crosslinking. The image also contains a depiction of how such processes would take place for chain-growth and step-growth of 3D assembled peptide sequences. (C) Structures for the chemical moieties used in this work.

Light activation provides a layer of temporal control, a strategy already utilized in modified natural polymers like GelMA or dityrosine silk fibroin.[211-213] This approach allows for a self-reactive molecule to remain inert until irradiated, facilitating purification and preventing premature reaction during material handling and application. However, many photoreactive groups, such as alkenes, are inherently hydrophobic, which can limit the aqueous solubility of the peptide.[214] The hydrophobicity of these groups must be balanced with hydrophilic amino acids, such as the POG motif commonly found in CLPs, to produce water "friendly" materials such as hydrogels. By combining a POG core with terminal cysteine sulfhydryl and lysine ε-alkene residues, thiol-ene reactive CLPs that produce hydrogels may be designed.

In this work, a library of photoactivated CLPs is synthesized, characterized, and screened for their ability to form hydrogel networks. Structure-function relationships are investigated for factors including peptide length, folding ability, type and number of reactive groups, and position of reactive group within the peptide. By combining triple helical assembly along with optimized thiol-ene reactivity, hydrogels are successfully formed from minimalistic solutions containing only peptide, photoinitiator, and buffer. The mechanical properties of these hydrogels can be significantly tuned by altering the molecular structure of the peptide used or simply increasing its concentration. This allows for the creation of mechanically stable peptide-only hydrogel biomaterials. The suitability of these materials to act as topically applied tissue sealants is characterized. A summary of this approach is found in Figure 1.6.

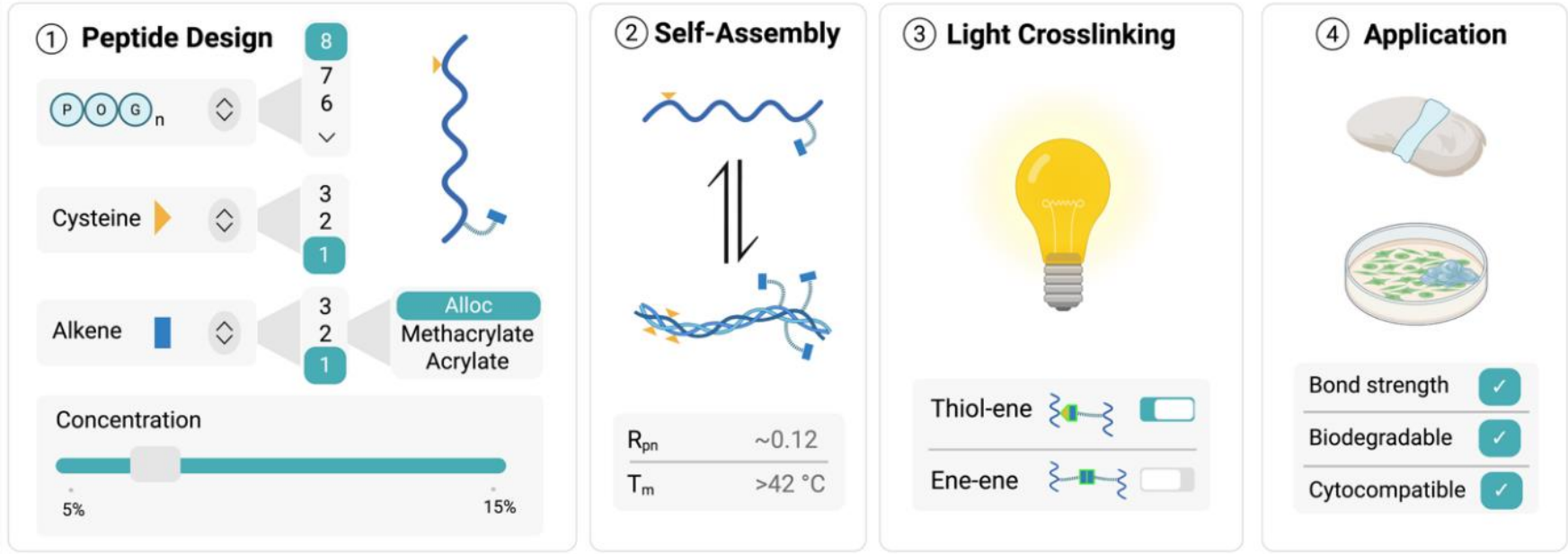

Figure 1.6. A collagen-like peptide hydrogel platform is developed using supramolecular self-assembly and light-triggered crosslinking. A central, hydrophilic POG core drives triple-helical assembly and ensures water solubility. Terminal cysteine and alkene residues provide tunable chemical reactivity. Upon irradiation in the presence of a photoinitiator, these groups undergo a rapid thiol-ene "click" reaction, covalently tethering the pre-assembled triple helices into a macroscopic, mechanically stable hydrogel network with applications in soft tissue adhesion.

1.14 Thesis Objectives and Scope

The main objective for this thesis was to develop CLPs as key structural components in peptide-based hydrogel biomaterials used for soft tissue repair. To accomplish this objective, a library of CLPs was designed, synthesized, characterized, and screened with a rapid, low-volume combinatory approach. After the screening process, the top CLP materials were applied to *in vitro*, *ex vivo*, and *in vivo* models to determine the suitability of the materials for soft tissue repair. The studies in this thesis can be divided into three specific aims.

Aim 1: Develop CLP-PEG hybrid materials utilizing the CLP as a crosslinking agent. Characterize and screen a library of CLPs for hydrogel formation to understand structure-function relationships and identify top candidates.

Aim 2: Characterize the biological performance of top CLP-PEG formulations. Assays used include *in vitro* cytocompatibility, *ex vivo* cornea sealing and filling, *ex vivo* skin adhesion, *in vivo* wound sealing and *in vivo* myocardial injection.

Aim 3: Develop CLP-only photoactivated materials through thiol-ene "click" chemistry. Characterize and screen a library of photo-CLPs for hydrogel formation to understand structure-function relationships and identify top candidates. Develop tissue adhesives and test performance using an *ex vivo* mouse skin bonding model.

2.0 Materials and Methods

2.1 Peptide Synthesis

Fmoc protected amino acids and low-loading Wang resin were purchased from CEM. All peptides were synthesized using microwave assisted Fmoc SPPS[81] in a Liberty Blue automated system. Briefly, the required amount of resin was swelled in dimethylformamide (DMF) for 5 min. Next, Fmoc deprotection was carried out with 20% piperidine at 90 °C for 60 s. Standard coupling cycles using diisopropylcarbodiimide (DIC)/Oxyma Pure were run at 90 °C for 240 s in each amino acid coupling. For difficult couplings, the temperature was increased to 100 °C and additional reagent equivalents/double couplings were used along with an increased reaction time and addition of urea as a chaotropic agent. Peptides were cleaved from the resin and deprotected with a cocktail of trifluoroacetic acid (TFA), triisopropylsilane (TIS), 1,2-ethanedithiol (EDT), and water (92.5/2.5/2.5/2.5% v/v) at 42 °C for 30 min and then precipitated in −20 °C diethyl ether. Peptide crude products were then dried under vacuum overnight and purified by preparative reversed-phase high-performance liquid chromatography (RP-HPLC) in an Agilent 1260 Infinity II system with a 30 × 100 mm Agilent C18 column at 50 mL min^{-1}. Peptide purity and identity were confirmed via analytical LC-UV/MS in an Agilent 1260 Infinity II system using a 4.6 × 100 mm Agilent C18 column. A gradient of 0% to 40% phase B over 20 minutes was utilized with phase A consisting of water/acetonitrile 5%/formic acid 0.1%/TFA 0.01% and phase B acetonitrile/water 2%/formic acid 0.1%/TFA 0.01% at a flow rate of 1.5 mL min^{-1}. A purity of >95% was determined through HPLC peak analysis. Detailed mass spectrometry data for the peptides along with representative HPLC profiles and crude data can be found in the Supporting Information.

2.2 Peptide Alkene Modification

For N-terminal methacrylation, resin was washed three times with dichloromethane (DCM, VWR) and treated with a 5% v/v solution of methacrylic anhydride (Sigma) in DMF for 5 minutes at room temperature. Following reaction completion, the resin was washed twice with DCM, once with acetic acid, and twice more with DCM then dried. Acid cleavage was then performed as usual. Acrylic anhydride (TCI Chemicals) was used to add acrylate. To switch lysine ε- allyloxycarbonyl (alloc) to (meth)acrylate, alloc containing peptides were deprotected according to a previously published methodology.[215] Briefly, the peptide resin was treated with 3 washes containing 0.25 eq of tetrakis(triphenylphosphine)palladium(0) [Pd(PPh3)4, AK Scientific] and 15 eq of phenylsilane (PhSiH3, Sigma) in DCM at a temperature of 38 °C for 3 min. The resin was then washed and treated with a 5% solution containing methacrylic anhydride or acrylic anhydride and left to react at room temperature for 5 min.

2.3 Circular Dichroism

Circular dichroism (CD) spectra were collected on a JASCO J-810 CD spectrometer with a bandwidth of 1.0 nm in the ultraviolet (UV) region (190–260 nm) using a 0.5 mm quartz cuvette, at 20 °C using a MPTC-490S accessory. To measure the ratio of positive to negative peaks (R_{pn}) and T_m, all samples were dissolved at a concentration of 200 μM using phosphate buffer 1 mM (pH 7.4). Then, different dilutions were prepared to obtain 6.25, 12.5, 25, 50, 100, and 200 μM concentrations of each sample to measure folding at different concentrations. The spectra were obtained with solvent background subtraction and were collected with 10 scans. The R_{pn} parameter was calculated as the ratio of the absolute molar ellipticities at 225 nm and 200 nm:

$$R_{\mathrm{pn}} = \frac{|\theta_{225}|}{|\theta_{200}|}$$

2.4 CLP-PEG Hydrogel Preparation

Hydrogels were prepared from three components: peptide, 8-Arm PEG-Maleimide 40 kDa, a long bearing chain that easily forms a network (Creative PEGworks, USA), and a buffer solvent. Reagents were freshly dissolved in buffer before use and kept on ice until application. Three different formulations of peptide to PEG-Mal were used: CM_{ratio} 1.0, 3.0, and 4.0. Solutions were loaded into syringes and administered to the target site for *in situ* gelation via custom applicators. Peptide concentrations ranged from 3.5 to 16 mM. PEG concentrations were kept at ≈ 4.0 ± 0.5 mM in all cases. Reagents were freshly dissolved in buffer and kept on ice until use. All hydrogels were prepared with freshly made solutions. Peptide selection included peptides that gel within 15 s and 120 s, with light transmittance >85%, and a refractive index of <1.38. For preparing the materials, the components were weighed in a 1.5 mL Eppendorf tube and then ice-cold solvent was added. Mixing was done by 30 s vortex followed by 5 min of centrifugation (10 000 rpm). Solutions were then transferred into two syringes that were capped by custom nozzles and stored on ice until use. After incisional wounds were made, the ice-cold material solution was immediately applied to the wound and the mixing of the two component solutions at murine body temperature resulted in rapid *in situ* gelation. There is a brief time window of ≈ 30–60 s before the material begins to solidify where it can be spread over the wound and molded into a desired shape.

2.5 UVA Irradiation Measurement

UVA irradiance within the photoreactor (LZC-4 V, Luzchem Inc.) was quantified using a calibrated UV sensor (FST100-UV, Firstrate Sensor Co., Ltd.) with a spectral range of 240–370 nm.

Measurements were performed with the sensor positioned at the sample plane to reflect the irradiation conditions experienced by the samples. The photoreactor was allowed to warm for 5 min prior to measurement. The system uses Hitachi T5 FL8BL-B Black Light Blue UV fluorescent lamps (8 W).

2.6 Photo-CLP Hydrogel Preparation

Hydrogels were prepared from three components: peptide, PBS buffer solution, and photoinitiator. The different peptides used are outlined in Table 3.2 while 1-20 mM solutions of Irgacure-2959 (Sigma) and 5-50 mM solutions of lithium phenyl-2,4,6-trimethylbenzoylphosphinate (LAP, Fisher Scientific) were used as photoinitiators. Lyophilized peptide would be weighed out and mixed with the solvent through vortex and centrifugation. After mixing, the solution would be chilled at 4 °C while the peptide folds for 0-24 h. After folding, the solution would be transferred to a 96 well plate and irradiated for 1-20 minutes at 37 °C in a UVA photoreactor (LZC4 V, Luzchem Inc).

Type I rat tail collagen (Corning) hydrogels were prepared as a reference material using the same preparation protocol previously validated by McLaughlin et al. for injectable intramyocardial delivery.[61]

2.7 Rheology

Oscillatory shear measurements of the elastic and viscous modulus (G′/G″) were obtained at 25 °C using a Malvern Kinexus rheometer with 20 mm parallel plate geometry. For a standard hydrogel prepared with 100 μL of volume, a 0.3 mm gap distance based on cylindrical geometry was selected with an oscillation frequency of 1 Hz and a strain sweep range of 0.1-100%.

2.8 Infrared Spectroscopy

Fourier-transform infrared (FTIR) spectra were recorded using a Nicolet iS5 FTIR with an Attenuated Total Reflectance (ATR) iD7 accessory and with a diamond crystal. All spectra were taken at 4 cm^{-1} of resolution with 64 scans in the 4000–500 cm^{-1} range at room temperature. Before measurements, the prepared peptides and hydrogels were freeze-dried. The FTIR spectra of the Amide I region (1750-1550 cm^{-1}) were then fitted by multiple Gaussian peaks, see further details in Supporting Information and Figures S16–S19.

2.9 Molecular Dynamics Simulations

The homology models for the entire set of multipurpose PEG-CLPs (see Figure S5) were obtained using the ColabFold tool.[216] This tool is a free and accessible platform for protein folding and provides accelerated predictions of protein structures and complexes using AlphaFold2. The 3D structure predictions from its sequences are achieved by using multiple sequence alignments (MSA) of related proteins as input for end-to-end training.[217] To build the diverse MSAs, a large collection of protein sequences from databases is searched using both HMMer[218] and HHblits[219] methods, both of which use profile hidden Markov Models.

As a first step in the modeling protocol, a single-stranded structure is generated for the entire set of peptides. These modeled strands were then replicated to generate the triple helix-like structure, using collagen type 1 as a reference.[99] Each peptide was then solvated with 15 Å in each of the 3 cartesian coordinates, using the TIP3P water model, resulting in water boxes of varying sizes depending on the peptide's dimensions. Sodium ions (Na^+) and chloride ions (Cl^-) were added to neutralize each system.

To investigate the self-assembly process of the photoactivated CLPs, MD simulations of triple-helix formation were carried out for Pep-8, Pep-10, Pep-14, and Pep-16. Initial configurations were generated by placing the individual helices at a distance shorter than the nonbonded interaction cut-off. The parameters for the Lys (alloc) residue were defined by analogy with related moieties that had already been implemented in the force field. The charges of the residues were defined with reference to the pKa of each residue at the pH at which the experiments were conducted (7.4).

For each system, six production runs of 100 ns were performed in explicit solvent using the TIP3P water model. The simulations utilized the CHARMM36 force field, as implemented in the GROMACS software package. All simulations were executed under isothermal–isobaric conditions, with periodic boundary conditions applied in all three dimensions. Prior to the production phase, each system underwent energy minimization, followed by 100 ps of equilibration at 300 K, employing a time step of 0.5 fs. Subsequently, production runs were executed with a 2 fs time step. The long-range electrostatic interactions were treated using the particle mesh Ewald method,[220, 221] with a real-space cutoff of 1.2 nm. The same cut-off was applied to Van der Waals interactions. Temperature control was achieved with the velocity rescaling thermostat,[222] using a coupling constant (sT) of 0.6 ps, while pressure was maintained at 1 bar using the Berendsen barostat[223] with isotropic coupling and a time constant (tP) of 1 ps.

All structural analyses and molecular visualizations were performed using Visual Molecular Dynamics (VMD)[224] and ChimeraX software. The determination of the assembly fraction was performed using a homemade Python script, which considered the total number of hydrogen bonds at each simulation time (calculated with the GROMACS hbond tool) and normalized them with respect to the theoretical maximum number of bonds.

2.10 Simulation Analysis

Each peptide model was aligned based on the CA atoms of the backbone to conduct distance measurements along the z-axis, only on the last 200 ns. The focus was on the cysteine residues of each peptide, specifically the sulfur atom, and for those sequences without cysteine, the analysis was conducted at the CA atom of the amino acid in the third position, which was the most common position of cysteine in each of the sequences. To assess the degree of openness at each terminal end of every peptide, the distance from the sulfur atom to the projection onto the z-axis passing through the center of the three strands forming the peptide was measured. Consequently, the distance from each sulfur atom in every chain was measured for each peptide, both at the upper and lower ends, along the last 200 ns of simulation. Additionally, to capture the positional fluctuation of each residue, the Root Mean Square Fluctuation (RMSF) analysis was performed for each peptide, with the initial model serving as a reference point. Similarly, the Root Mean Square Deviation (RMSD) was analyzed, indicating the average change in peptide structure during molecular dynamics relative to the initial simulation point; for both analyses, the last 200 ns of the simulation were also considered (see Figure S6).

2.11 Gelation Time Testing

Gelation time was calculated using fluid mechanics on an inclined plane.[225-227] The methodology presented here was adapted from international standards used to measure oil-like products and thickening agents on inclined planes for the purpose of finding the specific point where the liquid loses its flow characteristics. As fluid viscosity increases, the velocity of the flow reduces until it becomes static, indicating that the substance has transitioned from liquid to solid. The gelation time was measured using a 22.5° inclined plane with 50 μL samples placed on the glass inclined

plane. Sliding time and distance was recorded for up to 3 min (see Table S2) using a mounted 1080p HD iPhone 6 camera (software IOS 13.3) and the individual gel movement was tracked via iMovie (10.4). Average times for all samples (n = 5) were reported. Printable STL files used in the screening are available in https://figshare.com/s/f195a5a27ccfc9072225. Peptides 1 to 21 and control CLP were evaluated at CM_{ratio} of 1.0, 3.0, and 4.0. All experiments were carried out in a double-blind fashion. The operator and data analyzer had no information on the nature of the sample being experimented or processed.

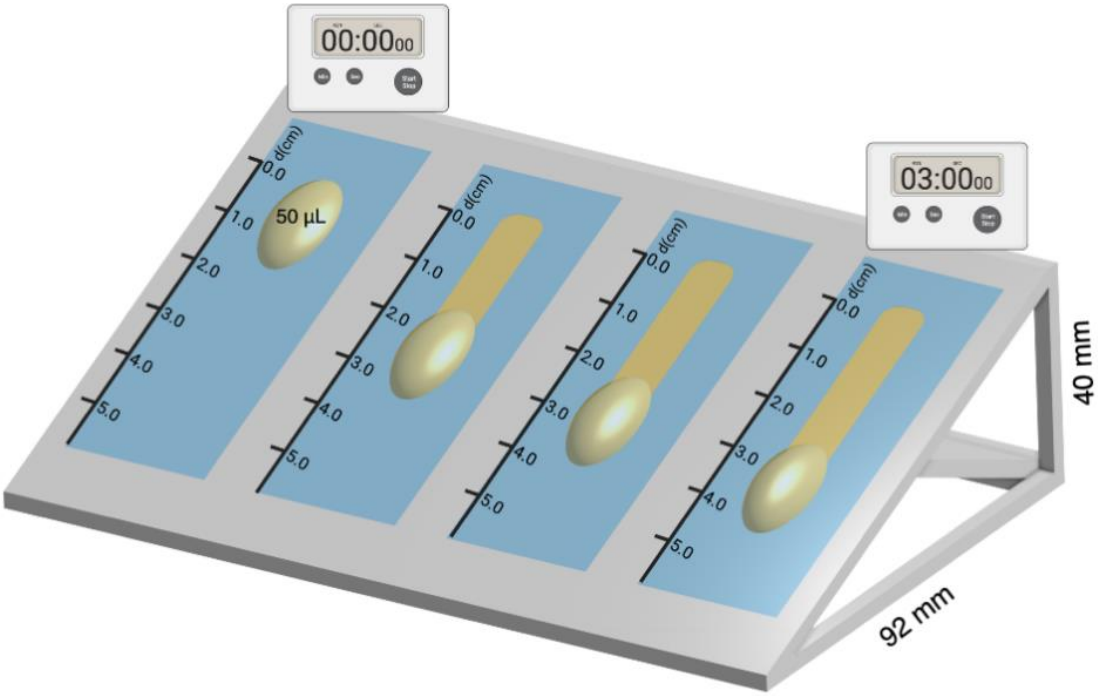

Figure 2.1. 3D render illustrating the system used for determining gelation time. Schematic representation illustrating the device and methodology used for evaluating gelation time using a low volume approach. The render also includes an illustration for the changes (displacement) of the material as a function of the time. Distance travelled was also used as a parameter to evaluate gelation time. Reproduced from *Ross et al. Advanced Functional Materials 2024.*

2.12 Transmittance

The absorbance and transmittance of the hydrogels was evaluated using a SpectraMax M2/M2e microplate reader (Molecular Devices, USA). The hydrogels (20 µL) were placed on a 96-well plate containing 150 µL of PBS, the absorbance was measured at a wavelength of 550 nm. As a control, the absorbance of wells containing 150 µL of PBS was measured. The method for calculating percent transmittance was: % Transmittance = $10^{(2 - \text{absorbance})}$. The peptides studied were 1 to 21, as well as control CLP at the CM_{ratios} of 1.0, 3.0, and 4.0.

2.13 Refractive Index Measurement

The refractive index was measured with an Abbemat 300 refractometer (Anton Paar, Canada) at a temperature of 37 °C. The hydrogel samples were made on a glass slide and transferred into the refractometer sensor where the nD index was recorded and reported.

2.14 Collagenase and Water Content

The stability of the hydrogels was assessed by soaking them in collagenase from Clostridium histolyticum (Sigma-Aldrich, USA) at 5 Unit mL^{-1} in 0.1 M Tris-HCL Buffer containing 5 mM $CaCl_2$ and measuring their loss of mass over time.[61] Percentage of residual weight was calculated as: residual mass (%) = W(total)/W(initial). The calculation of water content was evaluated by comparing the mass of the casted hydrogel against the lyophilized mass.

2.15 Lap-Shear Test

A modified American Society for Testing and Materials (ASTM) F2255-05 standard was utilized to conduct this test. This was performed at a pace of 10 mm min^{-1} on an Instron 3342 universal

testing machine (Instron, USA) and analyzed using INSTRON Series IX/S (Instron, USA) software. The samples consisted of applying the hydrogel to a 0.5 cm^2 section of pig skin. The force and strain of each sample were recorded as it was pulled to failure.

2.16 Viscosity

The viscosity of each formulation was measured using a Brookfield viscometer with an RCT-25-1 spindle. The micrometer ring of the rheometer was first set to zero and then the measuring head was lowered to the zero position. The spindle was tightened and then the micrometer was set to the measuring point (M) allowing for 50 μm of space between the spindle and the bottom plate. Equal volumes of peptide-5 solution and 8-arm PEG maleimide (100 μL total) were mixed and added to the center of the plate. The spindle was fully lowered, and excess sample was removed. The viscosity was measured between 0–200 s^{-1} shear rate at 25 °C using Rheo3000 v2 software.

2.17 Denaturation Temperature

The thermal properties of the gel were measured via differential scanning calorimetry analysis with a DSC-Q200 (TA instruments, USA). 8-10 mg of sample of the various CM_{ratio} were evaluated. The samples were equilibrated at 20 °C and then ramped up at 20 °C min^{-1} to 100 °C, and the total heat flow was recorded. The calibration standard used was Indium.

2.18 Material Porosity

Pore size was measured using a standard cryo-scanning electron microscopy (SEM) protocol previously established.[61] Briefly, samples were freshly prepared and flash-frozen with liquid nitrogen before being loaded into a Tescan VegaII XMU (20 kV) under ≈ 35 Pa pressure with a −50 °C cryostage. SEM images of hydrogels were captured at different magnifications. This

method of rapid freezing and measurement helps to preserve the material's structure and pore size before processing.[228] Hydrogel pore diameter was calculated from the average pore area observed in different regions of the gel using Fiji software.

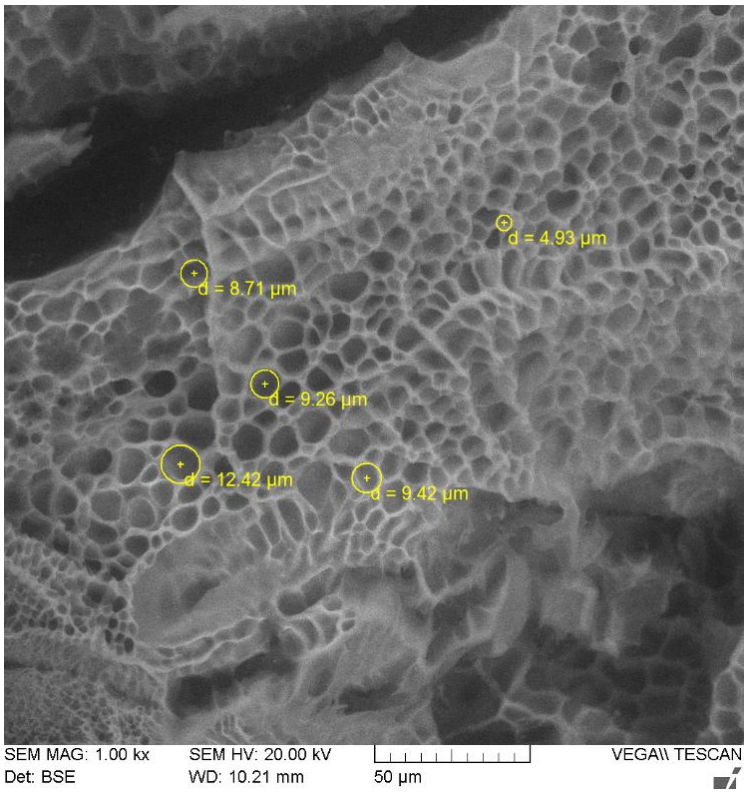

Figure 2.2. Fiji method of measuring pore size. Using the diameter tool, 50 measurements were taken from four independent sites per formulation.

2.19 Photo-CLP cytocompatibility

The cytotoxicity of the hydrogel was investigated using *in vitro* using a human skin fibroblast (HSF) culture. For 2D cytocompatibility, the hydrogels were prepared and then sterilized by incubation in 70% ethanol for 5 min, UVA exposure for 20 min, and washing with sterile PBS several times before being added to the tissue culture plate wells.[229] HSF were maintained in Dulbecco's Modified Eagle Medium/Nutrient Mixture F-12 (DMEM/F-12) media supplemented

with 10% fetal bovine serum (FBS) (Gibco) and 1% penicillin/streptomycin until 90% confluency. After 24 h, the live/dead assay was performed. Briefly, HSF were stained using a Calcein-AM and Ethidium Homodimer-1 viability kit (Fisher Scientific) according to the manufacturer's instructions. For the positive control, cells were treated with 10% dimethyl sulfoxide (DMSO) for 24 h and then 70% Ethanol for 30 mins before the live/dead assay. For 3D cytocompatibility tests, HSF cells were trypsinized, counted, and resuspended in serum-free DMEM. The cell suspension was mixed with Pep 10 in 1x PBS and 20 mM LAP to produce a peptide-based hydrogel at 5% w/v containing 4×10^6 cells/mL. LAP allowed the use of short UVA-irradiation times (5 to 60 s) to yield hydrogel formation in a 96 well culture plate (Corning cat# 3595). Culture medium was then immediately added. Each condition was performed in triplicate, and three random images were taken for each experimental group. Stained cells were imaged by fluorescence microscopy. Total cell numbers were calculated using ImageJ2 software (NIH, USA).

2.20 Wound Closure and Mechanical Strength

A modified ASTM F2458-05 test measured tissue adhesive and sealant wound closure strength.[230] All animal care and procedures were performed in strict compliance with protocols approved by the Institutional Animal Care and Use Committeeat the University of Ottawa Heart Institute. Skin samples were obtained from a cohort of male and female C57BL/6 mice (Charles Rivers Laboratories, Canada). The mouse skin was partitioned into strips of 30 ± 5 mm length, 5 ± 0.5 mm width, and 0.7 ± 0.2 mm thickness. A surgical blade was then used to completely sever the samples at mid-length and simulate a wound. The simulated wound was treated with 30 µL of hydrogel sample to bond the severed skin pieces back together. A few drops of PBS were applied to the ends of the skin strips every 5 min until testing to prevent the mouse skin from drying out. The hydrogel-bonded mouse skin was clamped on an Instron 3342 universal testing machine

(Instron, USA) at a 5 mm distance from the simulated wound. The Instron transductor sensor Model 2519 – 101 (Instron, USA) was used to record the formulation's resistance force during the tensile test at a crosshead speed of 5 mm min^{-1} until material failure. For the control group, the same clamping procedure was used but with an uncut skin sample. Young's modulus and strain % were obtained from the stress-strain graphs. Young's modulus calculations were carried by Instron Series IX/s advanced material tester – version 8.30.

For compressive testing, the same Instron machine was used with ASTM D695 standards.[231] Cylindrical hydrogel samples were compressed at 5 mm min^{-1}. The compressive modulus was calculated from the initial linear section of the stress-strain curves.

2.21 Design and 3D Printing of the Hand-Held Device and Nozzles

All 3D printed components were designed using Solidworks (Dassault Système) and printed on a Form 3B Stereolithography 3D printer (Formlabs). The structural components for the handheld device were printed using Black Resin V4 (RS-F2-GPBK-04) while the mechanical components were printed using Durable Resin V1 (RS-F2-DUCL-02). For the nozzles, the topical mixer was printed using Flexible 80A Resin V1 (RS-F2-FL80-01) while both injection mixers were printed using Clear Resin V4 (RS-F2-GPCL-04). All components for the hand-held device were printed at a resolution of 100 µm while the nozzles were printed at a resolution of 50 µm with automatically generated supports then washed using isopropanol and cured with a combination of UV light and heat treatment. In https://figshare.com/s/f195a5a27ccfc9072225 printable STL files are made available at no cost.

2.22 Skin Incision Sealing Model

C57BL6 female mice (12–14 weeks, weighing ≈ 22–25 g; Charles River Laboratories) were housed in groups of five until surgery. All animal care and procedures were approved by the University of Ottawa Animal Care Committee and performed in accordance with the National Institute of Health Guide for the Care and Use of Laboratory Animals. Before surgery, mice were given an epidural injection of buprenorphine and put under using general anesthesia (2.5% isoflurane). Dorsal hair was shaved, and the skin was prepared using ethanol swabs. Then, 1-cm full-thickness incisions were made on the back of each mouse using sterile scalpel blades (#15; Integra Miltex).[232] For suture-closed incisions, four evenly spaced simple interrupted knots were used to close a 1-cm incision using 7-0 nylon suture (#SN5699G; Medtronic; Monosof Black 18″ P-13 cutting). For the BioGlue control, 48 μL of bovine serum albumin and 12 μL of glutaraldehyde were topically applied to the incision site as specified in the manual. For the peptide/PEG-maleimide formulation, 30 μL peptide-5 and 30 μL of PEG-maleimide were mixed and topically applied to the incision site using a custom-made nozzle tip (CM_{ratio} 4.0). The mice were allowed to recover on heating pads until mobile and were housed individually. Incisions were assessed on days 1, 3, and 7 post-surgeries for any signs of infection, suture removal, or bleeding, and mice with any of these conditions were removed from the study. After harvesting of the skin, strips of 30 ± 5 mm length, 5 ± 0.5 mm width, and 0.7 ± 0.2 mm thickness were used for mechanical testing.

2.23 Histology

Skin tissue from the wound site was fixed in 4% paraformaldehyde for 72 h. Then, skin samples were washed and embedded in paraffin. Hematoxylin and eosin (H&E) staining was done

according to the standard protocol provided in a Leica Autostainer XL (Leica Biosystems, Buffalo Grove, IL). Skin epidermal thickness was measured at six different points along the wound site using Fiji and the average thickness was calculated for each mouse wound.[233] Masson's trichrome stains were done manually using a standard protocol with the Trichrome stain kit (Sigma-Aldrich, St. Louis, MO). To determine the area of blue stained collagen in Masson Trichrome images, a 400 μm x 400 μm region was selected inside the wound region using Fiji. Then, the collagen area for each skin section was calculated by taking the blue stained area and dividing it by the total selected area.[234] For immunohistochemistry, tissue sections were deparaffinized and washed with PBS and citric acid. Sections were blocked with goat serum and incubated at 4.0 °C with the specific primary antibody: Ab64693 (1:200) for CD206. Further labeling was performed with specific secondary antibodies: AF488 anti-rabbit secondary (ThermoFisher, A-11008 at 1:500 dilution). The fixed cell nuclei were subsequently stained with 4',6-diamidino-2-phenylindole (DAPI). Images of the samples were obtained under a microscope, with each section taken at 10× and 40× magnification, respectively.

2.24 *Ex Vivo* Pig Cornea Model Mounting

Pig eyes were obtained from certified local farms. Freshly harvested eyes were transported in an ice bucket and processed the same day. Eyes were disinfected in iodine-polyvinylpyrrolidone (PVP, 10%) for 2 min and then transferred to sterile 0.1% sodium thiosulphate solution for 1 min before immersion in sterile saline solution for 2 min. Using a scalpel blade, a small (5–8 mm) incision was made at the equatorial and carefully extended by 360° around the entire eyeball while avoiding perforation of the underlying choroid layer. Once the cut was made, the ciliary body-choroid was pulled downwards using forceps to avoid touching the corneoscleral disk. The corneoscleral disk was held in place using a pair of tweezers and the retina was peeled off the

inside of the corneoscleral disk using another pair of tweezers. Then, the corneoscleral disk was rinsed with PBS and placed in DMEM media containing 10% FBS, 1% Gentamicin antibiotics, and HEPES 15 mM. The corneoscleral disk was placed on the base of the perfusion chamber (size 18 mm, 45° angle).[235] The chamber was twisted clockwise while maintaining downwards pressure on the chamber base to prevent sliding of the cornea and to tightly seal it in place. The chamber was then filled with DMEM media with 5% dextran using two syringes attached to two irrigation ports that were then attached to maintain an intracorneal pressure within the physiological range.

2.25 Injection of Material into Pig Cornea

Following the dissection and mounting of the cornea on the *ex vivo* perfusion chamber, a 6 mm biopsy punch marked with hydrophobic pen ink was used to gently mark the central corneal surface (apex). A 2 mm incision was then made at the edge of this mark to initiate the dissection of an intrastromal tunnel, which was carefully enlarged using a crescent knife to create an intrastromal pocket under the marked corneal surface. For intrastromal injections, each cornea was slightly deflated and 30 µL of the peptide-based material or Viscoat was injected into the stromal pockets. Optical coherence tomography (OCT) imaging of injected corneas at 3 timepoints (before gel injection, after gel injection, and at 24 h) was done to assess the ability of the gel to remain constant in the corneal stroma. This was done by measuring the gel thickness in Fiji.

For the cornea reshaping experiments, corneal topographic images were taken using the CT-1000 optical coherence topographer and used to measure the change in corneal curvature before and after the injection of the peptide-based material or Viscoat. Measurements of corneal curvature were taken from two average K values of steepest meridian and the one perpendicular to it. Images were taken of the natural eye curvature before injection, with a pocket, after the injection, and of

the injection with a rigid contact lens (Centracone). Intraocular pressure was held at a maximum across all images, and the natural lubrication of the eyes was mimicked with saline and glycerol.

2.26 Burst Pressure Testing of Treated Pig Corneas

The same procedure to dissect and mount the pig corneas described above was followed. A perforation was created using a 4 mm biopsy punch at the corneal apex going halfway through the cornea. Following this, a 2 mm biopsy punch was inserted in the middle of the 4 mm perforation to fully penetrate the cornea. Treatment was applied to fill the perforation and the Luer locks of the cornea chamber system were sealed. The flow rate on the syringe pump was set to a steady rate of 18 mL h^{-1}, and the pressure was monitored until the pressure peaked due to the cornea bursting at the sealed perforation site. Windaq data acquisition software was used to monitor the pressure.

2.27 CLP-PEG *In Vitro* Human Cardiac Endothelial Cell Culture and Viability Assay

Human cardiac endothelial cells (HCECs) were cultured in tissue culture plates for 24 h and maintained in HCEC media (Sigma, C22022). The injectable PEG-Pep-5 hydrogel CM_{ratio} 1.0 formulation was pre-cast in two sterilized glass slides in a humidity box and in a 4 °C for 24 h. HCECs (1×10^4 cells per well) were seeded on top of PEG-Pep-5 hydrogel pieces after washing with PBS in a 96-well plate. After 24 h, HCECs were stained using a Calcein-AM and Ethidium Homodimer-1 viability kit (ThermoFisher Scientific, Cat#L3224) according to the manufacturer's instructions. Stained cells were imaged by fluorescence microscopy, and nine random images were taken for each experimental group. Total cell numbers were calculated using ImageJ software (NIH, USA). Each condition was performed in triplicate.

2.28 Myocardial Infarction Model and Intramyocardial Injection

All animal care and procedures were approved by the University of Ottawa Animal Care Committee and performed in accordance with the National Institute of Health Guide for the Care and Use of Laboratory Animals. MI was induced in 8-week-old C57BL/6 female mice (Charles River) and treatment delivery was performed using a previously established intramyocardial injection protocol.[61] Briefly, mice were anesthetized (2.5% isoflurane), intubated, and the heart was exposed via a fourth intercostal thoracotomy. The left anterior descending coronary artery was then ligated just below its emergence from the left atrium. At 1-week post-MI (baseline), mice were randomly assigned to receive one of 2 treatments: (1) PBS (control) and (2) Pep-5-PEG CM_{ratio} 1.0. The treatment was administered in five equivolumetric intramyocardial injections (10 µL each site, 50 µL total) through a G27 needle using a minimally invasive echocardiography-guided closed-chest procedure. Mice were euthanized by terminal anesthesia at 4 weeks post-treatment and hearts were collected for histological analysis.

2.29 Echocardiography and Strain Analysis

Transthoracic echocardiography was performed on parasternal long-axis views using a Vevo3100 system in B mode with a MX400 series real-time microvisualization scanhead probe and analysis performed with its accompanying Vevo LAB 3.1.1 software (VisualSonics). The imaging was carried out at 7 days (right before the treatment) and 4 weeks post-MI. To assess contractility, cardiac strain analysis was performed through the longitudinal axis. The longitudinal endocardial strain at the time of aortic valve closure (AVC, representing end systole) in segment 6 (anterior apex segment), corresponding to the infarct zone area, was calculated. Results for both

echocardiography and strain analyses were averaged from the analysis of two researchers blinded to the treatment groups.

2.30 *Ex Vivo* Imaging of CLP-PEG Hydrogel

The Pep-5-PEG hydrogel was labeled by adding Alexa-Fluor594 dye (25 nmol of dye per hydrogel) to the mixture prior to injection to the infarcted mouse heart, as described above. Animals were sacrificed at 2 and 7 days after treatment, and hearts were harvested and imaged *ex vivo* by IVIS Spectrum (PerkinElmer) to visualize Pep-5-PEG hydrogel retention within the hearts ($\lambda_{excitation}$: 570 nm; $\lambda_{emission}$: 640 nm).

2.31 Statistical Analysis

Statistical analysis was performed using KaleidaGraph or GraphPad Prism software. Statistically significant differences between more than two groups were determined by one-way analysis of variance (ANOVA) at a significance set at $p<0.05$. Statistical significance of data with two groups was performed using a two-tail unpaired t-test set at a $p<0.05$. Data was reported as mean ± standard deviation.

3.0 Results

3.1 Multipurpose On-the-Spot Peptide-Based Hydrogels for Skin, Cornea, and Heart Repair

The data presented in this section has been published as follows: A. Ross, X. Guo, A. Mercado Salazar, S. D. Garcia Schejtman, J. El-Hage, M. Comtois-Bona, A. Macadam, I. Guzman-Soto, H. Takaya, K. Hu, B. Liu, R. Tu, B. Siddiqi, E. Anderson, M. Muñoz, P. Briones-Rebolledo, T. Ning, M. Griffith, B. Rotstein, H. Poblete, J. Li, M. Ruel, E. J. Suuronen and E. I. Alarcon. Multipurpose on-the-spot gelling peptide-based engineered materials for skin, cornea, and heart repair. *Adv Funct Mater* 2024;34:202402564.

3.1.1 Brief Introduction to the Results for Aims 1 and 2

Herein, a low-volume rapid screening approach to identify candidate self-assembling peptide structures for building "on-the-spot" adhesive biomaterials with tunable mechanical properties ranging from 1 to 100 kPa in strength was used. The engineered peptide sequences feature a glycine-flanked cysteine at each terminus; this specific molecular orientation was designed to reduce steric hindrance during network formation, ensuring that the reactive sulfhydryl groups remain accessible despite the bulk of the triple-helical trimer.

As a structural polymeric backbone, polyethylene glycol, an FDA approved synthetic polymer,[236] with demonstrated safety and stability, was utilized. Long-chain, multi-armed PEG architectures bearing terminal maleimides were selected to facilitate the efficient formation of polymeric networks. By leveraging a Michael-addition reaction between these maleimide groups and the peptide sulfhydryls at physiological pH, rapid formation of adhesive 3D structures was achieved. This material design is unique in its integration of dual reinforcement mechanisms: covalent

chemical bonding and hierarchical molecular assembly. This biomimetic approach mirrors the strategies found in native tissues to maintain mechanical stability and structural integrity.[237] Furthermore, this specific chemistry minimizes potential cross-reactions with host proteins *in vivo* compared to more reactive groups like acrylamides, resulting in stable, long-term covalent bonds.[238, 239]

While the concept of "on-the-spot" peptide-PEG assembly is straightforward in principle, the practical implementation requires navigating complex structural and chemical constraints that often necessitate challenging peptide synthesis. The screening process allowed for the high-throughput evaluation of over 200 formulations across more than 20 distinct peptide sequences. This systematic interrogation was essential to identify the optimal candidate for clinical translation. Optimal peptide sequences were identified as those that: (1) formed a triple helix in solution and showed stability at physiological pH (7.4) and temperature (37 °C); (2) showed suitable gelation times, e.g., 15–120 s; and (3) formed 3D materials with suitable physical properties for use in soft tissue repair (e.g., transmittance, refractive index, denaturation temperature, water content, and resistance to collagenase degradation).

3.1.2 Peptide Engineering and Validation

Collagen is the most abundant protein in the human body, serving as the primary structural scaffold for tissues ranging from mineralized bone to highly vascularized myocardium.[89] The immense diversity in the mechanical properties of these tissues is a direct consequence of the unique nanosized triple-helical structure of collagen and its ability to macro-assemble into higher-order fibrils.[85, 89] Mimicking this supramolecular assembly is possible through the use of CLPs, where the repeating trimer sequence Proline-Hydroxyproline-Glycine may be utilized to drive triple-helix

formation. While it is well-established that more than four POG repeats are required to yield a stable helix, the process remains dynamic and is often thermodynamically favored when the CLP is conjugated to a polymeric backbone, which stabilizes the folded state.[85, 97]

The generated peptide library included 21 CLP sequences, including a reference collagen peptide previously utilized in implantable cornea development (Table 3.1).[198] The POG unit was selected as the repetitive building block due to its superior ability to stabilize the triple helix through an extensive network of inter-chain hydrogen bonds.[240] The synthesized sequences ranged from 18 to 38 amino acids in length (see Table S1 for mass spectrometry and crude purity data). To minimize steric repulsion and increase reactivity in peptides containing cysteines, unless otherwise mentioned, each cysteine residue was flanked by two flexible glycine residues that allowed the sulfhydryl group to move in space.[241] Further, in designing the peptide sequences, using terminal cysteines was avoided as this could make synthesis challenging and increase the cost.[242] Thus, the GCG motif was added to each end of the peptide sequences with the repetitive POG unit, from $(POG)_4$ (Pep-1, 18 amino acids) to $(POG)_{10}$ (Pep-7, 36 amino acids; see Table 3.1).

Notably, the addition of two cysteine residues did not result in significant formation of dimers in solution (Figure S1). In phosphate buffer (pH 7.4), the availability of free sulfhydryl groups was found to be greater than 90%, comparable to free L-cysteine (Figure S2). First, the impact of peptide length on the ability of the CLPs to maintain a stable triple helix at human physiological temperature was assessed. Analysis of the melting curves revealed that increasing the sequence length led to more pronounced cooperative melting transitions, confirming the formation of a stable, folded tertiary structure (Figure S3). To assess the functional impact of changes in the peptide sequence on 3D structure assembly when using nucleophilic Michael-addition to PEG-maleimide, a series of peptide sequences were designed and synthesized using Pep-5 as a building

block as it is cost-effective, has >70% crude yield (Table S1), and displayed a cooperative melting behavior (Figure S3). Table 3.1 summarizes the main modifications for this group of peptide sequences (Pep-8 to Pep-21).

Sample	Sequence	Sequence structural features	R_{pn}[a)]	T_m (°C)[b)]
Pep-1	NH_2-GCG**(POG)**$_4$GCG-OH	4 POG repetitive units containing two glycine flanking cysteines at each end	0.032 ± 0.005	44.1 ± 0.8
Pep-2	NH_2-GCG**(POG)**$_5$GCG-OH	5 POG repetitive units containing two glycine flanking cysteines at each end	0.034 ± 0.001	49.0 ± 1.0
Pep-3	NH_2-GCG**(POG)**$_6$GCG-OH	6 POG repetitive units containing two glycine flanking cysteines at each end	0.072 ± 0.008	52.0 ± 2.0
Pep-4	NH_2-GCG**(POG)**$_7$GCG-OH	7 POG repetitive units containing two glycine flanking cysteines at each end	0.084 ± 0.003	54.1 ± 0.4
Pep-5	NH_2-GCG**(POG)**$_8$GCG-OH	8 POG repetitive units containing two glycine flanking cysteines at each end	0.087 ± 0.002	59.0 ± 3.0
Pep-6	NH_2-GCG**(POG)**$_9$GCG-OH	9 POG repetitive units containing two glycine flanking cysteines at each end	0.094 ± 0.002	64.0 ± 4.0
Pep-7	NH_2-GCG**(POG)**$_{10}$GCG-OH	10 POG repetitive units containing two glycine flanking cysteines at each end	0.094 ± 0.001	50.0 ± 1.0
Pep-8	NH_2-GGG**(POG)**$_8$GCG-OH	Replacing amino terminal cysteine with glycine in the 8 POG repetitive containing sequence	0.113 ± 0.001	61.9 ± 0.4
Pep-9	NH_2-GCG**(POG)**$_8$GGG-OH	Replacing carboxy terminal cysteine with glycine in the 8 POG repetitive containing sequence	0.118 ± 0.002	49.4 ± 0.2
Pep-10	NH_2-GGG**(POG)**$_8$GGG-OH	Replacing both cysteines with glycine in the 8 POG repetitive containing sequence	0.120 ± 0.002	55.9 ± 0.2

Pep-11	NH_2-GGG**(POG)$_3$**(PCG)$_2$**(POG)$_3$**GGG-OH	Cysteine shift to middle of sequence in the 8 POG repetitive containing sequence	0.054 ± 0.002	43.1 ± 0.7
Pep-12	NH_2-GGG**(POG)$_2$**(PCG)**(POG)$_5$**GCG-OH	Amino terminal cysteine shift to centre of sequence in the 8 POG repetitive containing sequence	0.078 ± 0.001	50.7 ± 0.3
Pep-13	NH_2-GCG**(POG)$_5$**(PCG)**(POG)$_2$**GGG-OH	Carboxy terminal cysteine shift to centre of the 8 POG repetitive containing sequence	0.091 ± 0.001	50.5 ± 0.3
Pep-14	NH_2-GGG**(POG)$_2$**(PCG)**(POG)$_2$**(PCG)**(POG)$_2$**GGG-OH	Both cysteine shift to centre of sequence in the 8 POG repetitive containing sequence	0.074 ± 0.003	39.0 ± 0.3
Pep-15	NH_2-GCG**(POG)$_4$**POV**(POG)$_3$**GCG-OH	Disrupting folding by replacing one POG by POV at the centre of the sequence in the 8 POG repetitive containing sequence	0.028 ± 0.001	45.0 ± 2.0
Pep-16	NH_2-GCG(PPG)$_8$GCG-OH	Disrupting folding by replacing hydroxyproline with proline in the 8 POG repetitive containing sequence	0.007 ± 0.001	43.0 ± 2.0
Pep-17	NH_2-GC**(POG)$_8$**CG-OH	Removing glycine spacer in the 8 POG repetitive containing sequence	0.080 ± 0.002	58.0 ± 2.0
Pep-18	NH_2-GCV**(POG)$_8$**VCG-OH	Replacing glycine with valine as spacer in the 8 POG repetitive containing sequence	0.055 ± 0.001	65.0 ± 3.0
Pep-19	NH_2-GCR**(POG)$_8$**RCG-OH	Replacing glycine with arginine as spacer in the 8 POG repetitive containing sequence	0.081 ± 0.001	65.0 ± 4.0
Pep-20	NH_2-GCC**(POG)$_8$**CCG-OH	Multiple cysteine residues at both ends in the 8 POG repetitive containing sequence	0.062 ± 0.001	51.4 ± 0.6

Pep-21	NH_2-G**C**G**(POG)$_2$**(P**C**G)**(POG)$_2$**(P**C**G)**(POG)$_2$**G**C**G-OH	Multiple cysteine residues at ends and middle in the 8 POG repetitive containing sequence	0.055 ± 0.003	47.9 ± 0.3
CLP	NH_2-**C**G(PKG)$_4$**(POG)$_4$**(DOG)$_4$-OH	Control peptide	0.071 ± 0.009	42.0 ± 1.0

a) Peptide concentration: 200 μM; PBS is phosphate buffered saline (1.0 mM) pH 7.4 at 25ºC.

b) Representative melting curves are included in Figure S3 (Supporting Information).

Table 3.1. Sequences, including structural features, ellipticity, and denaturation temperature for on-the-spot peptide sequences prepared in this study. Further characterization of the peptides can be found in the Supplementary Information (Table S1). To facilitate visualization of the structural changes carried out, POG repetitive sequences and C residues are bolded in black and red, respectively. Peptide concentration: 200 μM; PBS is phosphate buffered saline (1.0 mM) pH 7.4 at 25 °C. Reproduced from *Ross et al. Advanced Functional Materials 2024.*

To differentiate between the triple-helix conformation and the poly(Pro)-II helix conformation, the R_{pn} parameter was utilized (defined as the ratio of the 225 nm to the 200 nm circular dichroism signal).[243] While poly(Pro)-II helices exhibit negligible R_{pn} values (<0.005), native collagen typically displays values ≈ 0.12.[243] Pep-1 to Pep-8 presented R_{pn} values ≥ 0.035 ± 0.004, which corresponds to ≈ 50% of the R_{pn} value measured for the CLP control sequence (≈ 0.071). Further, the structural G-X-G(POG)$_n$G-X-G motif, with X being G or C, and n > 7 results in R_{pn} values larger (0.087–0.084) than those measured for the control CLP, which was previously shown to assemble into a triple helix.[244]

Upon screening of the different lengths, sequences Pep-5 and Pep-6 showed the best ellipticity and higher denaturation temperature. The need for having the structural POG repetitive unit to yield highly elliptical peptides is illustrated when the POG repetitive unit is replaced with POV (Pep-15) or PPG (Pep-16), for example. In peptides whose peptide ellipticity is disrupted, such as Pep-15 that bears a single G to V substitution, there is no cooperative denaturation behavior, which aligns well with the low R_{pn} value of 0.028. Similar results were observed for Pep-16, which has the lowest R_{pn} value (0.007) of the peptides synthesized. Pep-5 increased its R_{pn} value as a function of the peptide concentration, similar to the control CLP (Figure S4). The observed concentration dependence of the R_{pn} value and denaturation cooperativity is significant, as it suggests an intermolecular, multi-chain process that mimics the cooperative assembly of native collagen. Further, the presence of cysteine decreases the peptide packing as seen by comparing the ellipticity of Pep-5 versus Pep-10.

Molecular dynamics (MD) calculations suggested that Pep-5 exhibits a divergent packing profile compared to the rest of the screened library. This is likely a synergistic effect of the internal cysteine residues and the specific length of the POG chain (Figure S5). Root Mean Square

Fluctuation (RMSF) analysis (Figure S6) revealed that while most of the peptide remains stable, Pep-5 exhibits significantly higher positional fluctuations at the N-terminus (residues 1–5), where the reactive cysteine is located. However, despite this fluctuation, Root Mean Square Deviation analysis of the entire peptide over the simulation time demonstrates high structural stability in all peptides, indicating for Pep-5 that this open conformation at the upper end is kept over time, potentially increasing the availability of the sulfhydryl group for subsequent crosslinking reactions.

In summary, the foundational peptide sequences, in particular Pep-1 to Pep-8, present suitable self-assembling properties for testing their ability to form on-the-spot hydrogels for soft tissue and organ applications. In the next section, the rationale and main findings for the preparation and testing of hydrogels using the peptide library developed herein is presented.

3.1.3 Fabrication of 3D Materials for Soft Tissue Repair

The hydrogel design is centered on a multi-arm polyethylene glycol polymer, crosslinked *in situ* through bio-orthogonal reactivity with engineered self-assembling peptides. PEG is a hydrophilic, cytocompatible polymer with extensive FDA approval, making it an ideal candidate for clinically translatable scaffolds.[236, 245, 246] As the PEG molecule itself possesses little chemical reactivity, a multi-armed maleimide functionalized (PEG-maleimide) version of this polymer to allow *in situ* assembling into a 3D material was used. Maleimide was selected as the electrophilic Michael-addition acceptor due to its superior kinetic profile and higher reactivity compared to other common groups, such as acrylamides.[238] Rapid kinetics are important to create a gel within a clinically relevant timeframe and to ensure complete reactivity to minimize cross-reactions upon application to the tissue.

For the nucleophilic Michael-addition donor, the sulfhydryl group of the natural amino acid cysteine was chosen for its ability to selectively and rapidly form stable Michael adducts.[238, 239] The peptide design, which incorporates two or more cysteine residues per strand (Table 3.1), enables high-order network dynamics. Specifically, if each CLP monomer reacts with two PEG-maleimides, the subsequent assembly of three monomers into a triple helix brings together six potential PEG handles. This creates unique network dynamics that result in the rapid formation of a durable, cytocompatible gel for tissue engineering. It is important to note that these large trimer structures are susceptible to steric hindrance; consequently, the removal of glycine spacer residues leads to significantly less efficient network formation and tissue bonding (Figure S7).

A simplified schematic of this peptide-PEG assembly and the low-volume screening strategy is provided in Figure 3.1A. A critical factor in this assembly is the stability of the maleimide handle in carbonate buffers due to its susceptibility to hydrolysis. While maleimide exhibits moderate stability at pH 7.4, it remains stable for up to 90 minutes at 4.0 °C (Figure S8). Therefore, the experimental protocol involves keeping the reagent solutions on ice until application to the tissue, at which point physiological temperatures trigger rapid gelation. Furthermore, having the hydrogels formed within 1/10th of the half-life of the maleimide in solution (i.e., < 5 min) was used to minimize potential side reactions. During the screening process (Figure S9), the material's properties were evaluated across three different peptide:PEG-maleimide ratios (CM_{ratio}): 1.0, 3.0, and 4.0. For peptides bearing two cysteines, a CM_{ratio} of 4.0 represents a stoichiometric balance where maleimide and cysteine residues are equimolar.

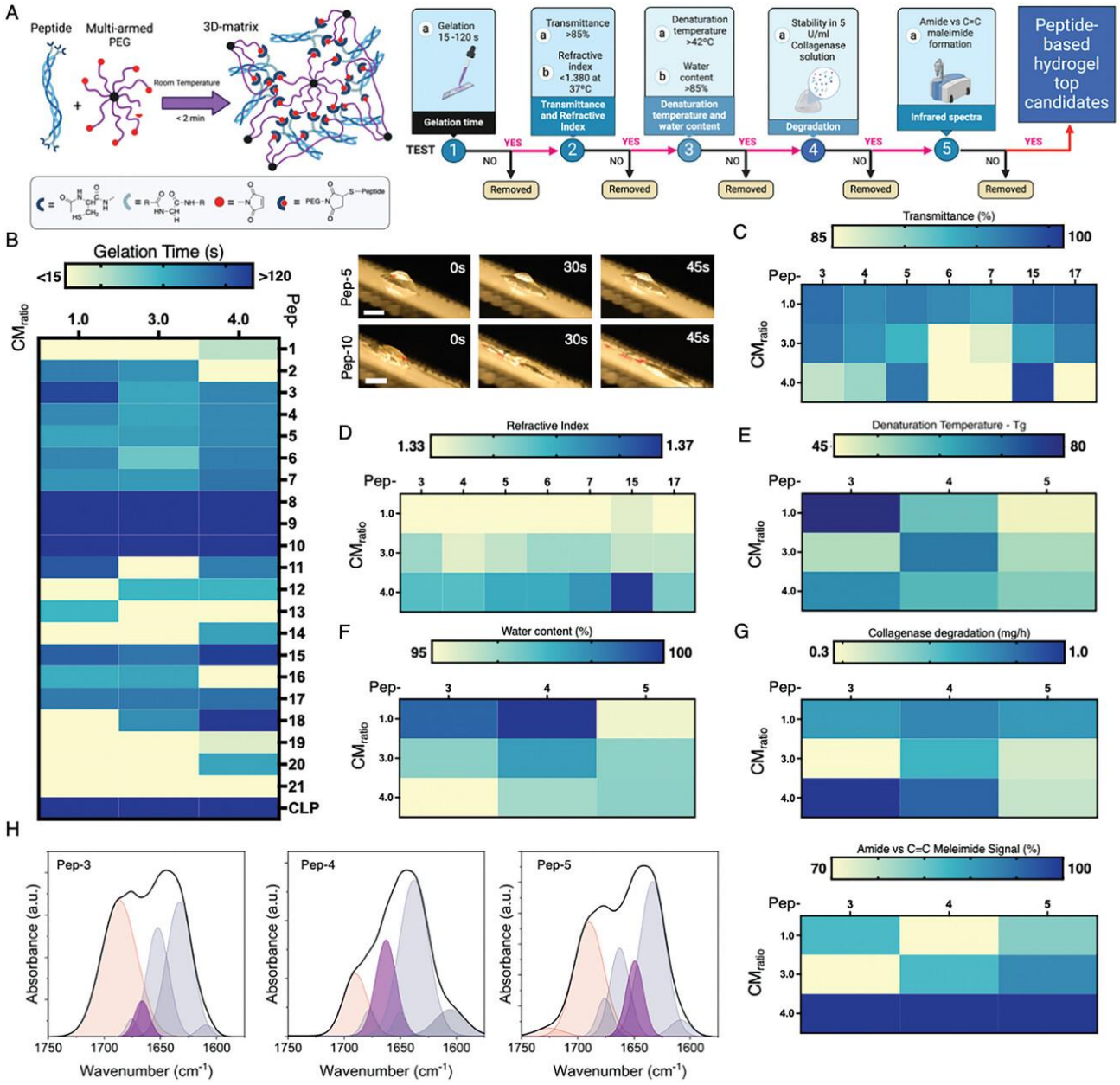
A
Peptide
Multi-armed PEG
3D-matrix
Room Temperature
< 2 min
Gelation 15 -120 s
Gelation time
Transmittance >85%
Refractive index <1.380 at 37°C
Transmittance and Refractive Index
Denaturation temperature >42°C
Water content >85%
Denaturation temperature and water content
Stability in 5 U/ml Collagenase solution
Degradation
Amide vs C=C maleimide formation
Infrared spectra
Peptide-based hydrogel top candidates
TEST
YES
NO
Removed
B
Gelation Time (s)
<15
>120
CMratio
1.0
3.0
4.0
Pep-
CLP
Pep-5
Pep-10
0s
30s
45s
C
Transmittance (%)
85
100
D
Refractive Index
1.33
1.37
E
Denaturation Temperature - Tg
45
80
F
Water content (%)
95
100
G
Collagenase degradation (mg/h)
0.3
1.0
H
Pep-3
Pep-4
Pep-5
Absorbance (a.u.)
Wavenumber (cm-1)
1750
1700
1650
1600
Amide vs C=C Meleimide Signal (%)
70
100

Figure 3.1. Engineered peptides for on-the-spot soft tissue repair. A) *Left*: schematic depiction for the strategy used in this study for the *in situ* assembling of the materials. Assembly of the hydrogel takes place within minutes at room temperature. Some of the key chemical motifs of the material components are depicted at the bottom of the schematic. *Right*: flow diagram showing the tests used to screen material formulations. This methodology was designed to narrow down the number of candidate formulations. B–H) Heatmaps are used to display changes in the properties measured following the schematic in Figure 3.1A. Each figure contains a colour scale illustrating changes in the parameters of materials with different CM_{ratio} and peptide formulations (abbreviated as Pep, raw data available in Table S2, n = 5) for: (B) *Left*: gelation time (s) and *Right*: representative still images of two selected peptide formulations (50 µL, CM_{ratio} of 4.0) taken at 0, 30, and 45 s after positioning the samples at a 22.5° inclination. Scale bar is 2 mm; (C) Transmittance (%); (D) refractive index; (E) denaturation temperature (°C); (F) water content (%); (G) collagenase degradation (mg h^{-1}); and (H) *Left*: ATR-FTIR (with the respective deconvoluted Gaussian fit) spectra of selected peptides at CM_{ratio} 1.0, where the light blue peaks correspond to the different Amide I signal of each peptide, and the light red and violet peaks correspond to the C = O and C = C of PEG-MAL, respectively. Experimental details are in the Materials and Methods and the Supplementary Information. Reproduced from *Ross et al. Advanced Functional Materials 2024.*

To identify the most promising peptide candidates for *in situ* gelation, a rigorous multi-parameter screening process based on clinically relevant benchmarks was established. To select peptides that would allow for rapid *in situ* gelation, a gelation time cut-off was set at a maximum of 120 s, with any formulations (CM_{ratio} 1.0, 3.0, or 4.0) exhibiting longer gelation times removing the peptide from further consideration. As illustrated in the heatmaps in Figure 3.1B, these kinetic constraints reduced the pool of candidates to seven; see Figure 3.1B whereby heatmaps are used to illustrate the findings. These cut-offs (seen as <15 s, beige, and >120 s, dark blue) reduced the number of peptide candidates to 7, as some peptides, such as peptides 8–10 with <2 cysteine residues per molecule, would gel very slowly and other candidates, such as peptides 19–20 with >2 cysteine residues per molecule, would gel very quickly (<15 s). Figure 3.1B also depicts representative images of small drops (50 μL) of the formulations prepared at CM_{ratio} 4.0 on a 22.5° inclined surface taken at different timepoints; 0 s, 30 s, and 45 s. The images illustrate that the material prepared using Pep-10 remains viscous for +120 s compared to the Pep-5 that rapidly becomes a gel (≈ 30 s). Gelation time was also measured using water applied with a nebulizer to create a wet surface. The gelation time measured on a wet surface (20 ± 11 s) was significantly faster than on the dry surface (55 ± 28 s) and comparable to the CM_{ratio} 1.0 gelation time (33 ± 1.0 s), one-way ANOVA. The alteration in measured gelation time is likely due to a combination of the surface water diluting the solution to achieve an effective lower CM_{ratio} as well as the surface properties of the glass slide being altered by the presence of water.

Target values for other evaluated parameters (also illustrated using heat maps) include: transmittance > 85%, comparable to human cornea (Figure 3.1C);[247] thus removing peptides 6, 7, and 17 from consideration. A refractive index < 1.380, like human cornea (Figure 3.1D), was used as additional criteria for selection;[248] thus peptide 15 was eliminated. Additional parameters

include: a denaturation temperature ≥ 45 °C, which is the highest temperature ever measured in a human (Figure 3.1E);[249] water content >60%, a value that covers soft organs such as skin, cornea, and heart in human adults (Figure 3.1F);[250, 251] and stability in type I collagenase solution, i.e., degradation of <5.0 mg h^{-1} which is the degradation rate for a 1.0% collagen hydrogel in solution (Figure 3.1G).

FTIR analysis for the best hydrogel candidates was also carried out using a Gaussian fit of the Amide I region and compared with the pure peptides (see Supporting Information for more details). A distinct peak appearing at 1650–1675 cm^{-1} was attributed to unreacted C=C bonds from the PEG-maleimide. For hydrogels prepared with Pep-3, -4, and -5 at various CM_{ratio} levels, at a CM_{ratio} of 4.0, the C=C signal was largely absent and replaced by the amide signal, indicating near-complete conversion (Figure 3.1H, Figures S16–S18). Table S2 displays the tabulated data for the heatmap plot results shown in Figure 3.1B–F. In summary, the low volume rapid screening process allowed for the reduction in the number of potential peptide-based formulations from ≈ 200 (each formulation repeated at least in triplicate) to only 9 top formulations with peptides 3, 4, and 5 as primary candidates for further testing.

To facilitate application of the hydrogels directly to the tissue, buffers were chosen that allow for fast reaction in a pH range safe for cells, such as bicarbonate or Hank's buffer (pH 7.0).[252] The materials showed hydrogel formation using all the buffers tested (see representative examples in Figure S9). Alongside high light transmittance, the gels exhibited good visual transparency with minimal scattering. Further, since the goal is to develop a clinically translatable material, the physical properties of the material were optimized prior to hydrogel formation to allow delivery via a ≈ 400 μm cannula (G27 needle) or in the form of a topical/superficial application. To precisely deliver the intended volumes of peptide formulation, a handheld device was developed that can

accurately deliver volumes ranging from 10 μL to 1.0 mL (Figure 3.2A). This handheld device is equipped with interchangeable nozzle adapters, which were specifically designed for the different applications reported here. Printable STL files for all components of the device are made available at no cost in https://figshare.com/s/f195a5a27ccfc9072225.

In the case of the injectable versions of the materials, a lower viscosity was desired along with shear-thinning properties, which are common in large polymer networks like the material is composed of.[253] To assess these properties, viscosity measurements were performed. The lower concentration CM_{ratio} 1.0 formulation had a much lower viscosity at 100 s^{-1} shear rates (3.8 ± 2.4 and 20 ± 9.0 Pa s, for CM_{ratio} 1.0 and 4.0, respectively), while demonstrating shear thinning properties like other injectable materials such as Viscoat (≈ 4.0 Pa s) and was thus chosen for injection applications. In the following sections, proof of concept experimental data is presented for assessing the feasibility of using the material for skin wound closure, for treating cornea perforations, *in situ* cornea reshaping, and as an injectable intramyocardial material.

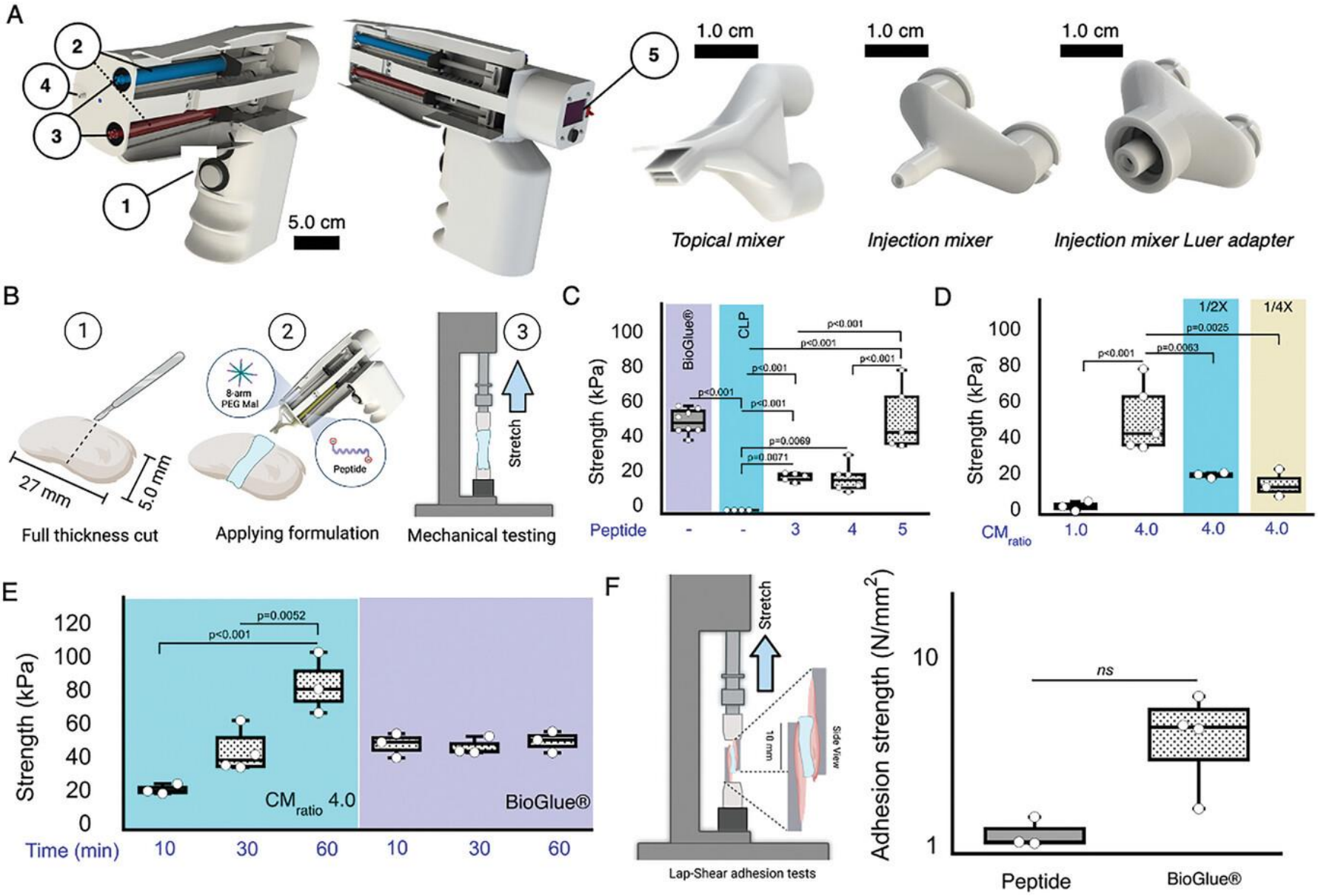
A
1
2
3
4
5
5.0 cm
1.0 cm
1.0 cm
1.0 cm
Topical mixer
Injection mixer
Injection mixer Luer adapter
B
1
2
3
27 mm
5.0 mm
8-arm PEG Mal
Peptide
Stretch
Full thickness cut
Applying formulation
Mechanical testing
C
Strength (kPa)
BioGlue®
CLP
p<0.001
p=0.0069
p=0.0071
Peptide
-
-
3
4
5
D
Strength (kPa)
1/2X
1/4X
p<0.001
p=0.0063
p=0.0025
CM ratio
1.0
4.0
4.0
4.0
E
Strength (kPa)
p=0.0052
p<0.001
CM ratio 4.0
BioGlue®
Time (min)
10
30
60
10
30
60
F
Stretch
10 mm
Slide
Lap-Shear adhesion tests
Adhesion strength (N/mm²)
ns
Peptide
BioGlue®

Figure 3.2. Peptide-based materials can be used to bond tissues. A) *Left*: 3D renders of the custom-designed hand-held device for delivering the peptide-based materials designed in this study. The render displays the main features of the device that include: (1) dispensing on/off control, (2) enclosed compartment for placing peptide-cartridges (preloaded syringes), (3) aperture for nozzle adapters, (4) camera port for live monitoring, and (5) digital controller screen for volume and speed settings. *Right*: three representative nozzles designed for the hand-held device presented herein for topical application (left), cornea sealant delivery (middle), and intratissue injection (right). B) Schematic depiction for the procedure followed to assess skin bonding in a full-thickness incision. Bonded tissue was assessed using uniaxial mechanical stretching tests perpendicular to the wound. Bonding strength was measured an hour after application for Figures 3.2C, D, and E. C) Mechanical strength (kPa), also known as wound closure strength test (ASTM F2458), measured for murine skin tissue after application of peptide-based formulations CM_{ratio} 4.0 (10 mm min^{-1} extension) for top peptide-based hydrogels prepared using peptide 3, 4, and 5. Values measured for applications of BioGlue® and the collagen-like peptides (CLP) are also included in the plot (n = 7-8). D) Mechanical strength (kPa) for murine skin tissue measured using the 4.0 ratio at two different dilutions (½ and ¼; n = 3-5). E) Changes in bond strength as a function of time post-application (10, 30, and 60 min). Samples were incubated at 37 °C in 100% humidity (n = 3-4). F) *Left*: illustration for lap-shear tests using porcine skin using a 10 mm min^{-1} extension. The adhesion surface was fixed at 50 mm^2. The adhesive (peptide-based formulation or BioGlue®) was applied within the two pieces of skin. *Right*: adhesion strength values measured for the peptide-based formulation CM_{ratio} 4.0 and BioGlue® (n = 3-4, ≈ 50 µm thickness for the peptide or BioGlue®). P-values for C, D, and F were calculated using One-Way ANOVA and a post-hoc Holmes correction. P-values for F were calculated using a student t-test (unpaired unequal variance). Reproduced from *Ross et al. Advanced Functional Materials 2024.*

3.1.4 Peptide-Based Materials for Skin Wound Healing

The skin-bonding performance of the candidate formulations was initially evaluated through *ex vivo* wound closure testing using murine skin (Figure 3.2B). In terms of the structure, murine skin and human skin are similar. The difference is that murine skin has a thinner dermis and no sweat glands, and wound healing occurs primarily through contraction, whereas human skin wounds close by granulation tissue formation.[254] The results indicated that only the Pep-5 formulation possessed skin bonding properties comparable to those obtained for BioGlue, a clinically used tissue adhesive comprising 45% bovine serum albumin with 10% glutaraldehyde[255] whose mechanical properties remain constant within the screened timeframe (Figure 3.2C).

The superior bonding strength of Pep-5 was matched only by variants 19, 20, and 21, which are variants of Pep-5 (Figure S10). However, the gelation for those peptides was too rapid, making them impractical for on-the-spot tissue repair application. Furthermore, the findings indicate that the structural properties and amino acid sequence of Pep-5 are critical for functional tissue bonding, as the effectiveness of these gels is affected by the self-assembly of the peptide chains. Thus, for example, removal of a cysteine from either side of the peptide (Pep-8 and -9) results in a bonding strength of only a few kPa while removing both cysteines (Pep-10) results in no gelation. Disruption of folding with a Gly-Val substitution in the middle of the sequence (Pep-15) results in a significant loss of ≈ 50% in bonding strength.

In addition to folding, CM_{ratio} and concentration are vital determinants of performance; utilizing a lower CM_{ratio} of 1.0 or diluting the 4.0 formulation significantly weakened the resulting bond (Figure 3.2D). For the optimized CM_{ratio} 4.0 formulation, bonding strength increased progressively over time, rising from ≈ 50 kPa at 30 minutes to ≈ 100 kPa at 60 minutes post-application (Figure

3.2E). While bonding is one of the key parameters, shear adhesion strength is also a useful parameter to evaluate. Note that in lap shear studies, porcine skin is more often used.[256, 257] However, the modulus of porcine skin, murine skin, and human skin are reported as similar.[258] Adhesivity testing of the Pep-5 CM_{ratio} 4.0 showed that the adhesivity of the peptide-based material is comparable to that of BioGlue (Figure 3.2F). Having identified Pep-5 as the top peptide candidate, the material porosity was then assessed. An average pore size of ≈ 10 μm was observed after swelling for the Pep-5 materials (Figure S11). The material's potential cytotoxicity was evaluated using *in vitro* tests for assessing the viability of human skin cells. The data indicated no adverse effect on the viability of cells exposed to the peptide-based materials (Figure S23).

Following these safety trials, wound closure was evaluated in a full-thickness murine model (Figure 3.3A). It should be noted that murine skin wound healing occurs primarily through contraction, whereas human skin wounds close by granulation tissue formation.[259] So, while the mouse skin model is useful for initial testing, it is not an ideal representation of human skin, and the use of other models will be needed in future studies to further elaborate the potential of the peptide-based hydrogels for skin repair. The animal model used a 7-day endpoint to evaluate the inflammatory response and tissue remodeling as previously reported.[59] Pictures of the wounds at 0, 1, 3, and 7 days clearly showed the peptide-based material is cosmetically superior to sutures or BioGlue (Figure 3.3B). The data presented here corresponds to those wounds that did not dehisce. Note that wound dehiscence after 1 day was observed in ≈ 25% of the animals that received BioGlue and <5.0% for animals that received the peptide material. Also, debonding of the peptide adhesives was not observed. Mechanical testing of wound skin freshly harvested after euthanasia indicated that the peptide-based material is superior to sutures and BioGlue, and comparable to unwounded skin (Figure 3.3C). Histological analyses of the tissues showed that the peptide-based

material presents a more functional wound healing, including increased collagen deposition and reduced epithelial thickness (Figure 3.3D). Further histological assays carried out to evaluate the number of pro-healing macrophages indicated that the animals treated with the peptide-based material have no difference in the number of CD206+ macrophages compared to the sutures or BioGlue groups (Figure S13).

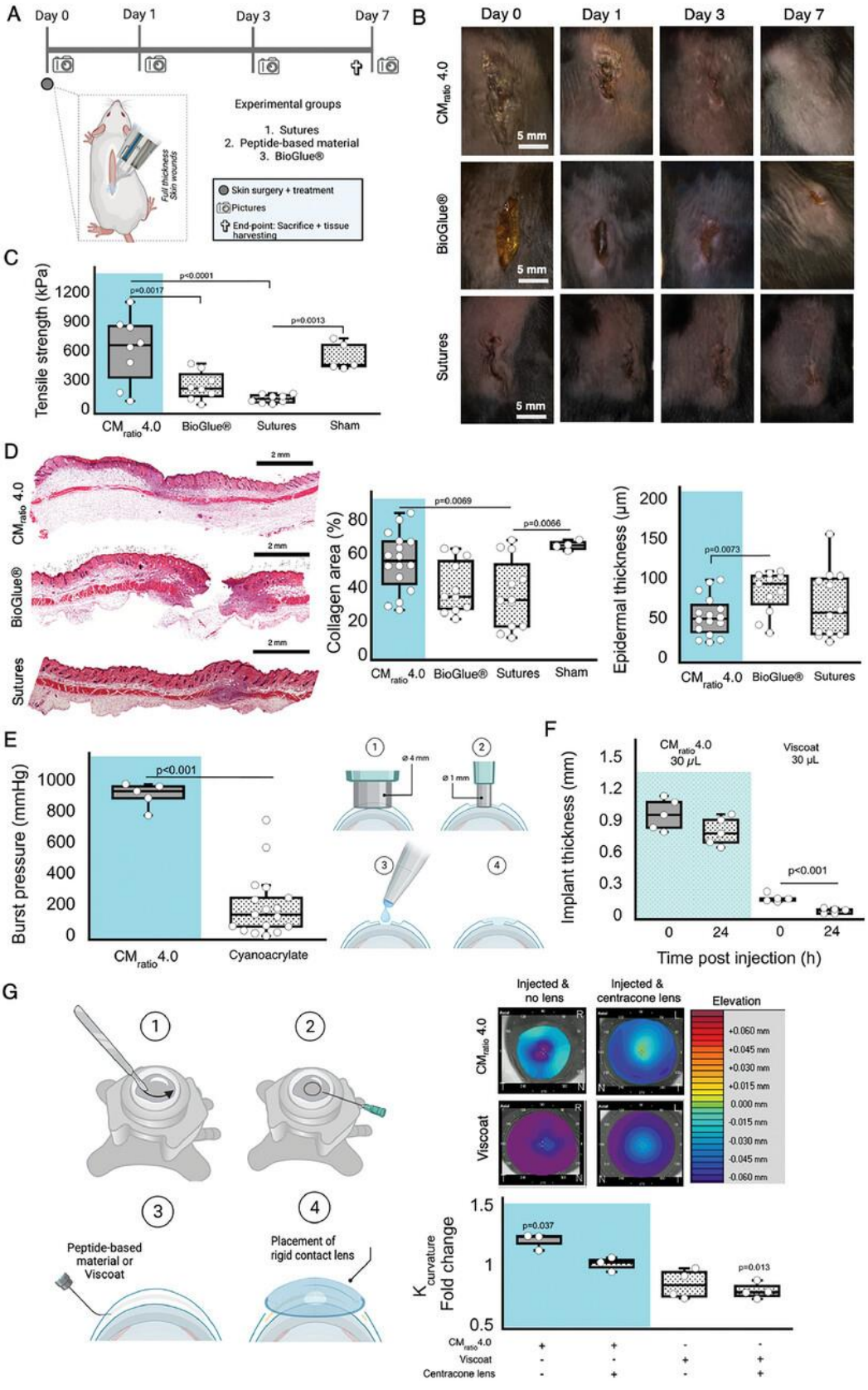
A
Day 0
Day 1
Day 3
Day 7
Full thickness Skin wounds
Experimental groups
1. Sutures
2. Peptide-based material
3. BioGlue®
Skin surgery + treatment
Pictures
End-point: Sacrifice + tissue harvesting
B
Day 0
Day 1
Day 3
Day 7
CMratio 4.0
BioGlue®
Sutures
5 mm
C
Tensile strength (kPa)
p<0.0001
p=0.0017
p=0.0013
CMratio 4.0
BioGlue®
Sutures
Sham
D
2 mm
CMratio 4.0
BioGlue®
Sutures
Collagen area (%)
p=0.0069
p=0.0066
Epidermal thickness (µm)
p=0.0073
E
Burst pressure (mmHg)
p<0.001
CMratio 4.0
Cyanoacrylate
Ø 4 mm
Ø 1 mm
F
CMratio 4.0
30 µL
Viscoat
30 µL
Implant thickness (mm)
p<0.001
Time post injection (h)
G
Peptide-based material or Viscoat
Placement of rigid contact lens
Injected & no lens
Injected & centracone lens
Elevation
+0.060 mm
+0.045 mm
+0.030 mm
+0.015 mm
0.000 mm
-0.015 mm
-0.030 mm
-0.045 mm
-0.060 mm
K curvature Fold change
p=0.037
p=0.013
CMratio 4.0
Viscoat
Centracone lens

Figure 3.3. Peptide-based materials as tissue bonding sealants and fillers. A) Schematic of the experimental design used for the *in vivo* testing of the tissue bonding capabilities of the peptide-based materials using C57BL/6 female mice (7-8 weeks). B) Representative images of the full-thickness wounds taken at 0-, 1-, 3-, and 7-days post-treatment for the different experimental groups. Scale bars = 5.0 mm. C) Mechanical strength (kPa) for murine skin tissue measured 7 days post-operation (n = 5–8) obtained for the different experimental groups. The Sham group corresponds to animals that underwent the same steps as those that received incisions, but the skin remained intact. D) *Left*: representative histological images of the skin at 7 days for the 3 treatment groups. *Right*: analysis of the histological sections obtained for the different treatment groups including collagen deposition (n = 4–16), and epidermal thickness (n = 11–16).[233, 260, 261] E) *Left*: burst pressure values measured for the peptide-based material CM_{ratio} 4.0 or cyanoacrylate (n = 5–17). *Right*: illustration for the pig cornea perforation *ex vivo* model used in this study. The numbers in the Figure illustrate: (1) initial perforation to create a wound bed, (2) inner full-thickness cornea perforation using a 1 mm biopsy puncher, (3) application of the treatment to seal the hole, and (4) formation of a "corneal" patch. F) Changes in implant thickness were obtained using 30 µL of the CM_{ratio} 4.0 peptide material or Viscoat (n = 5). G) *Left*: illustration of the *ex vivo* pig cornea pocket and cornea reshaping model used in this study. The numbers in the figure illustrate: (1) initial surgical incision to create a wound bed, (2) insertion of needle to open a cavity, (3) injection of the peptide-based material as an intracorneal patch, and (4) positioning of a solid contact lens. *Right top*: representative corneal topographic axial maps showing surface elevation of corneas injected with either CM_{ratio} 4.0 or Viscoat. The topographic maps are generated for corneas before injection, after injection, and injection in conjunction with insertion of a rigid contact lens (Centracone). The scale on the right shows the height in mm, with warmer colors representing steeper areas and cooler colors marking flatter ones. *Right bottom*: Fold change for K values of curvature (mm) obtained for corneas that have been injected with either CM_{ratio} 4.0 or Viscoat, with the placement of RGP/Centracone rigid contact lenses in conjunction with the peptide-based material (n = 4) with volumes ≈ 30 µL (compared to empty pocket). For C and D, p values were calculated using One-Way ANOVA and post-hoc Holmes test, while student t-tests were used for E and F (unpaired unequal variance) and G (paired data). Reproduced from *Ross et al. Advanced Functional Materials 2024.*

3.1.5 Peptide-Based Materials for Cornea Repair

The bonding capacity of the peptide-based hydrogel, which is comparable to that of BioGlue, suggests that this minimalistic platform is well-suited for the repair of specialized soft tissues. Next, the suitability of the material for the rapid closure of perforated corneal tissue, a clinical application facilitated by the high optical transparency of the hydrogel, was assessed. An *ex vivo* corneal perforation model was utilized which is a standard system for testing the sealing efficacy of ocular biomaterials.[60] Porcine corneas were selected for these experiments due to their physiological and anatomical similarities to the human cornea (Figure 3.3E).[262]

Data indicated that the burst pressure achieved by the peptide-based sealant was significantly higher and more reproducible than that of cyanoacrylate (Figure 3.3E). While cyanoacrylate remains one of the gold standards for rapid corneal sealing in emergency situations, its observed toxicity toward corneal tissues presents the main drawback for its safe use.[263] In contrast, the peptide-based material exhibited no significant cytotoxicity toward human corneal cells (Figure S14), positioning this technology as a safer, more biocompatible alternative for corneal repair.

Beyond its use as a sealant, the potential of the peptide-based material as an *in situ* corneal filler was tested. Data indicates that rapid injection of CM_{ratio} 4.0 into the pig cornea renders implants that are considerably thicker and more stable than those produced using Viscoat (Figure 3.3F). Furthermore, the ability of the peptide-based material to reshape cornea curvature in an *ex vivo* model was assessed. Figure 3.3G includes a schematic representation for the experiments, showing the creation of an intrastromal pocket in the pig cornea, which can be filled with a viscous material, such as the peptide hydrogel. After injection of the peptide-based material, an increase in cornea curvature was measured compared to the control (Figure 3.3G). Upon application of the rigid

contact lens, a change in the cornea shape is detected for the peptide-based material when compared to the injected cornea and no lens. Curvature changes for corneas treated with Viscoat and lens shows that injection of Viscoat does not achieve a significant change in curvature when compared to the pocket alone. In fact, there is an overall decline in cornea curvature for the corneas that received the centracone lens and Viscoat. Refractive index measurements for pig corneas containing the peptide-based material indicate no significant differences in refractive index [1.36 ± 0.011 and 1.35 ± 0.014 (n = 16, p = 0.43) for cornea and cornea + peptide, respectively]. While preliminary, this data suggests the peptide-based material developed in this work offers a cost-effective alternative to cyanoacrylate, including the possibility to *in situ* reshape the cornea.

3.1.6 Peptide-Based Materials for Treating the Infarcted Heart

The data presented in Figures 3.2 and 3.3 indicate that the CM_{ratio} 4.0 hydrogel has high potential as a tissue adhesive, sealant, and filler material; however, for intramyocardial injection, such materials are too viscous to be delivered using multiple injections through G27 diameter needles. Thus, for intramyocardial applications, the suitability was tested for the CM_{ratio} 1.0 formulation, which is approximately an order of magnitude less viscous at high shear rates (20, 3.8, and ≈ 4.0 Pa s for CM_{ratio} 4.0 and 1.0 and Viscoat at 100 s^{-1}). For *in vivo* testing, a clinically relevant murine MI model that recapitulates patients who have not responded to revascularization therapeutics or who have delayed seeking treatment was selected.[61] The model involves the permanent ligation of the artery descendent blood flow supply to induce MI, followed by treatment delivery at 7 days post-MI (Figure 3.4A). There were no toxicity concerns since the CM_{ratio} 1.0 material did not affect human cardiac endothelial cell viability *in vitro*. The percentage of viable cells was not statistically different for the peptide-based material compared to a collagen-based hydrogel after 2 days of culture (Figure 3.4B).

Assessment of the left ventricular ejection fraction 4 weeks after treatment delivery showed that the intramyocardial injection of the CM_{ratio} 1.0 material preserved cardiac function of the MI heart (i.e., no fold-change versus baseline, $p>0.05$) compared to the control group (Figure 3.4C) where function decreased over time. However, no differences in scar size (Figure 3.4D) or the number of pro-healing macrophages (Figure 3.4E) were observed. Use of fluorescent labeling to track the CM_{ratio} 1.0 material *in vivo* showed that it could still be visualized in the cardiac muscle for up to 7 days after injection (Figure 3.4F). This finding presents an interesting opportunity for use of the CM_{ratio} 1.0 material for the *in situ* delivery of therapeutic agents, such as small molecules, biopolymers, or extracellular vesicles that typically have low retention rates when delivered to the myocardium.

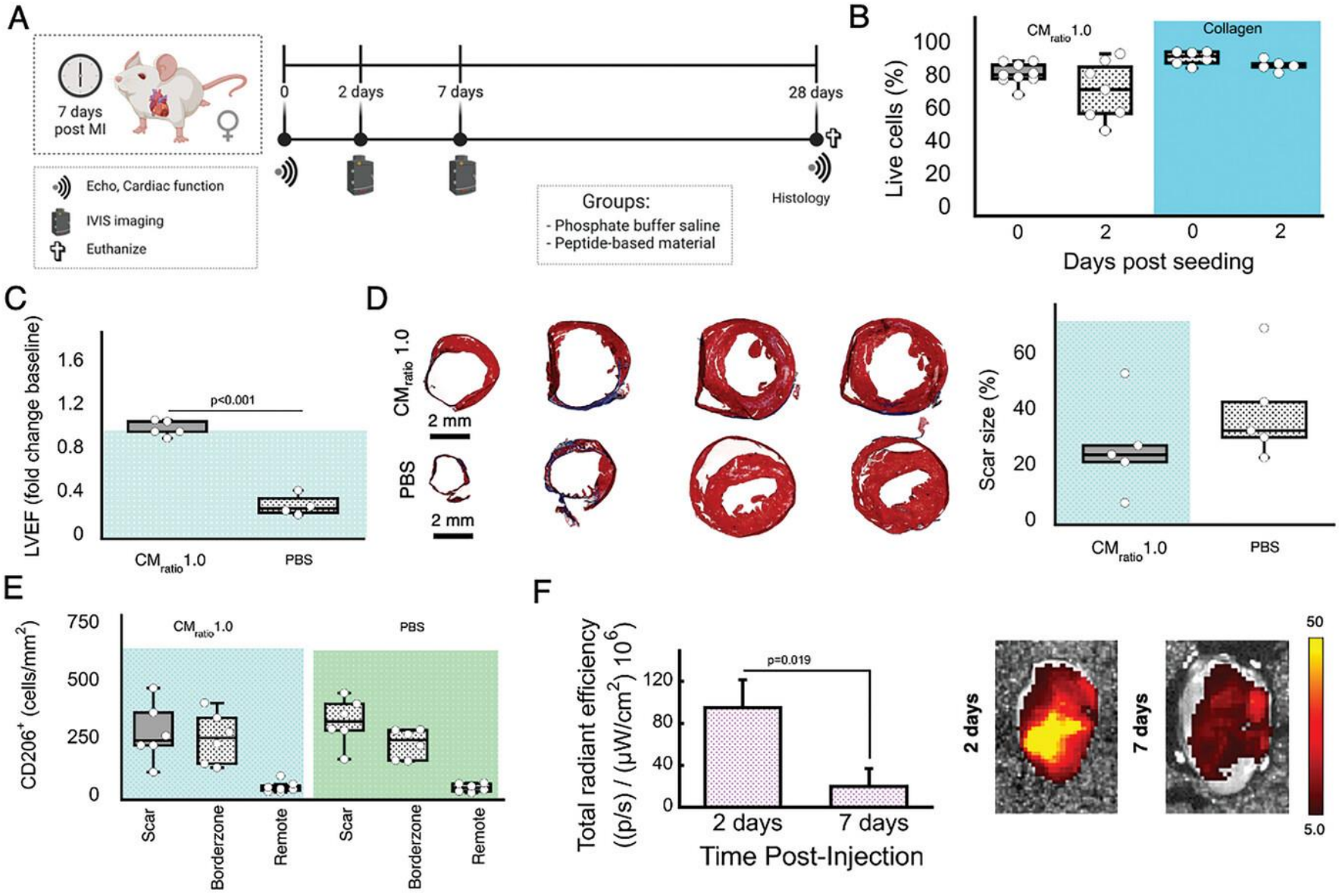
A
7 days post MI
Echo, Cardiac function
IVIS imaging
Euthanize
0
2 days
7 days
28 days
Histology
Groups:
- Phosphate buffer saline
- Peptide-based material
B
Live cells (%)
CM ratio 1.0
Collagen
Days post seeding
C
LVEF (fold change baseline)
p<0.001
CM ratio 1.0
PBS
D
CM ratio 1.0
PBS
2 mm
Scar size (%)
E
CD206+ (cells/mm2)
Scar
Borderzone
Remote
F
Total radiant efficiency ((p/s) / (μW/cm2) 10^6)
p=0.019
2 days
7 days
Time Post-Injection
50
5.0

Figure 3.4. Peptide-based materials can be safely injected intramyocardially and remain within the cardiac muscle. A) Schematic of the experimental design for *in vivo* testing of the intramyocardial injection application of the peptide-based materials. Experiments were carried out using C57BL/6 female mice (7-8 weeks). B) Percentage of live human cardiac endothelial cells measured at 0 and 2 days after seeding on the CM_{ratio} 1.0 material or collagen-based hydrogel (n = 5-9). C) Left ventricular ejection fraction (LVEF) fold change relative to baseline measured 28 days after treatment with CM_{ratio} 1.0 material or PBS (n = 4-5). D) *Left*: representative Masson trichrome staining images for hearts treated with CM_{ratio} 1.0 material or PBS. *Right*: analysis of the scar size for the two treatment groups (n = 5). E) Number of $CD206^+$ cells counted in myocardial tissue sections within the scar, border zone, and remote areas (n = 6). F) *Left*: quantification for *ex vivo* fluorescence imaging ($\lambda_{excitation}$ = 570 nm; $\lambda_{emission}$ = 640 nm) of hearts injected with the Alexa-Fluor@594-labelled CM_{ratio} 1.0 material at different days post-injection. *Right*: representative IVIS images of the MI hearts harvested after 2- or 7-days post-injection (n = 3). P values were calculated using student t-test (unpaired data & unequal variance). Reproduced from *Ross et al. Advanced Functional Materials 2024.*

3.2 Mechanically Stable and Tunable Photoactivated Peptide-Based Hydrogels for Soft Tissue Adhesion

The data presented in this section has been published as follows: A. Ross, D. Nguyen, A. Macadam, A. Mercado Salazar, M. Gianetti, R. Ileri, M. Ruel, E. J. Suuronen and E. I. Alarcon. Mechanically Stable and Tunable Photoactivated Peptide-Based Hydrogels for Soft Tissue Adhesion. *Adv Funct Mater* 2025;():202529084.

3.2.1 Brief Introduction to the Results of Aim 3

The development of peptide-based hydrogels requires precise control over crosslinking chemistry to ensure structural stability without compromising biological functionality. In this section of the study, the epsilon-amine of lysine was utilized as a versatile handle for functionalization with various alkenes, while cysteine served as the primary thiol source. The choice of alkene is critical, as electron-rich species significantly enhance reaction kinetics.[206]

A major consideration in designing these networks is the competition between thiol-ene step-growth kinetics and alkene-alkene chain-growth homopolymerization. In a 1:1 thiol-to-ene ratio, dominant chain-growth pathways can leave a surplus of unreacted thiols, particularly if the reaction occurs intramolecularly or between adjacent residues within a single triple-helical trimer, thereby reducing overall network functionality.[264-266] To mitigate this, the use of specific groups such as allyloxycarbonyl (alloc) was investigated. Alloc groups are notably less prone to chain growth due to the formation of resonance-stabilized allylic hydrogen abstraction intermediates; however, they remain highly reactive in the desired thiol-ene step-growth pathway.[265, 266]

The inherent secondary structure of the peptide further modulates its chemical reactivity.[267] By strategically positioning these reactive moieties within the peptide sequence, the macroscopic mechanical properties of the resulting hydrogel can be tuned. This work investigates how the identity and frequency of reactive groups in both short and long self-assembling sequences determine the ability of the peptide to form robust, biomimetic scaffolds. Through this rational design, light-activated hydrogel materials were generated using only synthetic peptides and a photoinitiator in aqueous buffer, eliminating the need for synthetic polymeric backbones like PEG. The synergistic combination of supramolecular triple-helical assembly and efficient thiol-ene "click" chemistry yields hydrogels with significant and tunable bonding strength. These fully synthetic yet biomimetic materials represent a promising platform for soft tissue repair, offering a biocompatible and biodegradable alternative to traditional tissue adhesives.

3.2.2 Peptide Conformation and Nature of Reactive Moiety Dictate its Ability to form Hydrogels

Figure 3.5A depicts a schematic diagram summarizing the core peptide structure used in the study along with the several variants of peptide sequences that were developed and screened for hydrogel formation. In this work, Irgacure-2959 (I-2959), a Norrish type I photoinitiator that photocleaves upon UVA irradiation,[268] was employed (see absorption spectra in Figure S21**)**. I-2959 is commonly used to produce light-activated hydrogels and absorbs UV light, whereas Pep 10 shows minimal UV absorption. To validate the irradiation protocol and serve as a performance benchmark, hydrogels were produced using an 8-arm 20 kDa PEG-acrylate system (see Figure 3.5B for workflow summary**)**. Further details on each peptide sequence that was designed for this study can be found in Table 3.2 .

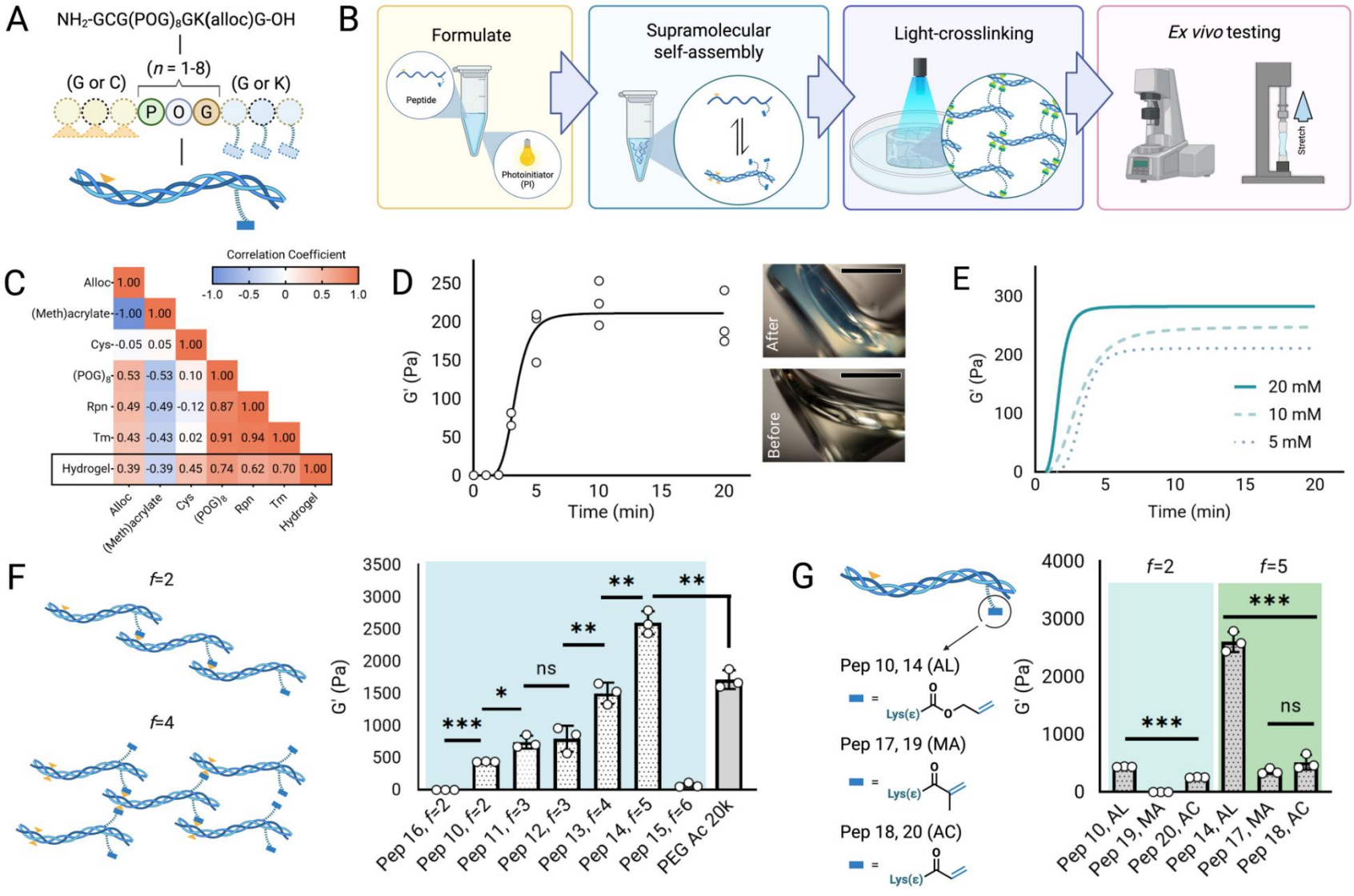
A
NH2-GCG(POG)8GK(alloc)G-OH
(G or C)
(n = 1-8)
(G or K)
P O G
B
Formulate
Peptide
Photoinitiator (PI)
Supramolecular self-assembly
Light-crosslinking
Ex vivo testing
Stretch
C
Correlation Coefficient
-1.0 -0.5 0 0.5 1.0
Alloc 1.00
(Meth)acrylate -1.00 1.00
Cys -0.05 0.05 1.00
(POG)8 0.53 -0.53 0.10 1.00
Rpn 0.49 -0.49 -0.12 0.87 1.00
Tm 0.43 -0.43 0.02 0.91 0.94 1.00
Hydrogel 0.39 -0.39 0.45 0.74 0.62 0.70 1.00
Alloc
(Meth)acrylate
Cys
(POG)8
Rpn
Tm
Hydrogel
D
G' (Pa)
Time (min)
After
Before
E
G' (Pa)
Time (min)
20 mM
10 mM
5 mM
F
f=2
f=4
G' (Pa)
***
*
ns
**
**
**
Pep 16, f=2
Pep 10, f=2
Pep 11, f=3
Pep 12, f=3
Pep 13, f=4
Pep 14, f=5
Pep 15, f=6
PEG Ac 20k
G
Pep 10, 14 (AL)
Lys(ε)
Pep 17, 19 (MA)
Lys(ε)
Pep 18, 20 (AC)
Lys(ε)
f=2
f=5
G' (Pa)
***
***
ns
Pep 10, AL
Pep 19, MA
Pep 20, AC
Pep 14, AL
Pep 17, MA
Pep 18, AC

Figure 3.5. Design and characterization of collagen-like peptide photoactivated hydrogels. (A) Design of peptide primary sequences. The core of proline-hydroxyproline-glycine (POG) is flanked by cysteine and lysine (ε-alkene) residues. (B) Workflow used to create and characterize peptide hydrogels in this study. A formulation consisting of buffer, photoinitiator, and self-assembling collagen-like peptide is irradiated by UVA light to form hydrogels for further testing. (C) Pearson correlation matrix of peptide structural parameters and the ability of these structures to form a hydrogel. (D) *Left*: kinetic study of Pep 10 (NH_2-GCG$(POG)_8$GK(alloc)G-OH) hydrogel formation using 5 mM I-2959 photoinitiator. A four-parameter logistic regression model is used to fit the data. *Right*: images of the peptide solution before (below) and after (above) gelation. (E) Kinetic study of Pep 10 hydrogel formation using different (5, 10, and 20 mM) concentrations of I-2959. (F) *Left*: simplified illustration showing the effect of junction functionality on the peptide polymer network. *Right*: elastic modulus (G') measurements for Pep 10–16 and PEG 20k 8-arm acrylate hydrogels. (G) *Left*: illustration showing the chemical structure of the different alkenes and their position within the peptide sequence. *Right*: elastic modulus (G') measurements for peptide hydrogels bearing allyloxycarbonyl (Pep 10/14), acrylate (Pep 18/20), and methacrylate (Pep 17/19) on the lysine epsilon amine. Data are presented as mean ± SD (n = 3). Statistical significance was assessed using two-tailed unpaired Student's t-tests with unequal variance. *$p < 0.05$, **$p < 0.01$, ***$p < 0.001$. Reproduced from *Ross et al. Advanced Functional Materials 2025.*

Sample code	Peptide sequence	Features	Molecular weight [g mol^{-1}]	R_{pn} value[a]	T_m [°C][b]
Pep 1	NH_2-(K**(alloc)**)$_2$GGGCC-NH_2	Short peptide with two Lys (alloc) and two cysteine	819.0	NA	NA
Pep 2	**MA**-K**(ε-MA)**GGG-OH	Short peptide with methacrylation at the N-terminus and lysine ε amine	453.5	NA	NA
Pep 3	**MA**-K**(ε-MA)**GGGC-NH_2	Short peptide with methacrylation at the N-terminus and lysine ε-amine along with a cysteine	555.6	NA	NA
Pep 4	**MA**-POGPCG-OH	Short peptide with one cysteine and N-terminal methacrylation	610.2	ND	NA
Pep 5	**MA**-(POG)$_3$PCG-OH	Peptide with 3 POG repeats, one cysteine, and N-terminal methacrylation	1144.5	ND	NA
Pep 6	**MA**-(POG)$_5$PCG-OH	(POG)$_5$ CLP with one cysteine and N-terminal methacrylation	1678.7	0.011 ± 0.004	24
Pep 7	**MA**-(POG)$_7$PCG-OH	(POG)$_7$ CLP with one cysteine and N-terminal methacrylation	2213.0	0.091 ± 0.004	45
Pep 8	NH_2-GK**(alloc)**G(POG)$_8$GK**(alloc)**G-OH	(POG)$_8$ CLP with Lys (alloc) at each end	2809.0	0.091 ± 0.005	60
Pep 9	NH_2-G(K**(alloc)**)$_2$(POG) (K**(alloc)**)$_2$G-OH	(POG)$_8$ CLP with two Lys (alloc) at each end	3119.3	0.088 ± 0.004	52
Pep 10	NH_2-GCG(POG)$_8$GK**(alloc)**G-OH	(POG)$_8$ CLP with one cysteine and one Lys (alloc) at the ends	2699.9	0.085 ± 0.002	61

Pep 11	NH_2-G<u>CC</u>$(POG)_8$GK**(alloc)**GG-OH	$(POG)_8$ CLP with two cysteines and one Lys (alloc) at the ends	2745.9	0.072 ± 0.001	53
Pep 12	NH_2-G<u>C</u>G$(POG)_8$K**(alloc)$_2$**G-OH	$(POG)_8$ CLP with one cysteine and two Lys (alloc) at the ends	2855.1	0.085 ± 0.001	61
Pep 13	NH_2-G<u>CC</u>$(POG)_8$K**(alloc)$_2$**G-OH	$(POG)_8$ CLP with two cysteines and two Lys (alloc) at the ends	2901.1	0.091 ± 0.001	58
Pep 14	NH_2-<u>CCC</u>$(POG)_8$K**(alloc)$_2$**G-OH	$(POG)_8$ CLP with three cysteines and two Lys (alloc) at the ends	2947.2	0.080 ± 0.001	71
Pep 15	NH_2-<u>CCC</u>$(POG)_8$K**(alloc)$_3$**-NH_2	$(POG)_8$ CLP with three cysteines and three Lys (alloc) at the ends	3102.4	0.069 ± 0.001	65
Pep 16	NH_2-G<u>C</u>G$(POG)_4$POV$(POG)_3$G**K(alloc)**G-OH	Pep 10 with Gly -> Val substitution to disrupt folding	2741.9	0.030 ± 0.002	31
Pep 17	NH_2-<u>CCC</u>$(POG)_8$K**(ε-MA)$_2$**G-OH	$(POG)_8$ CLP with three cysteines and two Lys (ε-methacrylate) at the ends	2915.2	0.082 ± 0.002	67
Pep 18	NH_2-<u>CCC</u>$(POG)_8$K**(ε-Ac)$_2$**G-OH	$(POG)_8$ CLP with three cysteines and two Lys (ε-acrylate) at the ends	2886.2	0.086 ± 0.001	60
Pep 19	NH_2-G<u>C</u>G$(POG)_8$GK**(ε-MA)**G-OH	$(POG)_8$ CLP with one cysteine and one Lys (ε-methacrylate) at the ends	2683.9	0.085 ± 0.002	64
Pep 20	NH_2-G<u>C</u>G$(POG)_8$GK**(ε-Ac)**G-OH	$(POG)_8$ CLP with one cysteine and one Lys (ε-acrylate) at the ends	2669.9	0.093 ± 0.002	61

Table 3.2. List of photoactivated peptides screened in this study. Cysteine residues are underlined while alkenes are in **bold**. ε-MA means methacrylated lysine epsilon amine while ε-Ac represents an acrylated residue. Conditions for the gelation test were 5% w/v peptide in solution of PBS (pH 7.4, 1.0 mM I-2959). Peptide denaturation temperatures are reported in the table as well (T_m). a) Peptide concentration of 200 μM in 1.0 mM phosphate buffer (pH 7.4) at 25 ºC. b) Melting curves are included in Figure S25. Reproduced from *Ross et al. Advanced Functional Materials 2025.*

The ability of synthetic peptides to transition from soluble monomers to stable 3D networks depends on a delicate balance between molecular hydrophilicity and the inclusion of hydrophobic reactive groups. Initial screening revealed that ene-functionalized short peptides (Pep 1–3) suffered from poor aqueous solubility, likely due to the hydrophobic character of the alkene handles. Short peptides with collagen-like POG trimers were soluble due to the hydrophilicity of POG motifs but failed to gel when methacrylated at the N-terminus (Pep 4-5). Longer CLPs were synthesized with either N-terminus methacrylate (Pep 6-7) or lysine (alloc) (Pep 8-9). The N-terminus methacrylated CLPs also failed to gel. This could be due to the N-terminus lacking steric flexibility in the folded CLP state compared to the lysine ε-alloc along with unproductive intra-trimer reactions. Furthermore, n = 8 $(POG)_n$ CLPs with only lysine (alloc) could not form a hydrogel (Pep 8-9, see Table 3.2) due to the lack of thiols and the alloc's poor ability to undergo ene-ene chain growth polymerization. However, the CLP employing a long, soluble structure containing both cysteine and lysine (alloc) formed a hydrogel at concentrations of ≥ 3% v/w (Pep 10). Pearson correlation analyses of the various peptide structural features are presented in Figure 3.5C. Heavy contributors for hydrogel formation are the presence of the POG motif and collagen-like triple helical structure while methacrylate groups proved detrimental for hydrogel formation.

Circular dichroism (CD) spectroscopy assessed peptide conformation and folding behaviour. Full-length collagen and CLPs exhibit a characteristic CD spectrum associated with a polyproline type II helix, consisting of a positive maximum near 225 nm and a negative minimum near 200 nm,[244, 269] which was observed for folded CLPs in this study (Figure S25, top left). To quantify triple-helix assembly, the R_{pn} parameter is reported, defined as the ratio of absolute CD ellipticities at 225 nm and 200 nm ($R_{pn} = |\theta_{225}| / |\theta_{200}|$). This parameter has been widely used as an indicator of collagen triple-helix packing, with a CLP known to form stable triple helices exhibiting an R_{pn} value around ~0.07[86] while full-length collagen approaches

values near ~0.12.[269] The peptides investigated here, based on the $(POG)_8$ folding template, displayed R_{pn} values ~0.07-0.09 (Table 3.2) which is consistent with triple-helix formation in CLPs. These observations were further supported by cooperative thermal melting transitions observed for folded peptides (Figure S25).

The gelation process is strictly photo-dependent; for a 5% w/v peptide solution with 1.0 mM I-2959 in phosphate buffer saline (PBS), gelation occurs only upon UVA irradiation (12.4 mW/cm^2), whereas peptide solutions without I-2959 do not form gels (Figure S22). There was a significant increase ($P = 0.014$) in storage modulus (G') if the solution was left to fold at 4 °C for 1 h prior to light exposure, indicating the need for peptide assembly before reaction. If the solution was left for 24 h there was a trend ($P = 0.26$) towards lower storage modulus with a larger variability, likely due to cysteine oxidation and disulfide bridge formation over time resulting in less reactive residues being available. Ellman assay results indicate that there is a significant reduction in reactive thiol after 24 h (Figure S23**)**. As photoactivated I-2959 can function as a reducing agent,[268] the effect of a higher I-2959 concentration (5.0 mM, Figure S24) was tested next. A folding time of 1 h vs 0 h again resulted in a significant increase in storage modulus ($P = 0.0022$), while the 24 h timepoint showed a similar G' to 1 h ($P = 0.94$) with the additional presence of reducing agent. Furthermore, a hydrogel was now formed at the 0 h timepoint. The kinetics of hydrogel assembly were investigated for the 5.0 mM concentration of I-2959 (Figure 3.5D). 5% Pep 10 gels reached 50% of max strength at 3.3 min, while increasing the concentration of I-2959 to 10 and 20 mM resulted in more rapid gelation (1.7 min 50% G' at 20 mM compared to 3.3 and 3.1 min at 5 and 10 mM) with a modest increase (283 Pa at 20 mM, 248 Pa at 10 mM, and 211 at 5 mM) in maximal strength (Figure 3.5E).

To further tune material properties, the junction functionality or the number of connections between each chain was altered.[32] For a peptide polymer network, junction functionality (f) can be increased by adding reactive groups and increasing f should result in stiffer gels. Thus, a

series of peptides (Pep 8-15) were designed with different numbers of reactive groups (Figure 3.5F). Although these molecules assemble into larger structures, for simplicity, *f* was listed as the number of reactive ends per peptide molecule. As *f* increased for the different peptides there was a significant increase in *G*' for each step up in value, while for Pep 11-12, where *f* = 3 in both cases, the storage modulus was comparable (*P* = 0.71). Further, as the number of alkenes was increased, the peptide's solubility in aqueous solutions decreased, with Pep 15 becoming insoluble at 5% w/v, preventing hydrogel formation. Highly functionalized peptides formed gels of comparable or greater stiffness relative to a PEG acrylate 8-arm 20 kDa control. Mesh size calculations[270, 271] for peptide hydrogels rendered values ranging from 13.8 to 27.4 nm (Table S3), providing a tunable range appropriate for the diffusion of most biomolecules.

To evaluate the contribution of peptide folding towards overall hydrogel strength, a Gly-Val amino acid substitution was introduced in the middle of the peptide changing Pep 10 (NH_2-GCG$(POG)_8$GK(alloc)G-OH) into Pep 16 (NH_2-GCG$(POG)_4$POV$(POG)_3$GK(alloc)G-OH)) to disrupt the peptide's supramolecular assembly (Figure S26). The substitution had a strong effect on the network properties as the resulting peptide failed to form a hydrogel despite having an identical *f* value to Pep 10. CD measurements indicate that the single amino acid change reduced the R_{pn} from ≈ 0.08 to ≈ 0.03, suggesting that folding was disrupted. Thus, in addition to their chemical reactivity, the ability of the CLPs to fold properly is vital to forming hydrogel networks.

With confirmation of the importance of both chemical reactivity and folding, the effect of changing the alkene group on material properties was then investigated. For this, some of the most commonly utilized reactive moieties in literature were used such as the methacrylate from GelMA.[272] Taking the peptide making the strongest hydrogel thus far (Pep 14, NH_2-CCC$(POG)_8$K$(alloc)_2$G-OH), the Lys (alloc) group was replaced with either methacrylate (Pep 17, K(ε-$MA)_2$) or acrylate (Pep 18, K(ε-$Ac)_2$); Figure 3.5G). *G*' was strongly reduced (~90%)

for both Pep 17 and 18. This could be due to the adjacent residues undergoing intramolecular ene-ene reactions rather than bonding to sulfur atoms from adjacent chains, resulting in network truncation. To test this hypothesis, variants of Pep 10 (NH_2-GCG$(POG)_8$GK(alloc)G-OH), which contains only a single alkene per strand, were synthesized with methacrylate (Pep 19, K(ε-MA)) and acrylate (Pep 20, K(ε-Ac)) groups (Figure 3.5G). The methacrylate variant failed to gel while the acrylated Pep 20 was weaker (~50%) than the alloc version. However, the difference between the single alkene peptides Pep 10 and Pep 20 was relatively smaller than the difference between the double alkene peptides Pep 14 and 18. This suggests that reactivity between adjacent residues may be a deleterious factor.

3.2.3 Molecular Dynamics Indicate Differential Folding and Hydrogen Bond Formation Amongst Peptides

To further investigate the molecular mechanisms governing peptide hydrogel assembly, molecular dynamics (MD) simulations were performed. In terms of supramolecular assembly, the $(POG)_8$ core peptides Pep 8, 10, and 14 had inter-chain hydrogen bonds rapidly form within the initial nanoseconds, initiating helix–helix recognition (see Figure 3.6A). After this initial association, the individual inter-chain interactions remain stable and mutually consistent, reflecting a cooperative stabilization that supports the formation of a well-defined triple helix. However, for the Gly-Val substitution in Pep 16, two helix–helix pairs gradually increase their interactions over time while the interaction between chains A and B (the "AB pair") remains essentially inactive, failing to establish stable hydrogen bonds (Figure 3.6A and 3.6B). This imbalance has the effect of preventing the formation of an organized triple helix, supporting the experimental R_{pn} measurements. Considering that Pep 16 fails to form a hydrogel, these results support the idea that stable peptide folding contributes to the material's mechanical properties.

The residues flanking the $(POG)_8$ core also influence helix stability. R_{pn} data suggests that Lys (alloc) residues increase the measured R_{pn} values by a small amount. Analysis of residue-specific interactions (Figure S27) demonstrates that the Lys (alloc) residues consistently engage in a high number of stabilizing contacts and that their contributions are approximately within the same range across Pep 8, 10, and 14. Conversely, the cysteine residues appear to contribute marginally to helix stabilization (Figure S28), as experimentally seen by the lack of an increase in the R_{pn} measured when cysteine residues are added to a chain. This suggests that the terminal Lys (alloc), but not cysteine residues, play a cooperative role in reinforcing the triple-helix assembly, complementing the stabilizing effect of the central $(POG)_8$ motifs.

Beyond structural stability, the interchain contacts made by Lys residues influence the chemical reactivity during radical photocrosslinking. Simulations were performed to measure the amount of interchain contacts made between C=C alkene atoms on a normalized basis per alkene (Figure 3.6C). For all peptides, contacts occurred between alkenes on the same triple helix, while no contact was made between alkene and cysteine groups on the same helix due to their greater distance from each other and the steric rigidity of the peptide structure. Under radical photocrosslinking conditions, these alkene contacts can lead to bond formation, resulting in intramolecular crosslinking that is unproductive in forming connections with the bulk hydrogel network. Thus, the lower reactivity of alloc towards the formation of these unproductive C-C bonds[273] may contribute to the greater mechanical strength of the alloc peptide materials.

In addition to being less reactive when contacts occur, systems based on alloc (Pep 8, 10) exhibit low alkene–alkene contact frequencies within the helix compared to acrylate (Pep 20) or methacrylate (Pep 10), suggesting a minimal probability of alkenes on chains A, B, and C reacting with each other. This may be to the due to the greater length and steric flexibility of the alloc group arising from the sp^3 hybridized carbon present between the alkene and carboxyl. Taken together, the lower number of contacts made and the lower chance for a reaction to occur

upon contact may explain the increased mechanical resilience of alloc peptide materials compared to (meth)acrylated ones.

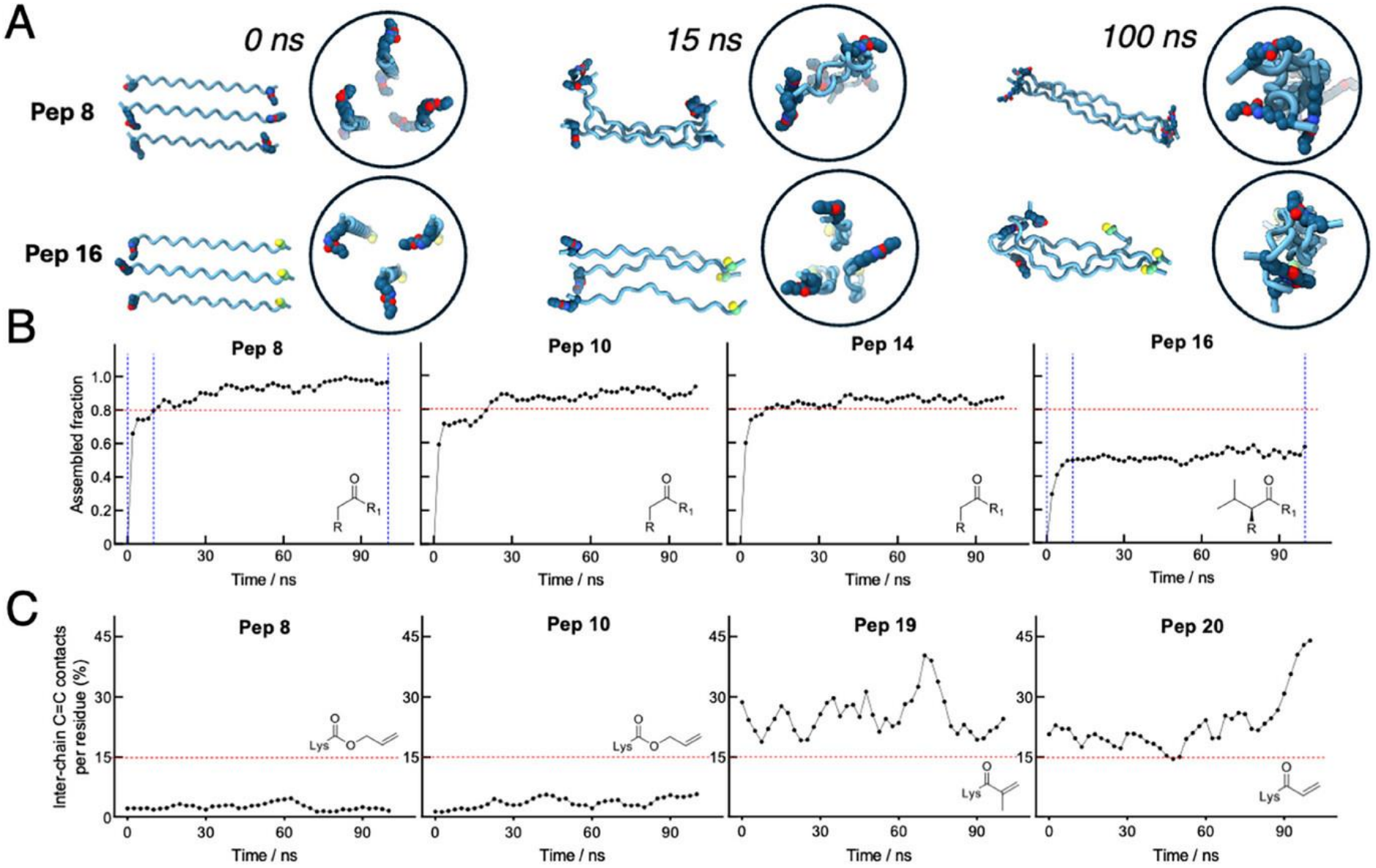
A
0 ns
15 ns
100 ns
Pep 8
Pep 16
B
Pep 8
Pep 10
Pep 14
Pep 16
Assembled fraction
Time / ns
C
Pep 8
Pep 10
Pep 19
Pep 20
Inter-chain C=C contacts per residue (%)
Time / ns

Figure 3.6. Molecular dynamics simulations for peptides indicate the impact of molecular features in triple helix folding and chemical reactivity. (A) Representative snapshots for Pep 8 and 16 taken at three different simulation times (0, 15, and 100 ns). Images within the circle correspond to a side view of the chain. (B) Average assembled fraction for peptides 8, 10, 14, and 16 for up to 100 ns simulation. The horizontal dashed red line corresponds to a well-assembled fraction. Values above the line indicate a stable helix, while values below indicate an unstable helix. The residue at position 18 (glycine or valine) is included in the figures to show the effect of amino acid substitution in the POG core. (C) Number of interchain contacts made between C=C alkene atoms on a normalized basis per alkene for peptides 8, 10, 19, and 20. The structure of the alkene present on each peptide is displayed to show the effect of alkene substitution. Values illustrated in B and C correspond to a selected dataset and only 5% of the data is shown to facilitate their depiction. Reproduced from *Ross et al. Advanced Functional Materials 2025.*

3.2.4 Mechanical Properties of Peptide-Based Hydrogels Can Be Tuned to Bond Skin *Ex Vivo*

In addition to junction functionality, the initial polymer fraction or concentration of peptide serves as a primary determinant of the hydrogel network's macroscopic properties.[32] Given the physical interactions and supramolecular assembly of these peptides, the effect of concentration could be non-linear with critical points.[34] Hydrogels using Pep 10 were formed at a minimal peptide concentration of ≈ 3% and *G*' quickly increased from a value of ≈ 400 Pa to ≈ 2000 Pa at peptide concentrations of 5% and 10%, respectively (Figure 3.7A), demonstrating a high degree of mechanical tunability achievable simply by altering the peptide loading.

To assess the translational potential of these materials, different concentrations of Pep 10 were evaluated for adhesive performance using an *ex vivo* murine skin wound closure model (Figure 3.7B). The ultimate tensile stress of the bonded skin-hydrogel construct for the 10% Pep 10 formulation (≈ 200 kPa) was significantly higher than that of the 5% gel (≈ 50 kPa) and was comparable to that of LiquiBand®, a clinically used cyanoacrylate tissue adhesive. Compressive tests showed that peptide hydrogels had a tunable compressive modulus ranging from 2-6 kPa (Figure 3.7C). For contextual benchmarking, a 1% type I collagen hydrogel was prepared using a previously validated protocol that has been shown to maintain structural integrity during intramyocardial injection and withstand cyclic deformation in the beating heart.[61] The collagen hydrogel displayed a significantly lower compressive modulus than both 5% Pep 14 and 10% Pep 10 gels, which were comparable in modulus but lower than the 15% Pep 10 formulation. Thus, peptide hydrogels achieve compressive moduli greater than a collagen formulation already proven suitable for intratissue injection in mechanically active environments.

In addition to their robust mechanical profiles, the peptide hydrogels displayed favorable biodegradation and safety characteristics (Figure 3.7D). The materials were stable in aqueous

solutions but underwent controlled degradation in the presence of collagenase, lasting approximately 24 hours, a duration longer than that of native type I collagen. Cytotoxicity assessments using human dermal fibroblasts indicated no adverse effects for cells seeded on top of Pep 10 hydrogels (Figure S29). For encapsulated cells, viability remained high at ≈ 90% with a 15-second UVA irradiation window, although longer exposures reduced viability to 70% (Figure S30). Notably, for the volumes used in these clinical applications, a 15-second exposure is sufficient to render a stable 3D scaffold.

The thermal stability of the materials, measured via differential scanning calorimetry (DSC), remained consistent across different concentrations of Pep 10. The denaturation temperatures were slightly higher than those measured via CD (Figure 3.7E, middle right), which likely reflects the added stabilizing effect of the covalent crosslinks on the triple-helical domains.[274] SEM analysis revealed a consistent pore size of ≈ 5.4 μm for Pep 10 gels across various concentrations, while Pep 14 gels exhibited larger pores of ≈ 13.8 μm (Figure 3.7E, right). These values are comparable to the 9.3 μm reported for recombinant human collagen hydrogels.[61] While the reason for these differences is not clear, one could speculate that supramolecular factors in the formation of the 3D structure might play a role.

Finally, lithium phenyl-2,4,6-trimethylbenzoylphosphinate (LAP) was evaluated as an alternative water-soluble photoinitiator, which is often favored in bioprinting for its high cytocompatibility and fast kinetics.[275] The elastic modulus of Pep 10 hydrogels remained stable across LAP concentrations ranging from 5 to 50 mM (Figure 3.7E, left). Additionally, the shape of Pep 10 hydrogel made with LAP could be controlled using a mold (Figure 3.7E, middle left), demonstrating that these hydrogels can be readily formed into defined geometries compatible with bioprinting workflows.

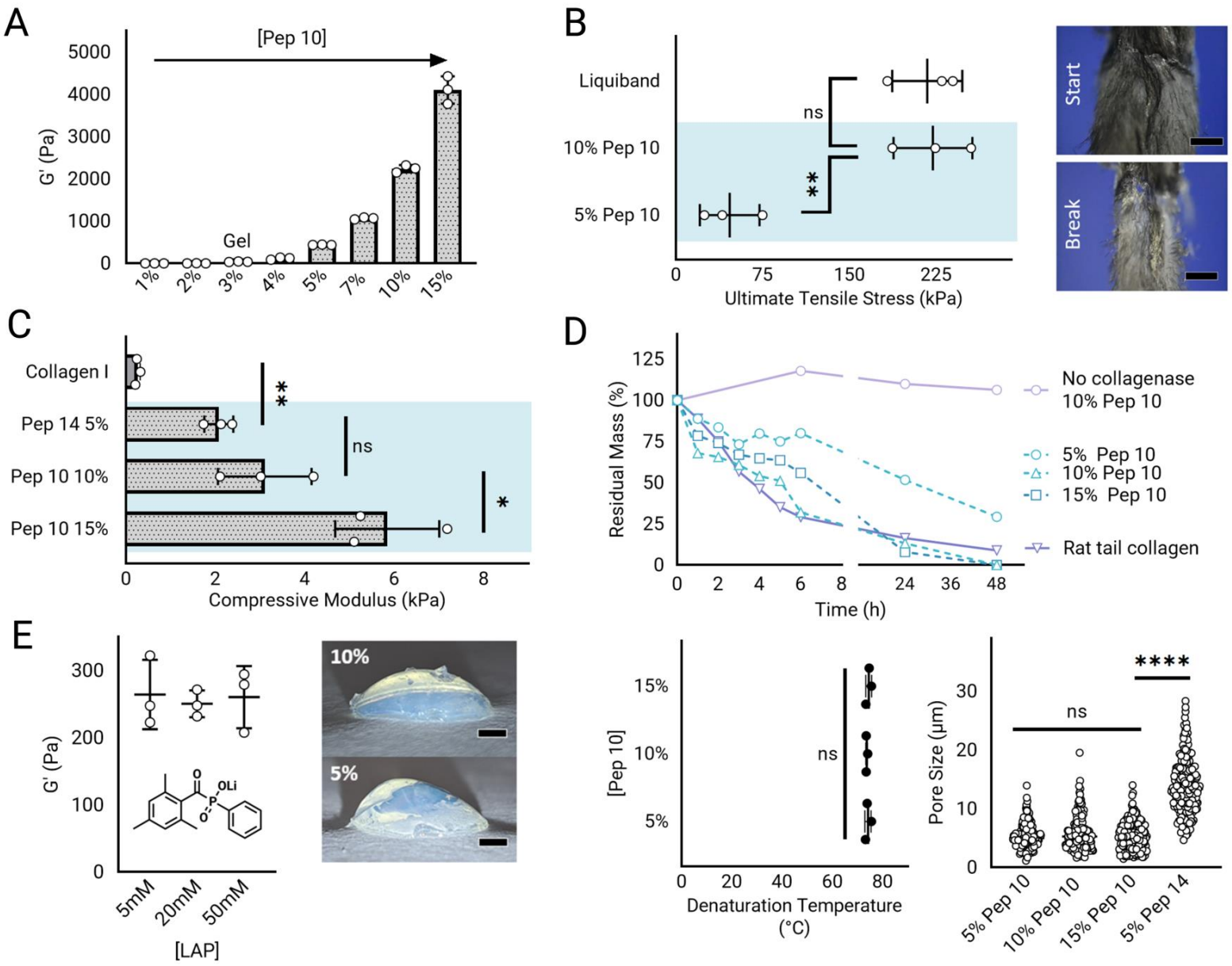
A
[Pep 10]
G' (Pa)
5000
4000
3000
2000
1000
0
Gel
1%
2%
3%
4%
5%
7%
10%
15%
B
Liquiband
10% Pep 10
5% Pep 10
ns
**
0
75
150
225
Ultimate Tensile Stress (kPa)
Start
Break
C
Collagen I
Pep 14 5%
Pep 10 10%
Pep 10 15%
**
ns
*
0
2
4
6
8
Compressive Modulus (kPa)
D
Residual Mass (%)
125
100
75
50
25
0
0
2
4
6
8
24
36
48
Time (h)
No collagenase
10% Pep 10
5% Pep 10
10% Pep 10
15% Pep 10
Rat tail collagen
E
G' (Pa)
300
200
100
0
5mM
20mM
50mM
[LAP]
OLi
10%
5%
[Pep 10]
15%
10%
5%
ns
0
20
40
60
80
Denaturation Temperature
(°C)
Pore Size (µm)
30
20
10
0
****
ns
5% Pep 10
10% Pep 10
15% Pep 10
5% Pep 14

Figure 3.7. Peptide hydrogels can be tuned to possess robust mechanical properties for skin bonding. (A) Hydrogel storage modulus increases along with Pep 10 concentration. Gelation occurs at a minimum of 3% peptide concentration. (B) *Left*: wound closure strength tests measuring the ultimate tensile stress of the bonded skin-hydrogel construct at bonding failure for Pep 10 hydrogels and LiquiBand. *Right*: images of the murine skin being stretched during the test. (C) Compressive modulus for peptide and rat tail collagen hydrogels. (D) Collagenase degradation assay for Pep 10 and collagen I hydrogels. (E) *Left*: Pep 10 hydrogel storage modulus using different concentrations (5, 20, and 50 mM) of LAP photoinitiator. *Middle left*: images of moulding experiments demonstrating the ability of 5% and 10% Pep 10 hydrogels to take on the shape of a cornea. *Middle right*: denaturation temperatures for different concentrations of Pep 10 hydrogels obtained from differential scanning calorimetry. *Right*: cryo-SEM pore size measurements for Pep 10 hydrogels. Pore size was quantified from 50 measurements taken across four independent regions per formulation. Data are presented as mean ± SD (n = 3 for all panels except cryo-SEM pore size analysis). Statistical significance was assessed using two-tailed unpaired Student's t-tests with unequal variance. *$p < 0.05$, **$p < 0.01$, ***$p < 0.001$. Reproduced from *Ross et al. Advanced Functional Materials 2025.*

4.0 Discussion

4.1 Summary

The central objective of this thesis was to develop and validate a library of synthetic collagen-like peptide hydrogels designed to address unmet needs in soft tissue repair. Two distinct crosslinking strategies, spontaneous thiol-maleimide Michael addition for "on-the-spot" application and photoactivated radical thiol-ene reactivity, were used to generate functional biomaterials. The first aim of this research resulted in spontaneously gelling CLP-PEG hydrogels, where the sequence NH_2-GCG$(POG)_8$GCG-OH was identified as the optimal candidate for clinical translation. These materials demonstrated rapid gelation in under 120 seconds and exhibited tunable mechanical properties along with good cytocompatibility for human cardiac and skin cells. For the second aim, *ex vivo* and *in vivo* models showed that these hydrogels proved effective as tissue sealants, achieving wound closure strengths in mouse skin comparable to commercial adhesives like BioGlue and successfully sealing corneal perforations while maintaining optical transparency. Furthermore, intramyocardial injection of these materials in a murine model of myocardial infarction led to the preservation of left ventricular ejection fraction over 28 days. Fluorescent tracking confirmed that the hydrogel remained within the myocardium for at least seven days, suggesting its potential as a localized reservoir for the sustained delivery of therapeutic agents or cells.

The third aim of this research resulted in mechanically robust, photoactivated peptide-only hydrogels with NH_2-GCG$(POG)_8$GK(alloc)G-OH and NH_2-CCC$(POG)_8$K$(alloc)_2$G-OH as the most promising sequences. By adjusting the peptide structure and concentration, the mechanical properties of the hydrogels could be turned. Molecular dynamics simulations provided insights

into how molecular features, such as the $(POG)_8$ core and the choice of alkene, dictate triple-helix stability and prevent unproductive intramolecular crosslinking. These photoactivated materials achieved significant bonding strength and were shown to be suitable for bioprinting workflows due to their ability to be molded into defined geometries.

4.2 Discussion of Aims 1 and 2

4.2.1 Multipurpose Peptide Screening and Material Design

The technological development of biomaterials remains costly and time consuming, particularly when large sample volumes are required for initial testing.[276] To overcome these barriers, a highly efficient screening strategy was implemented that utilized small sample volumes of approximately 50 μL. This approach reduced the necessary peptide quantities and experimental time by an order of magnitude compared to conventional methodologies. By intentionally limiting the number of amino acids in each sequence, synthetic complexity and cost were minimized while ensuring the final candidates possessed the necessary structural motifs for functional assembly. The choice of screening tests used in the strategy combined with the facile material assembly process enabled by the selection of effective chemistries allowed us to rapidly screen different formulations.

The material design relies on a synergistic dual mechanism inspired by the organization of natural structural collagen. By combining orthogonal Michael-addition chemistry with the supramolecular assembly of collagen-like triple helices, a hybrid peptide-copolymer network that is both robust and tunable was created. Unlike many peptide gels that rely solely on alpha-helix or beta-sheet folding, data presented here suggests that the triple-helical conformation provides significant mechanical reinforcement. Using a library of peptide structures and a rapid screening procedure for gelation, key structural components needed to render peptide structures that can assemble *in*

situ to a PEG backbone were identified. The resulting hybrid peptide-copolymer displayed desirable and tunable physical properties that can be adjusted simply by utilizing different peptide:PEG ratios (CM_{ratio}), thus making it amenable for use in different tissues. The resulting hydrogels feature a pore size of approximately 10 μm, which is optimized to facilitate host cell invasion and tissue integration. Furthermore, the material preparation is straightforward requiring only reagent solvation in minutes, without the need for external crosslinkers, special solvents, or purification and is sufficiently robust to be performed *in situ* when compared to other peptide-based biomaterials.[147, 198] For future clinical use, similar to other clinically used materials such as BioGlue, CLP-PEG technology will be delivered using a two barrel-syringe system that will allow for single-handed operation.

4.2.2 Comparison to Other Materials

CLP-PEG materials displayed adhesive properties comparable to those of BioGlue, which is remarkable when considering no specific adhesive moieties were added to the peptide sequence. Some key advantages of the material include simple, rapid *in situ* gelation, tunable hydrogel strength and adhesiveness, and a fully defined chemical composition. In contrast to animal-derived gelatin or collagen, which carry risks of immunogenicity and batch-to-batch variability, the synthetic approach ensures high consistency and safety for clinical translation. The modular nature of these sequences also allows for future refinements, such as the incorporation of cell-signaling motifs to promote targeted biological interactions. The tunable gelation of the material allows for its use as a topically applied material or in the form of an injectable material by simply using a syringe-mixing system.

In contrast, peptide gels that form solely from supramolecular assembly are weak and applied only as a topical dressing.[277] Instead, CLP-PEG materials can achieve a wound closure strength of up

to ≈ 100 kPa, whereas a pure peptide gel such as a recently reported tryptophan zipper system had a yield strength of 0.075 kPa.[278] Another LDLK12 peptide gel reported a failure stress of 0.019 kPa that could be increased to 0.035 kPa with EDC/NHS crosslinking.[279] Compared to other PEG-peptide systems,[201] CLP-PEG material renders stronger gels more quickly at physiological pH. Peptide hydrogels are often used as carriers for drug delivery,[280] which is another promising application for which CLP-PEG materials would be highly suited.

The relative simplicity and ease of application of CLP-PEG materials is a key advantage. CLP-PEG hydrogels are prepared rapidly, which is more convenient and simpler to operate with, thus making them more suitable to clinical application. In contrast, a previously reported peptide-based injectable material for treating heart tissue post-MI consisted of an elastin-mimetic peptide hydrogel with great mechanical strength under the action of upregulated trans-glutaminase.[281] However, the complex and time-consuming preparation methods that are needed result in a barrier to clinical implementation.[282]

While biomedical systems should be cost-effective and practical to find adaptation, the economic viability of this technology is supported by the increasing scalability of industrial peptide synthesis. As the number of peptide drugs in clinical trials continues to increase[283] and novel peptide drugs such as Semaglutide[284] receive media attention, peptide synthesis is becoming a scalable industrial process that can produce kilograms[285] or even tons[286] of finished product. Peptides of ≈ 30 amino acid residues, such as the 31 residue Semaglutide, are considered relatively short and can readily be scaled for industrial production.[102, 286] The cost to access peptides is reasonable for biomedical standards, with retail Semaglutide selling for ≈ 150 USD g^{-1} in the least expensive markets.[287] Therefore, the peptide-based materials, which consist of short peptide

sequences and are composed of only two easily-stored components, offer a cost-effective approach for generating peptide-based therapeutics for tissue and organ repair.

4.2.3 Therapeutic Efficacy in Corneal, Cutaneous, and Cardiac Models

The rapid gelation and robust adhesivity of these hydrogels make them versatile tools for various soft tissue injuries. In ophthalmic applications, the material successfully sealed corneal perforations and served as an intrastromal filler to alter corneal curvature without compromising optical clarity. When applied to skin wounds, the hydrogel provided a moist environment, reported to be beneficial toward wound healing,[288] that visibly accelerated healing and improved histological outcomes, including increased collagen deposition and a significant reduction in epithelial thickness. While data illustrated low macrophage polarization, this may be since macrophage expression varies across time during the process of wound healing. Initially M1 macrophages are seen, then replaced with M2 macrophages, and lastly both are gone from the wound as it heals and matures.[289] Since the skin was harvested late in this process, the macrophages may have already left the wound site at this point.

In the context of cardiac repair, the hydrogel was injected directly into the ischemic myocardium of a murine model. Over a 28-day period, the treatment effectively preserved heart function, preventing the characteristic loss of ejection fraction observed in control groups. While peptides and other biological molecules can be rapidly degraded in living organisms, fluorescent tracking revealed that the material persisted in the myocardium for at least seven days. This residence time suggests the hydrogel could serve as a protective depot for the localized delivery of drugs, extracellular vesicles, or cellular payloads. Further, the findings open new avenues for enabling modifications of the materials using the peptide structures and orthogonal click chemistry, such as

chemical functionalization of the PEG core,[290, 291] which would allow for the prolonged delivery of small drugs and molecules.

In summary, the cumulative data illustrate that engineering the chemical structure of collagen-like peptides allows for the development of functional crosslinking backbones suitable for the formation of hydrogels. The data also indicates that these peptides must contain at least two cysteine thiol-reactive groups for Michael addition click chemistry with adequate steric spacing, and that the supramolecular assembly of these peptides contributes to hydrogel strength. This unique combination of engineered click-self assembling peptides allows for the rapid *in situ* production of adhesive, multifunctional, and tunable hydrogels. These injectable materials were assessed and shown to be effective for therapy in three separate soft tissues including the skin, cornea, and heart. The simple yet robust chemistry, combined with the peptide engineering used to produce these gels leaves ample room for future biofunctionalization and/or loading of drugs, extracellular vesicles, or other payloads.

4.3 Discussion of Aim 3

4.3.1 Design and Assembly of Photoactivated Peptide Hydrogels

This study presents a rationally designed, peptide-only hydrogel platform that leverages supramolecular self-assembly and light activated thiol-ene crosslinking to form mechanically robust, cytocompatible, and tunable biomaterials. Materials were prepared entirely from collagen-like peptides, eliminating the need for synthetic polymer conjugates and offering a single-component formulation with advantages in reproducibility, scalability, and biocompatibility. Central to this approach is the use of $(POG)_n$ motifs to mimic the triple-helix architecture of native collagen and enable not only solubility and folding but also spatial organization of reactive residues

essential for crosslinking. Embedding thiol-ene reactivity directly into the peptide sequence further enables a highly specific, aqueous, and light-triggered mechanism that works synergistically with supramolecular assembly.

Screening of the peptide library provided essential insights into the structural prerequisites for successful hydrogel formation. Precursors bearing both cysteine and lysine (alloc) residues were highly effective for thiol-ene crosslinking when initiated by the UVA-activated photoinitiator I-2959, which is widely used due to its minimal toxicity.[292] Upon absorption of UVA light, I-2959 undergoes type I α-cleavage to split into a benzoyl and hydroxyalkyl radical, providing a source of radicals to drive polymerization.[293] Owing to its nucleophilic character, the hydroxyalkyl radical efficiently abstracts a hydrogen atom from a thiol group, driving reactive thiyl radical formation to initiate polymerization (Figure 1.5). While methacrylation is frequently used as a standard strategy in polymer hydrogel design,[134, 135] these findings indicate that methacrylated and acrylated peptides were less able to form hydrogels in comparison to the allyloxycarbonyl group. This is likely due to the alloc's reduced ability to form chain growth C-C bonds.[266, 273] The radical generated by thiol-ene addition to an acrylate is resonance-stabilized by the adjacent carbonyl (favoring further chain-growth addition to another alkene), while alloc's allylic radical lacks that conjugation and is more reactive toward hydrogen abstraction. In a system targeting a 1:1 stoichiometry of thiols and alkenes, the alloc group's preference for step-growth kinetics maximizes the number of effective intermolecular connections (Figure 1.5). Conversely, chain-growth reactions in this context likely lead to unproductive intramolecular cycling within a single triple helix, effectively truncating the network.

Furthermore, due to the spatial arrangement of the three-dimensional CLP structures, chain growth reactions may occur intramolecularly or within a single assembled triple-helix without creating

connections with the greater network. MD simulations indicated that these intra-helix reactions may be more likely for the non-alloc alkenes, further explaining the superior mechanical properties of alloc peptide hydrogels. Likely due to these factors, peptides containing only alkenes failed to form hydrogels. Short peptides bearing thiol-ene chemistry were also tested, but failed to form hydrogels, in some cases due to solubility issues. Peptides that contained a $(POG)_8$ structure were effective in forming gels, with this motif responsible for folding being highly correlated to the R_{pn} and melting temperature parameters associated with triple helix formation. Reduction of the R_{pn} parameter through a Gly-Val amino acid substitution prevented hydrogel formation, highlighting the contribution of supramolecular assembly to the hydrogel formation process.

4.3.2 Kinetic Profiling and Mechanical Benchmarking

Kinetic studies of photo-CLP hydrogels indicated that gel formation was completed in 5-10 min at a lower photoinitiator concentration and <2 min at a high concentration, a rapid timeframe enabled by efficient thiol-ene chemistry. This length of time is comparable to or shorter than suturing time, making it easy to use the material for wound closure applications. The mechanical properties of the peptide hydrogels were highly tunable through multiple parameters, including peptide concentration, junction functionality, and choice of alkene group. The collagen-like POG core of the peptides is highly hydrophilic, allowing a high concentration (15% +) of peptide or the use of multiple reactive residues per peptide. Photo-CLP optimized hydrogel enabled a tissue-hydrogel composite bonding strength of ≈ 200 kPa in an *ex vivo* skin wound closure model. This is equivalent to the performance of the commercial cyanoacrylate tissue adhesive Liquidband® and indicates a suitable level of mechanical performance. This overcomes the common limitation of insufficient mechanical strength in peptide-only hydrogels previously discussed. However, unlike cyanoacrylates, peptide hydrogels are biodegradable, being cleared by collagenase.

Cytocompatibility studies also show no detectable toxicity. Together, these results establish strong *ex vivo* performance and motivate future studies to further examine biodegradation, host response, and long-term tissue integration.

Beyond their utility as adhesives, the spatially controlled nature of light-triggered crosslinking opens significant possibilities for biofabrication. Data shows that Pep 10 hydrogels are compatible with both I-2959 and LAP, two common photoinitiators used in the field of 3D bioprinting.[294, 295] By utilizing simple molds, photo-CLP hydrogels were cast into complex, cornea-like geometries that maintained their structural definition after irradiation. This ability to stabilize specific shapes under mild, aqueous conditions provides a platform for future bioprinting strategies where the encapsulation of cells and the transport of biomolecules are required.

4.4 General Discussion

4.4.1 Limitations and Future Directions

While the collagen-like peptide technology presented in this dissertation presents several advantages, technical limitations remain. One constraint is the irreversible nature of the covalent crosslinking utilized in both the Michael addition and photoactivated thiol-ene systems. While these strong chemical bonds provide mechanical resilience, they lack the dynamic reversibility seen in purely supramolecular or self-healing hydrogels. Thus, unlike some other peptide hydrogels,[296-298] engineered CLP gels cannot self-heal due to the inability of the current CLP networks to reform bonds after mechanical failure. Future iterations of this work could incorporate dynamic covalent chemistries, such as boronate esters[299] or disulfide exchange[300] mechanisms, to confer self-healing properties without sacrificing the underlying stability of the triple-helical nodes.

Furthermore, the "on-the-spot" gelation of the CLP-PEG formulations, while advantageous for emergency surgical sealants, presents challenges in terms of spatial precision. Because the reaction kinetics begin immediately upon mixing, the window for fine-tuning the material's shape is relatively narrow compared to remotely activated systems.[301] While the photoactivated CLP system addressed this concern by providing temporal control over gelation, the potential for UVA-induced cell toxicity during prolonged exposures remains a variable that must be carefully managed. Transitioning toward visible or infrared light systems by utilizing photoinitiators such as riboflavin or eosin Y could further enhance the safety profile of these materials and allow for deeper tissue application.[302-304] This shift would address the biological concerns associated with ultraviolet exposure, specifically the risk of inducing DNA double-strand breaks and the generation of intracellular ROS.[305] Furthermore, the longer wavelengths found in visible light are less susceptible to scattering and absorption by the polymer network and surrounding tissue, thus providing a much greater depth of penetration than UVA light.[306, 307] This is critical for the development of thicker, 3D scaffolds required for where the hydrogel must be cured deep within a tissue defect.

The CLPs used in this study contained mostly $(POG)_n$ motifs along with some examples of $(PPG)_n$ to form a collagen-mimetic core. However, other amino acids such as lysine and aspartic acids can be used to form ionic cores that also result in folding.[244] Use of these amino acids can also result in the generation of 'sticky ends' that result in quaternary assembly of different triple helical barrels, allowing the generation of supramolecular hydrogels without covalent bonding.[244] Furthermore, heterotrimers where not all of the three monomers in a triple helix assembly contain the same molecular sequence can be generated.[308, 309] For a deeper future understanding of CLP

biomaterials, the effect of using these different folding strategies should be compared to the $(POG)_n$ approach utilized in this work.

The murine models used throughout this thesis provide valuable initial data, but the fundamental differences in physiology limit the reliability of the findings to humans.[310] The lack of common comorbidities seen in patients such as older age and diabetes is another limitation of the models.[311] These comorbidities are associated with defective progenitor cell populations and can reduce regenerative capacity within the tissue, decreasing the ability of biomaterials to stimulate endogenous repair.[312-314] Furthermore, real patient populations are on medications that the mice models do not receive, potentially leading to unexpected interactions. Lastly, the timepoints investigated of a month or less were relatively short. Longer follow-up times are necessary to show long-term safety. The use of emerging technologies such as organoid[315] and organ-on-a-chip[316] models along with large animal models and a longer timeframe of testing will improve translatability and regulatory approval.

The modular architecture of the collagen-like peptide platform developed in this research offers extensive opportunities for future modification, particularly in terms of biofunctionalization. One avenue for improvement involves the direct incorporation of specific amino acid sequences that mimic the native signaling environment of the extracellular matrix. For example, the inclusion of the GFOGER motif, a well-characterized sequence that facilitates binding to collagen-specific integrins, could significantly improve cell adhesion within the 3D matrix.[317] In addition to collagen-mimetic cues, the conjugation of other bioactive peptides, such as the ubiquitous RGD adhesion motif or specific immunomodulatory sequences, provides a versatile strategy to tailor the material's biological efficacy for diverse tissue repair applications.[318] Beyond the tethering of ligands, the CLP hydrogel network can serve as a potent delivery vehicle for a variety of

therapeutic payloads.[319] The internal porosity and degradability of the material make it suited for the sustained release of pharmacological agents, including small-molecule drugs or localized growth factors, as well as the encapsulation and protection of exogenous cells for regenerative medicine.[320, 321] However, increasing complexity can result in a growing regulatory burden.

The transition from the laboratory to clinical practice involves navigating significant hurdles in manufacturing, shelf-life, and regulatory approval.[322] The minimalist design philosophy adopted in this thesis with a focus on short, sequence-defined peptide should lessen the difficulty of meeting these challenges. Simple materials are generally easier to characterize and validate for regulatory bodies as they avoid the complexities associated with blended biopolymers or uncharacterized animal-derived extracts. Practical concerns such as integration into surgical workflows, shelf life, sterility and cost are of key importance in moving from the research stage to clinical use, highlighting the need for multidisciplinary collaboration between scientists and clinicians.[323] Biomaterials must be manufactured in large quantities without compromising structural integrity, bioactivity, or sterility, with industrial peptide synthesis providing a potential solution. In addition to practical concerns, the models used for materials testing should be examined.

Recent trends in peptide and protein-based biomaterials are characterized by a focus on the development of multifunctional biomaterials that can not only provide structural support but also promote healing and regeneration through modular bioactive motifs, immunomodulatory ligands, and molecular scavenging.[324-326] To meet these needs, multifunctional biomaterials must be designed with appropriate mechanical properties, but the optimal values of these properties for each organ system remain poorly characterized.[141] Optimizing the ability of a material to accomplish these goals will require further research into pathophysiological processes. Ideally, this

understanding should be personalized for each patient and their unique needs, including any comorbidities such as diabetes or advanced age.[327]

To realize this vision of personalized regenerative medicine, the design process must evolve from a linear progression to an iterative, data-informed cycle (Figure 4.1). By utilizing emerging technologies such as single-cell and spatially resolved transcriptomics, researchers can gain a better understanding of the exact biochemical pathways and receptors triggered by the presence of a material, revealing insights missed by conventional histological approaches.[328] For instance, analysis of individual cells can identify rare individuals that cause inflammation and fibrosis,[329] while spatial transcriptomics has recently shown a spatially distinct effect from hydrogel administration in a rat MI model.[330] Integrating these high-resolution biological insights with artificial intelligence and machine learning could allow for the predictive design of novel material formulations with optimized bioactivity. Combining these new technological insights with proven design principles will lead to the next generation of multifunctional and personalized therapies for soft tissue repair.

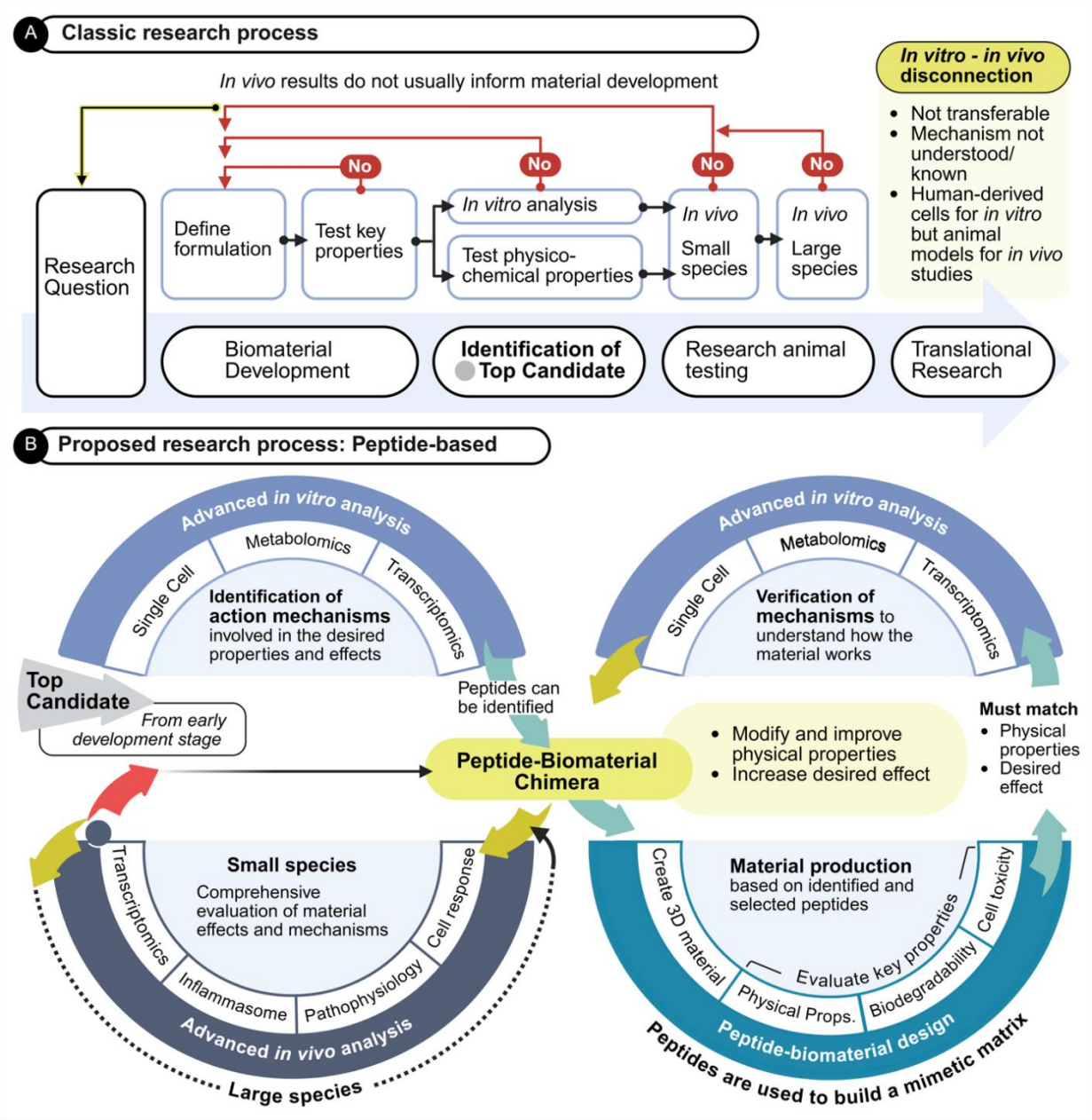

Figure 4.1. Classic research process vs proposed process for development of peptide biomaterials. (A) Traditional workflow for the development and assessment *in vitro* and *in vivo* of biomaterials for tissue and organ repair, including workflow drawbacks on the right. **(B)** Proposed iterative workflow for biomaterial development using advanced OMICS as tools for identifying mechanisms of action. The multi-staged design of the iterative process calls for assessment at several check-up points before moving into *in vivo* models.

4.4.2 Conclusion

The objective of this thesis was to develop CLP-based biomaterials for soft tissue repair. For *in situ* spontaneously gelling CLP-PEG hydrogels, the sequence NH_2-GCG$(POG)_8$GCG-OH was identified as the top candidate. Resulting CLP-PEG materials were cytocompatible and quickly gelled (<120 s) upon application to the target site. The materials could seal *ex vivo* mouse skin with comparable strength to BioGlue and accelerated wound healing *in vivo*. CLP-PEG hydrogels were transparent and could successfully both seal and fill corneal defects. Lastly, they were injectable and preserved heart function in a mouse MI model. Photoactivated CLP-only hydrogels were also developed, with the sequences NH_2-GCG$(POG)_8$GK(alloc)G-OH and NH_2-CCC$(POG)_8$K$(alloc)_2$G-OH identified as the most promising ones. CLP-only materials were cytocompatible and could seal *ex vivo* mouse skin with strength comparable to Liquiband. These minimalistic but tunable CLP biomaterials provide a multifunctional platform for soft tissue repair.

Appendices

5.1 Supplemental Data

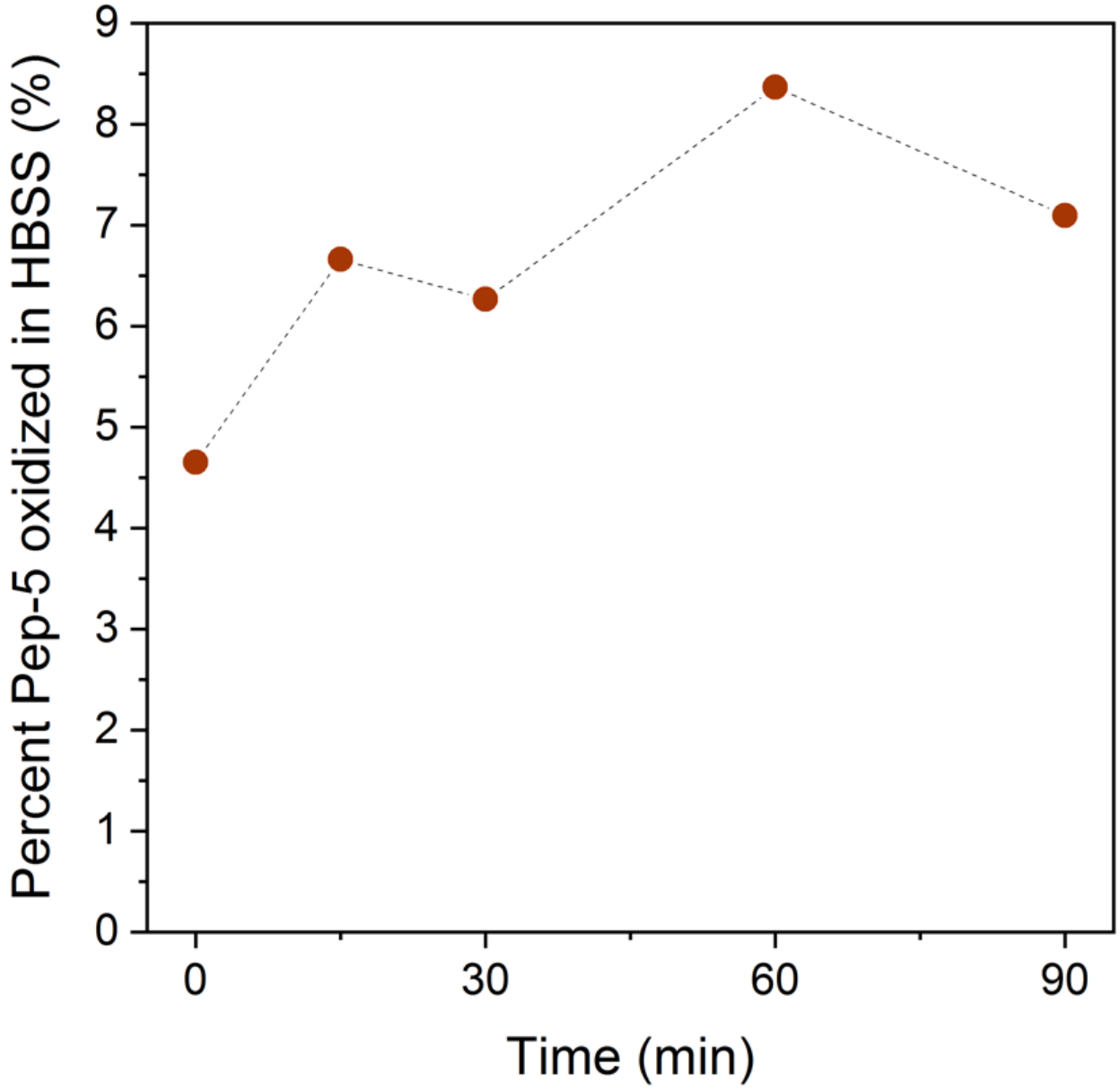

Figure S1. Engineered peptide sequences do not form dimers in solution. Relative abundance of Pep-5 monomer to disulfide dimer measured through mass spectroscopy identification of [M*2+3H] signal for the disulfide dimer product in Hank's buffer saline solution (HBSS). Dimer formation creates a new peptide mass of 2,591*2 – 2H = 5,180 Da that produces a +3H ion signal of 1,728 Da.

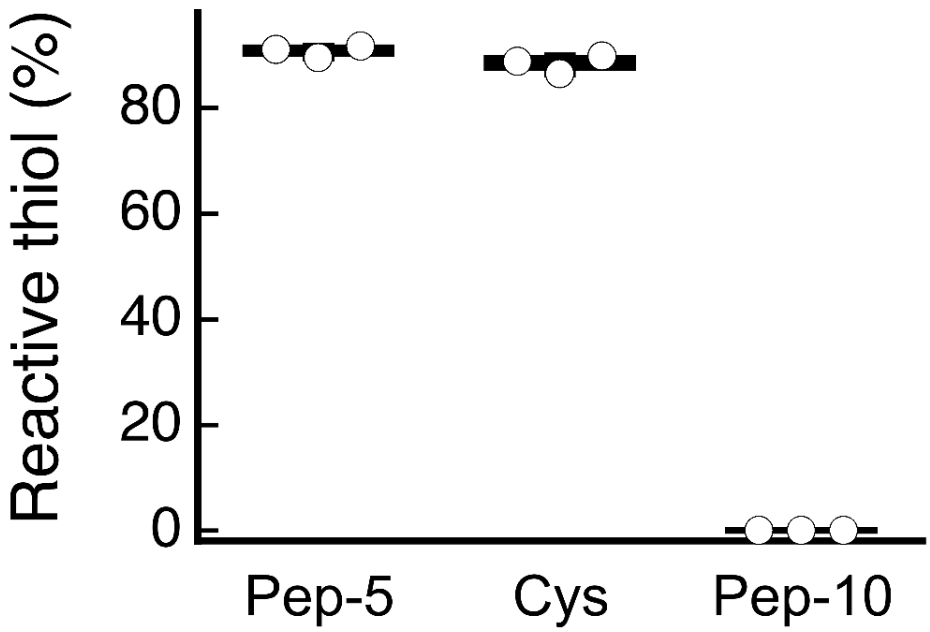

Figure S2. Engineered peptide sequences contain reactive thiols. Percent reactive thiol for Pep-5 (NH_2-GCG$(POG)_8$GCG-OH), Pep-10 (NH_2-GGG$(POG)_8$GGG-OH), and free cysteine (positive control). Reactivity was measured with Ellman's assay via reaction with 5,5′-dithiobis-(2-nitrobenzoic acid) (DTNB). All solutions were freshly prepared in 100 mM sodium phosphate buffer pH 7.4 while samples (n=3) prepared at a concentration of 0.5 mM for peptides (1.0 mM thiol concentration for Pep-5 containing two cysteines) and 1.0 mM free cysteine then diluted 21x with 0.5 mM DTNB and incubated for 30 minutes in the dark before measurement. The sequence containing cysteine (Pep-5) showed similar available cysteine compared to the control while the sequence with no cysteine residues (Pep-10) showed no available cysteine.

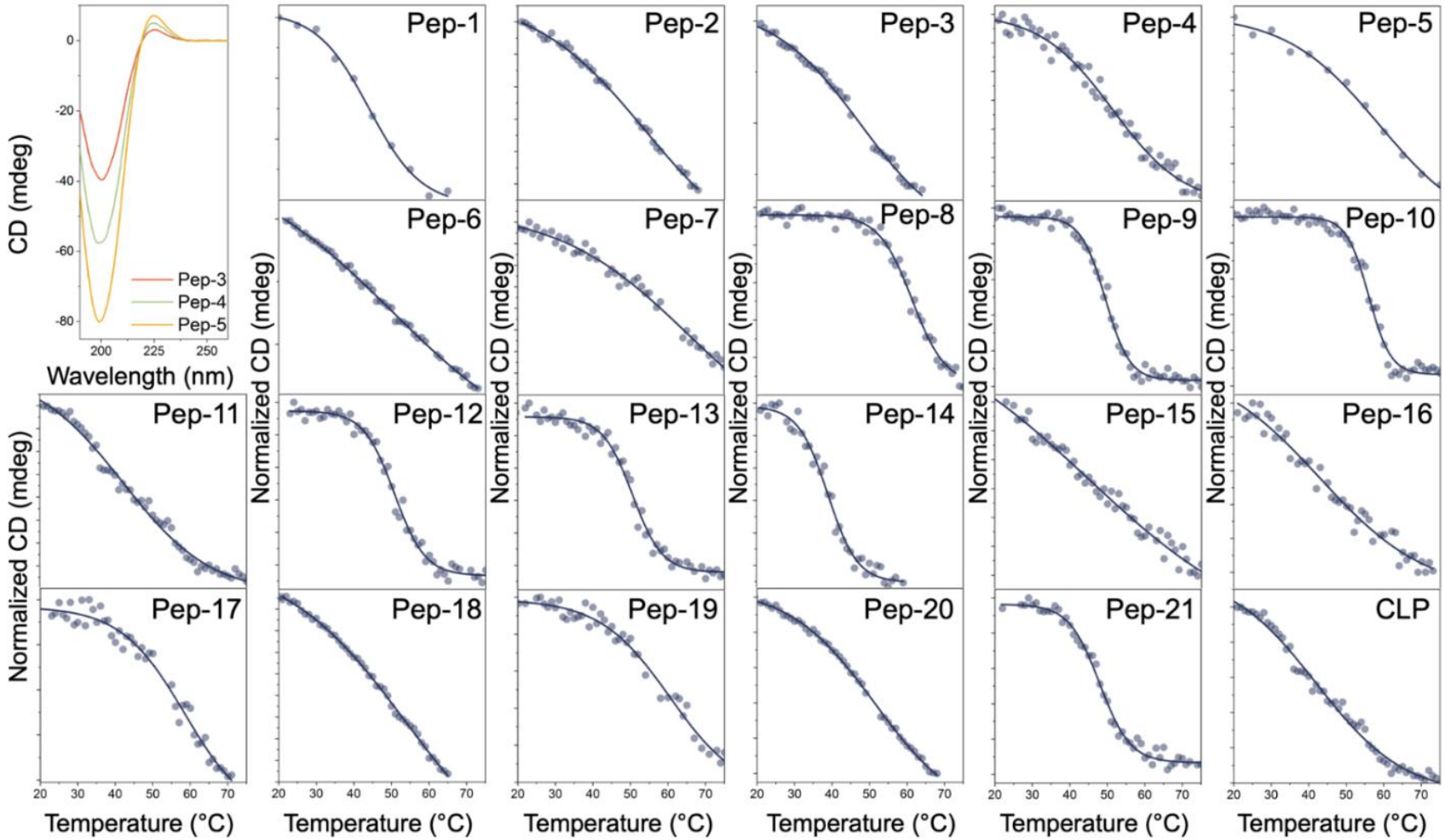

Figure S3. Engineered peptide sequences display melting curve profiles similar to collagen like peptide. *Top left*: CD spectra for selected peptides (3, 4, and 5) measured at 200 μM concentration in phosphate saline buffer pH 7.4. The other plots in the figure correspond to melting curve plots measured for the 21 peptides and CLP at 220 nm scanned from 20 to 75 ºC. Curves were fitted using a sigmoidal model with $R^2 > 0.99$.

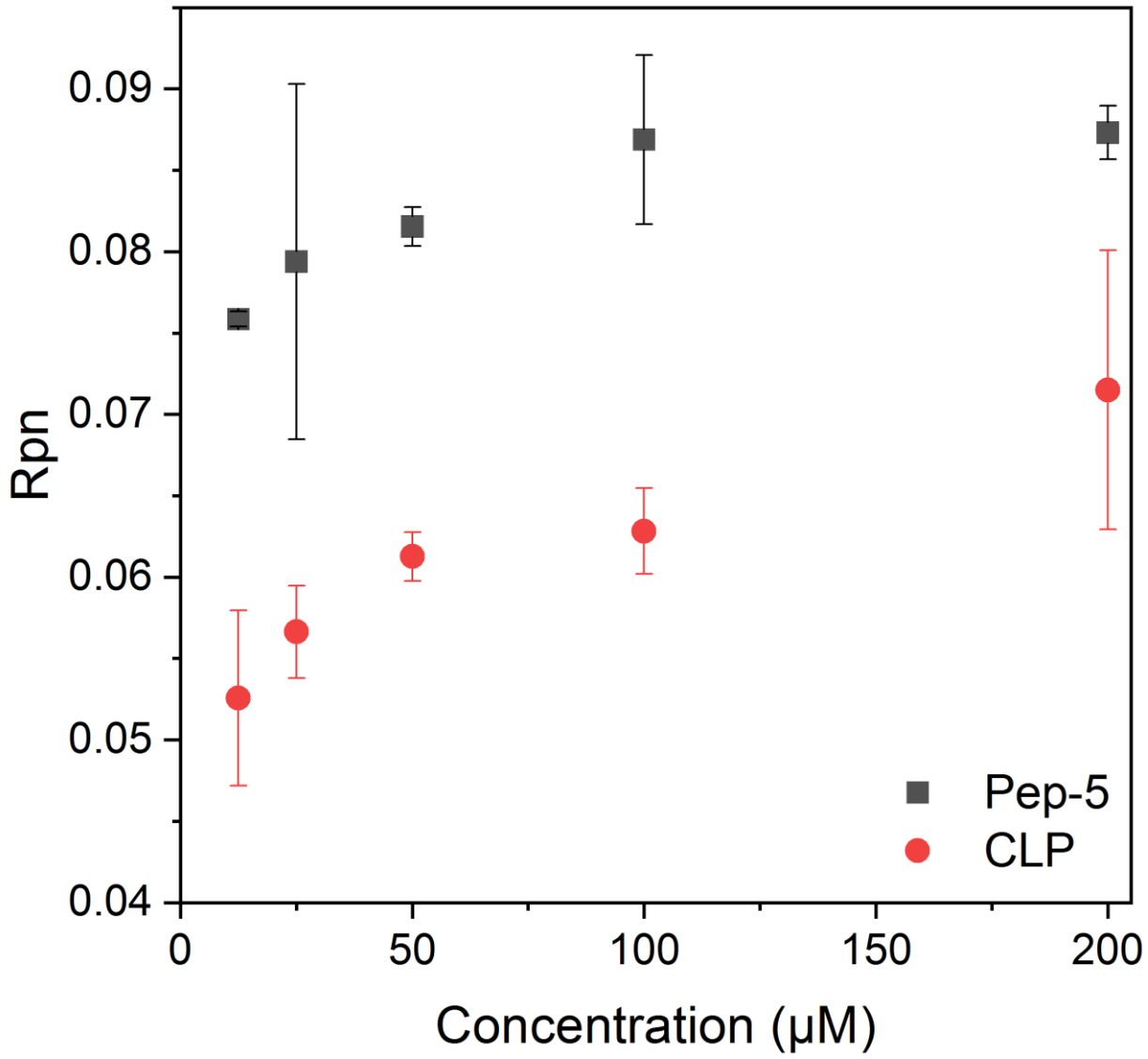

Figure S4. Engineered peptide sequences fold in a concentration dependent manner. The folding (R_{pn}) of the top candidate peptide Pep-5 and the control CLP at different concentrations. Experiments were carried out in phosphate saline buffer pH 7.4.

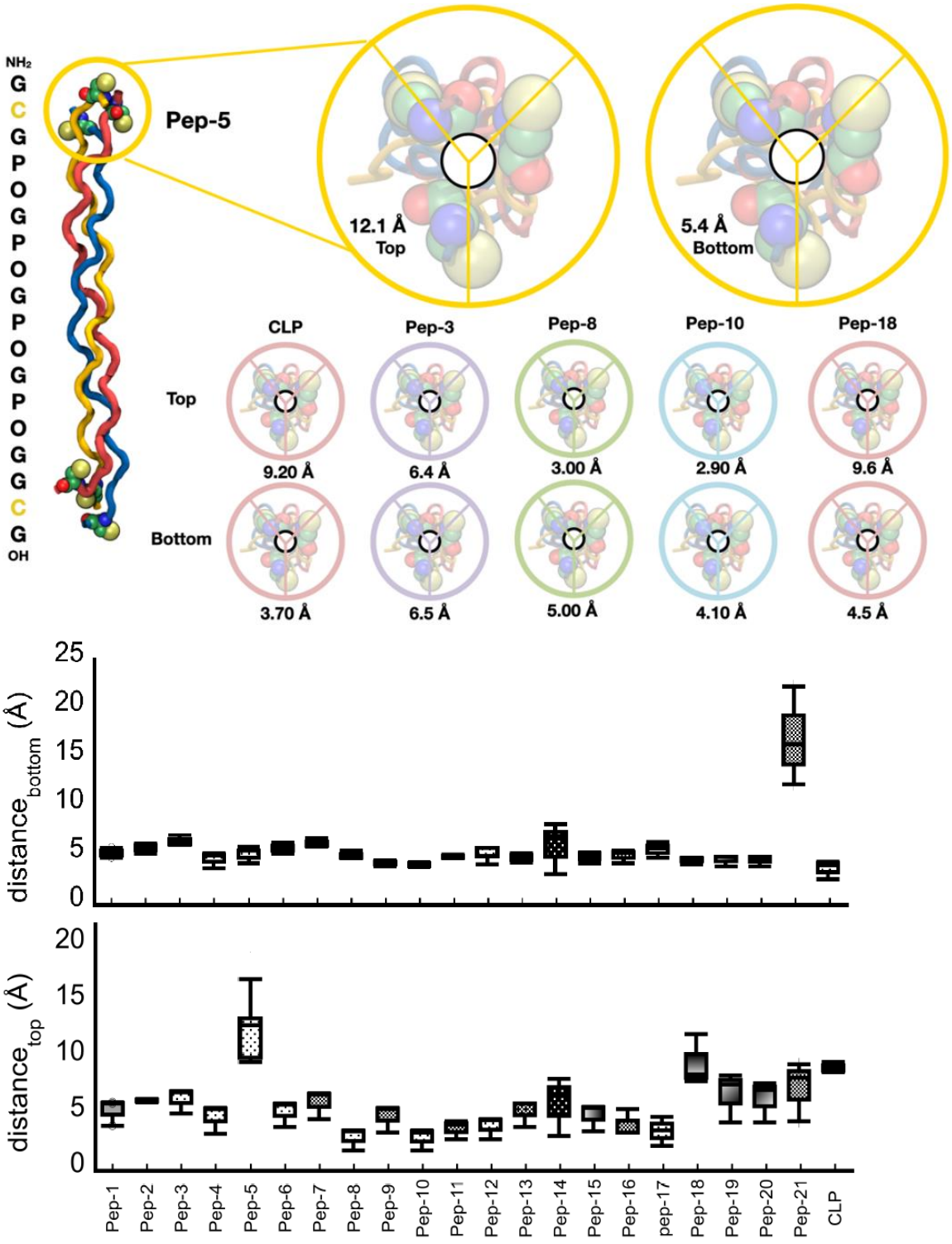

Figure S5. Amino acid sequence influences 3D structure of the engineered peptide. *Top*: Representative examples for modelled collagen-like peptides display a tight barrel-like core structure that unwinds at the ends as measured from the centre of the barrel. *Bottom*: Calculated distances (central vector model, see experimental) measured at the bottom (carboxy terminal) or top (amine terminal).

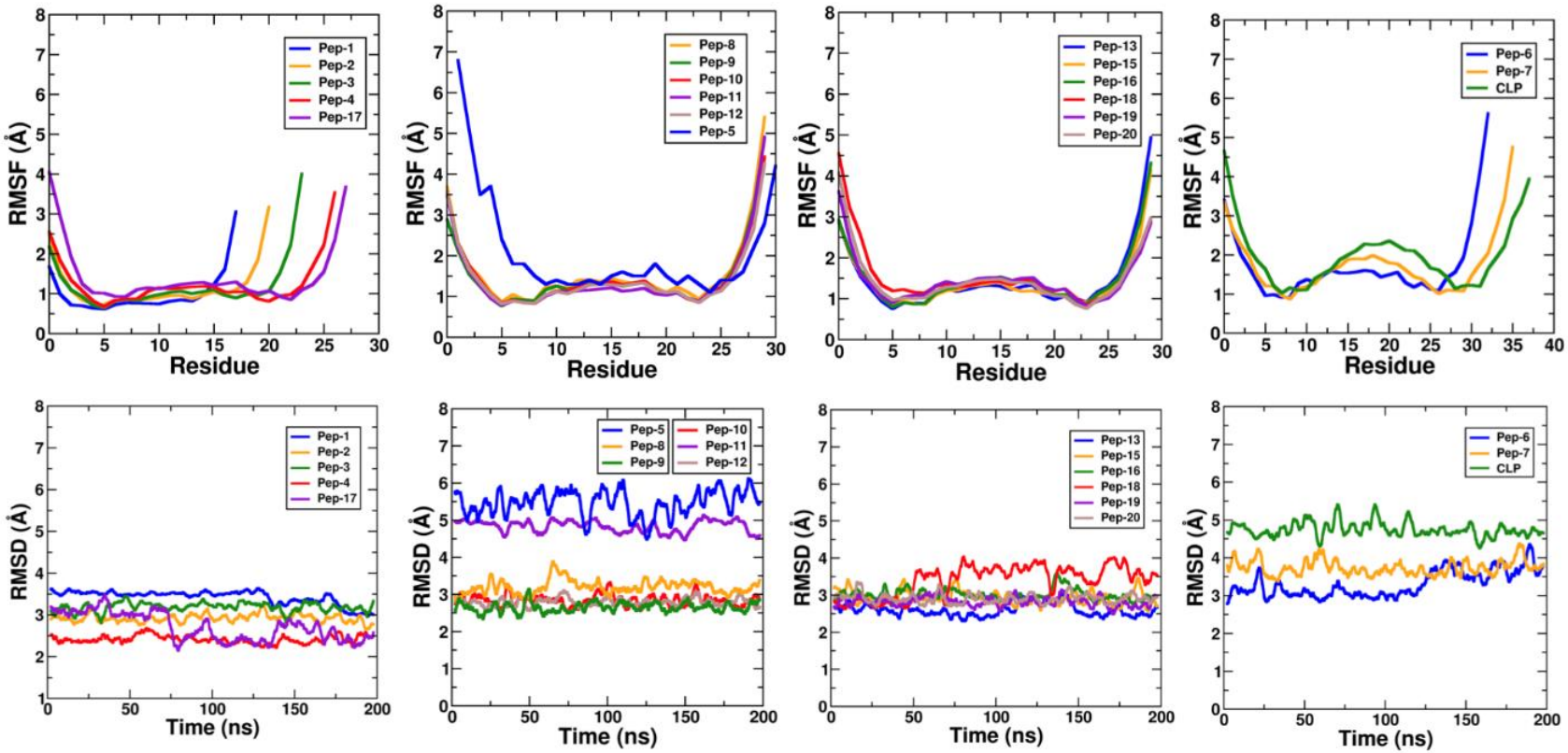

Figure S6. Root Mean Square Fluctuation (RMSF) and Root Mean Square Deviation (RMSD) analyses for peptides illustrate Pep-5's unique geometrical features while conserving folding stability. *Top:* Root Mean Square Fluctuation (RMSF) for each residue of the simulated peptides as a function of their initial conformation, highlighting residues with a higher average of motion over time (last 200 ns). The graphs were organized based on the length of each peptide. *Bottom:* Root Mean Square Deviation (RMSD) of each peptide in the final 200 ns of simulation relative to its initial conformation. This average distance of all atoms demonstrates that peptides achieve structural stability that persists over time. The graphs maintain the same distribution as in the case of RMSF.

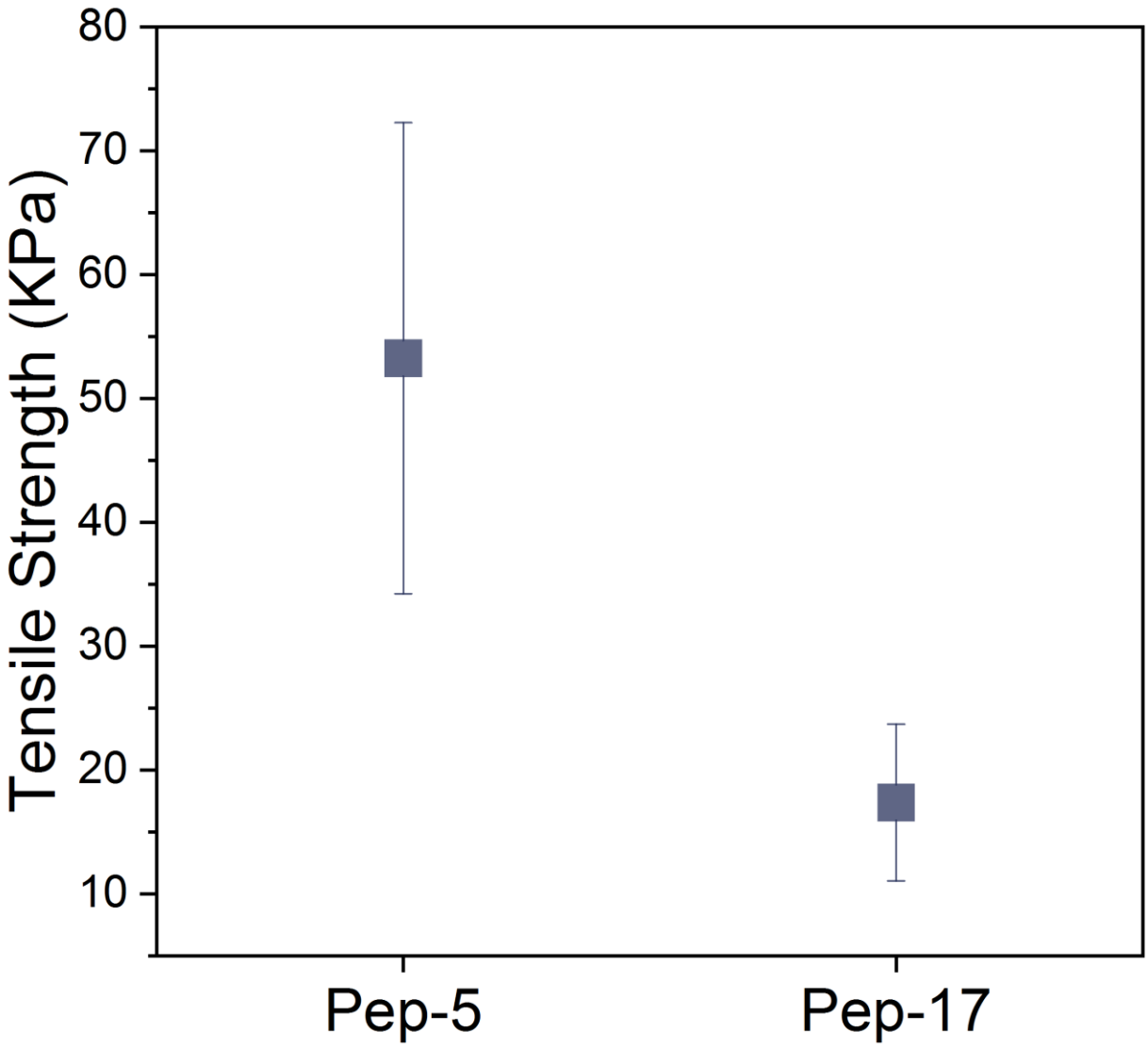

Figure S7. Modification of a single amino acid in peptide sequence affects bonding capacity of the engineered hydrogel. To investigate the effect of the glycine spacer the most effective sequence of Pep-5 was altered by removing a glycine spacer to produce the sequence Pep-17. Tensile strength testing was performed for these two peptides. The spacer peptide sequence was significantly stronger $p<0.05$ (~45 kPa, n=5) than the sequence lacking a spacer (~18 kPa, n=5) despite similar folding propensity (R_{pn} 0.087 vs 0.080 for Pep-5 and Pep-17, respectively) which could indicate a less efficient coupling reaction.

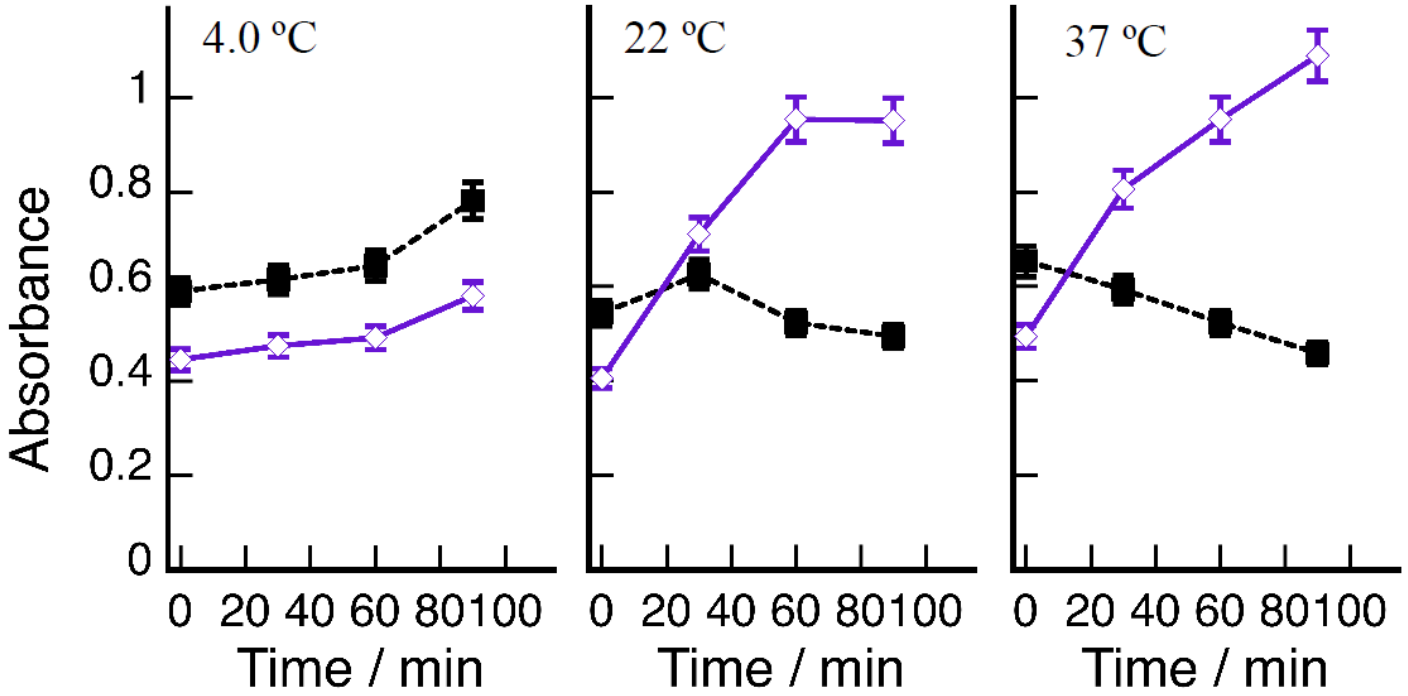

Figure S8. Maleimide stability is temperature dependant. Changes in absorption intensities at 300 nm (squares) and 260 nm (rhomboid) for maleimide solutions measured in carbonate buffer at three different temperatures (n = 3). Changes in absorption intensities are indicative of maleimide group hydrolysis.

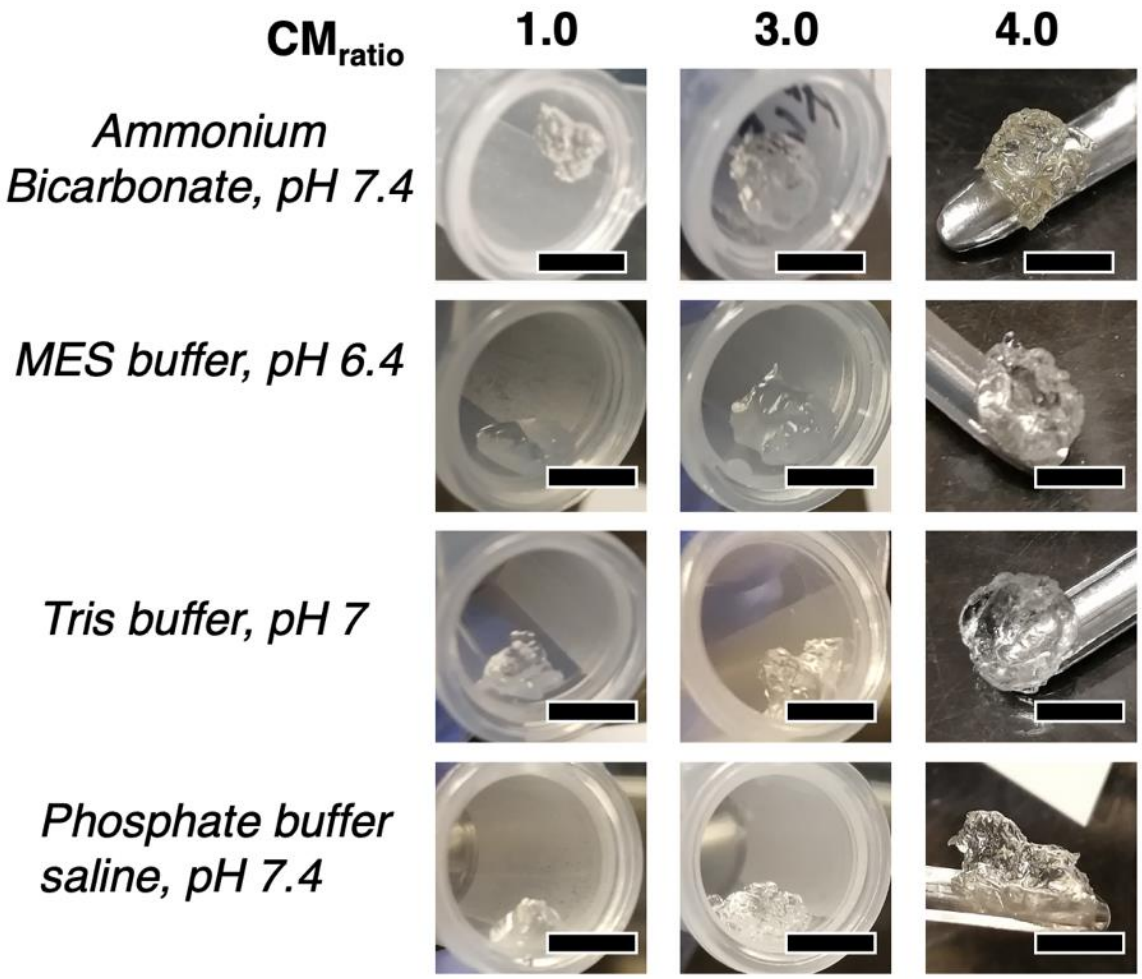

Figure S9. Peptide-based material can be prepared in different buffers. The ability of the top peptide candidate (Pep-5) to form hydrogels was tested in various common buffers (ammonium bicarbonate, MES, Tris, PBS) in a range of physiological pH values (6.4-7.4) and different ratios of peptide to PEG maleimide (CM_{ratio}). Representative pictures taken after 30 min hydrogel preparation. Hydrogel formation was visible in all buffers at the different CM_{ratio} tested. Note that for the 4.0 CM_{ratio}, the hydrogel must be removed from the Eppendorf tube as it was a solid material. Scale bars for 1.0 and 3.0 CM_{ratio} are 5 mm. For the 4.0 CM_{ratio} scale bar is 2 cm.

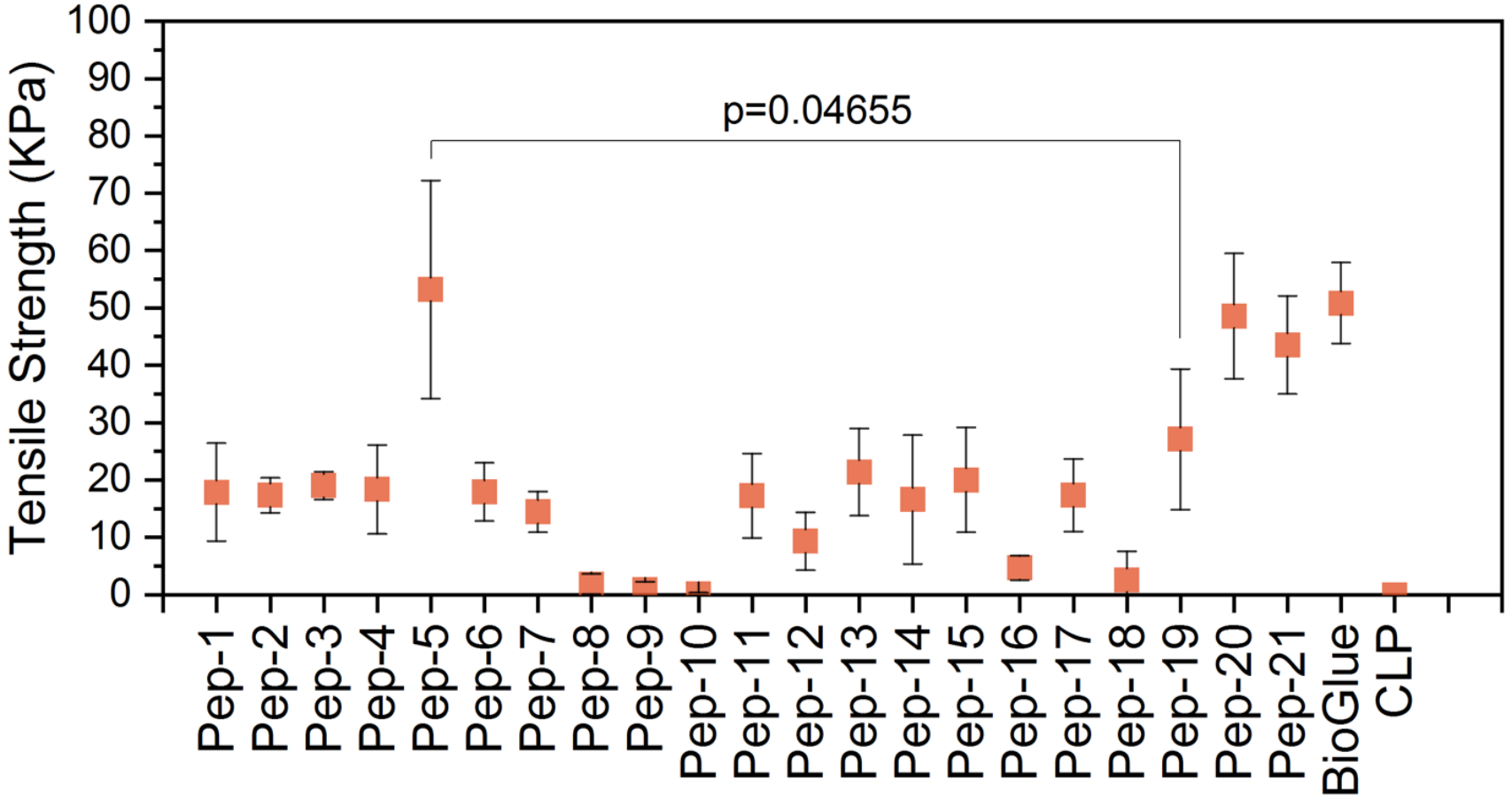

Figure S10. Pep-5 is the best peptide sequence for tissue bonding. Tensile strength in kPa for mice skin *ex vivo* bonding carried out using the different peptide variants (CM_{ratio} = 4.0, n = 5). Samples measured in quintuplicate. P value calculated from t-test (two tails unpaired data).

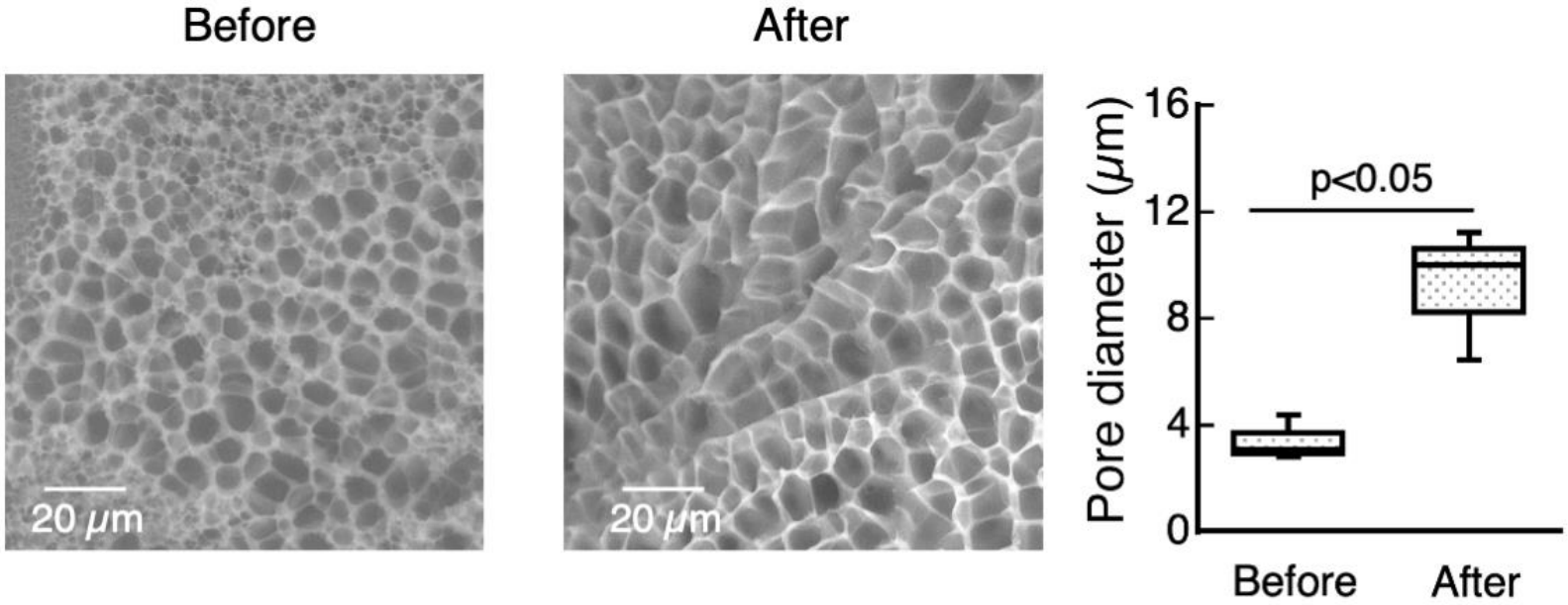

Figure S11. Pep-5 hydrogels are porous. Hydrogel samples of Pep-5 formulations were either tested right after preparation or swollen overnight in phosphate saline buffer. Then, the hydrogel structure was evaluated using a TESCAN scanning electron microscope, Model VegaII XMU, at low-vacuum conditions. SEM images of hydrogels were captured at varying magnifications. Setting conditions included an acceleration voltage of 20 kV, a Cryo-Stage temperature of −50 °C and a chamber vacuum ≈ 35 Pa.

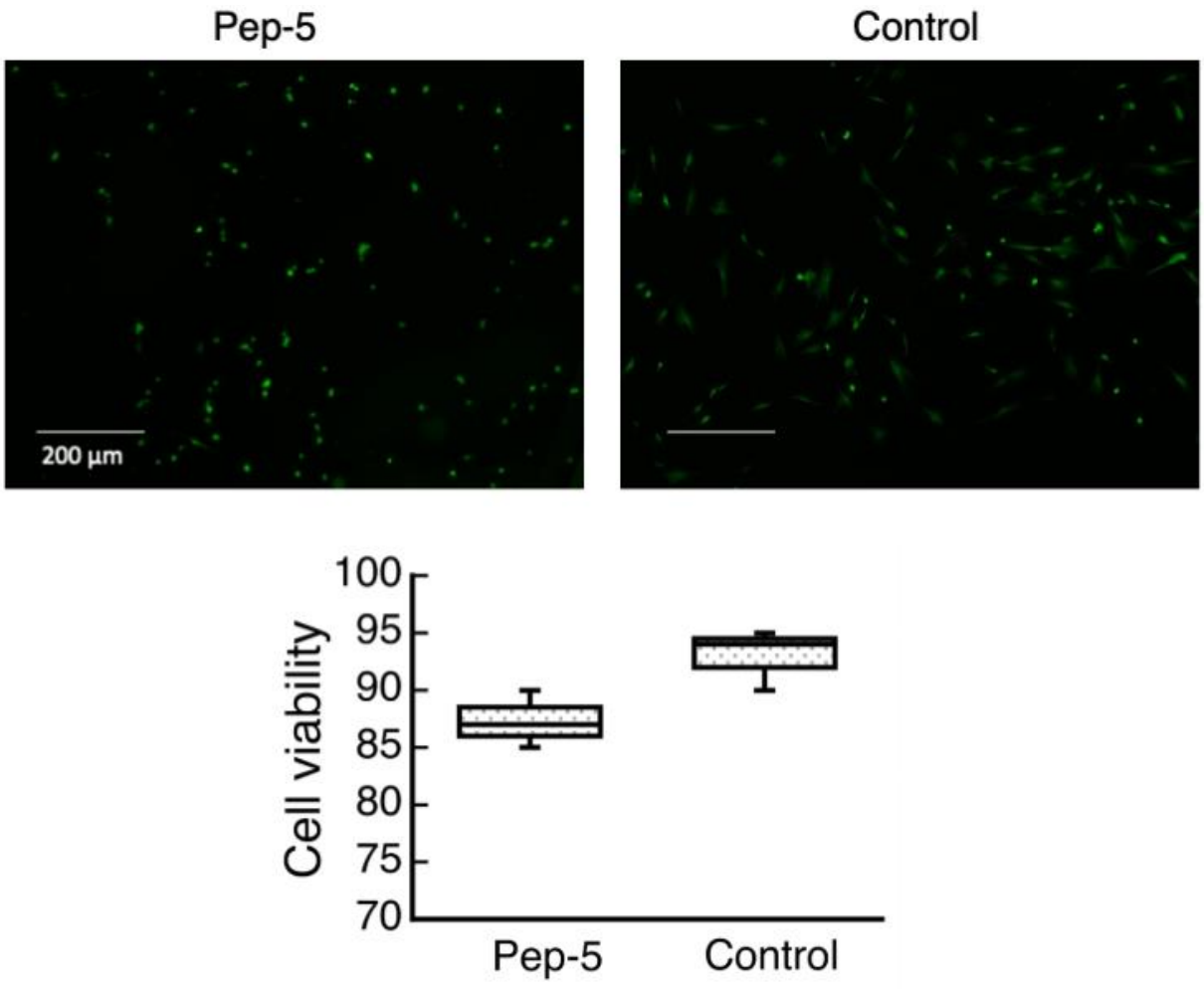

Figure S12. Engineered peptide sequences do not exhibit toxic side effects for human skin fibroblast cells. Cell viability measured using Live/Dead assay for fibroblast cells seeded on top of Pep-5 hydrogels or gelatin coated well plates (48 h post seeding, n = 3). Data was not statistically different between the two groups.

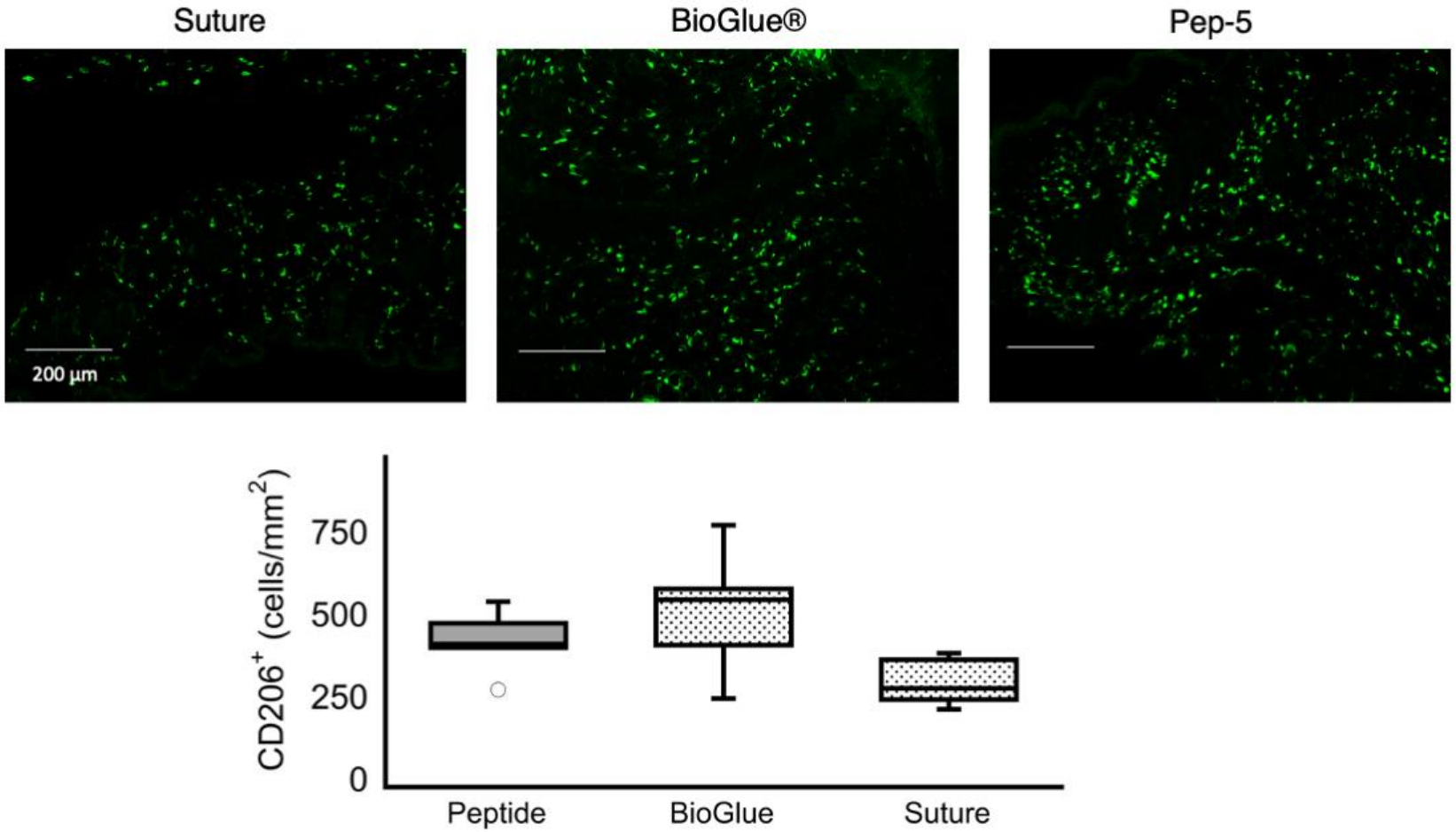

Figure S13. CD206+ positive cells in animals treated with the different experimental groups. Top images show representative images for tissue slides displaying CD206+ positive cells for suture, BioGlue, and peptide (Pep-5) treated groups. Data showed no statistically significant differences between all three groups.

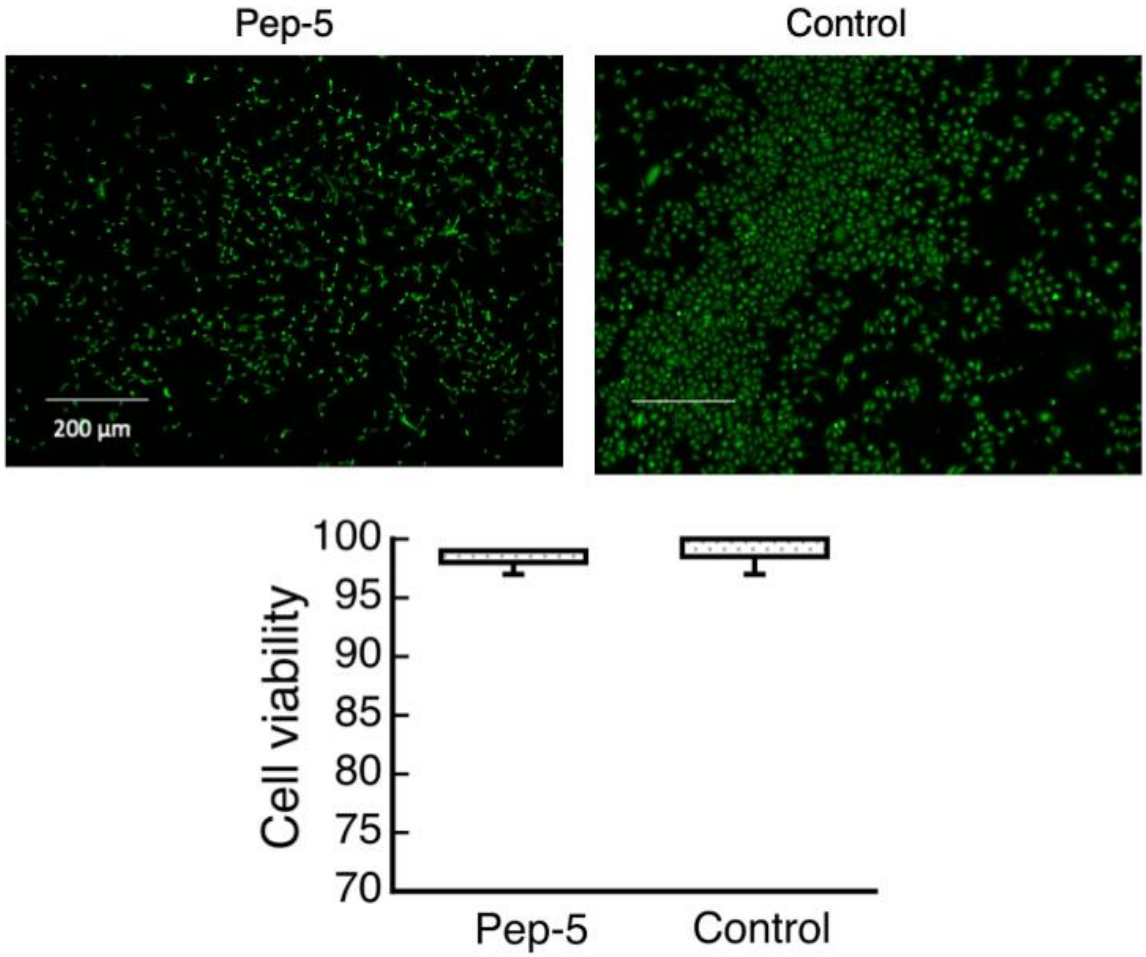

Figure S14. Engineered peptide sequences do not exhibit toxic side effects for human epithelial corneal cells. Cell viability measured using Live/Dead assay for human epithelial corneal cells seeded on top of Pep-5 hydrogels or gelatin coated well plates (48 h post seeding, n = 3). Data showed no statistically significant differences between all three groups.

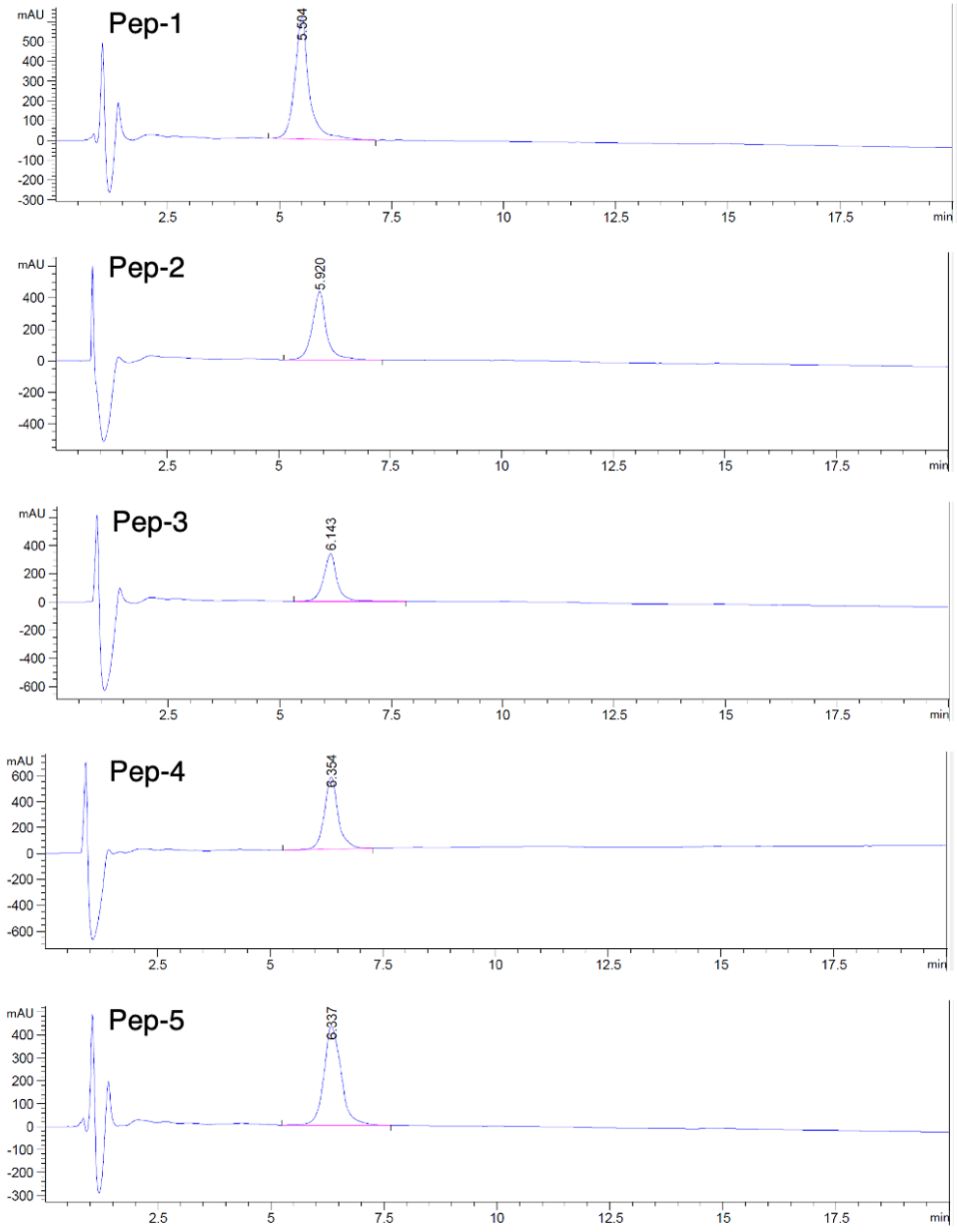

Figure S15. Selected HPLC traces for peptides 1-5. Peptide purity and identity was confirmed via HPLC-UV/MS in an Agilent 1260 Infinity II system using a 4.6 x 100 mm Agilent C18 column. A gradient of 0% to 40% phase B over 20 minutes was utilized with phase A consisting of water/acetonitrile 5%/formic acid 0.1%/TFA 0.01% and phase B acetonitrile/water 2%/formic acid 0.1%/TFA 0.01% at a flow rate of 1.5 mL/min.

Infrared characterization

A comparison of the FTIR spectra of reactants and Pep-5 hydrogel is shown in Figure S16. The spectrum of PEG-MAL shows characteristic signals at 1095 cm^{-1}, attributed to st C–O vibration, 1710 and 1738 cm^{-1}, corresponding to NC=O cyclic imide modes (symmetric and asymmetric), 1670 cm^{-1} attributed to the C=C of maleimide, and 2880 cm^{-1}, attributed to st C-H of PEG polymer chain. Moreover, the Pep-5 peptide shows the characteristic proteins and peptide signals: st N-H at 3310 cm^{-1}, Amide I at 1630 cm^{-1}, Amide II at 1544 cm^{-1}, and Amide III at 1444 cm^{-1}, among others. FTIR was also used to analyze the obtained hydrogel from Pep-5 and PEG-MAL. Characteristic signals of PEG and Pep-5 can be observed. Although the S-H bond of the thiol signal from Cys residue typically observed at 2300 – 2500 cm^{-1} cannot be elucidated, the shifting of the maleimide carbonyl signal in PEG from 1710 to 1698 cm^{-1} in the Pep-5 hydrogel could indicate the cross-linking reaction. Furthermore, the change in the Amide I region (1750-1550 cm^{-1}) could be understood as changes in the backbone conformation of the peptide-based hydrogel. Figure S22B-E shows the Gaussian fits of the Amide I region of Pep-5 and Pep-5 hydrogel at different CM_{ratio} values. In the same region of the spectra of the Pep-5 hydrogel, a change in the intensity of the folding peaks is observed, indicating a change in the arrangement due to the reaction with PEG-MAL. Besides, a new peak appeared at 1705 cm^{-1}, which could be attributed to the carbonyl signal of the now-reacted maleimide residue (red peaks). The comparison of PEG-MAL and Pep-5 hydrogel spectra at CM_{ratio} 4.0 denotes the absence of the C=C of maleimide groups, which indicates a complete functionalization of PEG-Maleimide with Pep-5. The appearance of a signal around 1650 cm^{-1} for CM_{ratio} 3.0 and 1.0 (violet peak) attributed to C=C stretching indicates the presence of unreacted maleimide groups. These results are expected due to a lower amount of thiol than maleimide groups. Considering that the S-H vibrational mode is not observed in the IR spectra of the peptides and the Cys thiol group is a highly reactive functional group, the presence and relative intensity of the C=C maleimide peak could indirectly indicate the efficiency of the reaction, giving lower values when the reaction is more efficient. Comparing the overall area of the Gaussian fit peak of the Amide signal (green, yellow and blue peaks) with the peak area of C=C maleimide, the results indicate that in a 4:1 ratio, the reaction is more efficient due to a 100% amide area, as explained before. For the Pep-5 hydrogel at CM_{ratio} 3.0, a relative peak area of the maleimide double bond is evidenced. This peak increases at CM_{ratio} 1.0, indicating more C=C groups in the hydrogels with a lower ratio. The same analysis was carried out using Pep-10, corresponding to a sequence without thiol groups (Figure S17), to corroborate this point. The Gaussian fit in the Amide I region of the mixing of PEG-MAL and Pep-10 shows the characteristic signals of maleimide at 1738, 1707 and 1670 cm^{-1}, indicating the non-reaction between maleimide groups and Pep-10. In summary, comparing the hydrogels prepared with Pep-3 (Figure S18), Pep-4 (Figure S19) and Pep-5 at different CM_{ratio} values, it is possible to rationalize the ability of each peptide to react with PEG-MAL, giving a higher relative area percent of Amide I/C=C signal for those efficient hydrogels, as shown in Figure 3.1H.

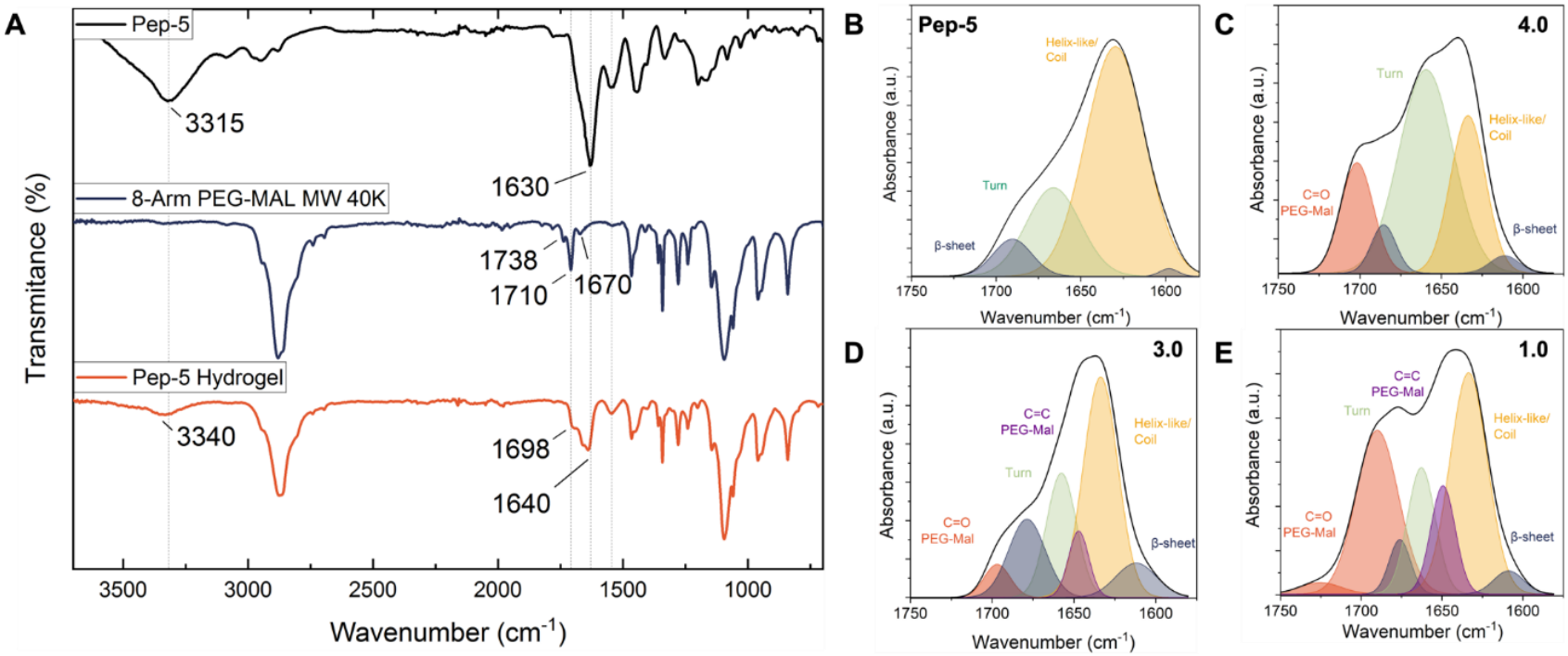

Figure S16. FTIR analysis of Pep-5 and other components. (A) FTIR spectra for the different components of the peptide-based material prepared using Pep-5. (B-E) Gaussian fit analysis for Pep-5 alone or mixed with PEG-Mal at different CM_{ratio} values.

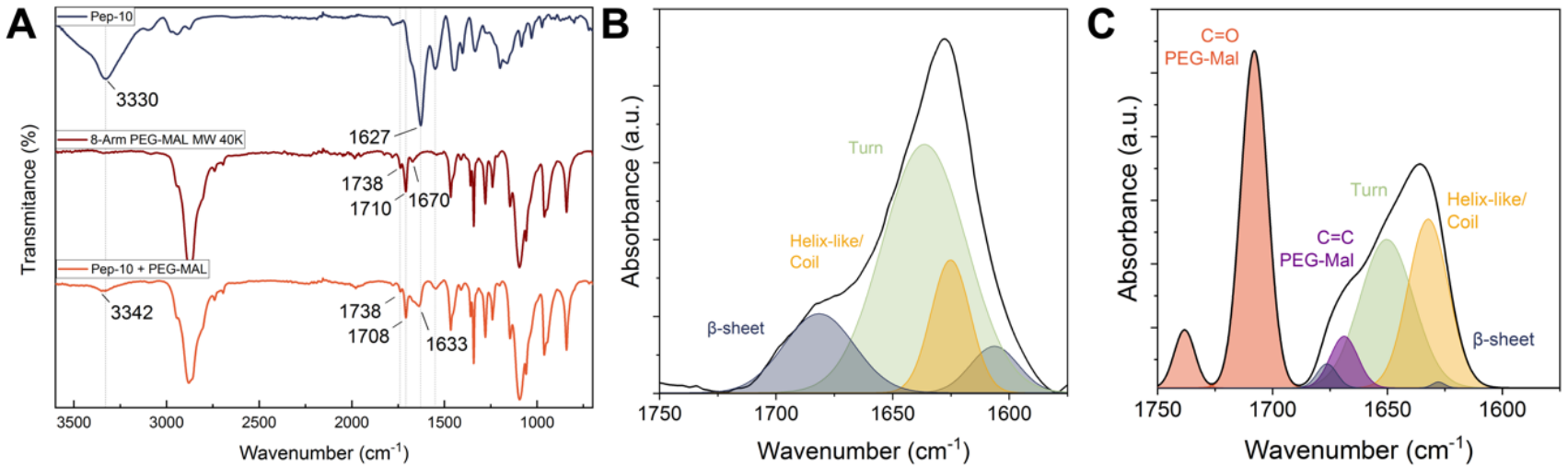

Figure S17. FTIR analysis of Pep-10 and other components. (A) FTIR spectra for the different components of the peptide-based material prepared using Pep-10. (B-C) Gaussian fit analysis for Pep-10 alone or mixed with PEG-Mal.

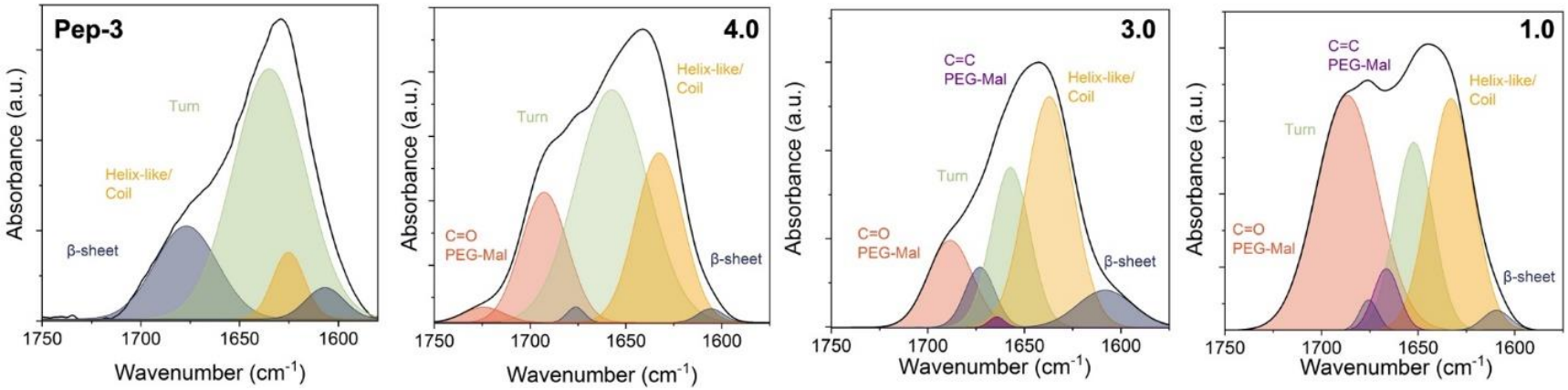

Figure S18. Gaussian fit analysis for Pep-3 alone or mixed with PEG-Mal at different CM_{ratio} values.

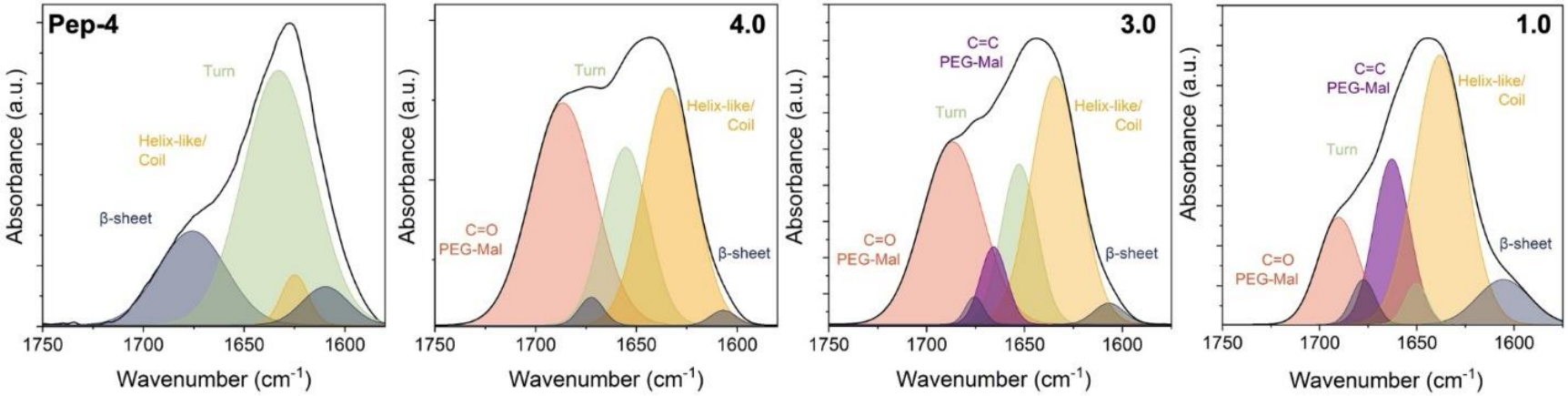

Figure S19. Gaussian fit analysis for Pep-4 alone or mixed with PEG-Mal at different CM_{ratio} values.

Sample	Sequence	Molecular Weight (g/mol)	Residue Number	M+2H Ion	M+3H Ion	Crude purity (%)
Pep-1	NH_2-GCG**(POG)**$_4$GCG-OH	1522	18	761.8	508.2	73
Pep-2	NH_2-GCG**(POG)**$_5$GCG-OH	1789	21	895.5	597.3	64
Pep-3	NH_2-GCG**(POG)**$_6$GCG-OH	2056	24	1029.1	686.4	79
Pep-4	NH_2-GCG**(POG)**$_7$GCG-OH	2323	27	1162.7	775.5	74
Pep-5	NH_2-GCG**(POG)**$_8$GCG-OH	2591	30	1296.4	864.6	75
Pep-6	NH_2-GCG**(POG)**$_9$GCG-OH	2858	33	1430.0	953.7	54
Pep-7	NH_2-GCG**(POG)**$_{10}$GCG-OH	3125	36	1563.7	1042.8	43
Pep-8	NH_2-GGG**(POG)**$_8$GCG-OH	2545	30	1273.3	849.2	54
Pep-9	NH_2-GCG**(POG)**$_8$GGG-OH	2545	30	1273.3	849.2	61
Pep-10	NH_2-GGG**(POG)**$_8$GGG-OH	2499	30	1250.3	833.9	69
Pep-11	NH_2-GGG**(POG)**$_3$(PCG)$_2$**(POG)**$_3$GGG-OH	2479	30	1240.3	827.2	75
Pep-12	NH_2-GGG**(POG)**$_2$(PCG)**(POG)**$_5$GCG-OH	2535	30	1268.3	845.9	67
Pep-13	NH_2-GCG**(POG)**$_5$(PCG)**(POG)**$_2$GGG-OH	2535	30	1268.3	845.9	74
Pep-14	NH_2-GGG**(POG)**$_2$(PCG)**(POG)**$_2$(PCG)**(POG)**$_2$GGG-OH	2479	30	1240.3	827.2	69
Pep-15	NH_2-GCG**(POG)**$_4$POV**(POG)**$_3$GCG-OH	2633	30	1317.5	878.7	64
Pep-16	NH_2-GCG(PPG)$_8$GCG-OH	2463	30	1232.4	821.9	64

Pep-17	NH_2-GC**(POG)$_8$**CG-OH	2477	30	1239.3	826.6	73
Pep-18	NH_2-GCV**(POG)$_8$**VCG-OH	2675	30	1338.5	892.6	68
Pep-19	NH_2-GCR**(POG)$_8$**RCG-OH	2789	30	1395.5	930.7	56
Pep-20	NH_2-GCC**(POG)$_8$**CCG-OH	2683	30	1342.5	895.3	72
Pep-21	NH_2-GCG**(POG)$_2$**(PCG)**(POG)$_2$**(PCG)**(POG)$_2$**GCG-OH	2571	30	1286.4	857.9	57
CLP	NH_2-CG(PKG)$_4$**(POG)$_4$**(DOG)$_4$-OH	3518	38	1759.9	1173.6	NA

Table S1. List of peptide codes, their sequences, molecular weights, and crude purity for on-the-spot peptides. List of peptide codes, their sequences, molecular weights, and crude purity for on-the-spot peptides. Mass spectra illustrating detected ions are also included in the table. A set of selected HPLC profiles is included in **Figure S15** and representative mass spectrometry data for each peptide are presented in the following pages.

Figure S20. Mass spectra for on-the-spot peptides.

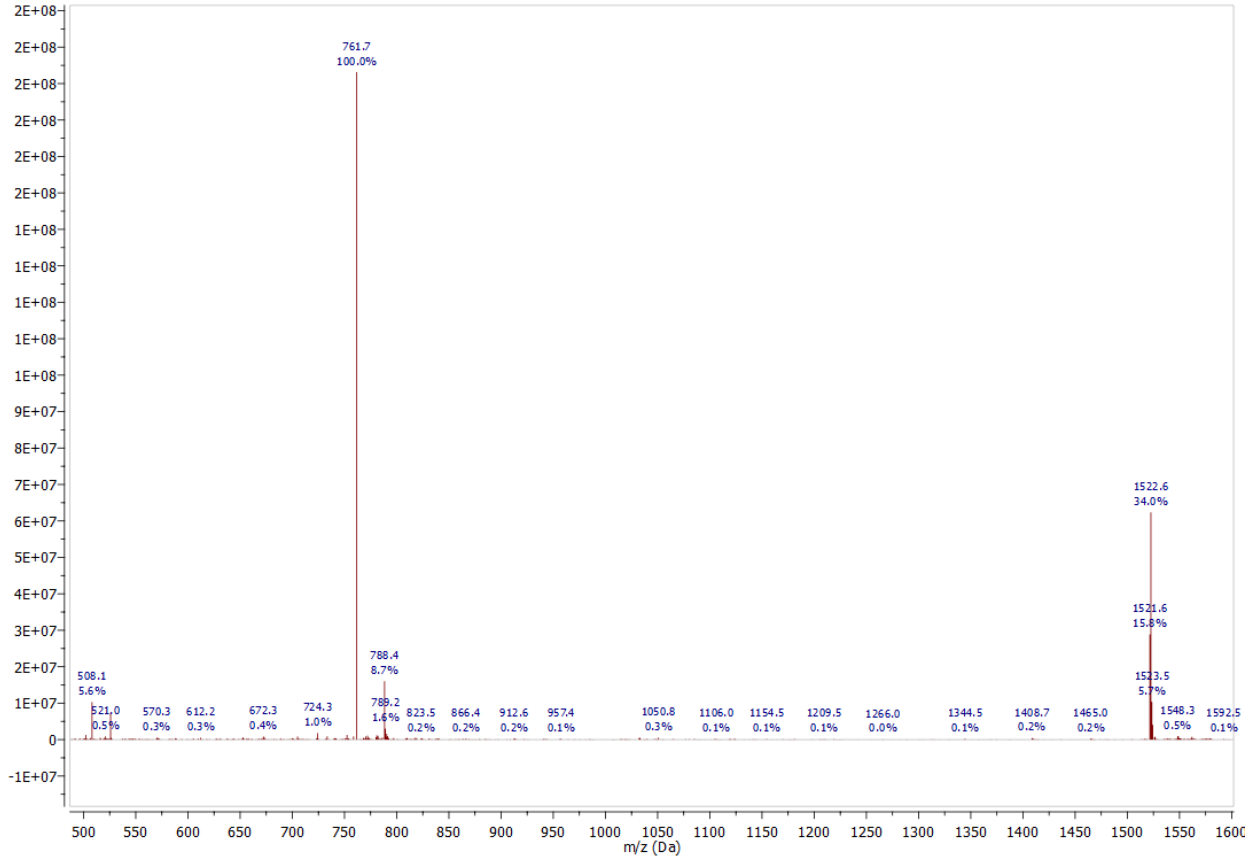

Sample	Sequence	Molecular Weight (g/mol)	Residue Number	M+2H Ion	M+1H Ion
Pep-1	NH_2-GCG(POG)$_4$GCG-OH	1522	18	761.8	1522.6

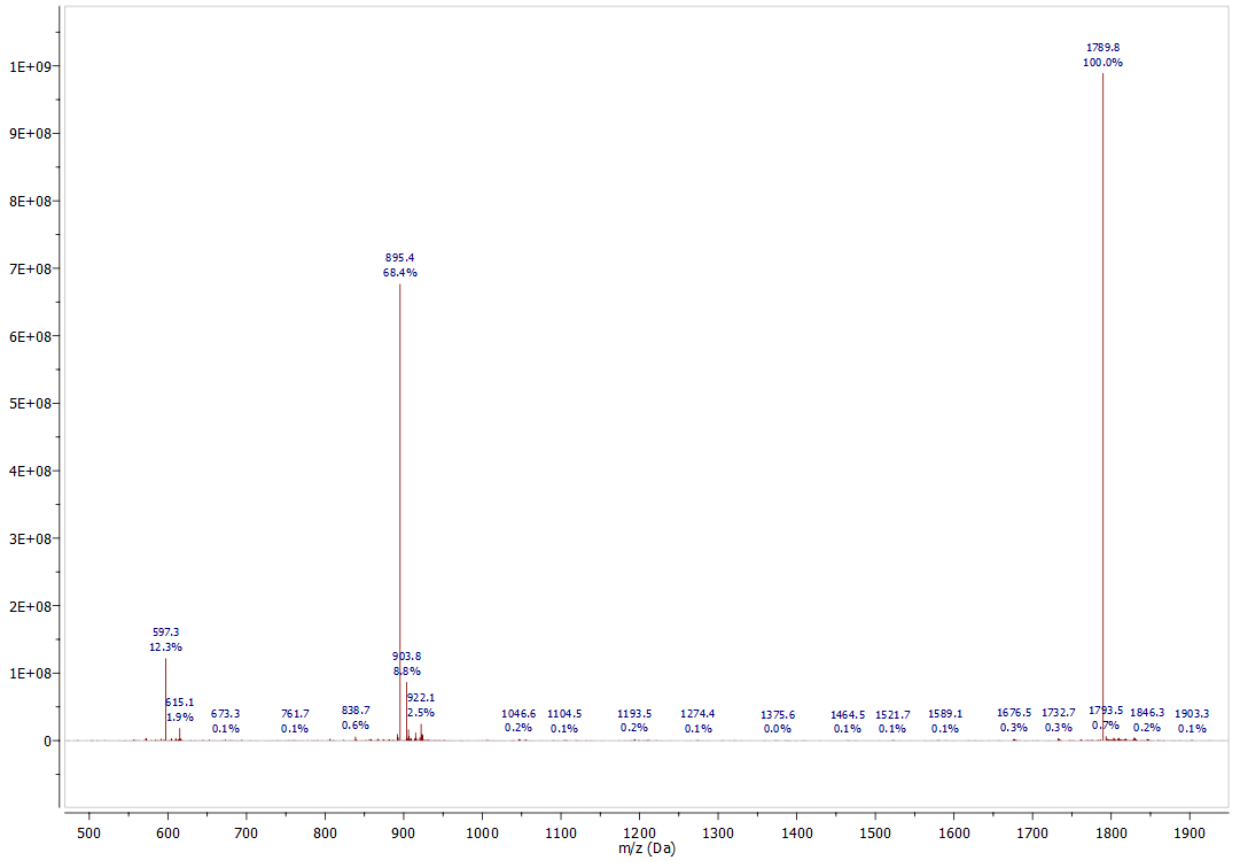

Sample	Sequence	Molecular Weight (g/mol)	Residue Number	M+2H Ion	M+3H Ion
Pep-2	NH_2-GCG(POG)$_5$GCG-OH	1789	21	895.5	1789.9

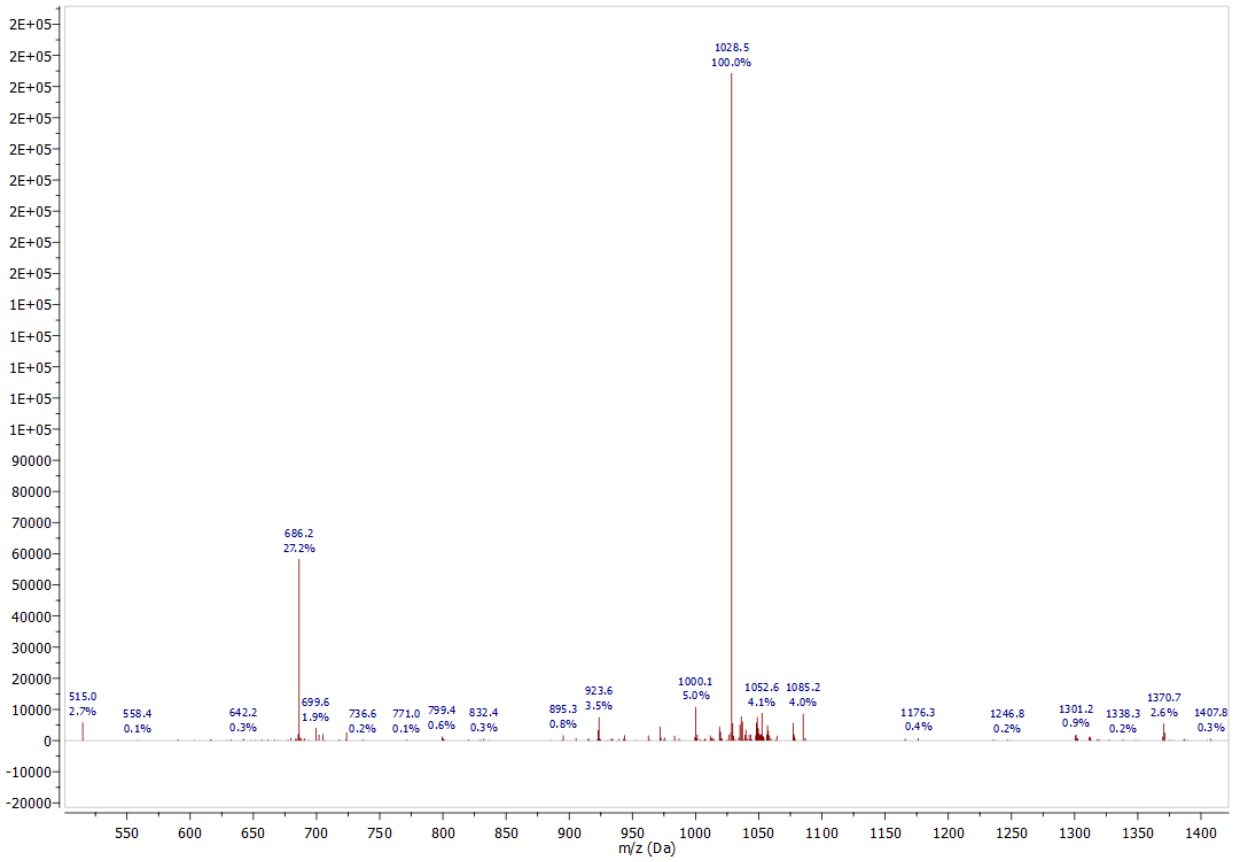

Sample	Sequence	Molecular Weight (g/mol)	Residue Number	M+2H Ion	M+3H Ion
Pep-3	NH_2-GCG(POG)$_6$GCG-OH	2056	24	1029.1	686.4

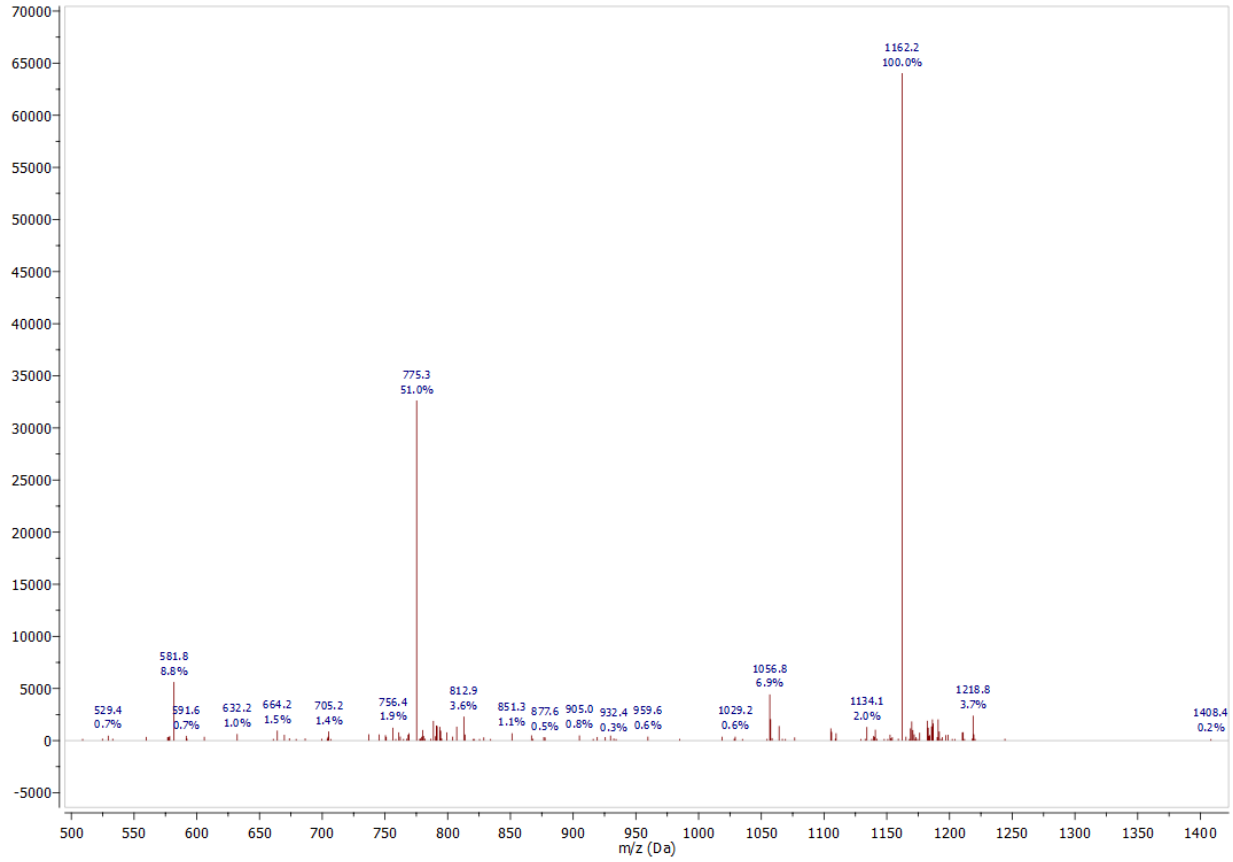

Sample	Sequence	Molecular Weight (g/mol)	Residue Number	M+2H Ion	M+3H Ion
Pep-4	**NH_2-GCG$(POG)_7$GCG-OH**	**2323**	**27**	**1162.7**	**775.5**

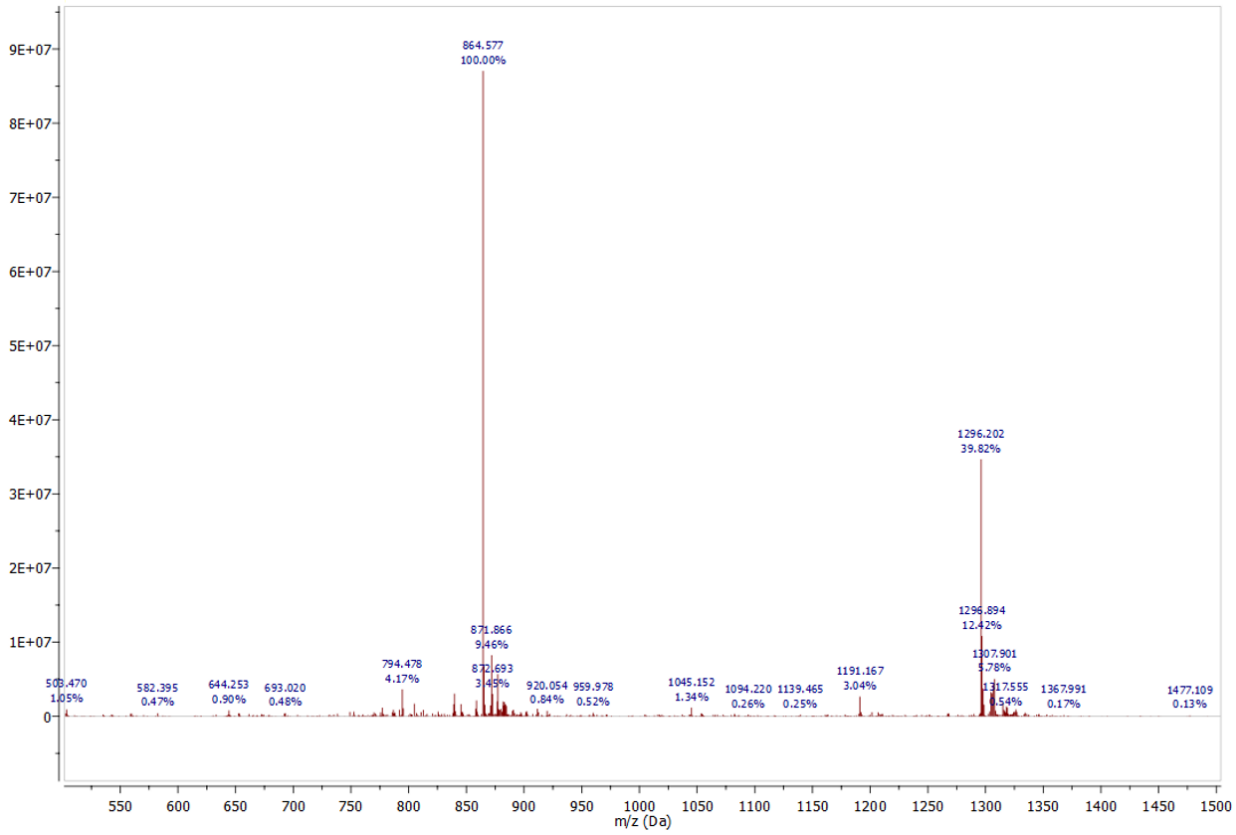

Sample	Sequence	Molecular Weight (g/mol)	Residue Number	M+2H Ion	M+3H Ion
Pep-5	**NH_2-GCG(POG)$_8$GCG-OH**	**2591**	**30**	**1296.4**	**864.6**

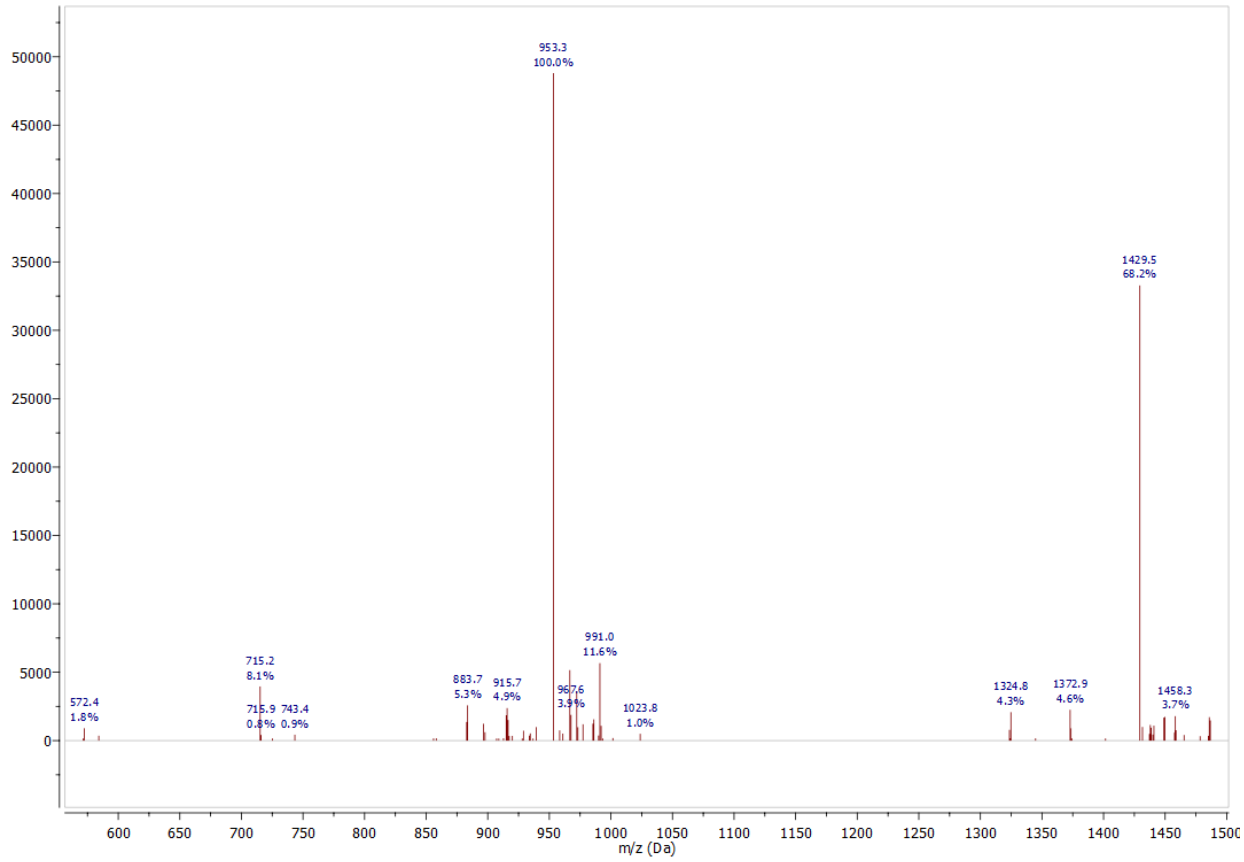

Sample	Sequence	Molecular Weight (g/mol)	Residue Number	M+2H Ion	M+3H Ion
Pep-6	**NH_2-GCG(POG)$_9$GCG-OH**	**2858**	**33**	**1430.0**	**953.7**

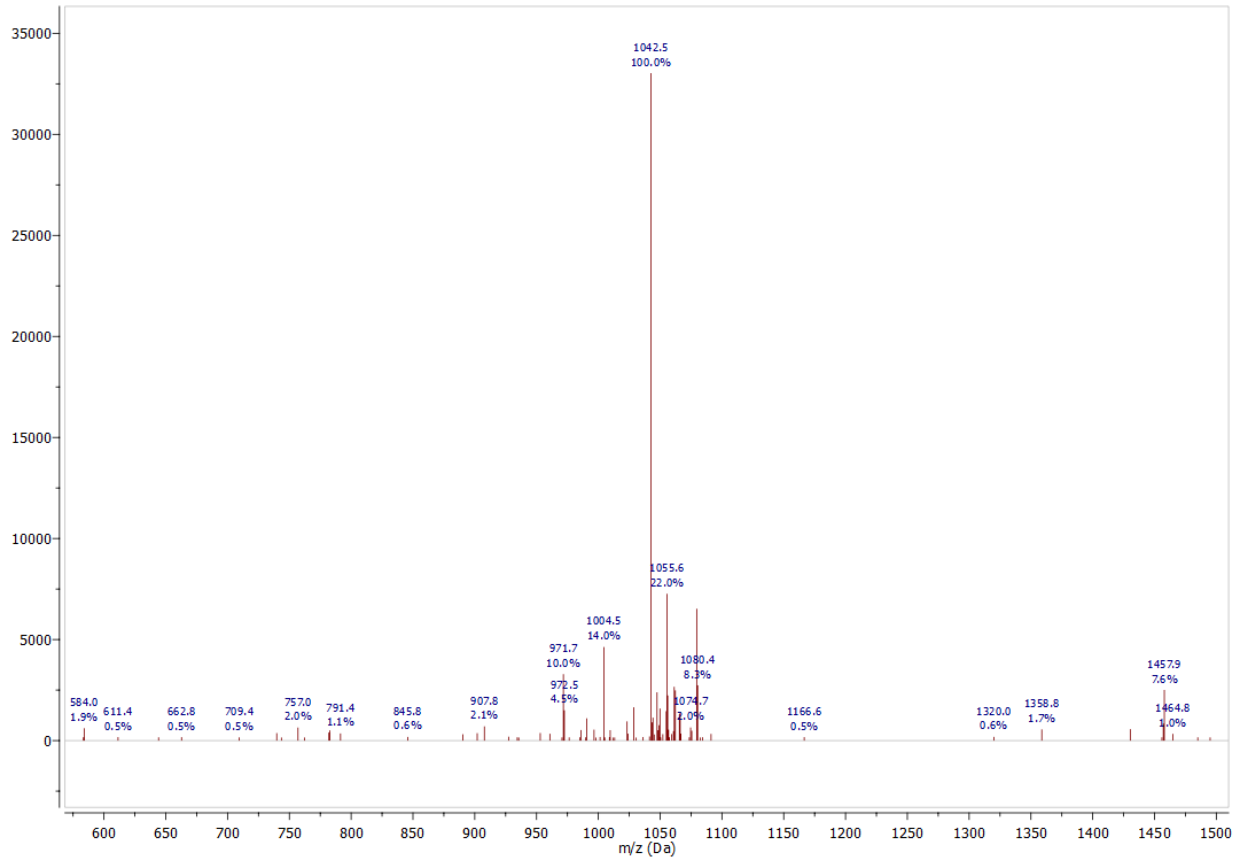

Sample	Sequence	Molecular Weight (g/mol)	Residue Number	M+2H Ion	M+3H Ion
Pep-7	NH_2-GCG$(POG)_{10}$GCG-OH	3125	36	1563.7	1042.8

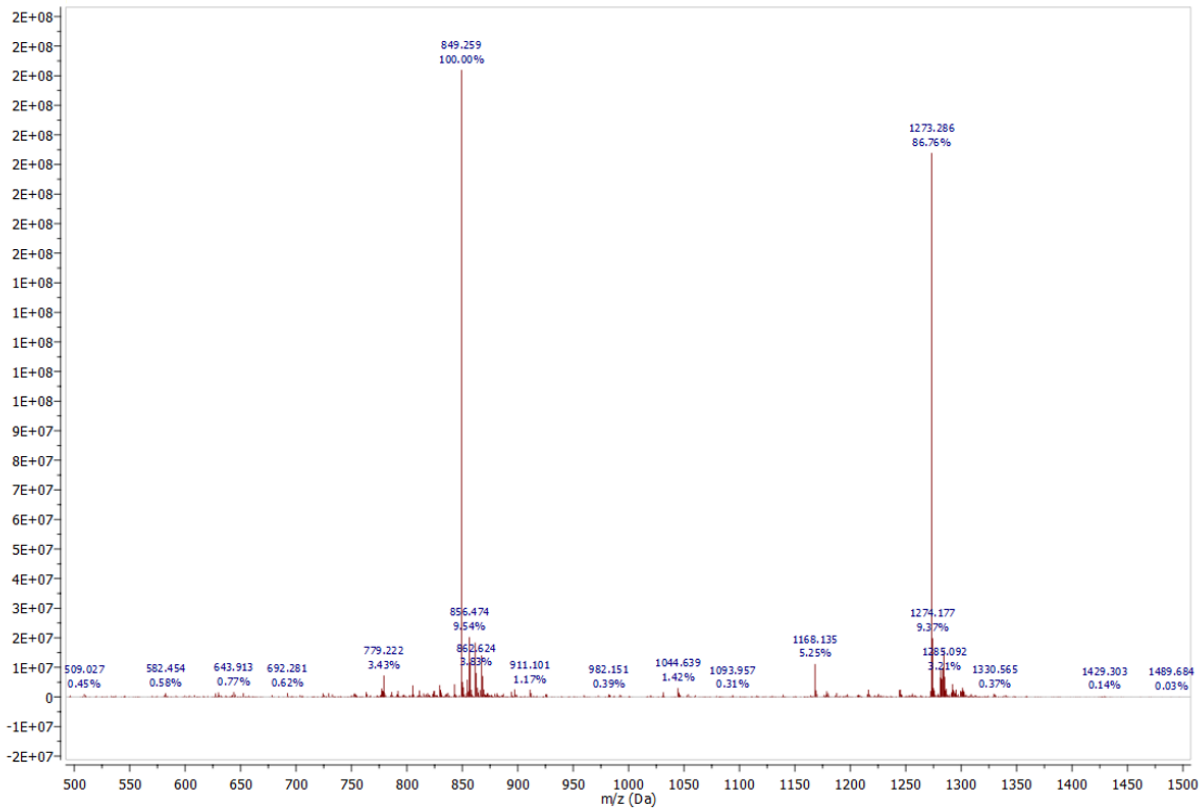

Sample	Sequence	Molecular Weight (g/mol)	Residue Number	M+2H Ion	M+3H Ion
Pep-8	NH_2-GGG(POG)$_8$GCG-OH	2545	30	1273.5	849.3

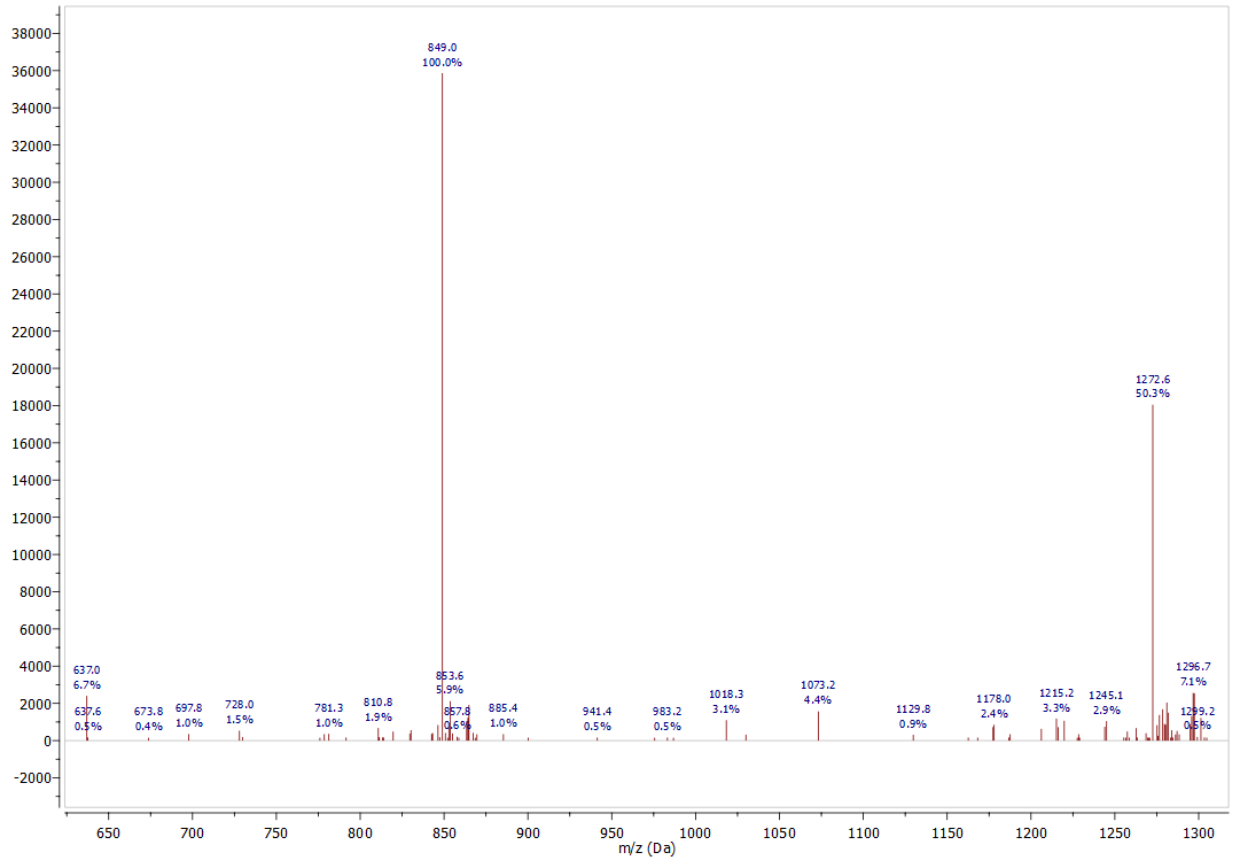

Sample	Sequence	Molecular Weight (g/mol)	Residue Number	M+2H Ion	M+3H Ion
Pep-9	**NH_2-GCG$(POG)_8$GGG-OH**	**2545**	**30**	**1273.3**	**849.2**

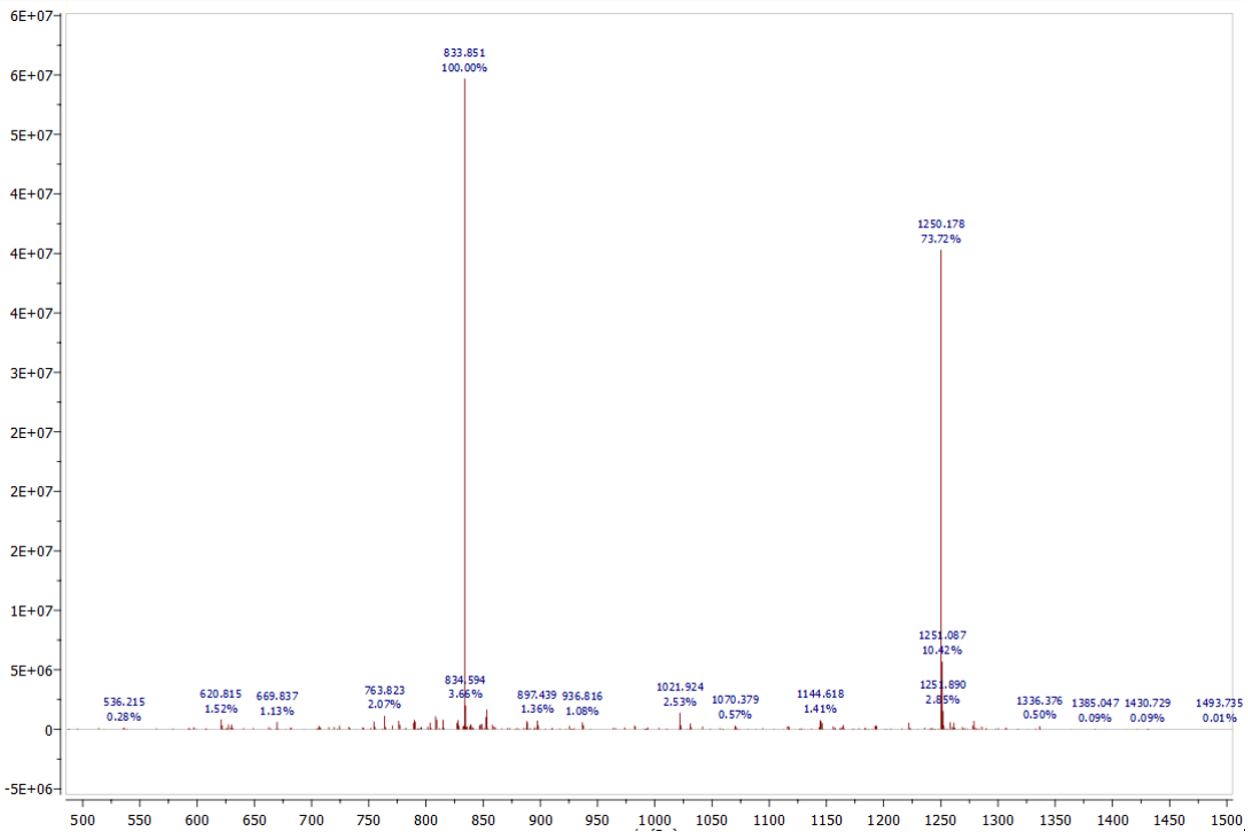

Sample	Sequence	Molecular Weight (g/mol)	Residue Number	M+2H Ion	M+3H Ion
Pep-10	**NH_2-GGG(POG)$_8$GGG-OH**	**2499**	**30**	**1250.3**	**833.9**

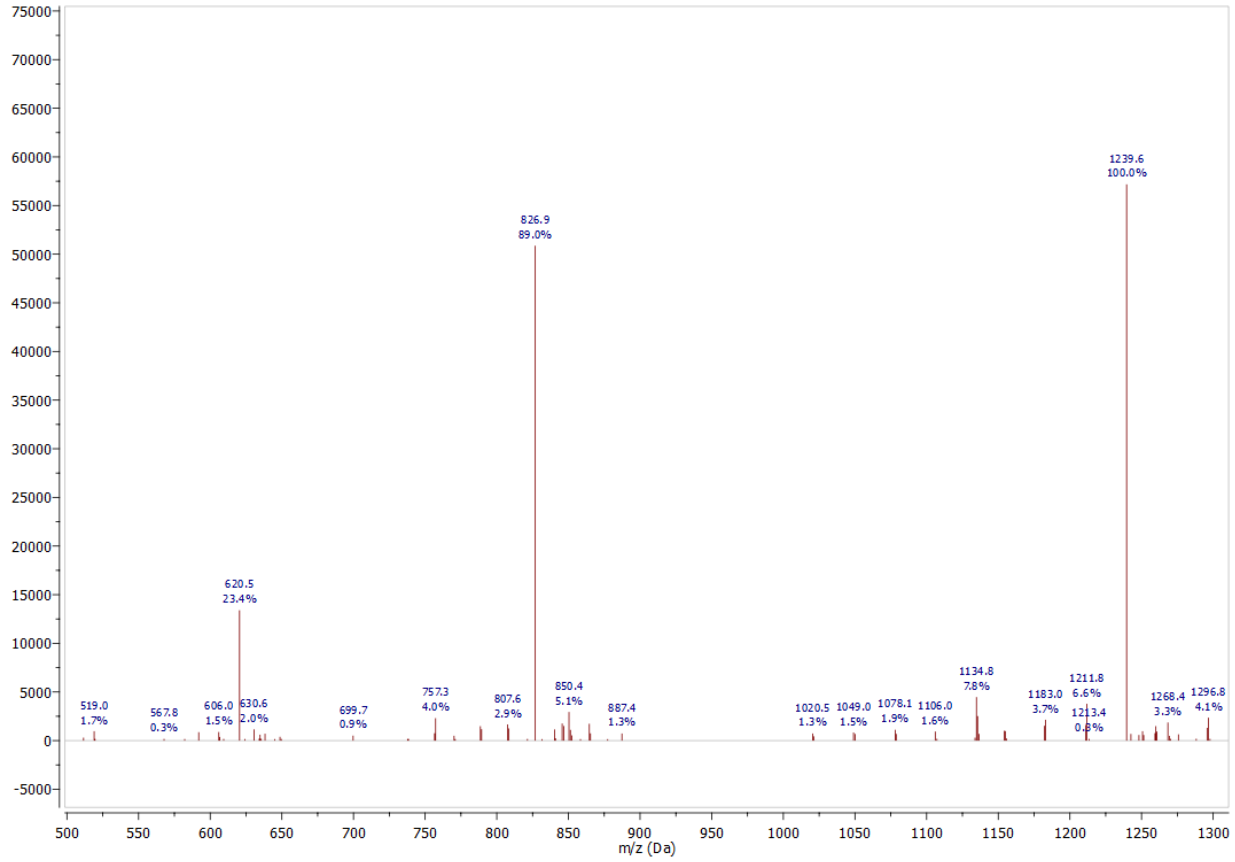

Sample	Sequence	Molecular Weight (g/mol)	Residue Number	M+2H Ion	M+3H Ion
Pep-11	**NH_2-GGG(POG)$_3$(PCG)$_2$(POG)$_3$GGG-OH**	**2479**	**30**	**1240.3**	**827.2**

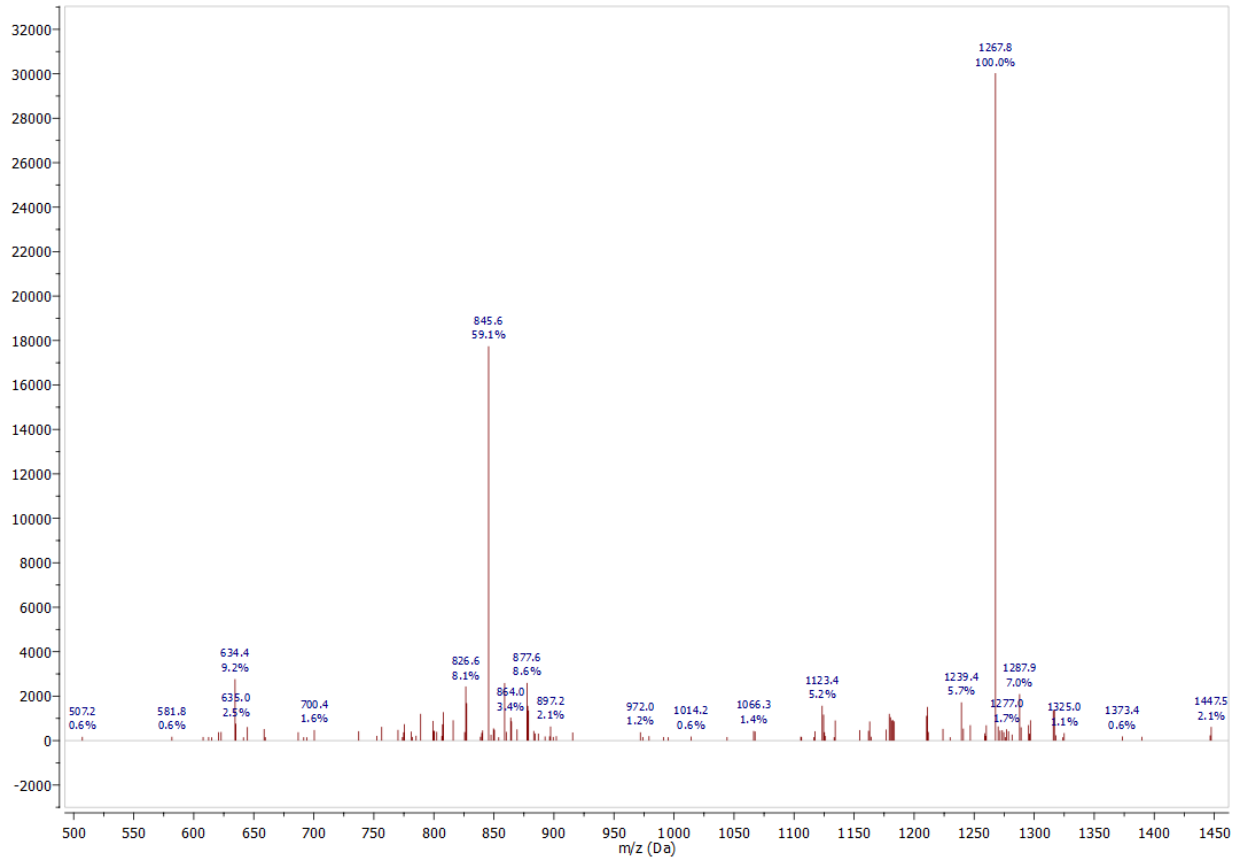

Sample	Sequence	Molecular Weight (g/mol)	Residue Number	M+2H Ion	M+3H Ion
Pep-12	**NH_2-GGG(POG)$_2$(PCG)(POG)$_5$GCG-OH**	**2535**	**30**	**1268.3**	**845.9**

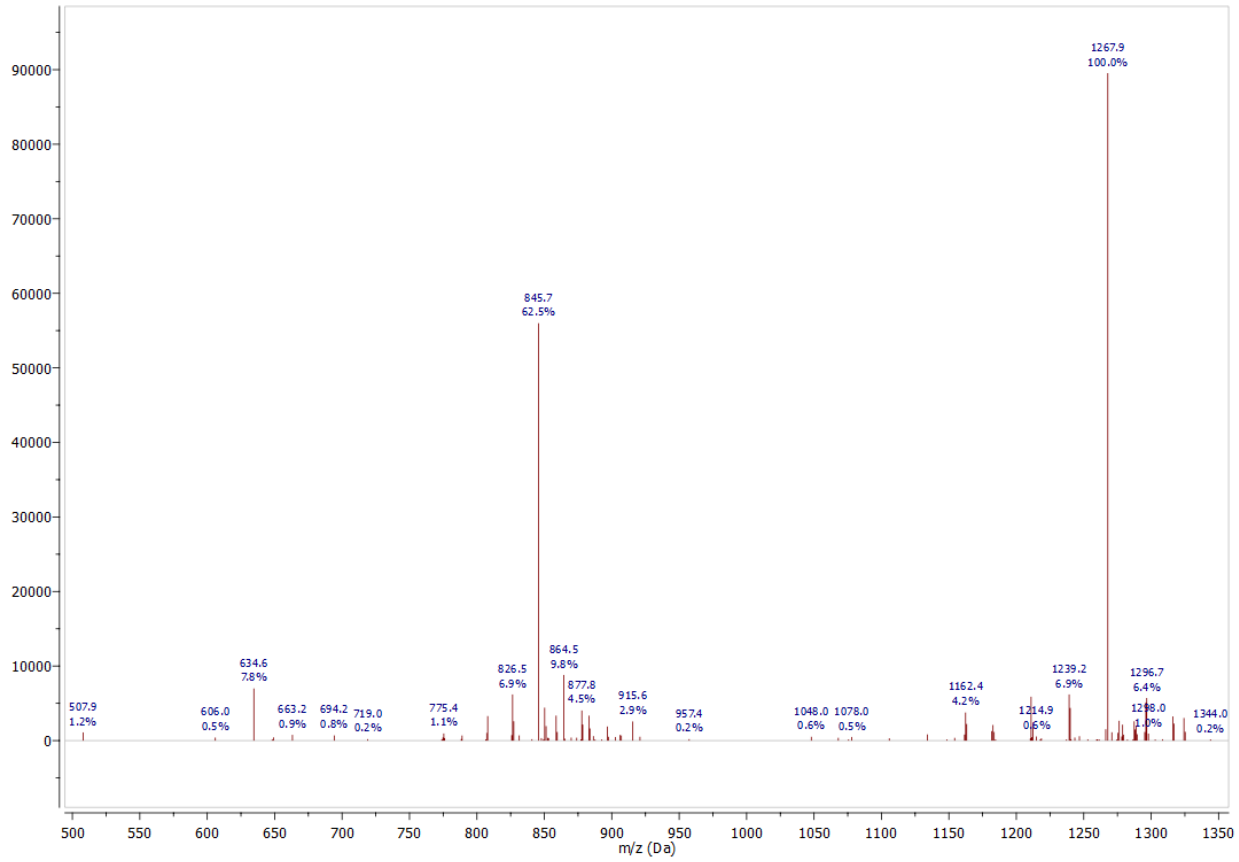

Sample	Sequence	Molecular Weight (g/mol)	Residue Number	M+2H Ion	M+3H Ion
Pep-13	**NH_2-GCG(POG)$_5$(PCG)(POG)$_2$GGG-OH**	**2535**	**30**	**1268.3**	**845.9**

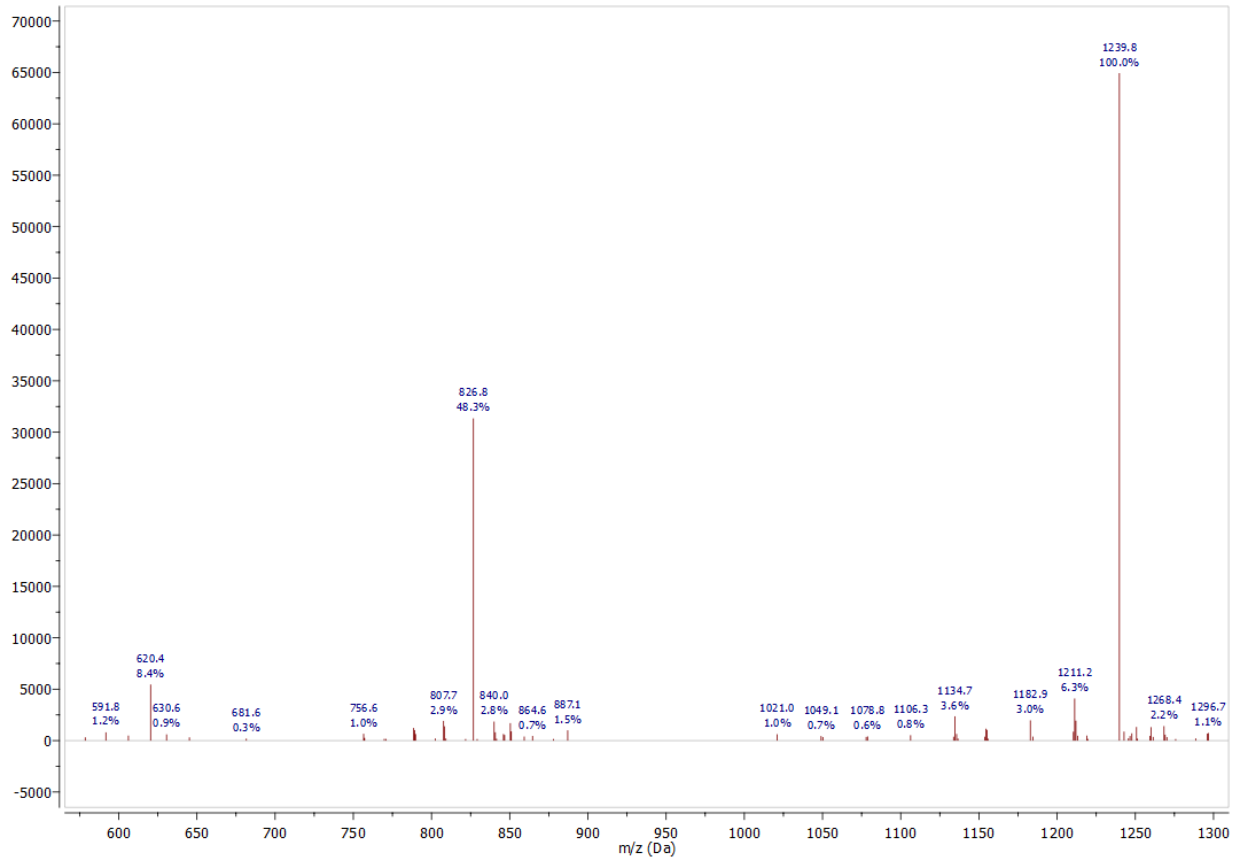

Sample	Sequence	Molecular Weight (g/mol)	Residue Number	M+2H Ion	M+3H Ion
Pep-14	**NH_2-GGG(POG)$_2$(PCG)(POG)$_2$(PCG)(POG)$_2$GGG-OH**	**2479**	**30**	**1240.3**	**827.2**

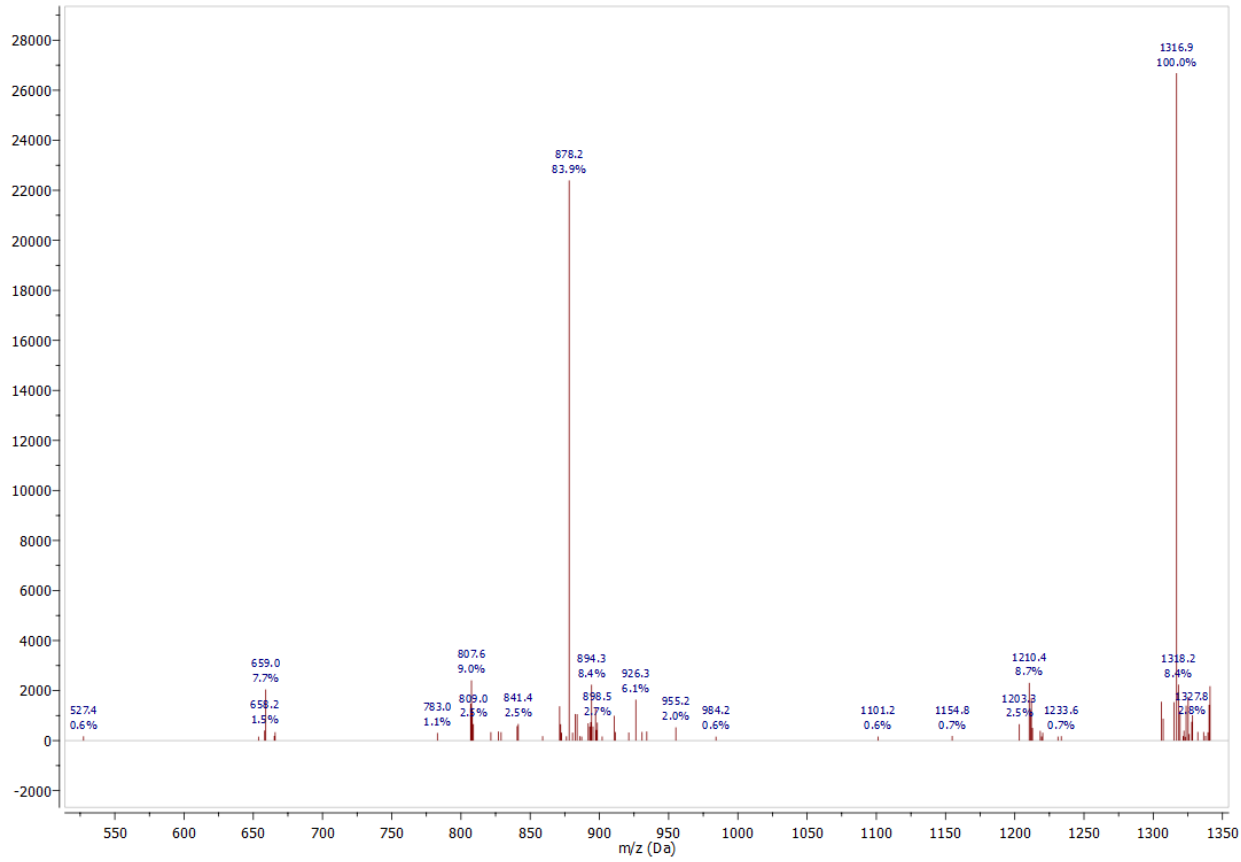

Sample	Sequence	Molecular Weight (g/mol)	Residue Number	M+2H Ion	M+3H Ion
Pep-15	**NH_2-GCG$(POG)_4$POV$(POG)_3$GCG-OH**	**2633**	**30**	**1317.5**	**878.7**

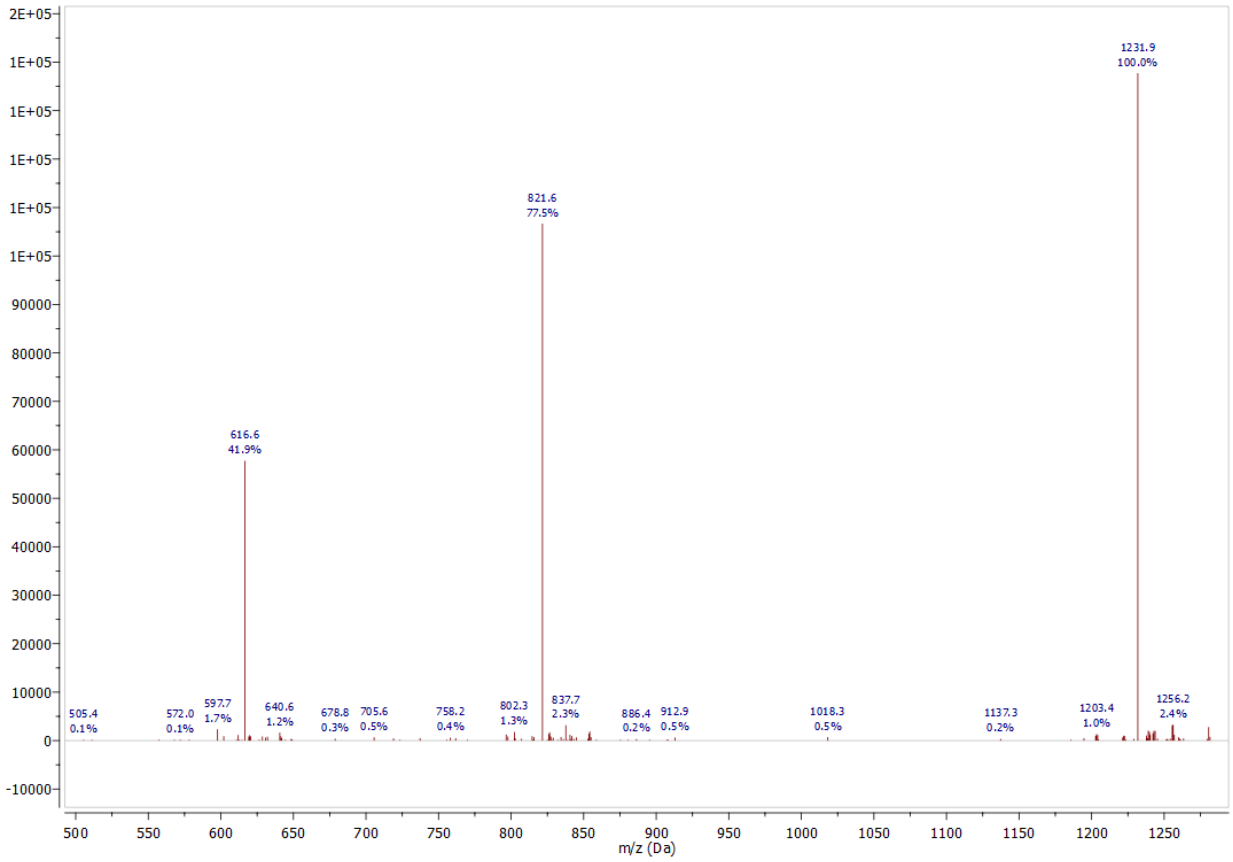

Sample	Sequence	Molecular Weight (g/mol)	Residue Number	M+2H Ion	M+3H Ion
Pep-16	**NH_2-GCG(PPG)$_8$GCG-OH**	**2463**	**30**	**1232.4**	**821.9**

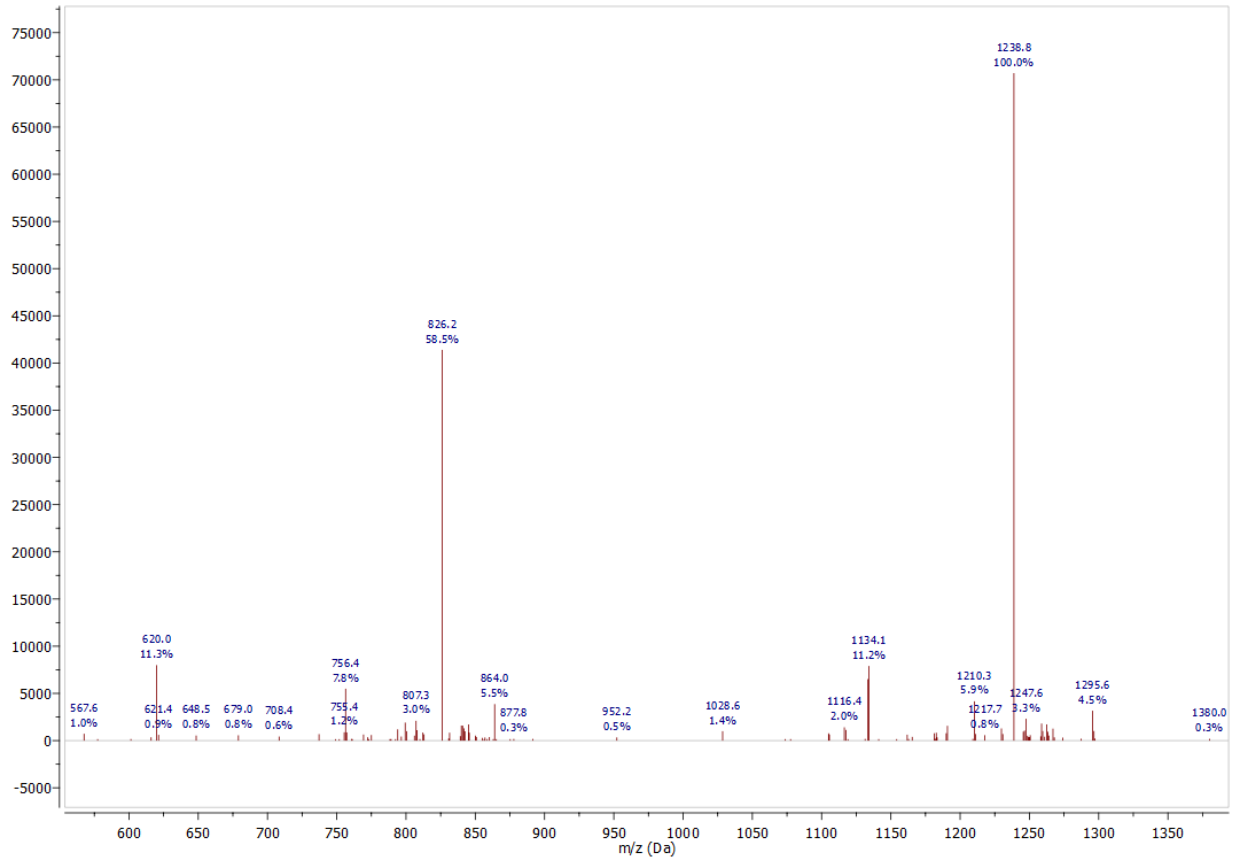

Sample	Sequence	Molecular Weight (g/mol)	Residue Number	M+2H Ion	M+3H Ion
Pep-17	**NH_2-GC(POG)$_8$CG-OH**	**2477**	**30**	**1239.5**	**826.7**

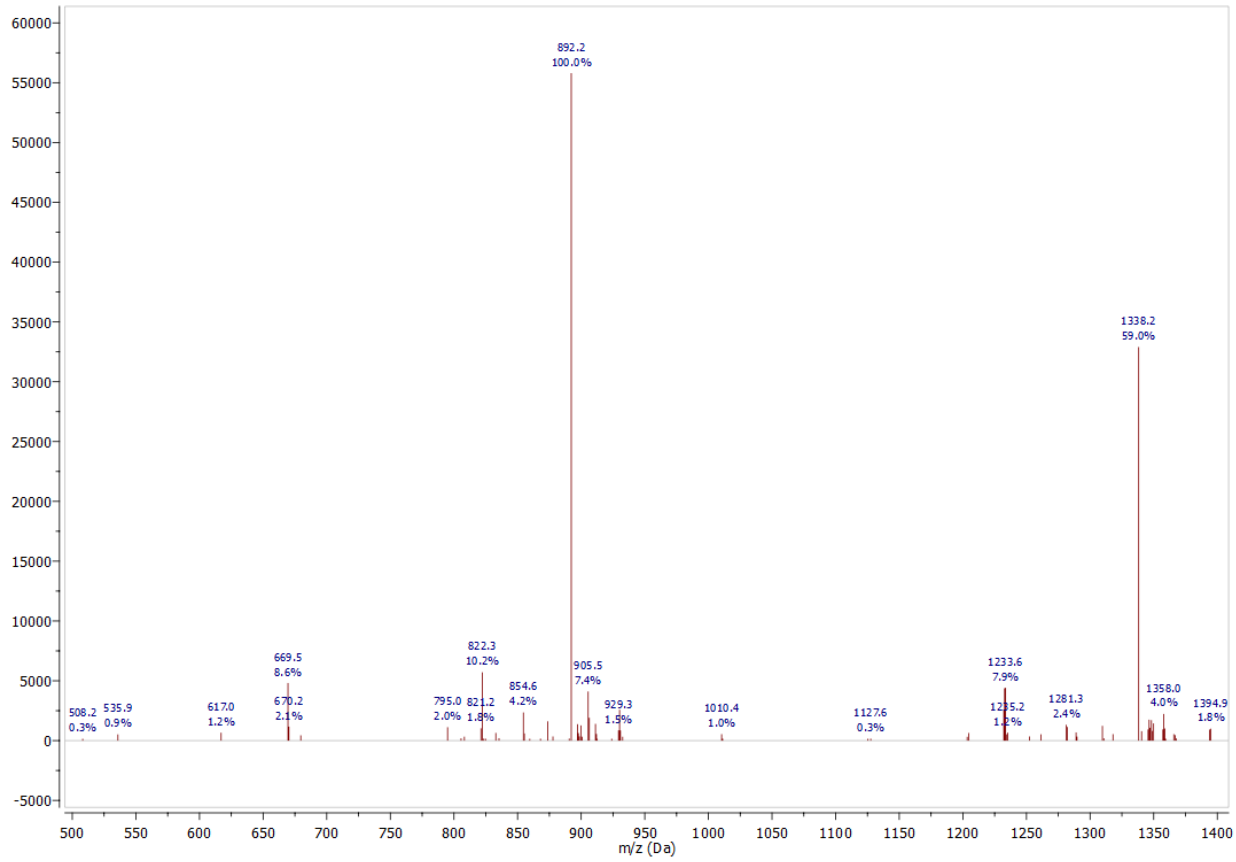

Sample	Sequence	Molecular Weight (g/mol)	Residue Number	M+2H Ion	M+3H Ion
Pep-18	NH_2-GCV(POG)$_8$VCG-OH	2675	30	1338.5	892.6

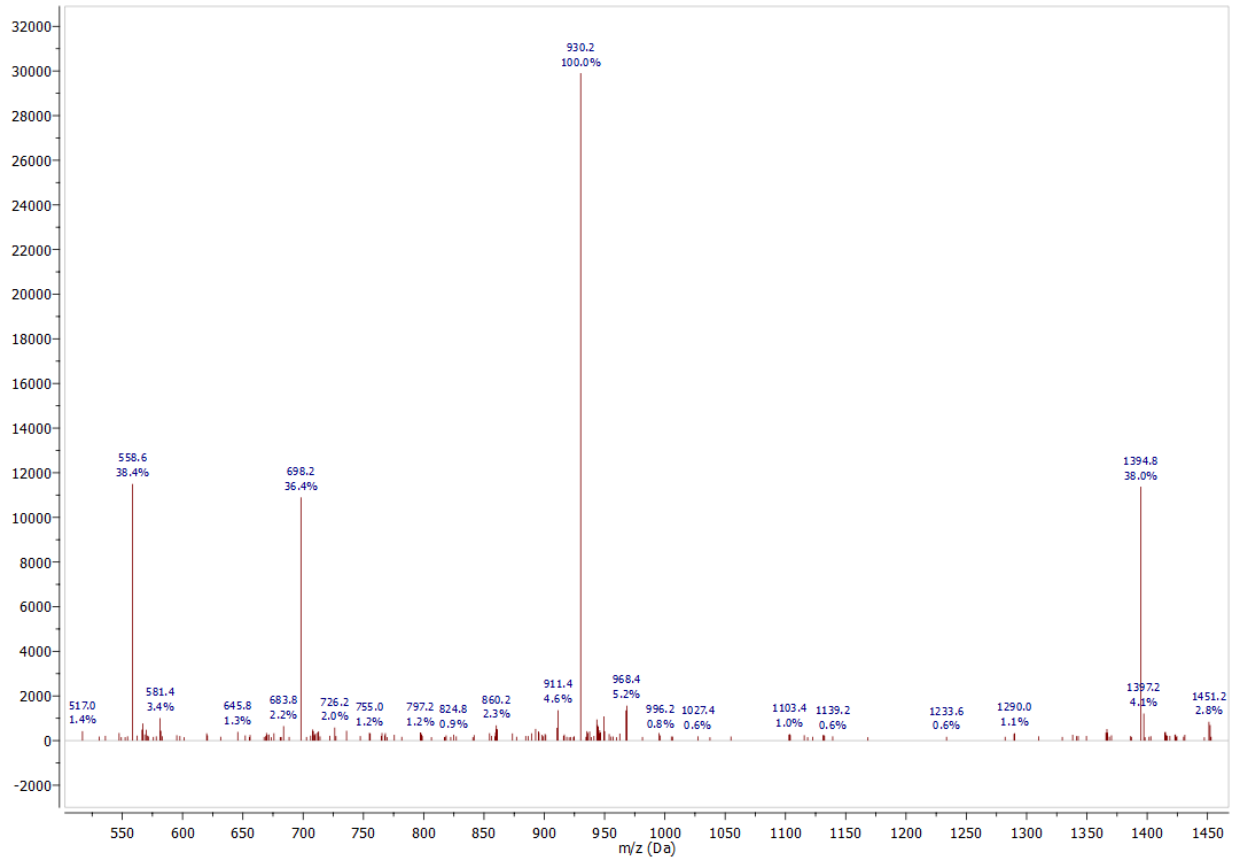

Sample	Sequence	Molecular Weight (g/mol)	Residue Number	M+2H Ion	M+3H Ion
Pep-19	**NH_2-GCR(POG)$_8$RCG-OH**	**2789**	**30**	**1395.5**	**930.7**

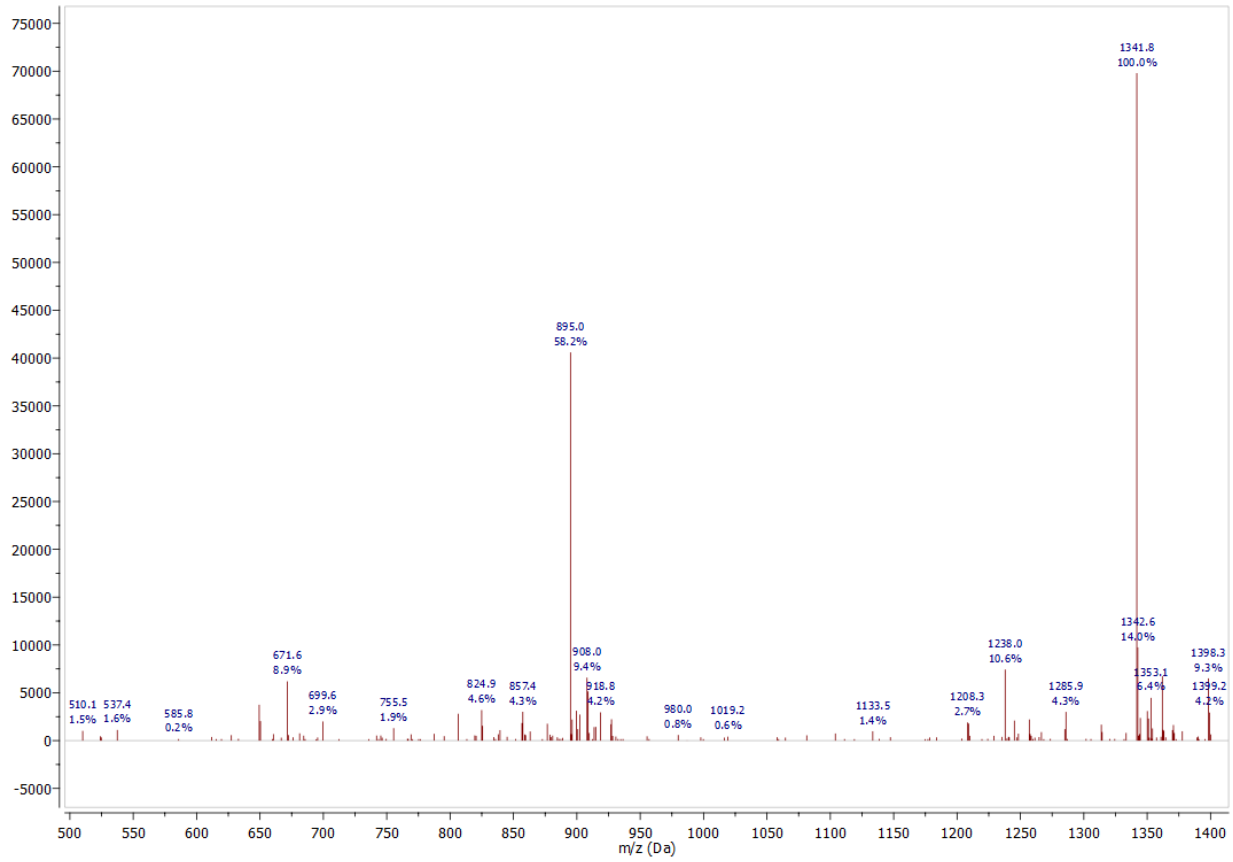

Sample	Sequence	Molecular Weight (g/mol)	Residue Number	M+2H Ion	M+3H Ion
Pep-20	**NH_2-GCC(POG)$_8$CCG-OH**	**2683**	**30**	**1342.5**	**895.3**

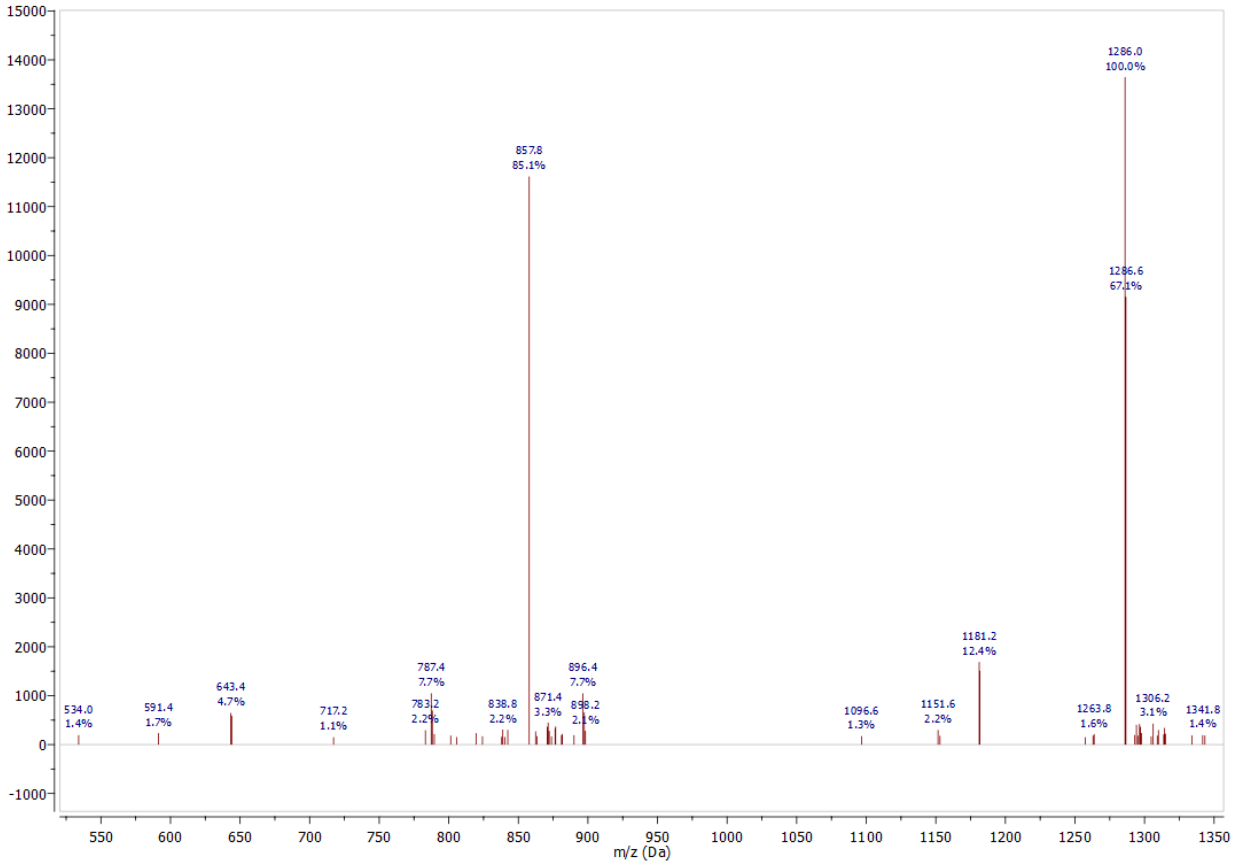

Sample Sequence		Molecular Weight (g/mol)	Residue Number	M+2H Ion	M+3H Ion
Pep-21	NH_2-GCG$(POG)_2$(PCG)$(POG)_2$(PCG)$(POG)_2$GCG-OH	2571	30	1286.4	857.9

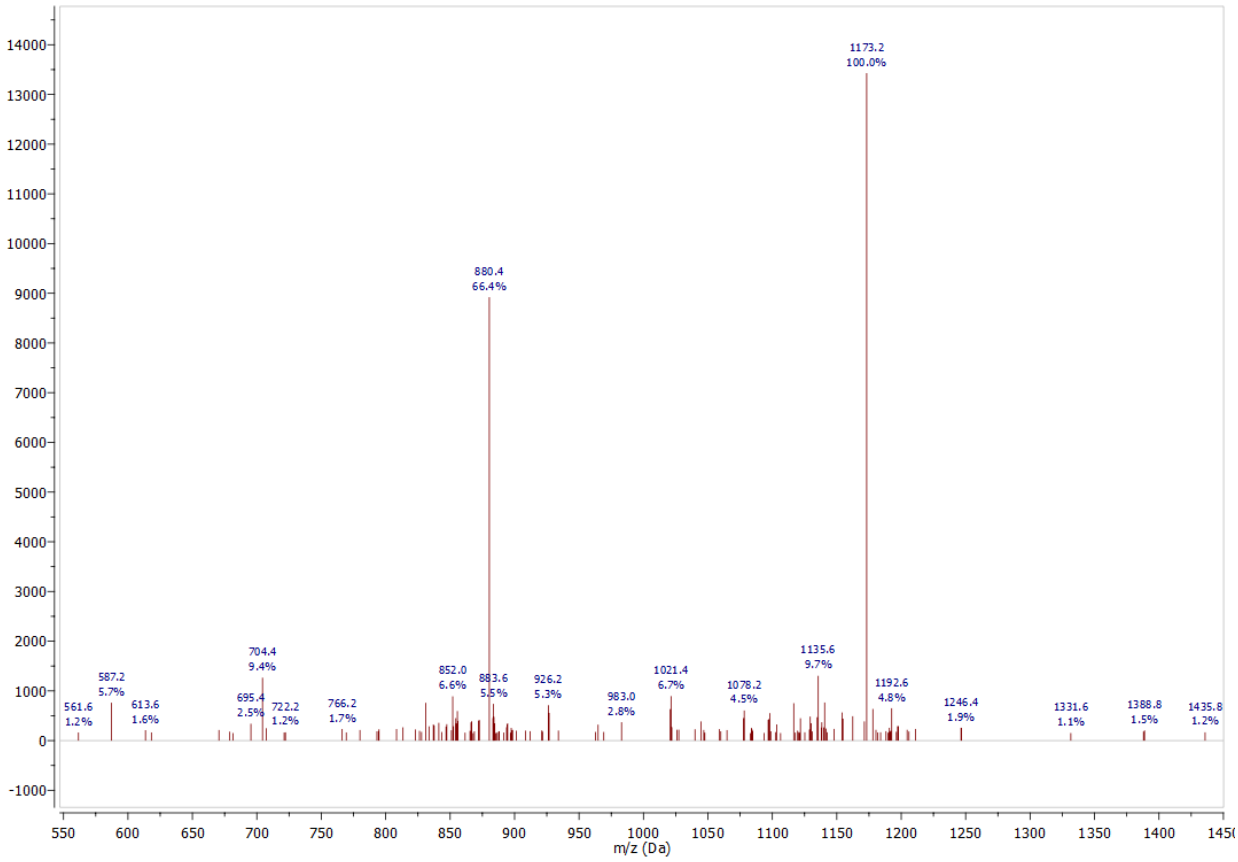

Sample	Sequence	Molecular Weight (g/mol)	Residue Number	M+2H Ion	M+3H Ion
CLP	**NH_2-CG$(PKG)_4(POG)_4(DOG)_4$-OH**	**3518**	**38**	**880.2**	**1173.6**

	Gelation time (s)*			Transmittance (%)**			Refractive Index***			Water Content (%)†			Denaturation Temperature (°C)††		
CM_{ratio}	1	3	4	1	3	4	1	3	4	1	3	4	1	3	4
Pass criteria	<15 and >90			>85%			>1.33			>90%			>42°C		
Pep-1	120 ± 20	13 ± 6	16 ± 15	98.592 ± 0.86	83.21 ± 23.60	91.18 ± 12.24	1.33727 ± 0.00261	1.34897 ± 0.00374	1.35480 ± 0.00091	N/A	N/A	N/A	N/A	N/A	N/A
Pep-2	65 ± 30	48 ± 25	14 ± 3	96.464 ± 3.58	96.41 ± 3.10	85.23 ± 9.33	1.34017 ± 0.00306	1.35104 ± 0.00030	1.35485 ± 0.00686	N/A	N/A	N/A	N/A	N/A	N/A
Pep-3	108 ± 8	31 ±19	58 ± 6	97.689 ± 1.04	97.10 ± 7.62	87.97 ± 0.84	1.33872 ± 0.00243	1.34807 ± 0.0009	1.35584 ± 0.00559	97.17 ± 0.20	96.55 ± 0.20	96.15 ± 0.17	79.3 ± 18	50.3 ± 0.5	66 ± 12.6
Pep-4	57 ± 19	34 ± 42	56 ± 17	95.896 ± 4.37	95.35 ± 6.49	89.61 ± 7.68	1.33853 ± 0.00257	1.34411 ± 0.01066	1.35677 ± 0.00512	97.38 ± 0.06	96.89 ± 0.34	96.47 ± 0.28	57 ± 13	68.0 ± 10.0	59 ± 5.3
Pep-5	33 ± 1	38 ± 28	55 ± 28	96.721 ± 1.16	93.01 ± 1.85	97.47 ± 3.71	1.33991 ± 0.00181	1.34728 ± 0.00494	1.36068 ± 0.00425	96.31 ± 0.35	96.54 ± 0.22	96.54 ± 0.16	44 ± 6.6	51 ± 1.0	54 ± 5.6
Pep-6	59 ± 10	16 ± 11	66 ± 10	95.938 ± 3.21	53.4 ± 28.34	55.38 ± 34.78	1.34120 ± 0.00082	1.35074 ± 0.00300	1.35859 ± 0.00499	96.72 ± 0.20	96.65 ± 0.05	96.00 ± 0.30	N/A	N/A	N/A
Pep-7	47 ± 35	42 ± 30	74 ± 16	94.736 ± 0.99	86.46 ± 8.97	53.37 ± 15.94	1.34484 ± 0.00140	1.35222 ± 0.01363	1.36312 ± 0.00417	N/A	N/A	N/A	N/A	N/A	N/A
Pep-8	120+	120+	120+	N/A	N/A	N/A	1.34484 ± 0.00084	1.34861 ± 0.00171	1.35858 ± 0.00204	N/A	N/A	N/A	N/A	N/A	N/A

Pep-9	**120+**	**118 ± 4.5**	**115 ± 11**	**N/A**	**N/A**	**N/A**	**1.34703 ± 0.00186**	**1.35964 ± 0.00411**	**1.37796 ± 0.01191**	**N/A**	**N/A**	**N/A**	**N/A**	**N/A**	**N/A**
Pep-10	**120+**	**120+**	**120+**	**N/A**	**N/A**	**N/A**	**1.34495 ± 0.00028**	**1.35812 ± 0.00542**	**1.37639 ± 0.02138**	**N/A**	**N/A**	**N/A**	**N/A**	**N/A**	**N/A**
Pep-11	**96 ± 37**	**9 ± 4**	**65.± 34**	**82.2701 ± 32.1264**	**69.3057± 32.5870**	**87.45 ± 18.42**	**1.34395 ± 0.003306**	**1.35160 ± 0.00485**	**1.36180 ± 0.00447**	**N/A**	**N/A**	**N/A**	**N/A**	**N/A**	**N/A**
Pep-12	**4 ± 3**	**17 ± 12**	**19 ± 9**	**99.31 ± 0.6041**	**99.2358 ± 0.3488**	**80.3464 ± 34.0854**	**1.33894 ± 0.0007022**	**1.34766 ± 0.00043**	**1.36180 ± 0.00447**	**N/A**	**N/A**	**N/A**	**N/A**	**N/A**	**N/A**
Pep-13	**17 ± 29**	**8 ± 2**	**9 ± 5**	**98.40 ± 0.6003**	**99.1600 ± 0.4748**	**98.6291 ± 0.6017**	**1.35504 ± 0.0001044**	**1.35204 ± 0.00303**	**1.34778± 0.00029**	**N/A**	**N/A**	**N/A**	**N/A**	**N/A**	**N/A**
Pep-14	**3 ± 1**	**8 ± 7**	**36 ± 50**	**99.23757 ± 0.8020**	**98.1086 ± 1.6418**	**100.4622 ± 0.4011**	**1.34569 ± 0.000197**	**1.346036 ± 6.4444E-05**	**1.36857 ± 0.000846**	**N/A**	**N/A**	**N/A**	**N/A**	**N/A**	**N/A**
Pep-15	**88 ± 21**	**73 ±22**	**115 ± 28**	**98.350 ± 2.6815**	**94.44 ± 6.34**	**100.0947 ± 2.3251**	**1.34100 ± 0.00275**	**1.34919 ± 0.00304**	**1.37974 ± 0.01914**	**N/A**	**N/A**	**N/A**	**N/A**	**N/A**	**N/A**
Pep-16	**24 ± 41**	**33 ± 21**	**118 ± 73**	**99.009 ± 0.8651**	**98.19 ± 2.33**	**97.42 ± 0.90**	**1.33948 ± 0.00582**	**1.35655 ± 0.00016**	**1.35160 ± 0.00106**	**N/A**	**N/A**	**N/A**	**N/A**	**N/A**	**N/A**
Pep-17	**70 ± 27**	**70 ± 25**	**76 ± 14**	**98.290 ± 0.7821**	**96.65 ± 1.89**	**17.06 ± 4.37**	**1.33948 ± 0.00582**	**1.34784 ± 0.00312**	**1.35425 ± 0.00628**	**N/A**	**N/A**	**N/A**	**N/A**	**N/A**	**N/A**
Pep-18	**2 ± 2**	**52 ± 30**	**120+**	**97.249 ± 1.9054**	**88.67 ± 7.35**	**93.51 ± 1.47**	**1.34082 ± 0.00478**	**1.35228 ± 0.0027**	**1.36469 ± 0.00173**	**N/A**	**N/A**	**N/A**	**N/A**	**N/A**	**N/A**

Pep-19	**6 ± 4**	**6 ± 5**	**15 ± 12**	**99.617 ± 0.4769**	**98.25 ± 0.72**	**90.91 ± 13.94**	**1.33928 ± 0.00271**	**1.34469 ± 0.00032**	**1.36398 ± 0.00201**	**N/A**	**N/A**	**N/A**	**N/A**	**N/A**	**N/A**
Pep-20	**4 ± 1**	**5 ± 4**	**33 ± 23**	**99.696 ± 0.9287**	**97.87 ± 1.13**	**98.25 ± 1.13**	**1.34007 ± 0.00435**	**1.34393 ± 0.00611**	**1.36782 ± 0.00440**	**N/A**	**N/A**	**N/A**	**N/A**	**N/A**	**N/A**
Pep-21	**10 ± 3**	**2 ± 2**	**8 ± 4**	**98.932 ± 0.6951**	**85.97 ± 4.32**	**91.56 ± 8.89**	**1.33396 ± 6.22E-05**	**1.36386 ± 0.00039**	**1.36961 ± 0.00046**	**N/A**	**N/A**	**N/A**	**N/A**	**N/A**	**N/A**
CLP	**120+**	**120+**	**120+**	**99.314 ± 0.9940**	**104.74 ± 3.41**	**87.89 ± 10.15**	**1.35556 ± 0.00581**	**1.36317 ± 0.00108**	**1.37916 ± 0.00714**	**N/A**	**N/A**	**N/A**	**N/A**	**N/A**	**N/A**

Sample sizes: *n = 5, **n = 3, ***n = 3, † n = 3, ††n=3

Table S2. Raw data used to prepare heatmaps presented in Figure 3.1 B-F. Experimental details can be found in the methods section. Sample sizes for each group are listed at the bottom of the Table.

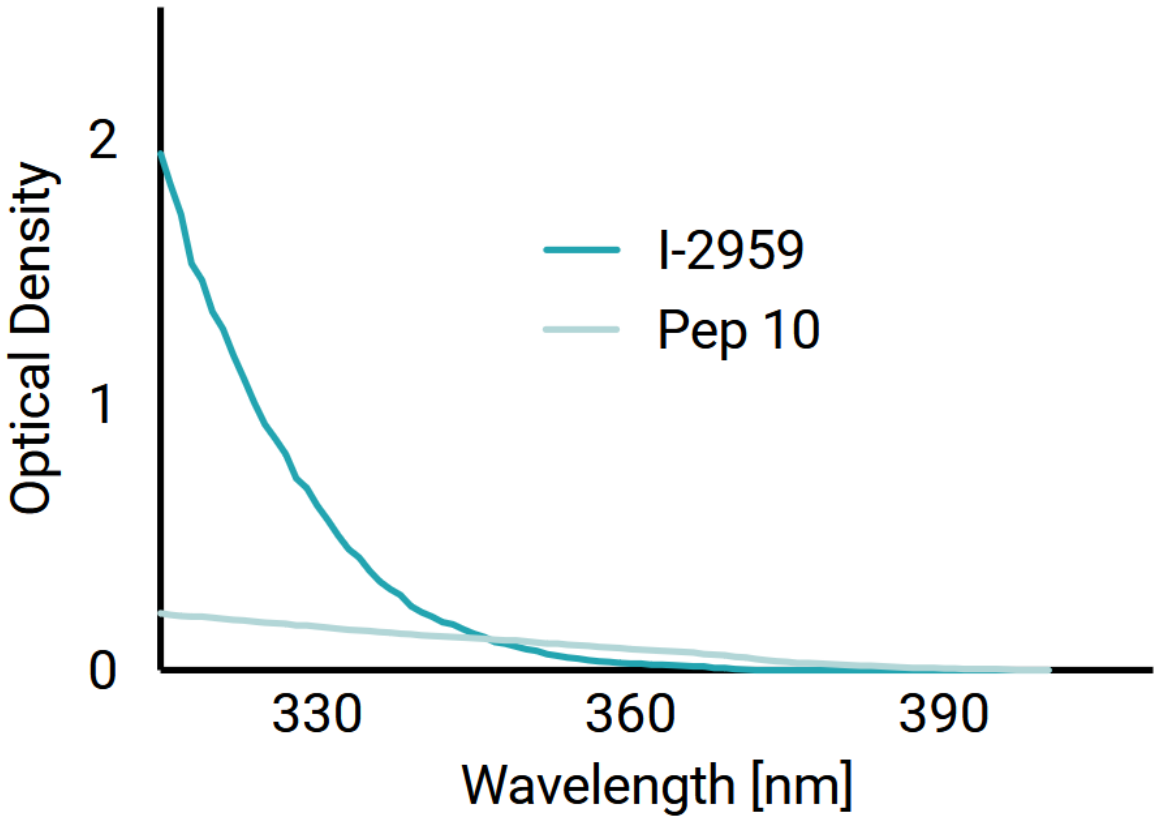

Figure S21. UVA absorbance spectra of peptide and Irgacure-2959 photoinitiator. Optical density in the UVA (315-400 nm) region was measured for 5% w/v Pep 10 ($(NH_2$-GCG$(POG)_8$GK(alloc)G-OH), light teal) and 5 mM Irgacure-2959 (dark teal) in 1X PBS solution (pH 7.4).

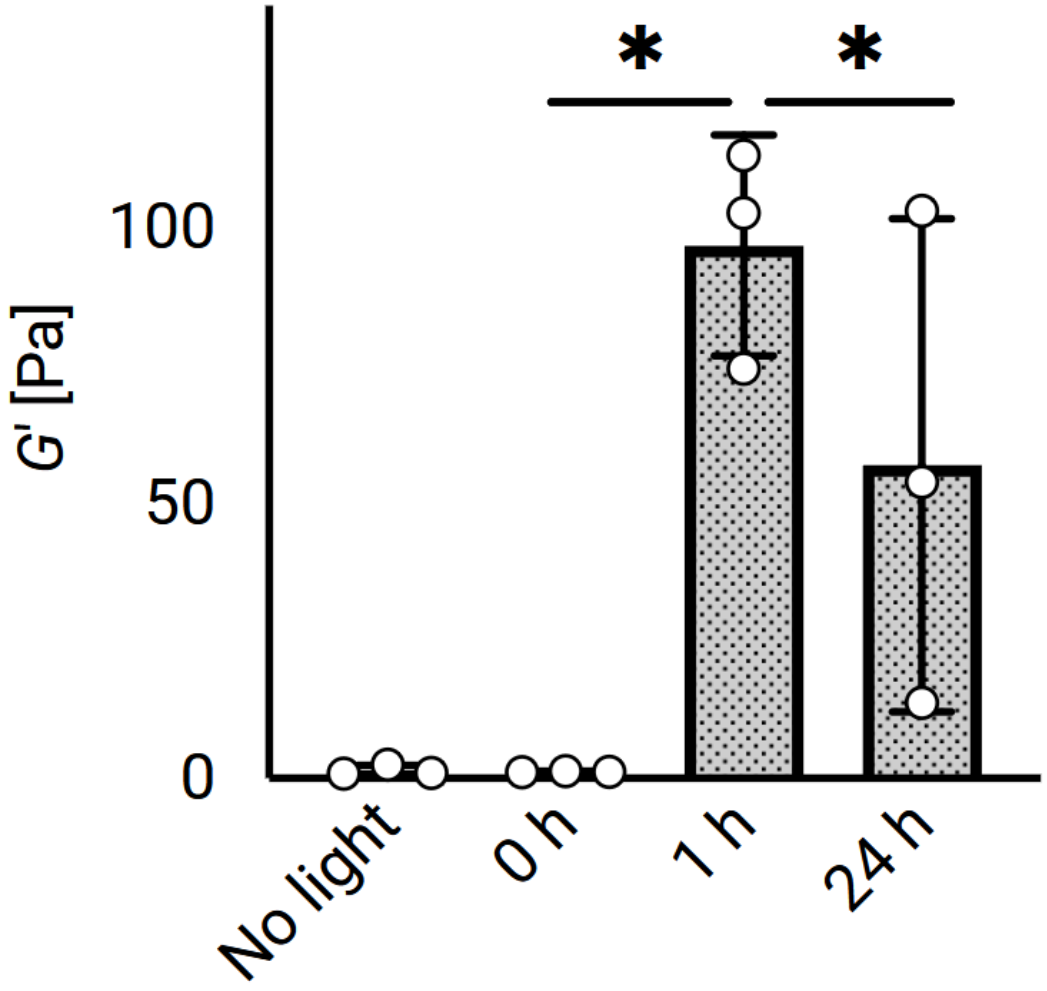

Figure S22. Effect of peptide folding time on hydrogel mechanical properties. A 5% w/v solution of Pep 10 (NH2-GCG(POG)8GK(alloc)G-OH) in 1× PBS (pH 7.4) was stored at 4 °C for 0, 1, or 24 h prior to UV irradiation with 0 or 1 mM Irgacure-2959. Storage modulus (G') was measured by oscillatory strain sweep (0.1-1%) in the linear viscoelastic region. Values represent mean ± standard deviation (n = 3). Statistical comparisons were performed using an unpaired t-test with unequal variance. *P < 0.05, **P < 0.01, ***P < 0.001.

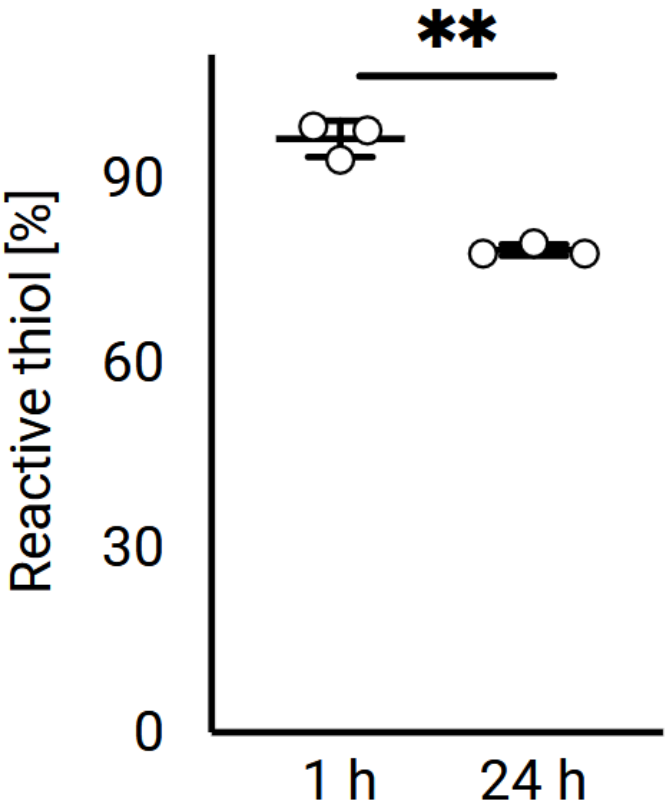

Figure S23. Time-dependent oxidation of cysteine-containing peptides in solution. Percent reactive thiol content of Pep 10 (NH_2-GCG(POG)$_8$GK(alloc)G-OH) was quantified over time using Ellman's assay via reaction with 5,5'-dithiobis-(2-nitrobenzoic acid) (DTNB). Peptide solutions were freshly prepared at 0.5 mM in 100 mM sodium phosphate buffer (pH 7.4), diluted 21-fold into 0.5 mM DTNB, and incubated for 30 min in the dark prior to absorbance measurement. A progressive decline in reactive thiol percentage was observed over time, indicating oxidation of free thiol groups during storage in solution. Values represent mean ± standard deviation (n = 3). Statistical comparisons were performed using an unpaired t-test with unequal variance. *P < 0.05, **P < 0.01, ***P < 0.001.

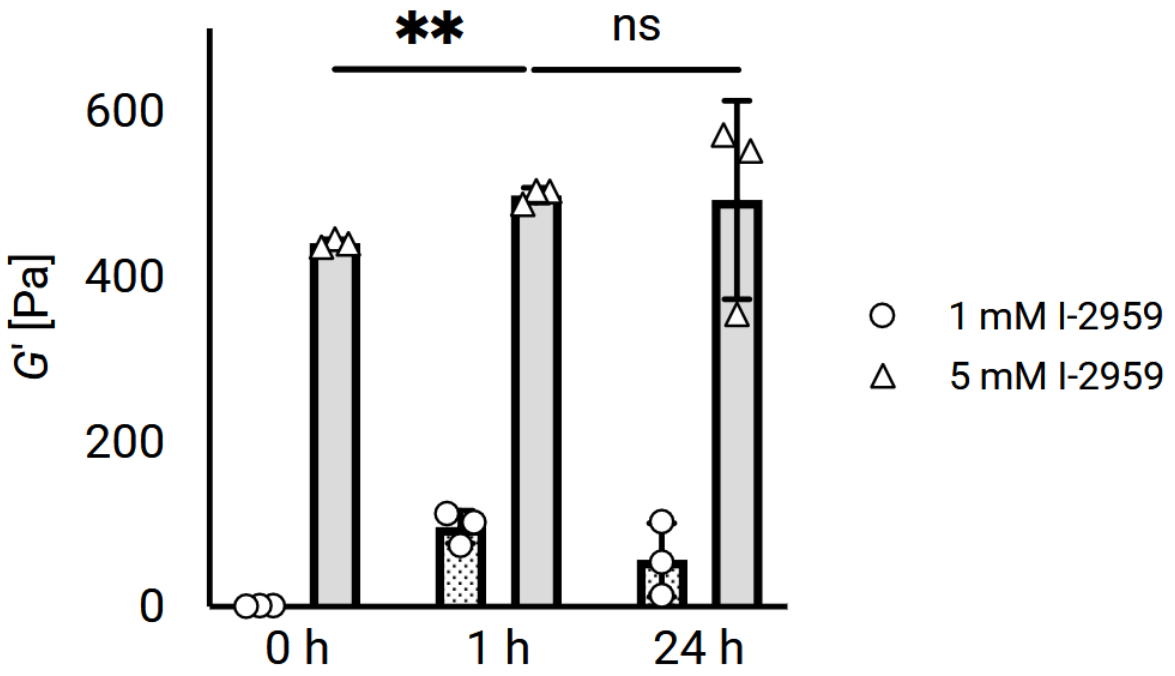

Figure S24. Influence of peptide folding time and photoinitiator concentration on hydrogel mechanical properties. A 5% w/v solution of Pep 10 (NH_2-GCG$(POG)_8$GK(alloc)G-OH) in 1× PBS (pH 7.4) was incubated at 4 °C for 0, 1, or 24 h prior to UV irradiation with either 1 mM (circle) or 5 mM (triangle) I-2959. Storage modulus (*G*') was measured via oscillatory strain sweep (0.1-1%) within the linear viscoelastic region. Values represent mean ± standard deviation ($n = 3$). Statistical comparisons were performed using an unpaired *t*-test with unequal variance. *$P < 0.05$, **$P < 0.01$, ***$P < 0.001$.

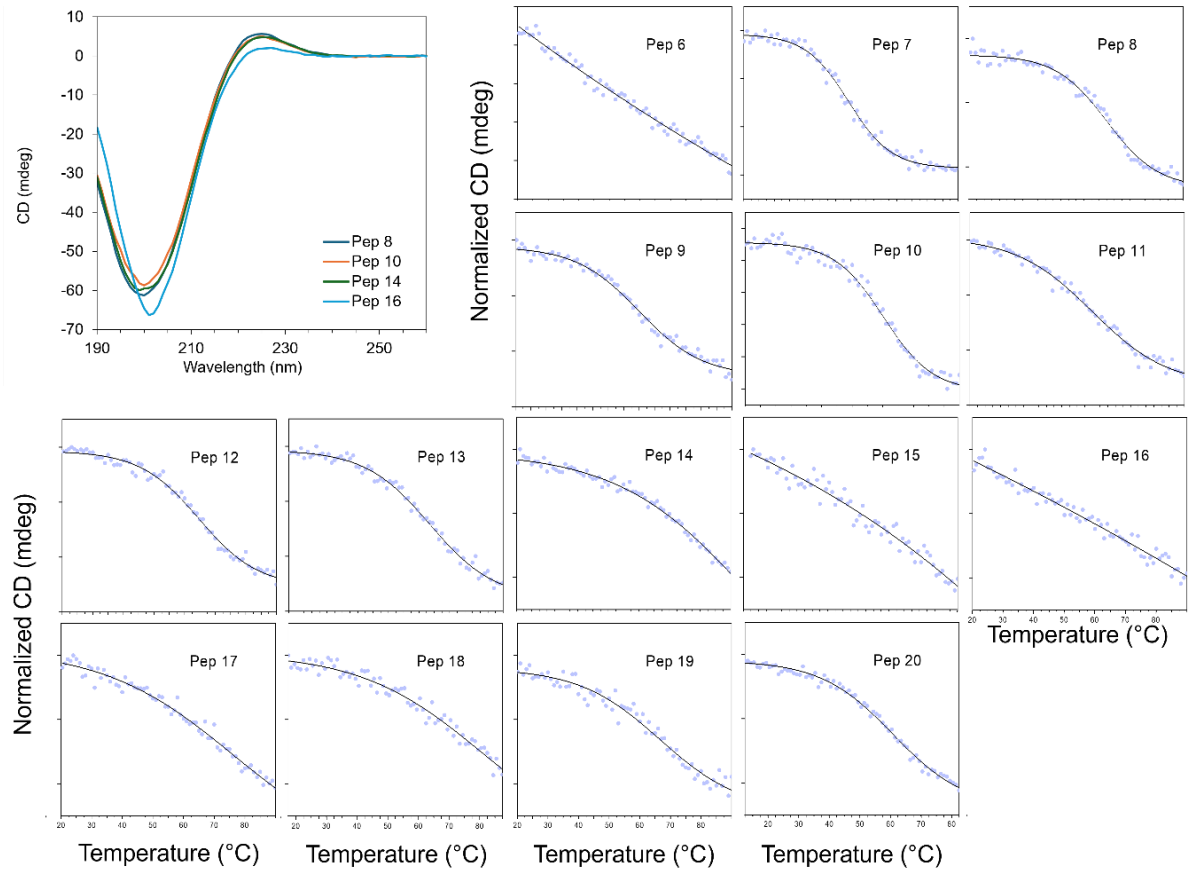

Figure S25. Circular dichroism spectra and thermal denaturation profiles of engineered peptides. Top left: far-UV CD spectra of selected peptides (Pep 8, 10, 14, 16) were recorded at 200 µM in 1 mM phosphate buffer (pH 7.4) at 20 °C, confirming triple-helix secondary structure with a characteristic maximum near 225 nm. Right and bottom panels: thermal unfolding profiles of all collagen-like peptides (Pep 6-20) were acquired by monitoring ellipticity at 225 nm from 15 °C to 85 °C.

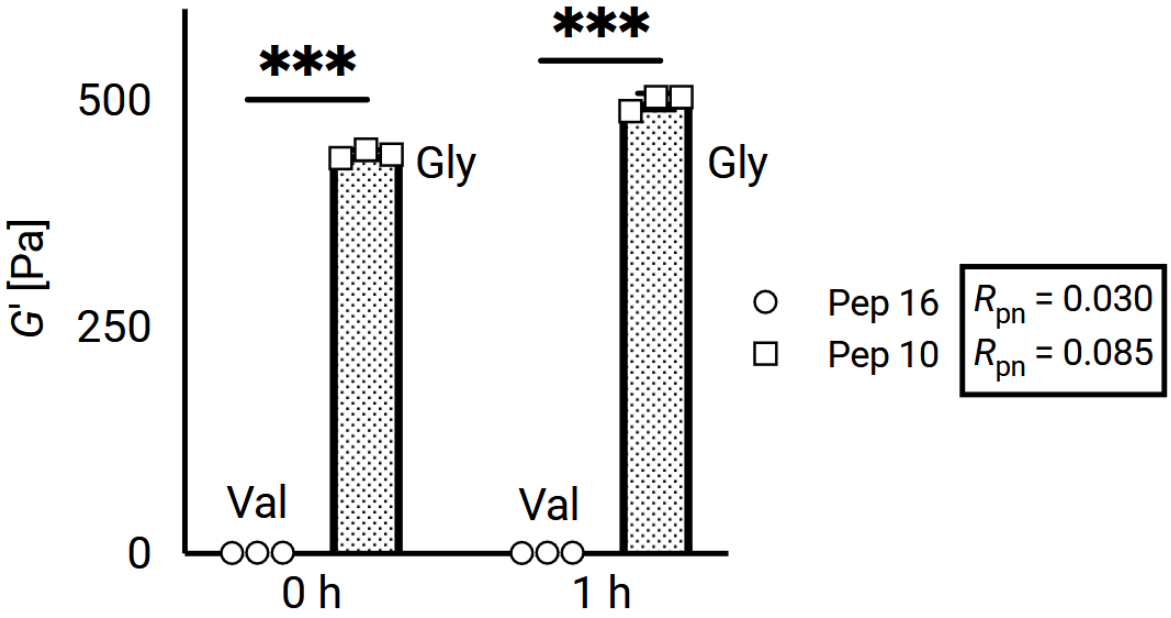

Figure S26. A single glycine-to-valine substitution within the triple-helix domain disrupts folding and reduces hydrogel mechanical strength. A 5% w/v solution of Pep 10 (NH_2-GCG$(POG)_8$GK(alloc)G-OH, square) was compared to an amino acid substitution variant (Pep 16, NH_2-GCG$(POG)_4$POV$(POG)_3$GK(alloc)G-OH, circle) in which a single glycine was replaced with valine. Circular dichroism (CD) spectra were collected with 200 μM peptide in 1 mM phosphate buffer (pH 7.4) and the ratio of positive to negative peak intensities (R_{pn}) was calculated as a measure of triple-helix content. The valine substitution resulted in a significantly reduced R_{pn} value (0.030 vs 0.085), indicating impaired folding, and correspondingly led to a drastic reduction in hydrogel storage modulus (G'). Values represent mean ± standard deviation (n = 3). Statistical comparisons were performed using an unpaired t-test with unequal variance. *P < 0.05, **P < 0.01, ***P < 0.001.

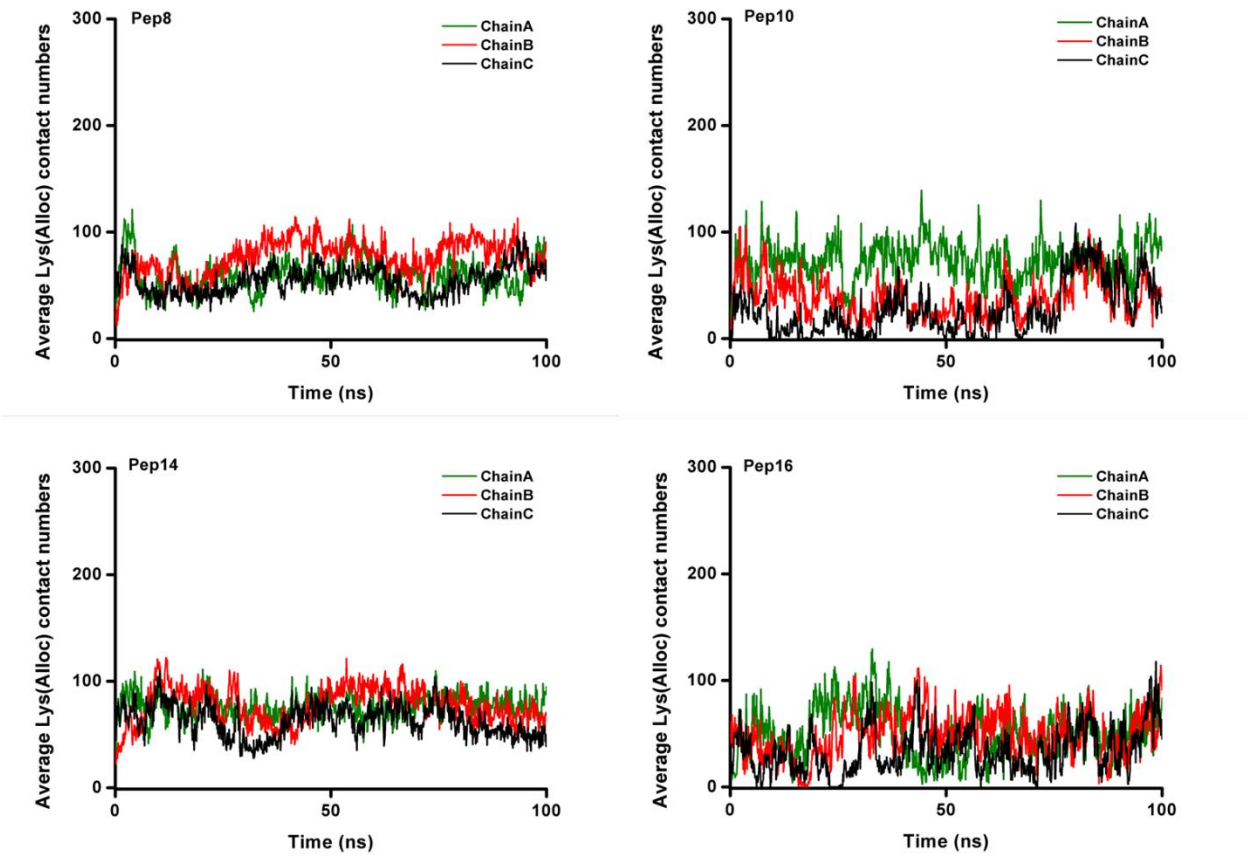

Figure S27. Molecular dynamics simulations of average lysine (alloc) interchain interactions. Initial configurations were generated by placing the individual helices at a distance shorter than the nonbonded interaction cut-off. For each system, six production runs of 100 ns were performed in explicit solvent using the TIP3P water model. The simulations utilized the CHARMM36 force field, as implemented in the GROMACS software package.

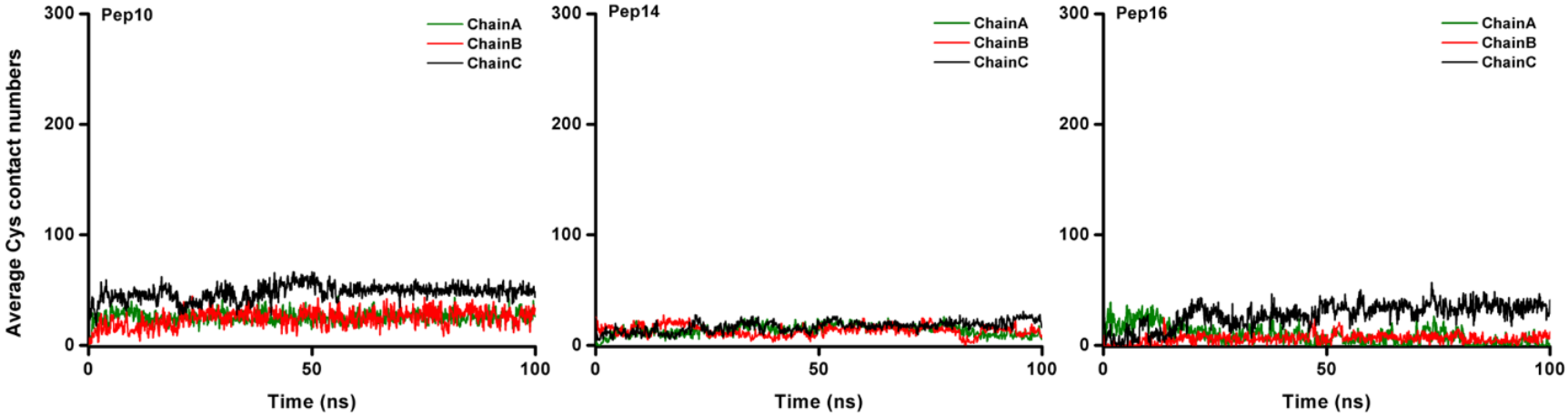

Figure S28. Molecular dynamics simulations of average cysteine interchain interactions. Initial configurations were generated by placing the individual helices at a distance shorter than the nonbonded interaction cut-off. For each system, six production runs of 100 ns were performed in explicit solvent using the TIP3P water model. The simulations utilized the CHARMM36 force field, as implemented in the GROMACS software package.

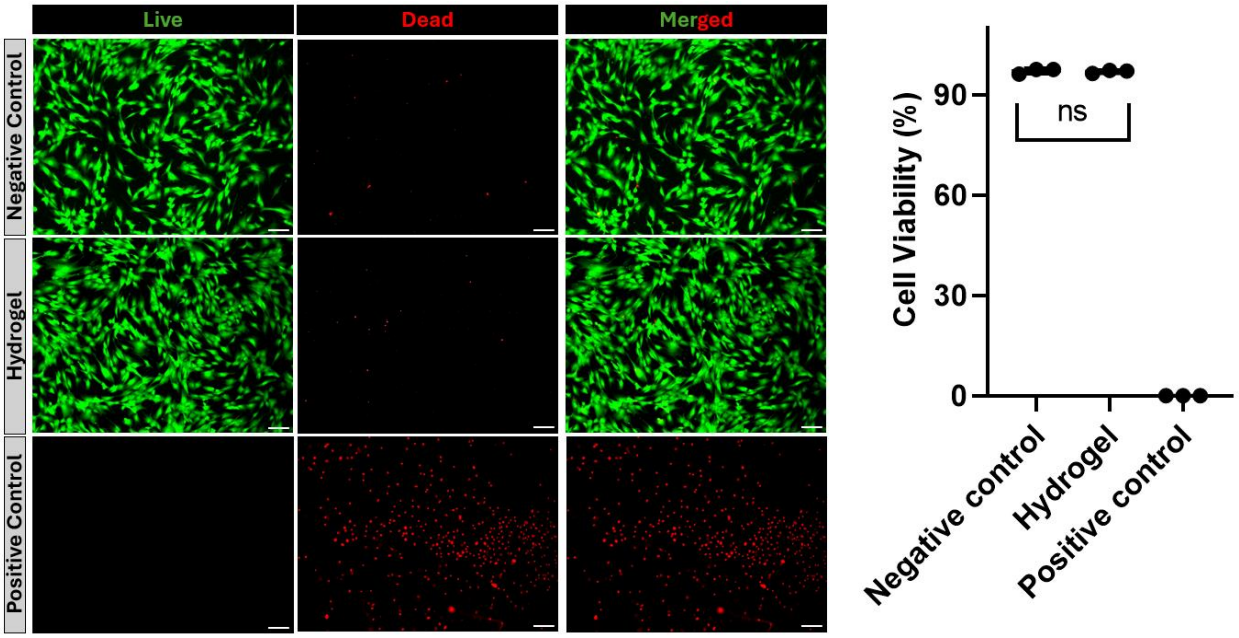

Figure S29. 2D Cytocompatibility of Pep 10 hydrogels with human skin fibroblasts. Hydrogels (5% w/v Pep 10 in 1× PBS with 5 mM Irgacure-2959) were UV-irradiated for 20 min, sterilized, and seeded with HSF cells (5×10^4 cells/well). After 24 h, viability was assessed using a Calcein-AM/EthD-1 live/dead assay. Quantification showed no significant difference in viability to tissue culture plastic negative control. 10% DMSO treatment was used as a positive control for cell death. Values represent mean ± standard deviation (n = 3). Statistical comparisons were performed using an unpaired t-test with unequal variance. *$P < 0.05$, **$P < 0.01$, ***$P < 0.001$. Representative fluorescence images shown. Scale bars = 100 μm.

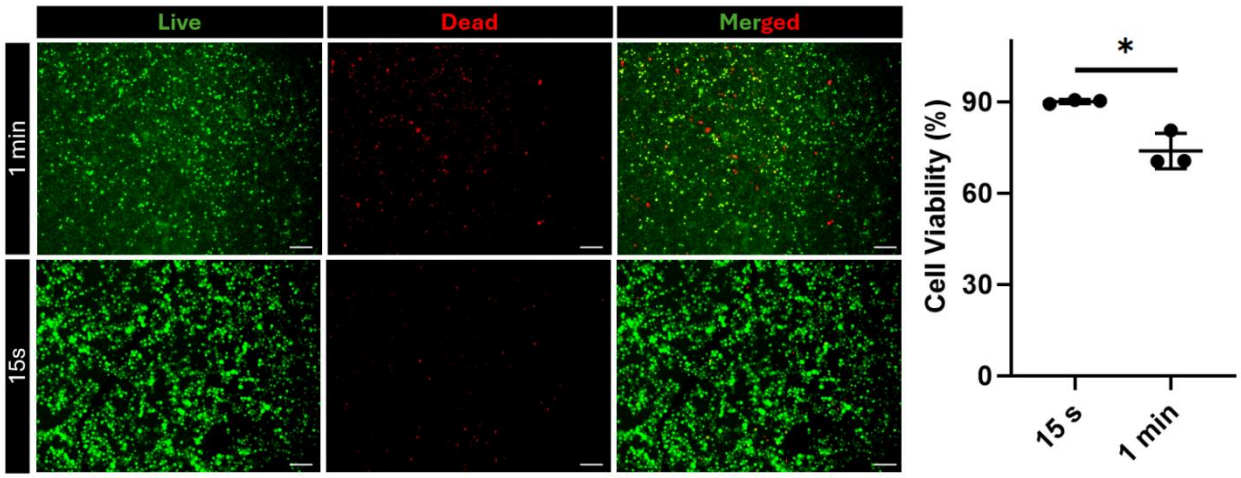

Figure S30. 3D Cytocompatibility of Pep 10 hydrogels with human skin fibroblasts. HSF cells in serum-free DMEM were mixed with Pep 10 in 1× PBS with 20 mM LAP to produce a peptide and cell concentration of 5% w/v and 4×10^6 cells/mL, respectively, before UV-irradiation for 15 s or 1 min. After 24 h, viability was assessed using a Calcein-AM/EthD-1 live/dead assay. Values represent mean ± standard deviation (n = 3). Statistical comparisons were performed using an unpaired t-test with unequal variance. *P < 0.05, **P < 0.01, ***P < 0.001. Representative fluorescence images shown. Scale bars = 100 μm.

Peptide (junction chemistry)	*G*' [Pa]	ξ(affine) [nm]	ξ(phantom) [nm]
Pep 10 (*f* = 2, AL)	440 ± 5	26.1 ± 0.1	22.83 ± 0.08
Pep 11 (*f* = 3, AL)	700 ± 100	22 ± 1	20.2 ± 0.9
Pep 12 (*f* = 3, AL)	800 ± 200	22 ± 2	20 ± 2
Pep 13 (*f* = 4, AL)	1500 ± 200	17.4 ± 0.6	16.4 ± 0.6
Pep 14 (*f* = 5, AL)	2600 ± 200	14.5 ± 0.3	13.8 ± 0.3
Pep 17 (*f* = 5, MA)	350 ± 50	28 ± 1	27 ± 1
Pep 18 (*f* = 5, AC)	500 ± 100	25 ± 2	24 ± 2
Pep 20 (*f* = 2, AC)	254 ± 6	31.4 ± 0.3	27.4 ± 0.2

Table S3. Storage modulus (G') and estimated network mesh size (ξ) for peptide-based hydrogels (5% w/v). Storage moduli were obtained from oscillatory shear measurements in the linear viscoelastic region (0.01-1 Hz). Network mesh size (ξ)[270, 271]was estimated from rubber elasticity theory using:

$$\xi = \left(\frac{6M_c}{\pi c N_A}\right)^{\frac{1}{3}}$$

The molecular weight between crosslinks (M_c) was derived from *G*' under either affine or phantom network assumptions. Values represent mean ± standard deviation (n = 3).

Sample	Sequence	Molecular weight (g/mol)	M+2H Ion	M+3H Ion
Pep 1	NH_2-(K**(alloc)**)$_2$GGGCC-NH_2	819.0	410.5	--
Pep 2	**MA**-K**(ε-MA)**GGG-OH	453.5	--	--
Pep 3	**MA**-K**(ε-MA)**GGGC-NH_2	555.6	--	--
Pep 4	**MA**-POGPCG-OH	610.2	--	--
Pep 5	**MA**-(POG)$_3$PCG-OH	1144.5	573.3	--
Pep 6	**MA**-(POG)$_5$PCG-OH	1678.7	840.4	560.2
Pep 7	**MA**-(POG)$_7$PCG-OH	2213.0	1107.5	738.7
Pep 8	NH_2-GK**(alloc)**G(POG)$_8$GK**(alloc)**G-OH	2809.0	1405.5	937.0
Pep 9	NH_2-G(K**(alloc)**)$_2$(POG) (K**(alloc)**)$_2$G-OH	3119.3	1560.7	1040.4
Pep 10	NH_2-GCG(POG)$_8$GK**(alloc)**G-OH	2699.9	1351.0	900.6
Pep 11	NH_2-GCC(POG)$_8$GK**(alloc)**GG-OH	2745.9	1374.0	916.0
Pep 12	NH_2-GCG(POG)$_8$K**(alloc)**$_2$G-OH	2855.1	1428.6	952.4
Pep 13	NH_2-GCC(POG)$_8$K**(alloc)**$_2$G-OH	2901.1	1451.6	967.7
Pep 14	NH_2-CCC(POG)$_8$K**(alloc)**$_2$G-OH	2947.2	1474.6	983.1
Pep 15	NH_2-CCC(POG)$_8$K**(alloc)**$_3$-NH_2	3102.4	1552.2	1034.8
Pep 16	NH_2-GCG(POG)$_4$POV(POG)$_3$G**K(alloc)**G-OH	2741.9	1372.0	914.6
Pep 17	NH_2-CCC(POG)$_8$K**(ε-MA)**$_2$G-OH	2915.2	1458.6	972.4
Pep 18	NH_2-CCC(POG)$_8$K**(ε-Ac)**$_2$G-OH	2886.2	1444.1	962.7
Pep 19	NH_2-GCG(POG)$_8$GK**(ε-MA)**G-OH	2683.9	1343.0	895.6
Pep 20	NH_2-GCG(POG)$_8$GK**(ε-Ac)**G-OH	2669.9	1336.0	890.1

Table S4. List of peptide codes, their sequences, molecular weights, and theoretical ions. Representative mass spectrometry data for each peptide illustrating detected ions are presented in the following pages.

Figure S31. Mass spectra for photoactivated peptides.

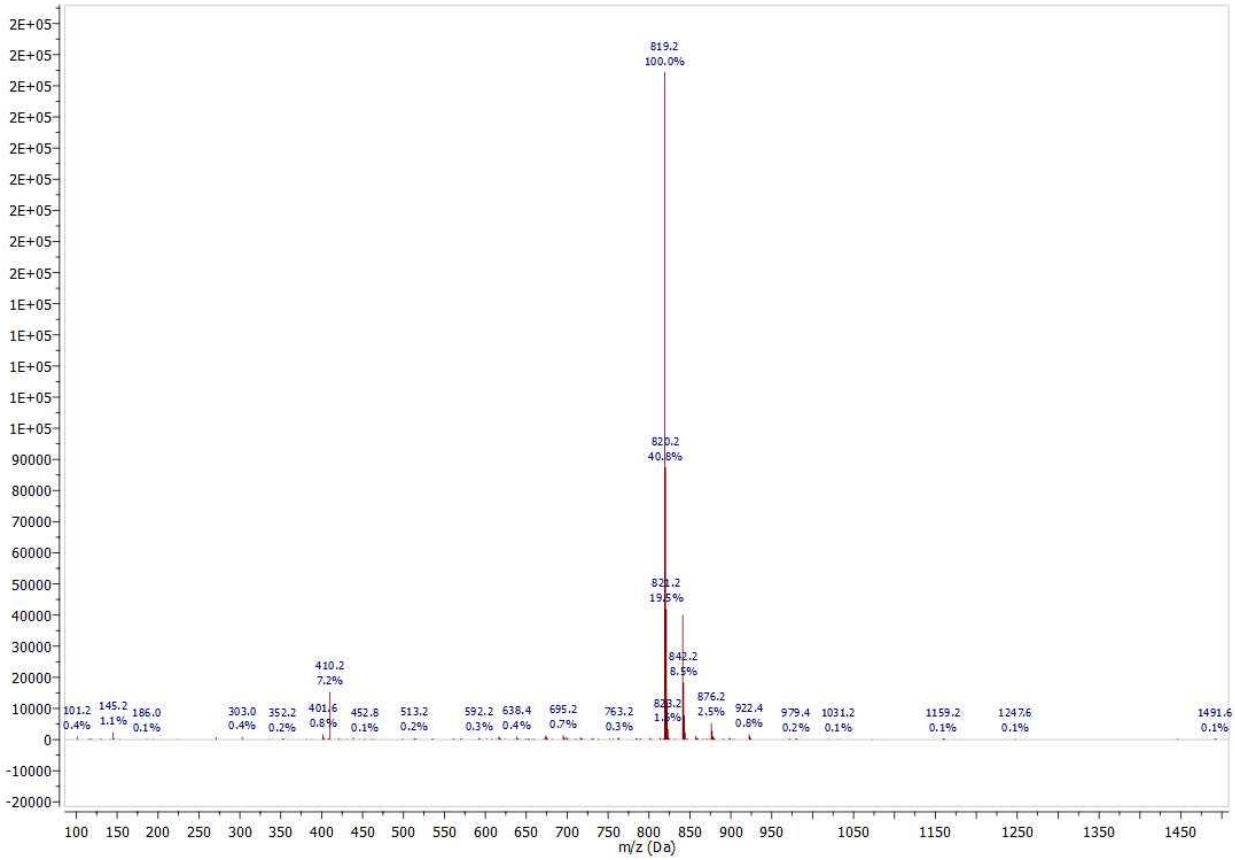

Sample	Sequence	Molecular weight (g/mol)	M+1H Ion	M+2H Ion
Pep 1	**H-GCG(POG)$_8$GK(alloc)G-OH**	**819.0**	**820.0**	**410.5**

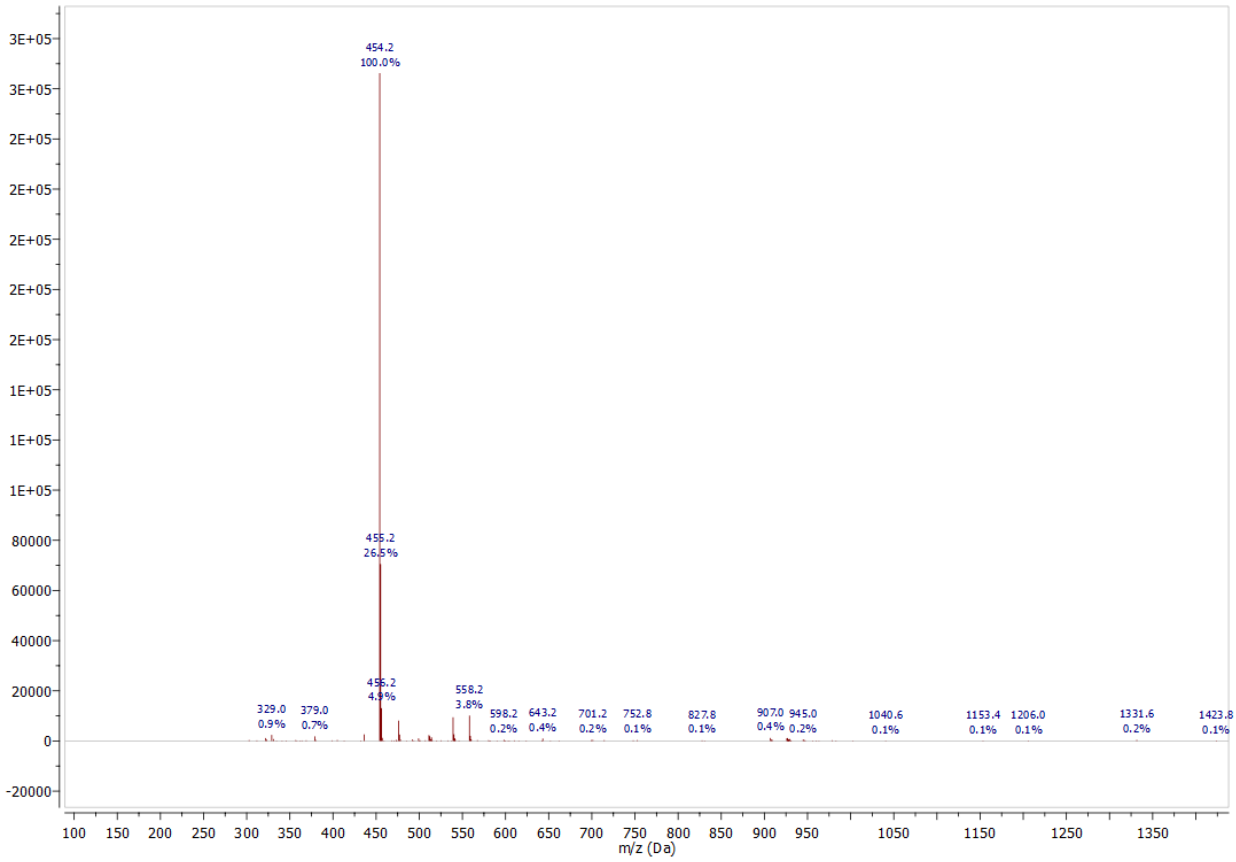

Sample	Sequence	Molecular weight (g/mol)	M+1H Ion
Pep 2	**MA-K(ε-MA)GGG-OH**	**453.5**	**454.5**

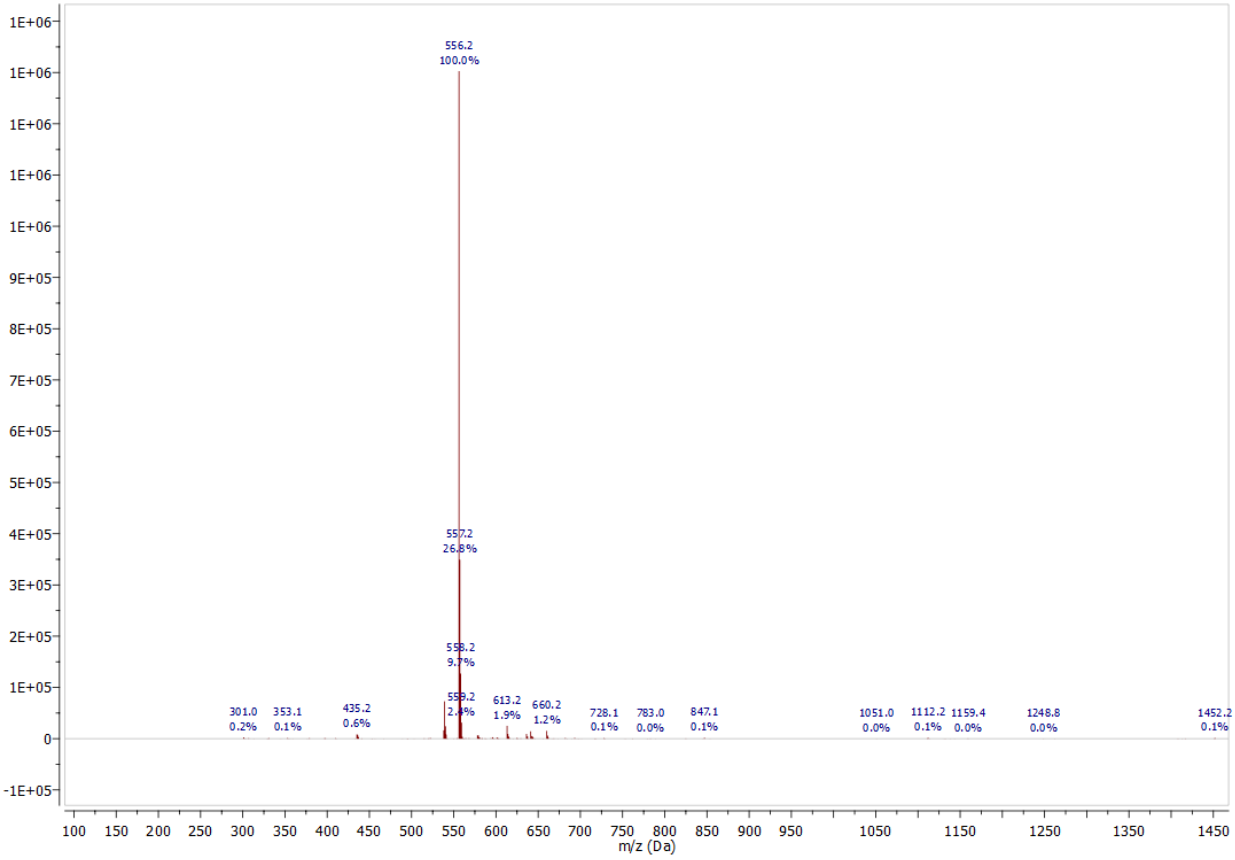

Sample	Sequence	Molecular weight (g/mol)	M+1H Ion
Pep 3	**MA-K(ε-MA)GGGC-NH₂**	**555.6**	**556.6**

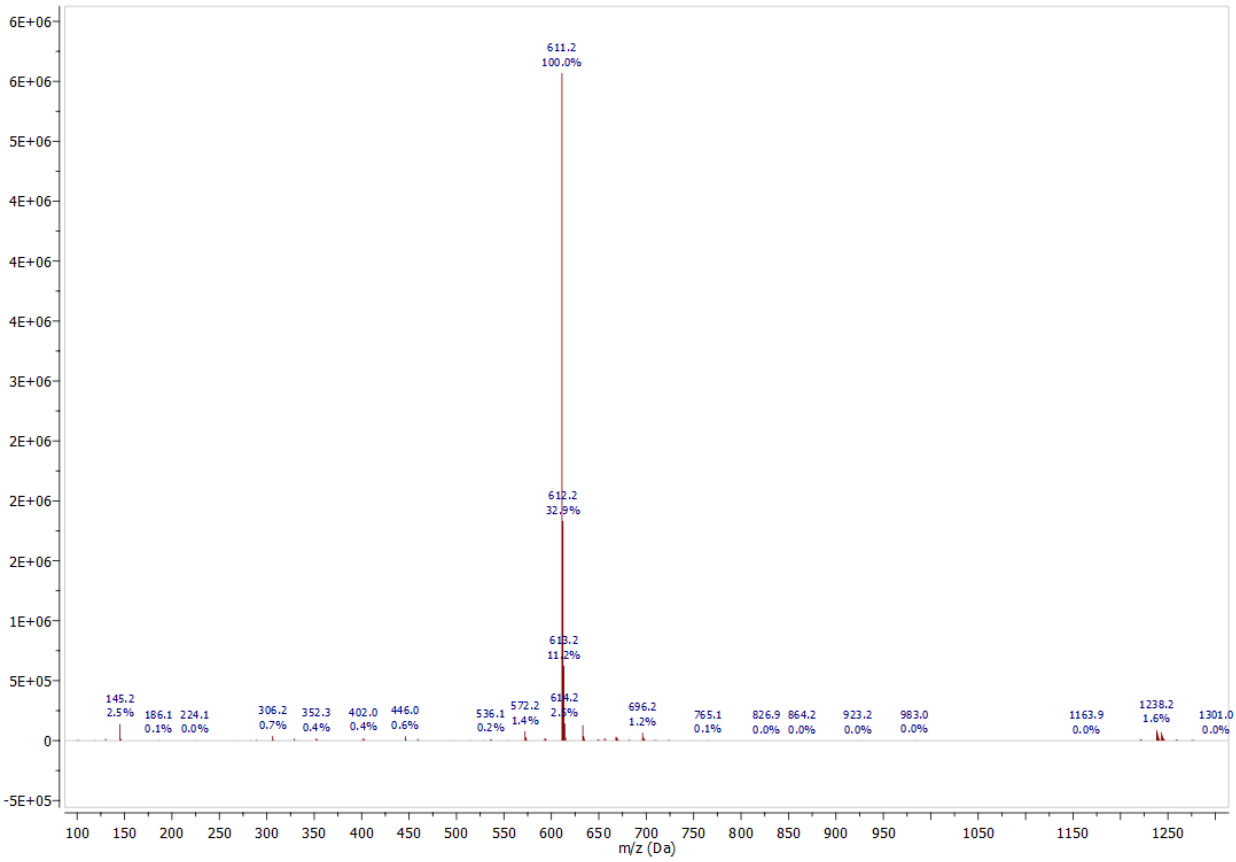

Sample	Sequence	Molecular weight (g/mol)	M+1H Ion
Pep 4	**MA-POGPCG-OH**	**610.2**	**611.2**

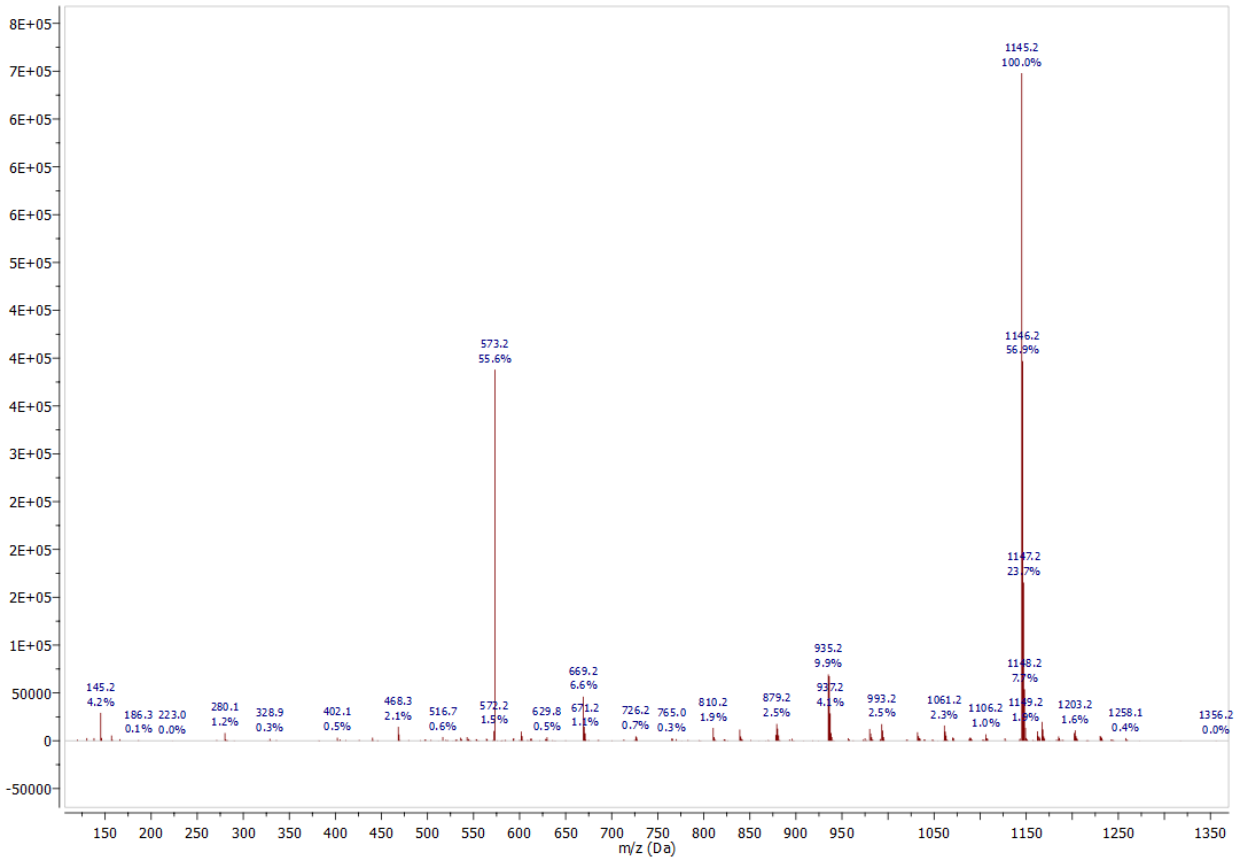

Sample	Sequence	Molecular weight (g/mol)	M+1H Ion	M+2H Ion
Pep 5	**MA-(POG)$_3$PCG-OH**	**1144.5**	**1145.5**	**573.3**

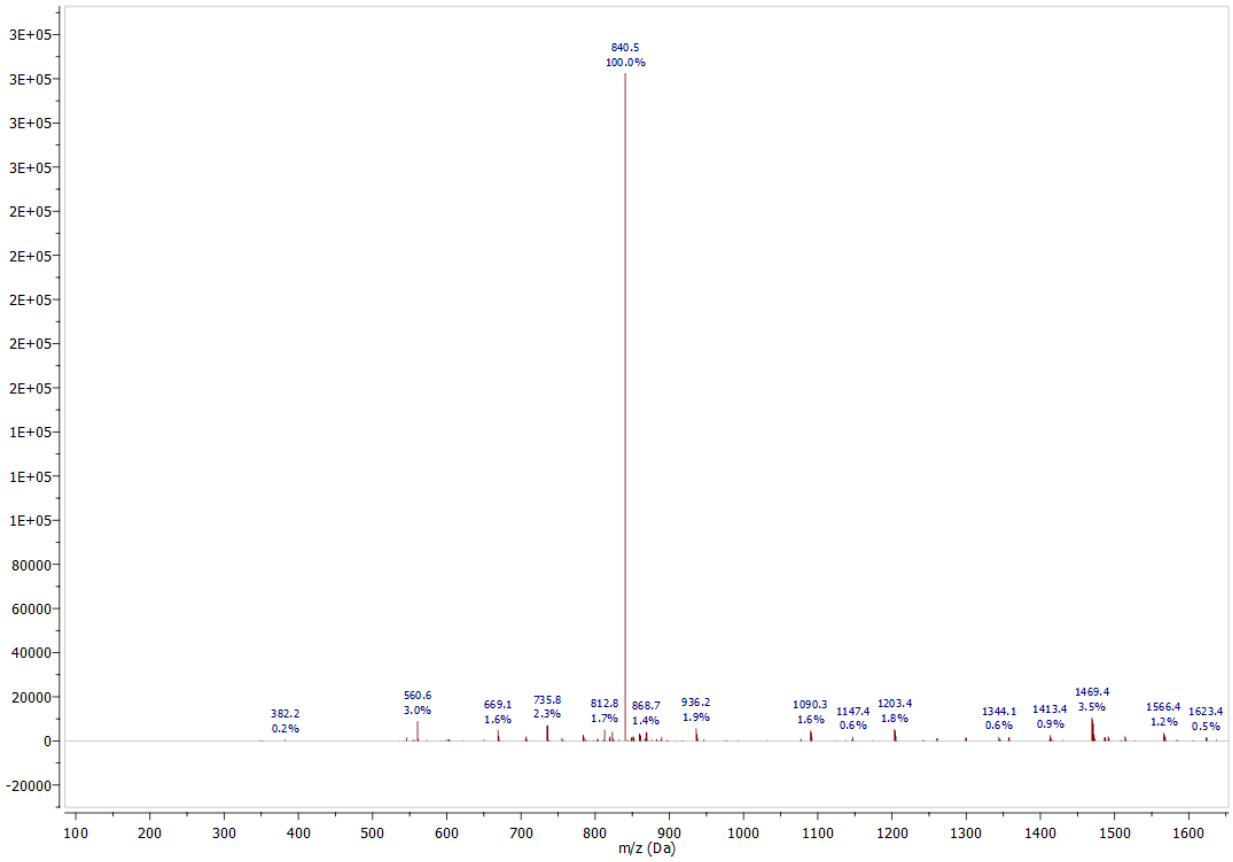

Sample	Sequence	Molecular weight (g/mol)	M+2H Ion	M+3H Ion
Pep 6	**MA-(POG)$_5$PCG-OH**	**1678.7**	**840.4**	**560.2**

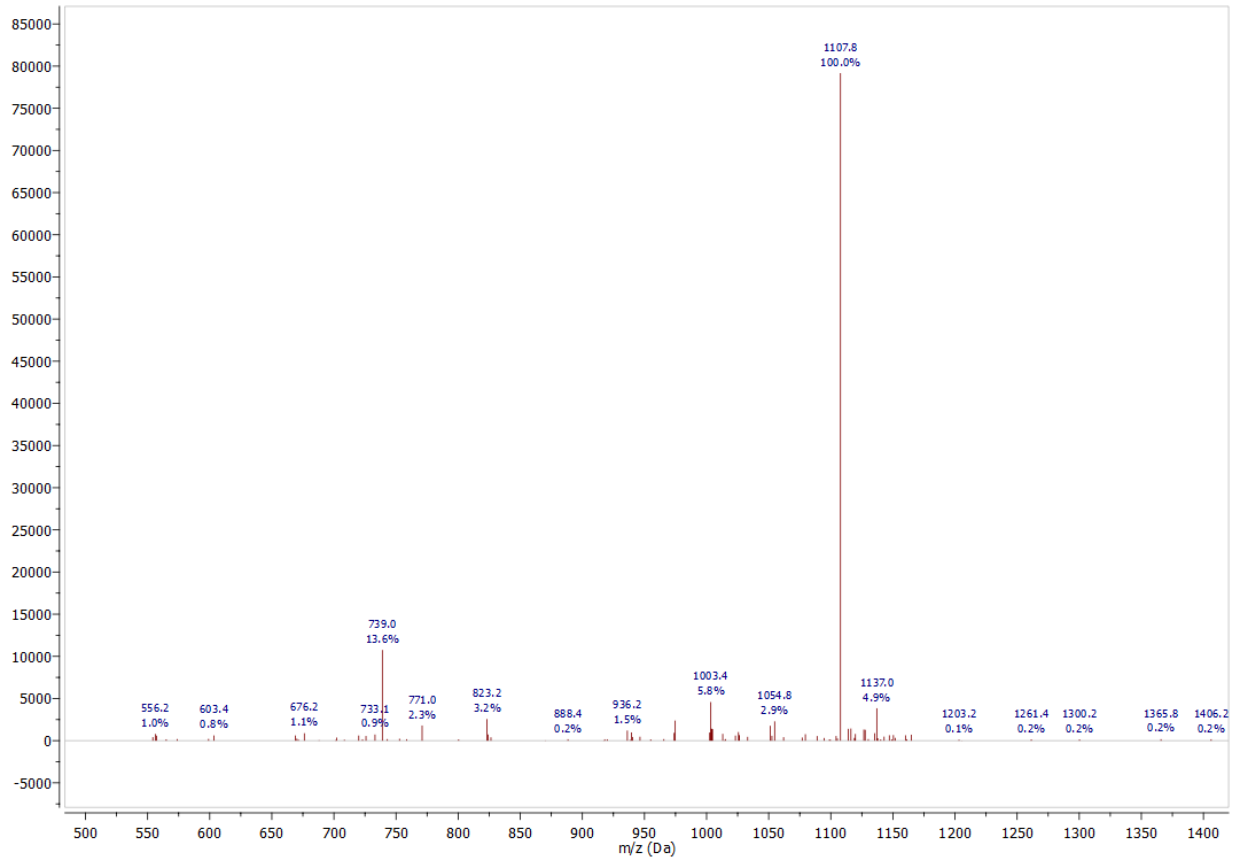

Sample	Sequence	Molecular weight (g/mol)	M+2H Ion	M+3H Ion
Pep 7	**MA-(POG)$_7$PCG-OH**	**2213.0**	**1107.5**	**738.7**

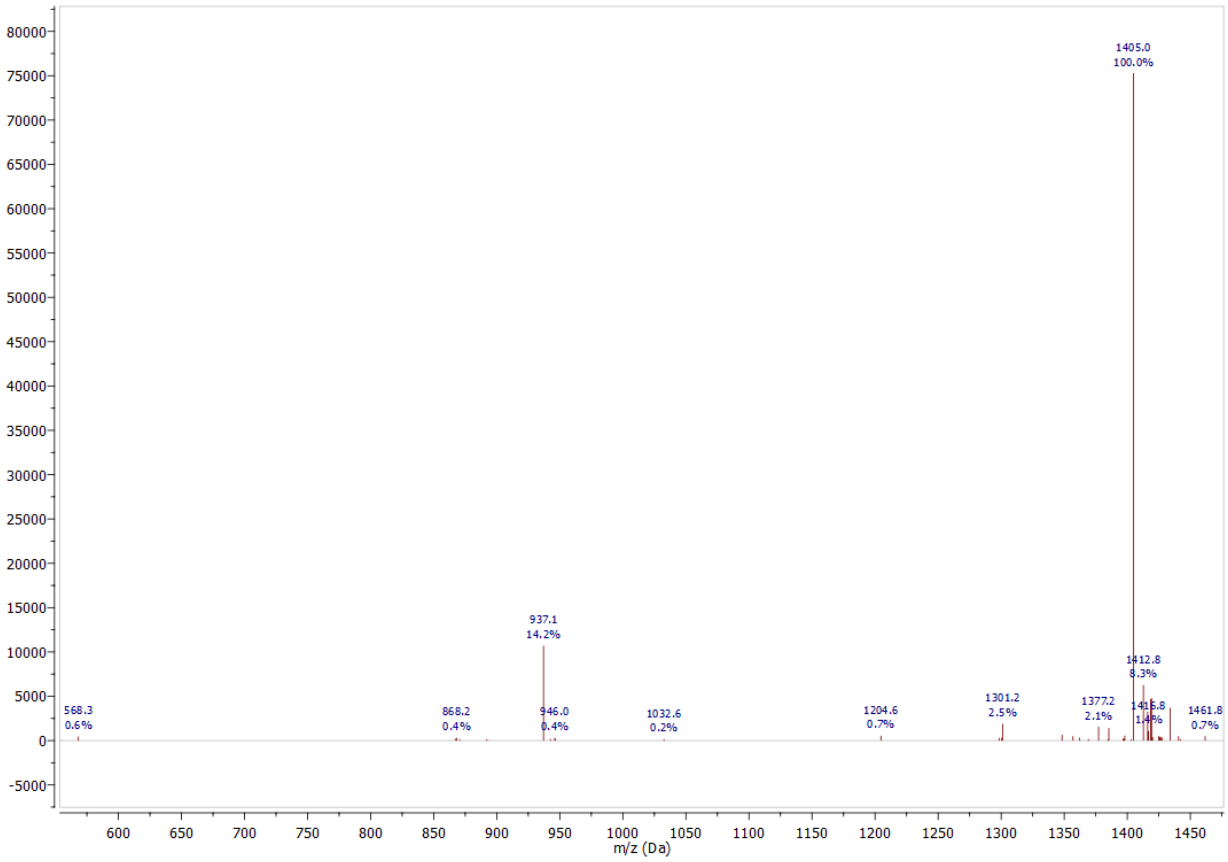

Sample	Sequence	Molecular weight (g/mol)	M+2H Ion	M+3H Ion
Pep 8	**H-GK(alloc)G(POG)$_8$GK(alloc)G-OH**	**2809.0**	**1405.5**	**937.0**

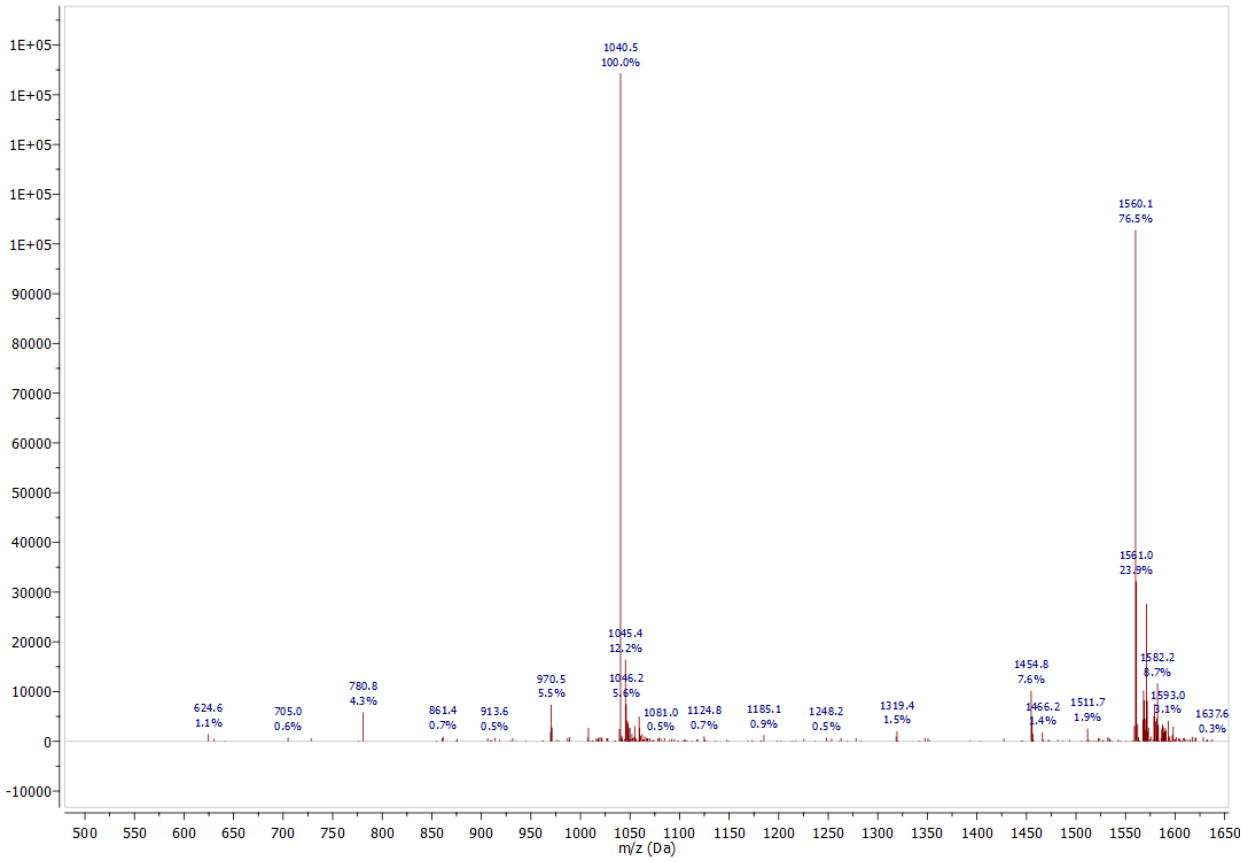

Sample	Sequence	Molecular weight (g/mol)	M+2H Ion	M+3H Ion
Pep 9	**H-G(K(alloc))$_2$(POG)$_8$(K(alloc))$_2$G-OH**	**3119.3**	**1560.7**	**1040.4**

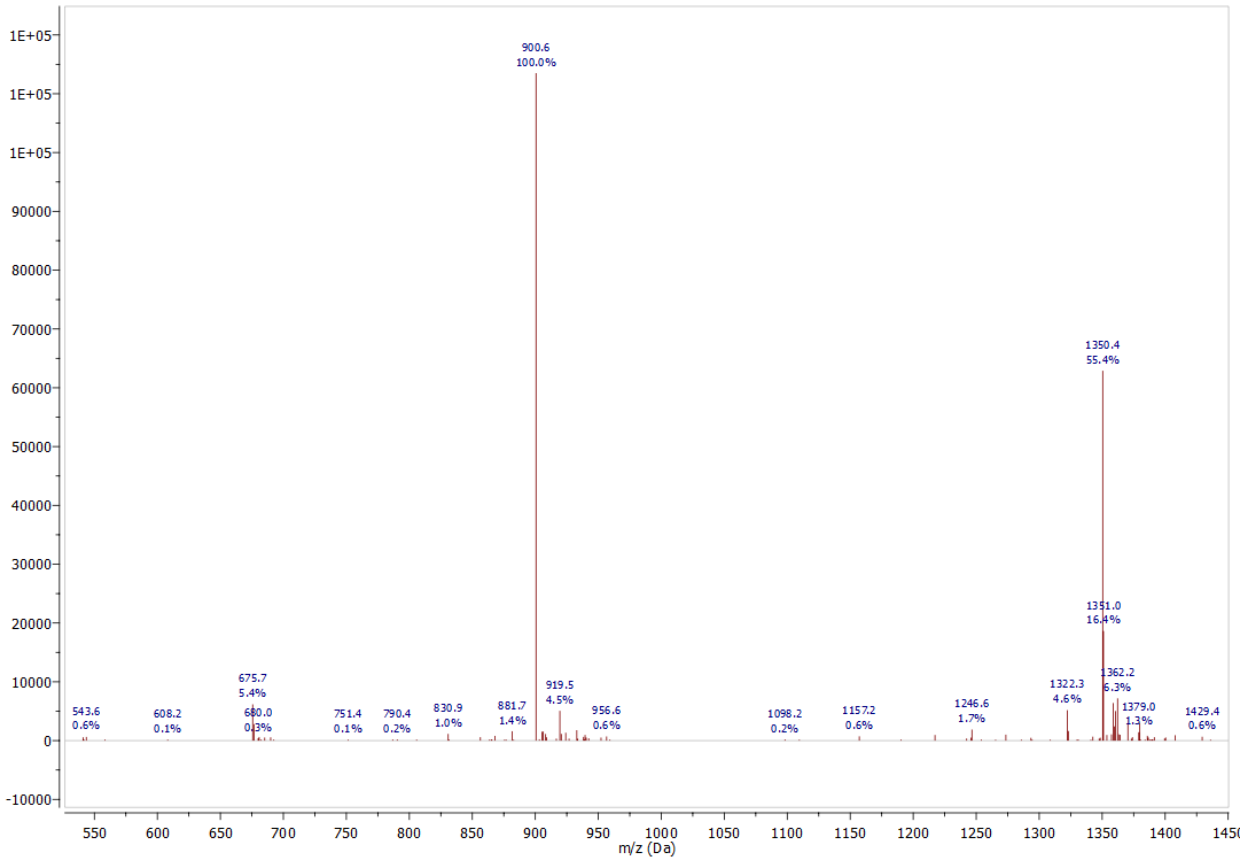

Sample	Sequence	Molecular weight (g/mol)	M+2H Ion	M+3H Ion
Pep 10	**H-GCG(POG)$_8$GK(alloc)G-OH**	**2699.9**	**1351.0**	**900.6**

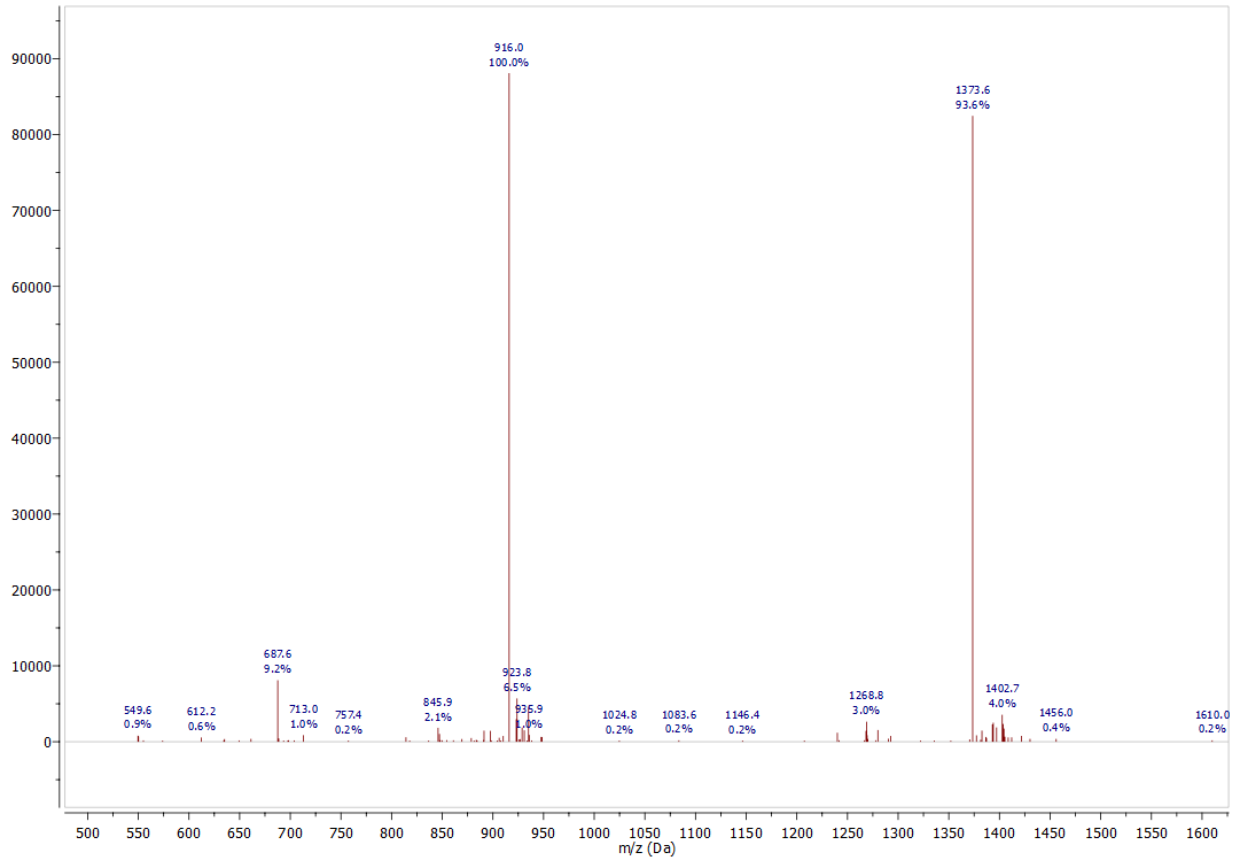

Sample	Sequence	Molecular weight (g/mol)	M+2H Ion	M+3H Ion
Pep 11	**H-GCC(POG)$_8$GK(alloc)GG-OH**	**2745.9**	**1374.0**	**916.0**

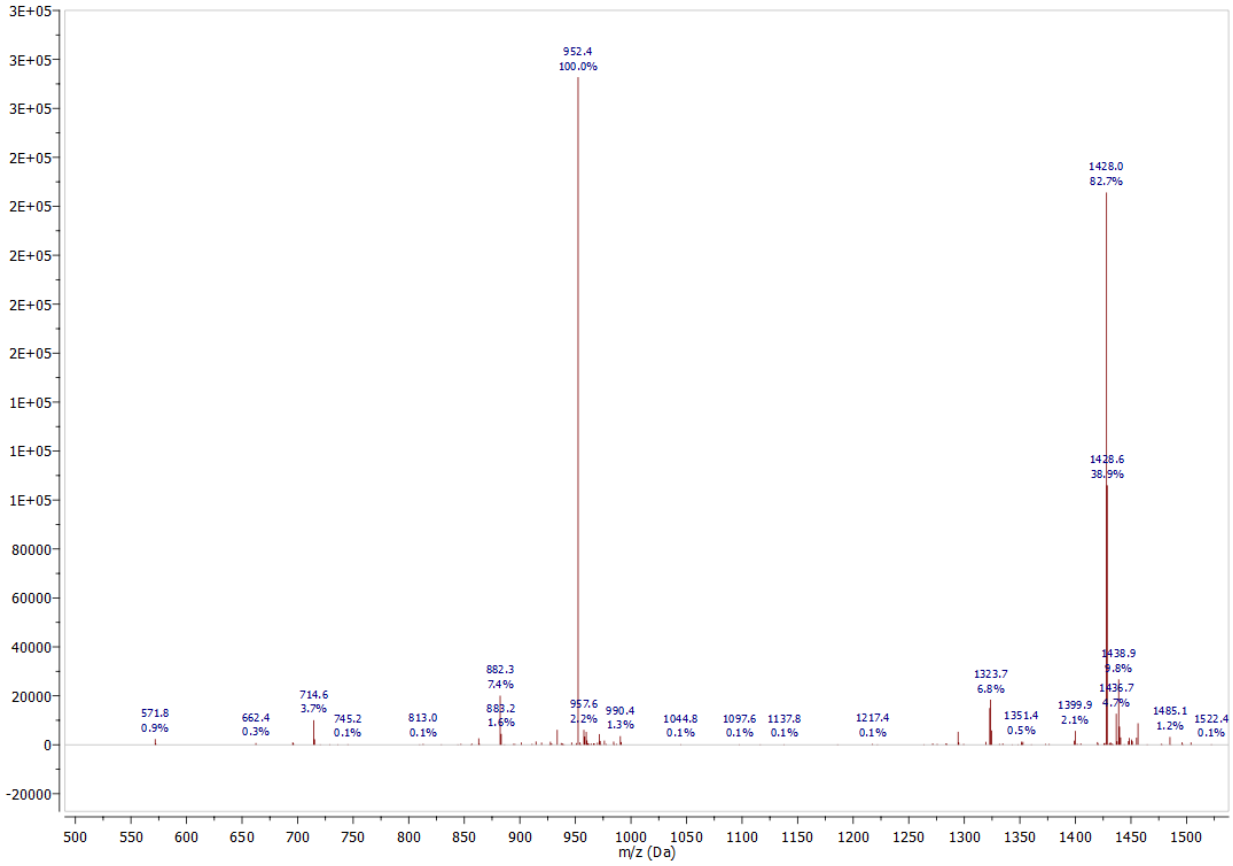

Sample	Sequence	Molecular weight (g/mol)	M+2H Ion	M+3H Ion
Pep 12	**H-GCG(POG)$_8$K(alloc)$_2$G-OH**	**2855.1**	**1428.6**	**952.4**

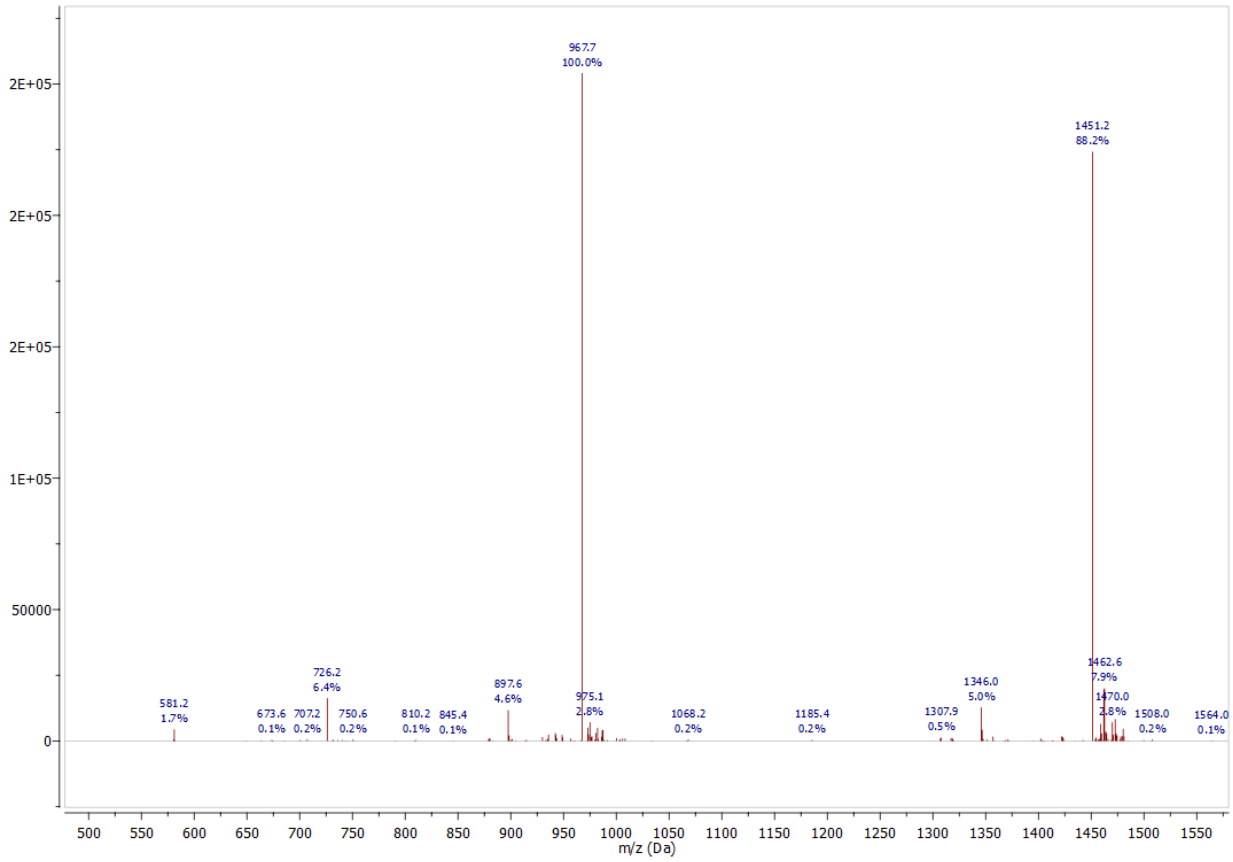

Sample	Sequence	Molecular weight (g/mol)	M+2H Ion	M+3H Ion
Pep 13	**H-GCC(POG)$_8$K(alloc)$_2$G-OH**	**2901.1**	**1451.6**	**967.7**

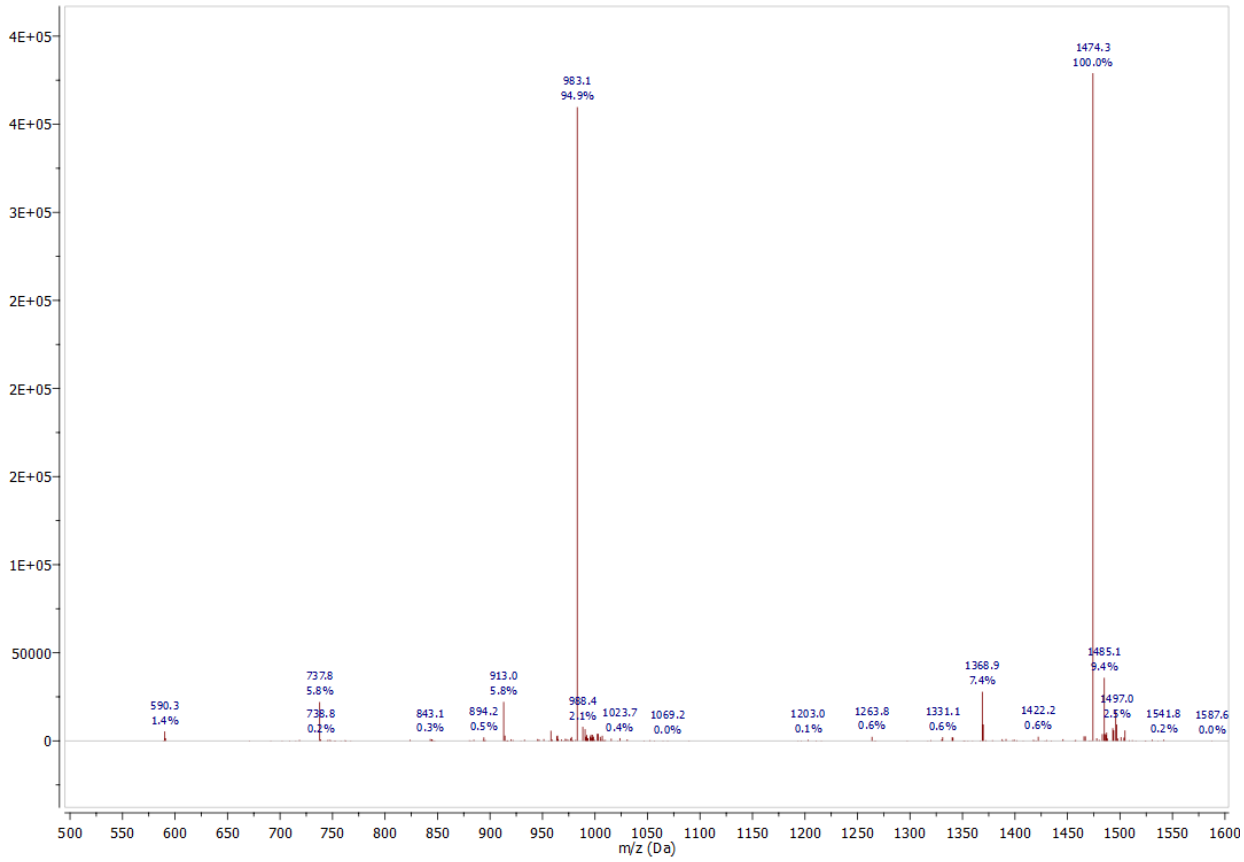

Sample	Sequence	Molecular weight (g/mol)	M+2H Ion	M+3H Ion
Pep 14	**H-CCC(POG)$_8$K(alloc)$_2$G-OH**	**2947.2**	**1474.6**	**983.1**

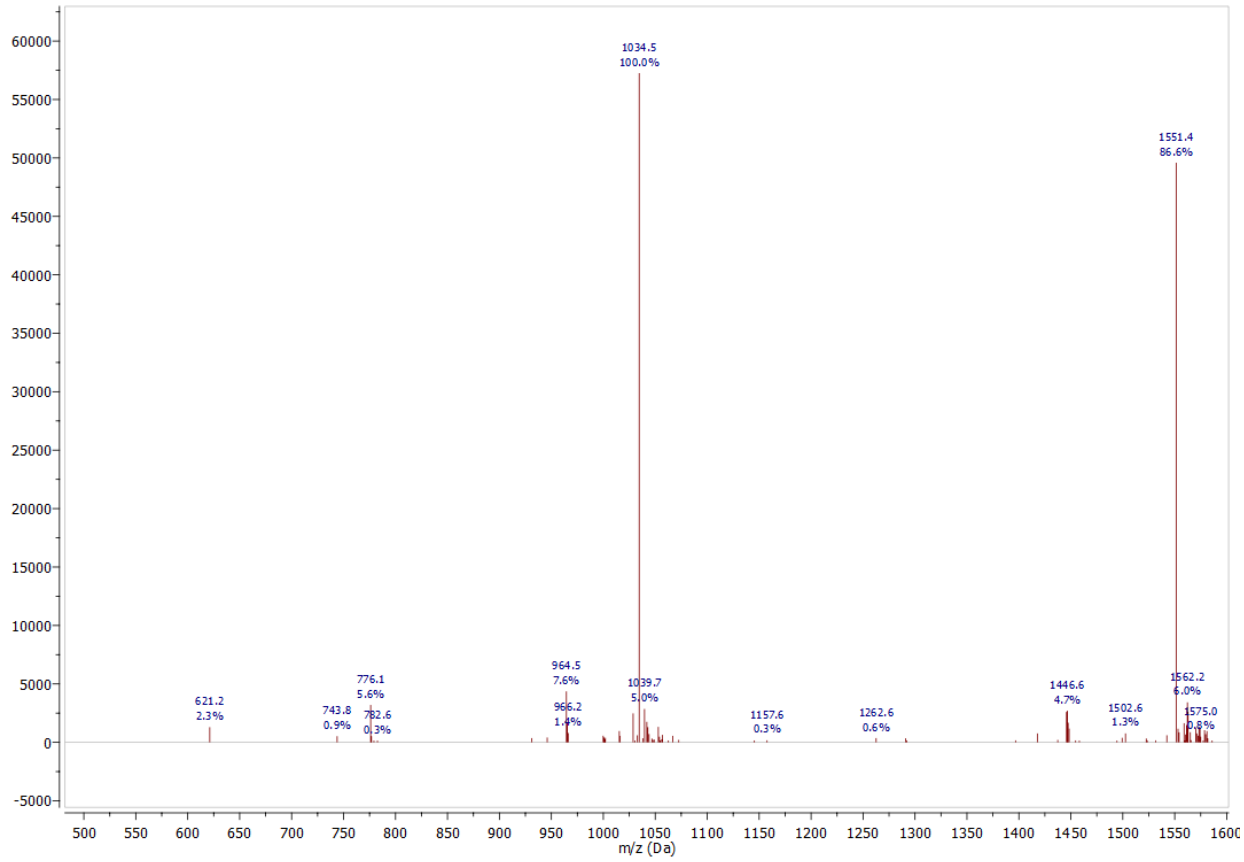

Sample	Sequence	Molecular weight (g/mol)	M+2H Ion	M+3H Ion
Pep 15	**H-CCC(POG)$_8$K(alloc)$_3$-NH$_2$**	**3102.4**	**1552.2**	**1034.8**

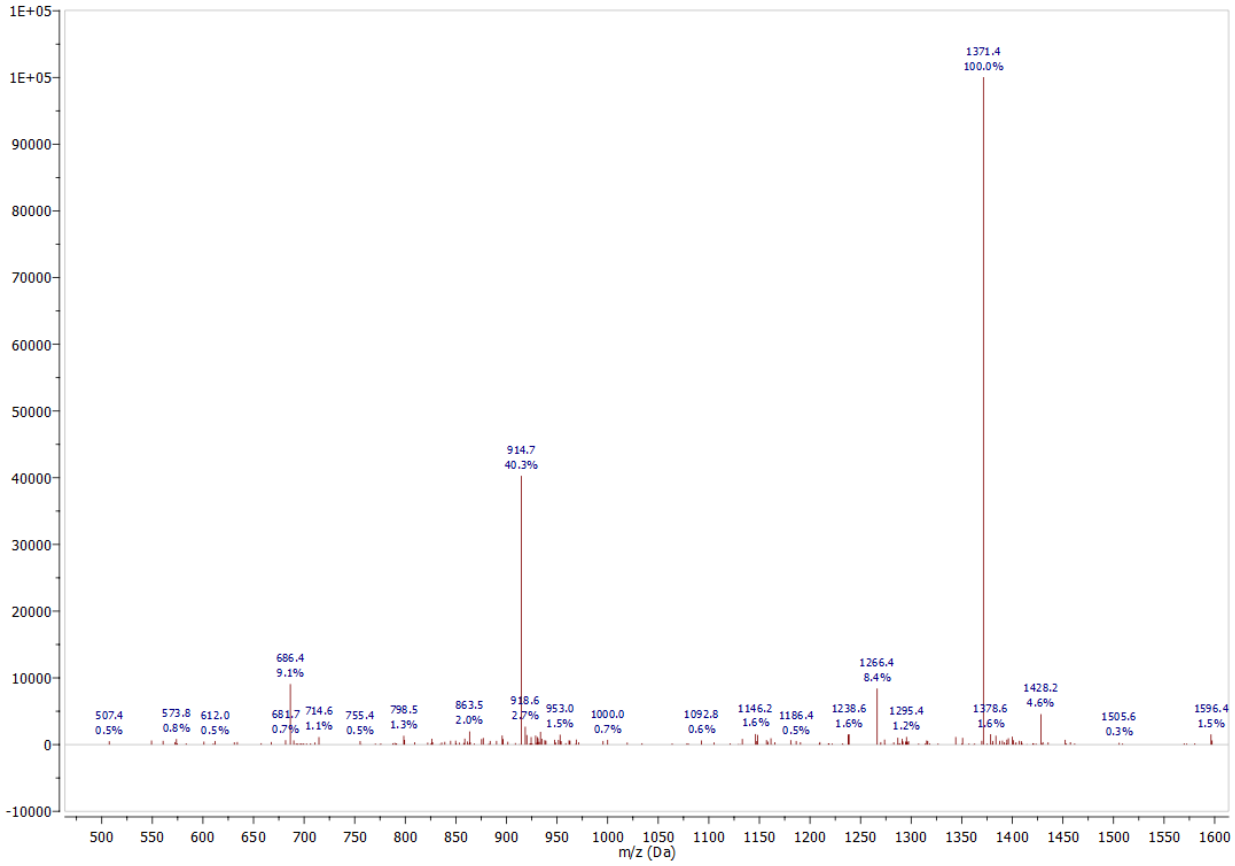

Sample	Sequence	Molecular weight (g/mol)	M+2H Ion	M+3H Ion
Pep 16	H-GCG(POG)$_4$POV(POG)$_3$GK(alloc)G-OH	2741.9	1372.0	914.6

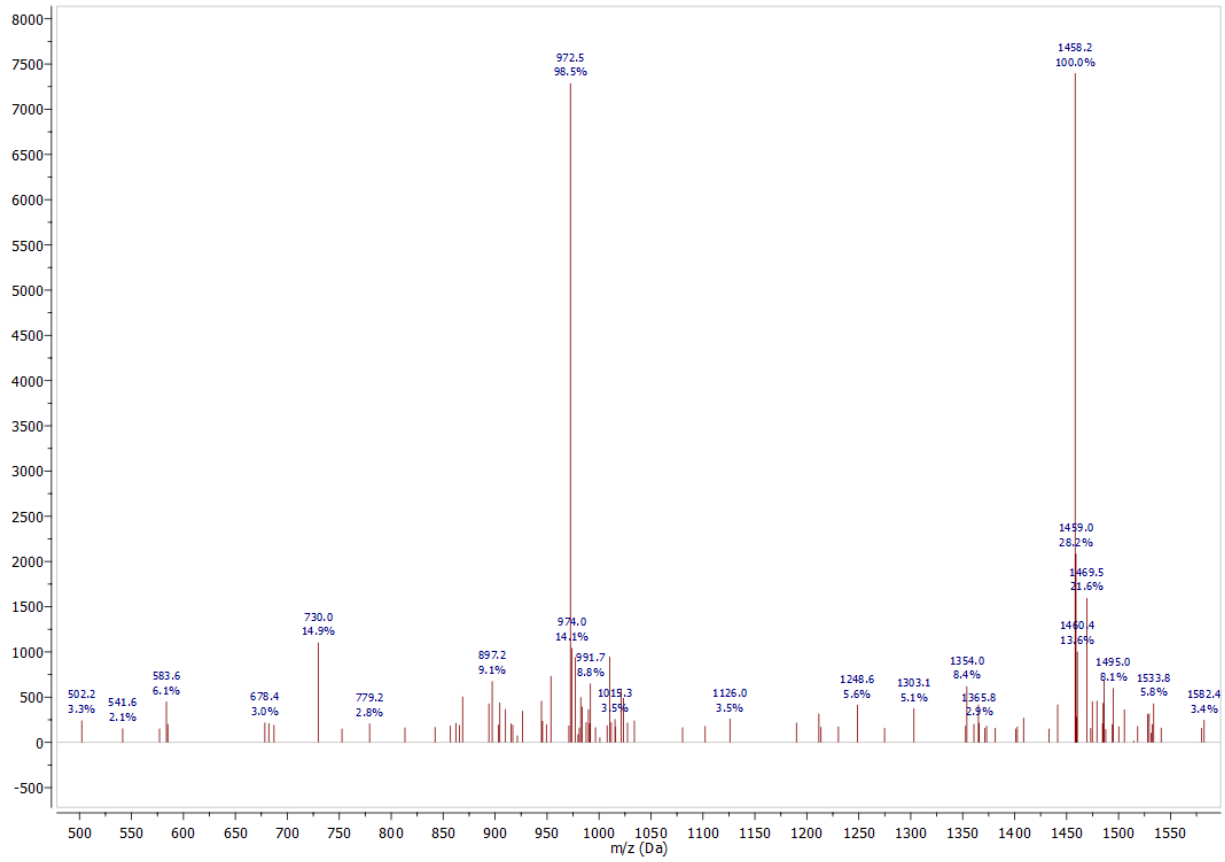

Sample	Sequence	Molecular weight (g/mol)	M+2H Ion	M+3H Ion
Pep 17	**H-CCC(POG)$_8$K(ε-MA)$_2$G-OH**	**2915.2**	**1458.6**	**972.4**

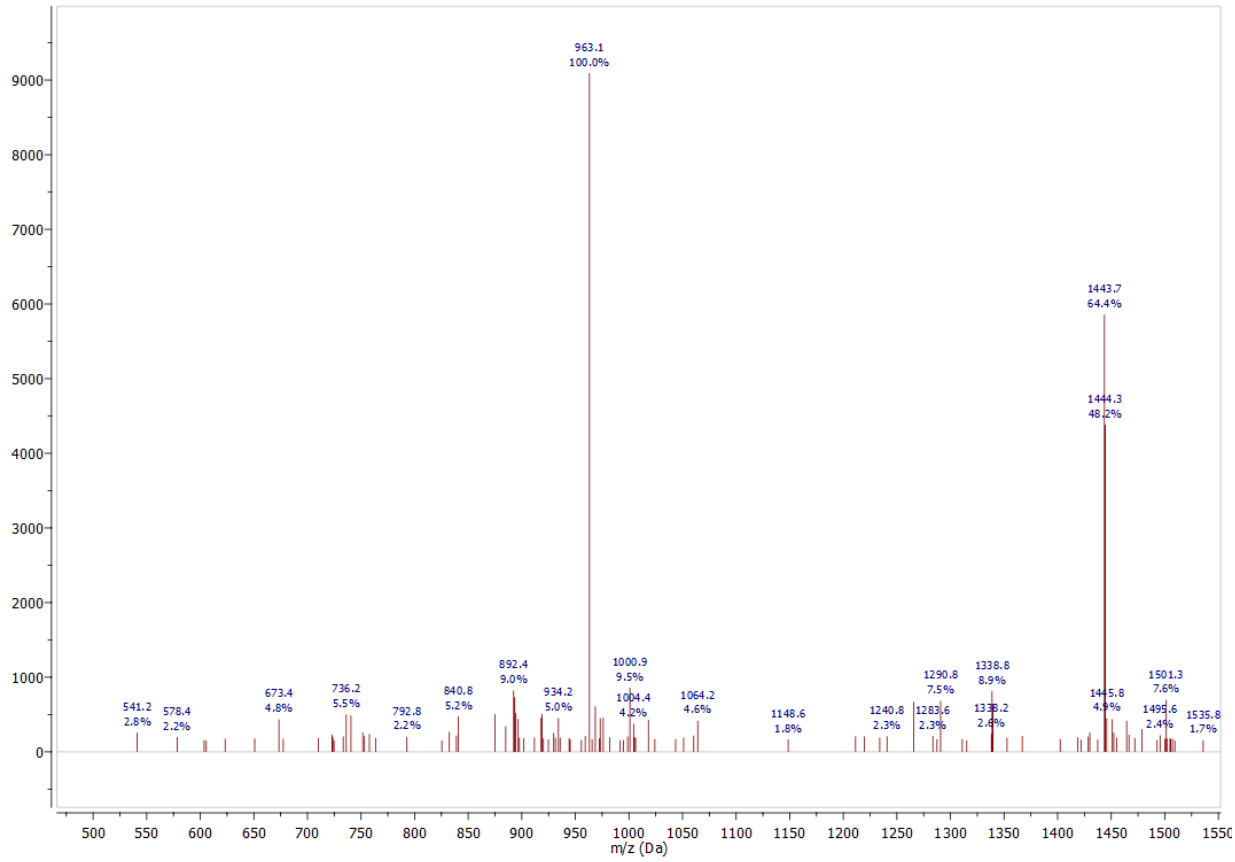

Sample	Sequence	Molecular weight (g/mol)	M+2H Ion	M+3H Ion
Pep 18	**H-CCC(POG)$_8$K(ε-Ac)$_2$G-OH**	**2886.2**	**1444.1**	**962.7**

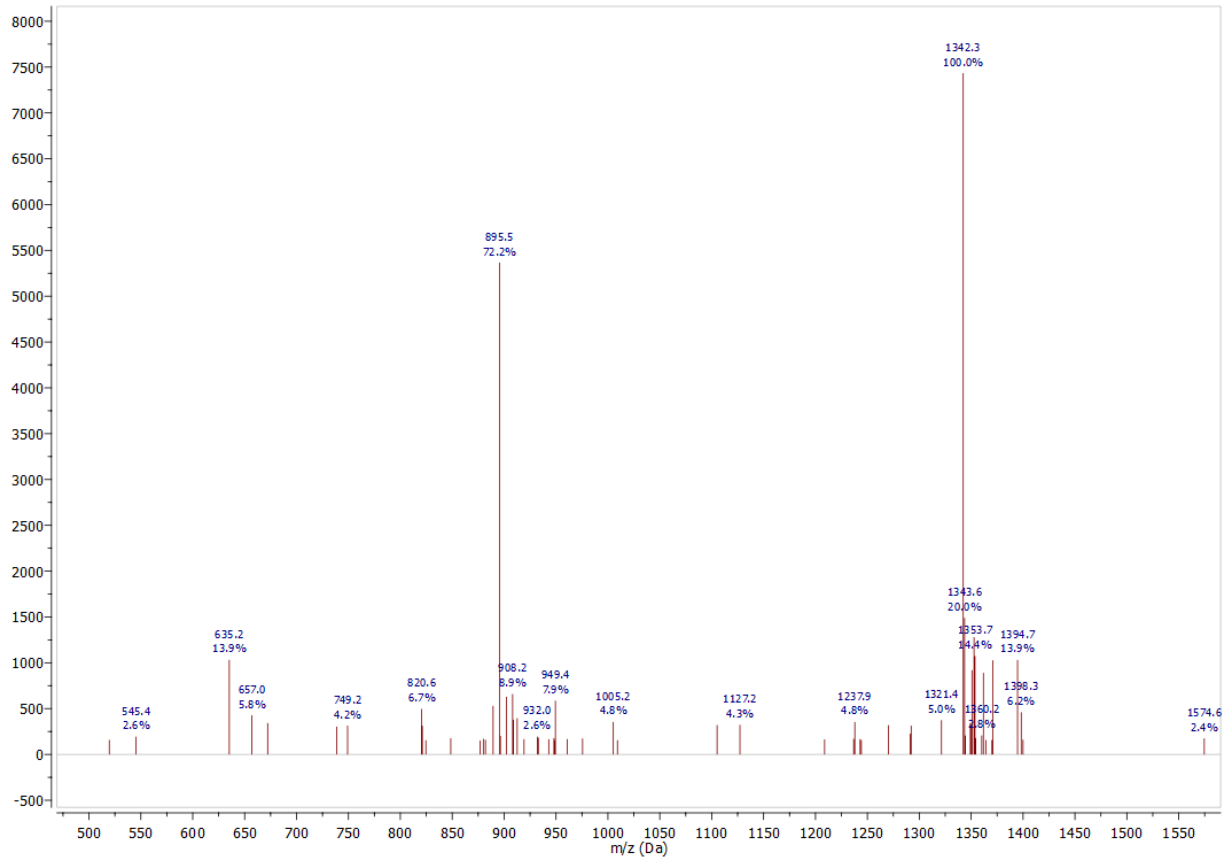

Sample	Sequence	Molecular weight (g/mol)	M+2H Ion	M+3H Ion
Pep 19	**H-GCG(POG)$_8$GK(ε-MA)G-OH**	**2683.9**	**1343.0**	**895.6**

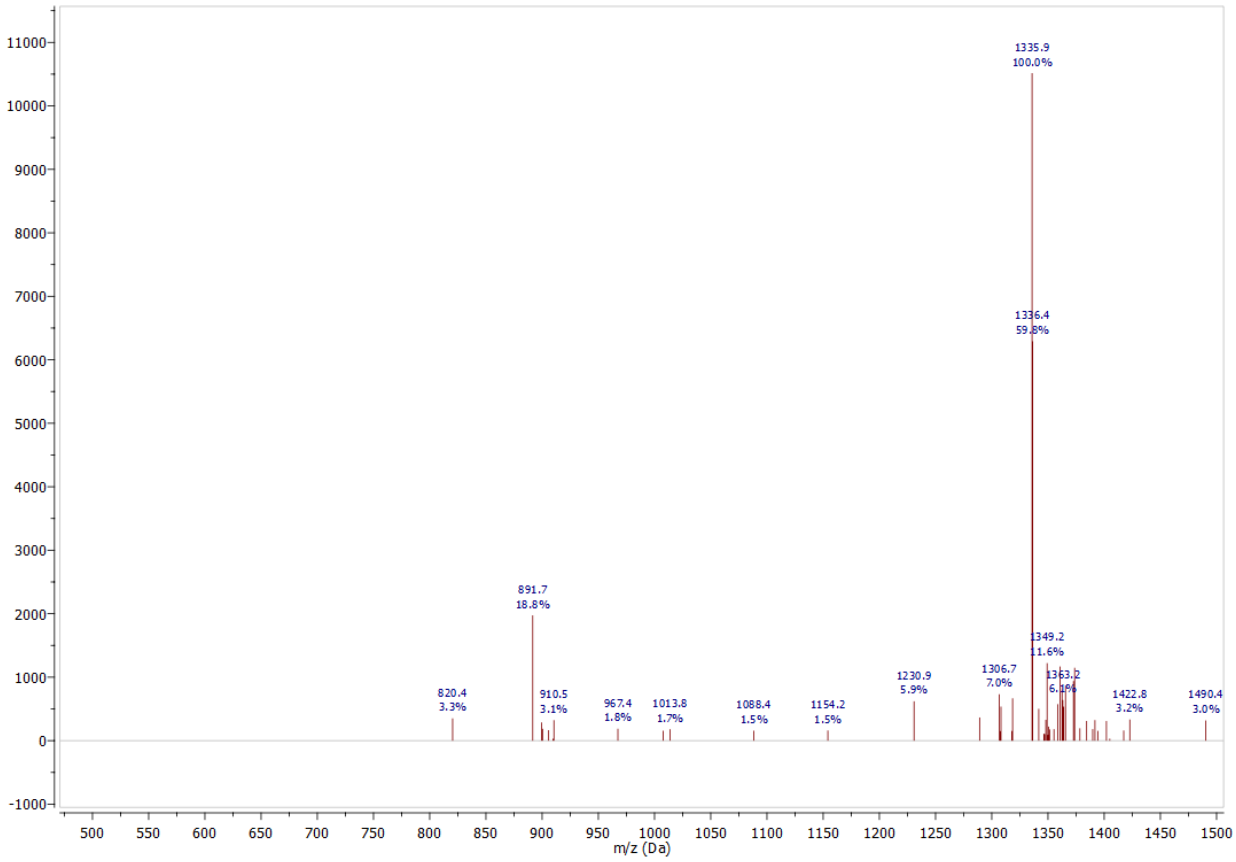

Sample	Sequence	Molecular weight (g/mol)	M+2H Ion	M+3H Ion
Pep 20	**H-GCG(POG)$_8$GK(ε-Ac)G-OH**	**2669.9**	**1336.0**	**890.1**

5.2 Permissions

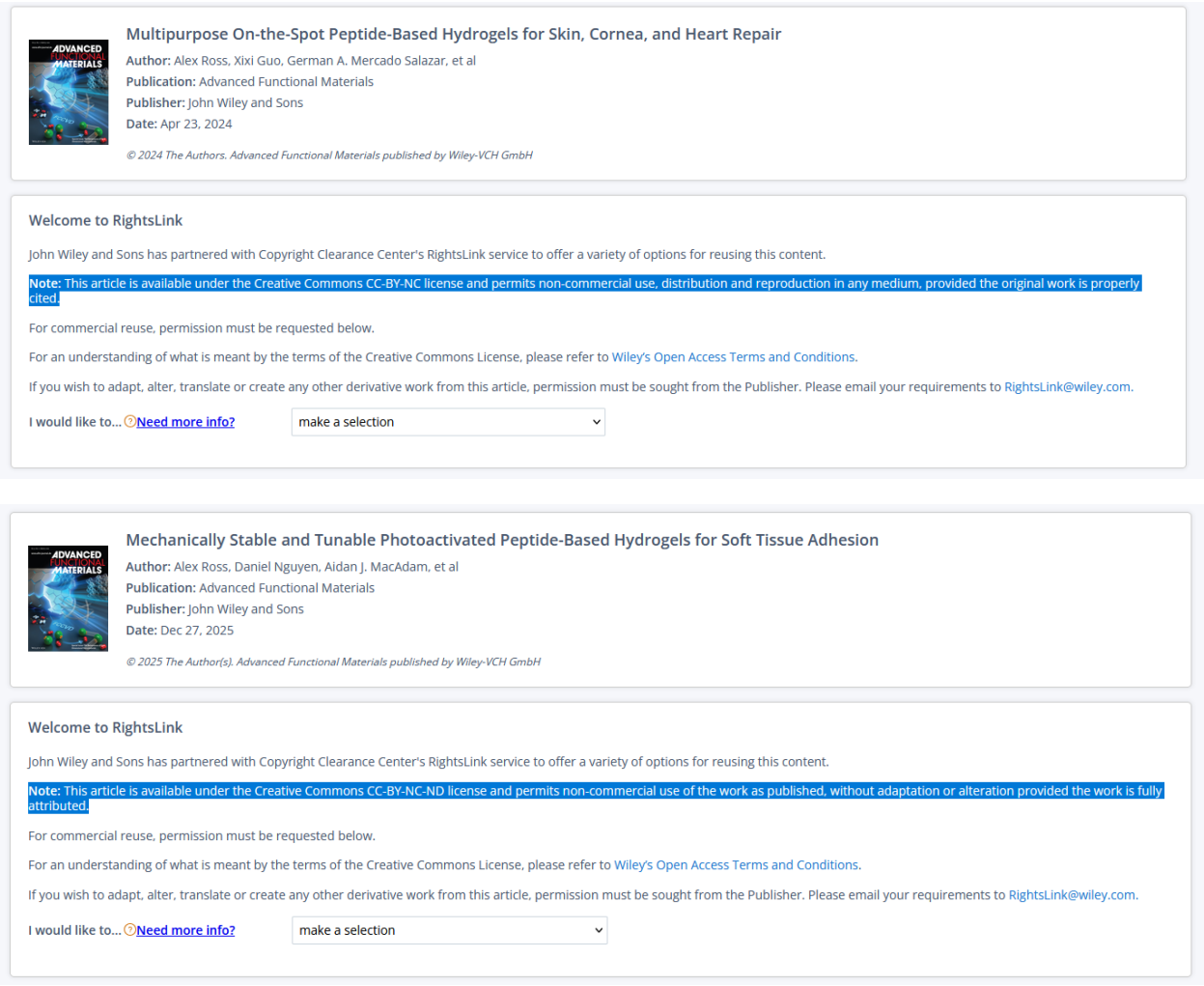

Multipurpose On-the-Spot Peptide-Based Hydrogels for Skin, Cornea, and Heart Repair

Author: Alex Ross, Xixi Guo, German A. Mercado Salazar, et al
Publication: Advanced Functional Materials
Publisher: John Wiley and Sons
Date: Apr 23, 2024

© 2024 The Authors. Advanced Functional Materials published by Wiley-VCH GmbH

Welcome to RightsLink

John Wiley and Sons has partnered with Copyright Clearance Center's RightsLink service to offer a variety of options for reusing this content.

Note: This article is available under the Creative Commons CC-BY-NC license and permits non-commercial use, distribution and reproduction in any medium, provided the original work is properly cited.

For commercial reuse, permission must be requested below.

For an understanding of what is meant by the terms of the Creative Commons License, please refer to Wiley's Open Access Terms and Conditions.

If you wish to adapt, alter, translate or create any other derivative work from this article, permission must be sought from the Publisher. Please email your requirements to RightsLink@wiley.com.

I would like to... Need more info? make a selection

Mechanically Stable and Tunable Photoactivated Peptide-Based Hydrogels for Soft Tissue Adhesion

Author: Alex Ross, Daniel Nguyen, Aidan J. MacAdam, et al
Publication: Advanced Functional Materials
Publisher: John Wiley and Sons
Date: Dec 27, 2025

© 2025 The Author(s). Advanced Functional Materials published by Wiley-VCH GmbH

Welcome to RightsLink

John Wiley and Sons has partnered with Copyright Clearance Center's RightsLink service to offer a variety of options for reusing this content.

Note: This article is available under the Creative Commons CC-BY-NC-ND license and permits non-commercial use of the work as published, without adaptation or alteration provided the work is fully attributed.

For commercial reuse, permission must be requested below.

For an understanding of what is meant by the terms of the Creative Commons License, please refer to Wiley's Open Access Terms and Conditions.

If you wish to adapt, alter, translate or create any other derivative work from this article, permission must be sought from the Publisher. Please email your requirements to RightsLink@wiley.com.

I would like to... Need more info? make a selection

Creative Commons License: https://creativecommons.org/licenses/by-nc/4.0/

6.0 References

1. Pramanik, B.; Islam, M. M.; Patra, H. K., Rational design of peptide-based implants for corneal bioengineering. *Current Opinion in Biotechnology* **2023,** *81*, 102947.
2. Santodomingo-Rubido, J.; Carracedo, G.; Suzaki, A.; Villa-Collar, C.; Vincent, S. J.; Wolffsohn, J. S., Keratoconus: An updated review. *Contact Lens and Anterior Eye* **2022,** *45* (3).
3. Rabinowitz, Y. S., Keratoconus. *Surv Ophthalmol* **1998,** *42* (4), 297-319.
4. Singh, A.; Maurya, O. P.; Jagannadhan, M. V.; Patel, A., Matrix metalloproteinases (MMP-2 and MMP-9) activity in corneal ulcer and ocular surface disorders determined by gelatin zymography. *J Ocul Biol Dis Infor* **2012,** *5* (2), 31-5.
5. Chen, S.; Mienaltowski, M. J.; Birk, D. E., Regulation of corneal stroma extracellular matrix assembly. *Exp Eye Res* **2015,** *133*, 69-80.
6. Meek, K. M.; Holmes, D. F., Interpretation of the electron microscopical appearance of collagen fibrils from corneal stroma. *International Journal of Biological Macromolecules* **1983,** *5* (1), 17-25.
7. Shetty, R.; Ghosh, A.; Lim, R. R.; Subramani, M.; Mihir, K.; Reshma, A. R.; Ranganath, A.; Nagaraj, S.; Nuijts, R. M.; Beuerman, R.; Shetty, R.; Das, D.; Chaurasia, S. S.; Sinha-Roy, A.; Ghosh, A., Elevated expression of matrix metalloproteinase-9 and inflammatory cytokines in keratoconus patients is inhibited by cyclosporine A. *Invest Ophthalmol Vis Sci* **2015,** *56* (2), 738-50.
8. Kim, W. J.; Rabinowitz, Y. S.; Meisler, D. M.; Wilson, S. E., Keratocyte apoptosis associated with keratoconus. *Exp Eye Res* **1999,** *69* (5), 475-81.
9. Edrington, T. B.; Szczotka, L. B.; Barr, J. T.; Achtenberg, J. F.; Burger, D. S.; Janoff, A. M.; Olafsson, H. E.; Chun, M. W.; Boyle, J. W.; Gordon, M. O.; Zadnik, K., Rigid contact lens fitting relationships in keratoconus. Collaborative Longitudinal Evaluation of Keratoconus (CLEK) Study Group. *Optom Vis Sci* **1999,** *76* (10), 692-9.
10. Wittig-Silva, C.; Chan, E.; Islam, F. M.; Wu, T.; Whiting, M.; Snibson, G. R., A randomized, controlled trial of corneal collagen cross-linking in progressive keratoconus: three-year results. *Ophthalmology* **2014,** *121* (4), 812-21.
11. McCall, A. S.; Kraft, S.; Edelhauser, H. F.; Kidder, G. W.; Lundquist, R. R.; Bradshaw, H. E.; Dedeic, Z.; Dionne, M. J.; Clement, E. M.; Conrad, G. W., Mechanisms of corneal tissue cross-linking in response to treatment with topical riboflavin and long-wavelength ultraviolet radiation (UVA). *Invest Ophthalmol Vis Sci* **2010,** *51* (1), 129-38.
12. Subasinghe, S. K.; Ogbuehi, K. C.; Dias, G. J., Current perspectives on corneal collagen crosslinking (CXL). *Graefes Arch Clin Exp Ophthalmol* **2018,** *256* (8), 1363-1384.
13. Chan, C., Corneal Cross-Linking for Keratoconus: Current Knowledge and Practice and Future Trends. *Asia Pac J Ophthalmol (Phila)* **2020,** *9* (6), 557-564.
14. Sen, C. K., Human Wounds and Its Burden: An Updated Compendium of Estimates. *Advances in Wound Care* **2019,** *8* (2), 39-48.
15. desJardins-Park, H. E.; Gurtner, G. C.; Wan, D. C.; Longaker, M. T., From Chronic Wounds to Scarring: The Growing Health Care Burden of Under- and Over-Healing Wounds. *Adv Wound Care (New Rochelle)* **2022,** *11* (9), 496-510.
16. Raja, J. M.; Maturana, M. A.; Kayali, S.; Khouzam, A.; Efeovbokhan, N., Diabetic foot ulcer: A comprehensive review of pathophysiology and management modalities. *World J Clin Cases* **2023,** *11* (8), 1684-1693.

17. Velnar, T.; Bailey, T.; Smrkolj, V., The wound healing process: an overview of the cellular and molecular mechanisms. *J Int Med Res* **2009,** *37* (5), 1528-42.
18. Pastar, I.; Stojadinovic, O.; Yin, N. C.; Ramirez, H.; Nusbaum, A. G.; Sawaya, A.; Patel, S. B.; Khalid, L.; Isseroff, R. R.; Tomic-Canic, M., Epithelialization in Wound Healing: A Comprehensive Review. *Adv Wound Care (New Rochelle)* **2014,** *3* (7), 445-464.
19. Caley, M. P.; Martins, V. L.; O'Toole, E. A., Metalloproteinases and Wound Healing. *Adv Wound Care (New Rochelle)* **2015,** *4* (4), 225-234.
20. Schultz, G. S.; Sibbald, R. G.; Falanga, V.; Ayello, E. A.; Dowsett, C.; Harding, K.; Romanelli, M.; Stacey, M. C.; Teot, L.; Vanscheidt, W., Wound bed preparation: a systematic approach to wound management. *Wound Repair Regen* **2003,** *11 Suppl 1*, S1-28.
21. Shi, C.; Wang, C.; Liu, H.; Li, Q.; Li, R.; Zhang, Y.; Liu, Y.; Shao, Y.; Wang, J., Selection of Appropriate Wound Dressing for Various Wounds. *Frontiers in Bioengineering and Biotechnology* **2020,** *Volume 8 - 2020*.
22. Huang, C.; Leavitt, T.; Bayer, L. R.; Orgill, D. P., Effect of negative pressure wound therapy on wound healing. *Current Problems in Surgery* **2014,** *51* (7), 301-331.
23. Löndahl, M.; Katzman, P.; Nilsson, A.; Hammarlund, C., Hyperbaric Oxygen Therapy Facilitates Healing of Chronic Foot Ulcers in Patients With Diabetes. *Diabetes Care* **2010,** *33* (5), 998-1003.
24. Halim, A. S.; Khoo, T. L.; Mohd Yussof, S. J., Biologic and synthetic skin substitutes: An overview. *Indian J Plast Surg* **2010,** *43* (Suppl), S23-8.
25. Dean, J.; Hoch, C.; Wollenberg, B.; Navidzadeh, J.; Maheta, B.; Mandava, A.; Knoedler, S.; Sherwani, K.; Baecher, H.; Schmitz, A.; Alfertshofer, M.; Heiland, M.; Kreutzer, K.; Koerdt, S.; Knoedler, L., Advancements in bioengineered and autologous skin grafting techniques for skin reconstruction: a comprehensive review. *Frontiers in Bioengineering and Biotechnology* **2025,** *Volume 12 - 2024*.
26. Wynn, T. A., Cellular and molecular mechanisms of fibrosis. *J Pathol* **2008,** *214* (2), 199-210.
27. Li, D. J.; Berry, C. E.; Wan, D. C.; Longaker, M. T., Clinical, mechanistic, and therapeutic landscape of cutaneous fibrosis. *Sci Transl Med* **2024,** *16* (766), eadn7871.
28. Mony, M. P.; Harmon, K. A.; Hess, R.; Dorafshar, A. H.; Shafikhani, S. H., An Updated Review of Hypertrophic Scarring. *Cells* **2023,** *12* (5).
29. Nguyen, A.; Li, R.; Galiano, R., Early Patient-Reported Outcomes as Predictors of Long-Term Scar Satisfaction: An Exploratory Cohort Study. *Wound Repair and Regeneration* **2025,** *33* (5), e70094.
30. Gauglitz, G. G.; Korting, H. C.; Pavicic, T.; Ruzicka, T.; Jeschke, M. G., Hypertrophic scarring and keloids: pathomechanisms and current and emerging treatment strategies. *Mol Med* **2011,** *17* (1-2), 113-25.
31. Gauglitz, G. G., Management of keloids and hypertrophic scars: current and emerging options. *Clin Cosmet Investig Dermatol* **2013,** *6*, 103-14.
32. Jagannathan, R.; Patel, S. A.; Ali, M. K.; Narayan, K. M. V., Global Updates on Cardiovascular Disease Mortality Trends and Attribution of Traditional Risk Factors. *Curr Diab Rep* **2019,** *19* (7), 44.
33. Reed, G. W.; Rossi, J. E.; Cannon, C. P., Acute myocardial infarction. *Lancet (London, England)* **2017,** *389* (10065), 197-210.
34. Saha, T.; Soliman-Aboumarie, H., Review of Current Management of Myocardial Infarction. *J Clin Med* **2025,** *14* (17).

35. Tsutsui, H.; Kinugawa, S.; Matsushima, S., Oxidative stress and heart failure. *Am J Physiol Heart Circ Physiol* **2011,** *301* (6), H2181-90.
36. Peyret, H.; Konecki, C.; Terryn, C.; Dubuisson, F.; Millart, H.; Feliu, C.; Djerada, Z., Methylglyoxal induces cardiac dysfunction through mechanisms involving altered intracellular calcium handling in the rat heart. *Chemico-Biological Interactions* **2024,** *394*, 110949.
37. Lai, S. W. T.; Lopez Gonzalez, E. J.; Zoukari, T.; Ki, P.; Shuck, S. C., Methylglyoxal and Its Adducts: Induction, Repair, and Association with Disease. *Chemical research in toxicology* **2022,** *35* (10), 1720-1746.
38. Prabhu, S. D.; Frangogiannis, N. G., The Biological Basis for Cardiac Repair After Myocardial Infarction: From Inflammation to Fibrosis. *Circ Res* **2016,** *119* (1), 91-112.
39. Bergmann, O.; Bhardwaj, R. D.; Bernard, S.; Zdunek, S.; Barnabé-Heider, F.; Walsh, S.; Zupicich, J.; Alkass, K.; Buchholz, B. A.; Druid, H.; Jovinge, S.; Frisén, J., Evidence for cardiomyocyte renewal in humans. *Science* **2009,** *324* (5923), 98-102.
40. Pfeffer, M. A.; Braunwald, E., Ventricular remodeling after myocardial infarction. Experimental observations and clinical implications. *Circulation* **1990,** *81* (4), 1161-72.
41. Xu, Q.; Xiao, Z.; Yang, Q.; Yu, T.; Deng, X.; Chen, N.; Huang, Y.; Wang, L.; Guo, J.; Wang, J., Hydrogel-based cardiac repair and regeneration function in the treatment of myocardial infarction. *Materials Today Bio* **2024,** *25*, 100978.
42. Khattar, R. S., Effects of ACE-inhibitors and beta-blockers on left ventricular remodeling in chronic heart failure. *Minerva Cardioangiol* **2003,** *51* (2), 143-54.
43. Slaughter Mark, S.; Rogers Joseph, G.; Milano Carmelo, A.; Russell Stuart, D.; Conte John, V.; Feldman, D.; Sun, B.; Tatooles Antone, J.; Delgado Reynolds, M.; Long James, W.; Wozniak Thomas, C.; Ghumman, W.; Farrar David, J.; Frazier, O. H., Advanced Heart Failure Treated with Continuous-Flow Left Ventricular Assist Device. *New England Journal of Medicine 361* (23), 2241-2251.
44. Jou, S.; Mendez, S. R.; Feinman, J.; Mitrani, L. R.; Fuster, V.; Mangiola, M.; Moazami, N.; Gidea, C., Heart transplantation: advances in expanding the donor pool and xenotransplantation. *Nature Reviews Cardiology* **2024,** *21* (1), 25-36.
45. Trachtenberg, B. H.; Cordero-Reyes, A.; Elias, B.; Loebe, M., A review of infections in patients with left ventricular assist devices: prevention, diagnosis and management. *Methodist Debakey Cardiovasc J* **2015,** *11* (1), 28-32.
46. Khush, K. K.; Cherikh, W. S.; Chambers, D. C.; Harhay, M. O.; Hayes, D., Jr.; Hsich, E.; Meiser, B.; Potena, L.; Robinson, A.; Rossano, J. W.; Sadavarte, A.; Singh, T. P.; Zuckermann, A.; Stehlik, J., The International Thoracic Organ Transplant Registry of the International Society for Heart and Lung Transplantation: Thirty-sixth adult heart transplantation report - 2019; focus theme: Donor and recipient size match. *J Heart Lung Transplant* **2019,** *38* (10), 1056-1066.
47. Xu, Y.; Yu, Y.; Guo, Z., Hydrogels in cardiac tissue engineering: application and challenges. *Molecular and cellular biochemistry* **2025,** *480* (4), 2201-2222.
48. Almouemen, N.; Kelly, H. M.; O'Leary, C., Tissue Engineering: Understanding the Role of Biomaterials and Biophysical Forces on Cell Functionality Through Computational and Structural Biotechnology Analytical Methods. *Computational and Structural Biotechnology Journal* **2019,** *17*, 591-598.
49. Silva-López, M. S.; Alcántara-Quintana, L. E., The Era of Biomaterials: Smart Implants? *ACS Applied Bio Materials* **2023,** *6* (8), 2982-2994.

50. Huang, Y.; Ding, Z., Biomaterials for cardiovascular diseases. *Biomedical Technology* **2024,** *7*, 1-14.
51. Tibbitt, M. W.; Dahlman, J. E.; Langer, R., Emerging Frontiers in Drug Delivery. *Journal of the American Chemical Society* **2016,** *138* (3), 704-717.
52. Peppas, N. A.; Van Blarcom, D. S., Hydrogel-based biosensors and sensing devices for drug delivery. *Journal of Controlled Release* **2016,** *240*, 142-150.
53. Wagner, W. R.; Sakiyama-Elbert, S. E.; Zhang, G.; Yaszemski, M. J., *Biomaterials Science*. Elsevier: 2020.
54. Discher, D. E.; Mooney, D. J.; Zandstra, P. W., Growth factors, matrices, and forces combine and control stem cells. *Science* **2009,** *324* (5935), 1673-7.
55. Engler, A. J.; Sen, S.; Sweeney, H. L.; Discher, D. E., Matrix elasticity directs stem cell lineage specification. *Cell* **2006,** *126* (4), 677-89.
56. Dupont, S.; Morsut, L.; Aragona, M.; Enzo, E.; Giulitti, S.; Cordenonsi, M.; Zanconato, F.; Le Digabel, J.; Forcato, M.; Bicciato, S.; Elvassore, N.; Piccolo, S., Role of YAP/TAZ in mechanotransduction. *Nature* **2011,** *474* (7350), 179-183.
57. Handorf, A. M.; Zhou, Y.; Halanski, M. A.; Li, W. J., Tissue stiffness dictates development, homeostasis, and disease progression. *Organogenesis* **2015,** *11* (1), 1-15.
58. Hoffman, A. S., Hydrogels for biomedical applications. *Advanced Drug Delivery Reviews* **2012,** *64*, 18-23.
59. McTiernan, C. D.; Cortes, D. C.; Lazurko, C.; Amrani, S.; Rosales-Rojas, R.; Zuñiga-Bustos, M.; Sedlakova, V.; Poblete, H.; Stamplecoskie, K.; Suuronen, E. J.; Alarcon, E. I., Light-Activated Peptide-Based Materials for Sutureless Wound Closure. *ACS Applied Materials & Interfaces* **2019,** *11* (48), 45007-45015.
60. MacAdam, A. J.; Munoz, M.; Hage, J. E.; Hu, K.; Ross, A.; Chandra, A.; Edwards, J. D.; Shahid, Z.; Mourcos, S.; Comtois-Bona, M. E.; Juarez, A.; Groleau, M.; Dégué, D. S.; Djallali, M.; Piché, M.; Thériault, M.; Grenier, M.; Griffith, M.; Brunette, I.; Alarcon, E. I., Low Energy Blue Pulsed Light-Activated Injectable Materials for Restoring Thinning Corneas. *Advanced Functional Materials* **2023,** *33* (45), 2302721.
61. McLaughlin, S.; McNeill, B.; Podrebarac, J.; Hosoyama, K.; Sedlakova, V.; Cron, G.; Smyth, D.; Seymour, R.; Goel, K.; Liang, W.; Rayner, K. J.; Ruel, M.; Suuronen, E. J.; Alarcon, E. I., Injectable human recombinant collagen matrices limit adverse remodeling and improve cardiac function after myocardial infarction. *Nature Communications* **2019,** *10* (1), 4866.
62. Katona, G.; Sipos, B.; Csóka, I., Advancements in the Field of Protein-Based Hydrogels: Main Types, Characteristics, and Their Applications. *Gels* **2025,** *11* (5).
63. Agrawal, R.; Kumar, A.; Mohammed, M. K. A.; Singh, S., *Biomaterial types, properties, medical applications, and other factors: a recent review*. J. Zhejiang Univ. Sci. A. 2023 Mar 2:1-16. doi: 10.1631/jzus.A2200403.
64. Gaspar-Pintiliescu, A.; Stanciuc, A. M.; Craciunescu, O., Natural composite dressings based on collagen, gelatin and plant bioactive compounds for wound healing: A review. *Int J Biol Macromol* **2019,** *138*, 854-865.
65. Hu, T.; Fang, J.; Shen, Y.; Li, M.; Wang, B.; Xu, Z.; Hu, W., Advances of naturally derived biomedical polymers in tissue engineering. *Frontiers in Chemistry* **2024,** *Volume 12 - 2024*.
66. Kantak, M. N.; Bharate, S. S., Analysis of clinical trials on biomaterial and therapeutic applications of chitosan: A review. *Carbohydr. Polym.* **2022,** *278*, 118999.

67. Bhat, S.; Kumar, A., Biomaterials and bioengineering tomorrow's healthcare. *Biomatter* **2013,** *3* (3).
68. Zhang, W.; Chen, L.; Chen, J.; Wang, L.; Gui, X.; Ran, J.; Xu, G.; Zhao, H.; Zeng, M.; Ji, J.; Qian, L.; Zhou, J.; Ouyang, H.; Zou, X., Silk Fibroin Biomaterial Shows Safe and Effective Wound Healing in Animal Models and a Randomized Controlled Clinical Trial. *Adv. Healthc. Mater.* **2017,** *6* (10), 1700121.
69. Spotnitz, W. D., Fibrin Sealant: The Only Approved Hemostat, Sealant, and Adhesive—a Laboratory and Clinical Perspective. *ISRN Surg.* **2014,** *2014*, 203943.
70. Roberts, I. V.; Bukhary, D.; Valdivieso, C. Y. L.; Tirelli, N., Fibrin Matrices as (Injectable) Biomaterials: Formation, Clinical Use, and Molecular Engineering. *Macromol. Biosci.* **2020,** *20* (1), 1900283.
71. Willerth, S. M.; Sakiyama-Elbert, S. E., Combining stem cells and biomaterial scaffolds for constructing tissues and cell delivery. In *StemBook*, Harvard Stem Cell Institute

72. Troy, E.; Tilbury, M. A.; Power, A. M.; Wall, J. G., Nature-Based Biomaterials and Their Application in Biomedicine. *Polymers (Basel)* **2021,** *13* (19).
73. Liu, S.; Yu, J.-M.; Gan, Y.-C.; Qiu, X.-Z.; Gao, Z.-C.; Wang, H.; Chen, S.-X.; Xiong, Y.; Liu, G.-H.; Lin, S.-E.; McCarthy, A.; John, J. V.; Wei, D.-X.; Hou, H.-H., Biomimetic natural biomaterials for tissue engineering and regenerative medicine: new biosynthesis methods, recent advances, and emerging applications. *Military Medical Research* **2023,** *10* (1), 16.
74. Singh, G.; Chanda, A., Mechanical properties of whole-body soft human tissues: a review. *Biomedical materials (Bristol, England)* **2021,** *16* (6).
75. Ganewatta, M. S.; Wang, Z.; Tang, C., Chemical syntheses of bioinspired and biomimetic polymers toward biobased materials. *Nature reviews. Chemistry* **2021,** *5* (11), 753-772.
76. Reddy, M. S. B.; Ponnamma, D.; Choudhary, R.; Sadasivuni, K. K., A Comparative Review of Natural and Synthetic Biopolymer Composite Scaffolds. *Polymers* **2021,** *13* (7).
77. Zhu, J., Bioactive modification of poly(ethylene glycol) hydrogels for tissue engineering. *Biomaterials* **2010,** *31* (17), 4639-4656.
78. Hamley, I. W., Small Bioactive Peptides for Biomaterials Design and Therapeutics. *Chemical Reviews* **2017,** *117* (24), 14015-14041.
79. Caplan, M. R.; Schwartzfarb, E. M.; Zhang, S.; Kamm, R. D.; Lauffenburger, D. A., Control of self-assembling oligopeptide matrix formation through systematic variation of amino acid sequence. *Biomaterials* **2002,** *23* (1), 219-27.
80. Elsawy, M. A.; Wychowaniec, J. K.; Castillo Díaz, L. A.; Smith, A. M.; Miller, A. F.; Saiani, A., Controlling Doxorubicin Release from a Peptide Hydrogel through Fine-Tuning of Drug–Peptide Fiber Interactions. *Biomacromolecules* **2022,** *23* (6), 2624-2634.
81. Merrifield, R. B., Solid Phase Peptide Synthesis. I. The Synthesis of a Tetrapeptide. *J. Am. Chem. Soc.* **1963,** *85* (14), 2149-2154.
82. Harel, O.; Jbara, M., Chemical Synthesis of Bioactive Proteins. *Angewandte Chemie International Edition* **2023,** *62* (13), e202217716.
83. Rozans, S. J.; Moghaddam, A. S.; Wu, Y.; Atanasoff, K.; Nino, L.; Dunne, K.; Pashuck, E. T., Quantifying and Controlling the Proteolytic Degradation of Cell Adhesion Peptides. *ACS Biomaterials Science & Engineering* **2024,** *10* (8), 4916-4926.
84. Mehdizadeh, M.; Yang, J., Design strategies and applications of tissue bioadhesives. *Macromol Biosci* **2013,** *13* (3), 271-88.

85. Shoulders, M. D.; Raines, R. T., Collagen structure and stability. *Annual review of biochemistry* **2009,** *78*, 929-58.
86. Ross, A.; Guo, X.; Salazar, G. A. M.; Schejtman, S. D. G.; El-Hage, J.; Comtois-Bona, M.; Macadam, A.; Guzman-Soto, I.; Takaya, H.; Hu, K.; Liu, B.; Tu, R.; Siddiqi, B.; Anderson, E.; Muñoz, M.; Briones-Rebolledo, P.; Ning, T.; Griffith, M.; Rotsein, B.; Poblete, H.; Li, J.; Ruel, M.; Suuronen, E. J.; Alarcon, E. I., Multipurpose On-the-Spot Peptide-Based Hydrogels for Skin, Cornea, and Heart Repair. *Advanced Functional Materials* **2024,** *34* (37), 2402564.
87. Stahl, P. J.; Romano, N. H.; Wirtz, D.; Yu, S. M., PEG-based hydrogels with collagen mimetic peptide-mediated and tunable physical cross-links. *Biomacromolecules* **2010,** *11* (9), 2336-44.
88. Jangamreddy, J. R.; Haagdorens, M. K. C.; Mirazul Islam, M.; Lewis, P.; Samanta, A.; Fagerholm, P.; Liszka, A.; Ljunggren, M. K.; Buznyk, O.; Alarcon, E. I.; Zakaria, N.; Meek, K. M.; Griffith, M., Short peptide analogs as alternatives to collagen in pro-regenerative corneal implants. *Acta biomaterialia* **2018,** *69*, 120-130.
89. Ricard-Blum, S., The collagen family. *Cold Spring Harb Perspect Biol* **2011,** *3* (1), a004978.
90. Gelse, K.; Pöschl, E.; Aigner, T., Collagens—structure, function, and biosynthesis. *Advanced Drug Delivery Reviews* **2003,** *55* (12), 1531-1546.
91. Khare, E.; Yu, C.-H.; Gonzalez Obeso, C.; Milazzo, M.; Kaplan, D. L.; Buehler, M. J., Discovering design principles of collagen molecular stability using a genetic algorithm, deep learning, and experimental validation. *Proceedings of the National Academy of Sciences* **2022,** *119* (40), e2209524119.
92. Sorushanova, A.; Delgado, L. M.; Wu, Z.; Shologu, N.; Kshirsagar, A.; Raghunath, R.; Mullen, A. M.; Bayon, Y.; Pandit, A.; Raghunath, M.; Zeugolis, D. I., The Collagen Suprafamily: From Biosynthesis to Advanced Biomaterial Development. *Advanced materials (Deerfield Beach, Fla.)* **2019,** *31* (1), e1801651.
93. Engel, J.; Bächinger, H. P., Cooperative equilibrium transitions coupled with a slow annealing step explain the sharpness and hysteresis of collagen folding. *Matrix Biol* **2000,** *19* (3), 235-44.
94. Luo, T.; Kiick, K. L., Collagen-like peptides and peptide-polymer conjugates in the design of assembled materials. *Eur Polym J* **2013,** *49* (10), 2998-3009.
95. Koide, T., Designed triple-helical peptides as tools for collagen biochemistry and matrix engineering. *Philos Trans R Soc Lond B Biol Sci* **2007,** *362* (1484), 1281-91.
96. Qi, Y.; Zhou, D.; Kessler, J. L.; Qiu, R.; Yu, S. M.; Li, G.; Qin, Z.; Li, Y., Terminal repeats impact collagen triple-helix stability through hydrogen bonding. *Chemical Science* **2022,** *13* (42), 12567-12576.
97. Persikov, A. V.; Ramshaw, J. A.; Brodsky, B., Prediction of collagen stability from amino acid sequence. *J Biol Chem* **2005,** *280* (19), 19343-9.
98. Huang, C.; Chen, R.; Ke, Q.; Morsi, Y.; Zhang, K.; Mo, X., Electrospun collagen-chitosan-TPU nanofibrous scaffolds for tissue engineered tubular grafts. *Colloids and surfaces. B, Biointerfaces* **2011,** *82* (2), 307-15.
99. Pupkaite, J.; Ahumada, M.; McLaughlin, S.; Temkit, M.; Alaziz, S.; Seymour, R.; Ruel, M.; Kochevar, I.; Griffith, M.; Suuronen, E. J.; Alarcon, E. I., Collagen-Based Photoactive Agent for Tissue Bonding. *ACS Applied Materials & Interfaces* **2017,** *9* (11), 9265-9270.

100. K. S. Silvipriya, K. K. K., A. R. Bhat, B. Dinesh Kumar, Anish John, Panayappan lakshmanan, *Collagen: Animal Sources and Biomedical Application*. Issue: 3: 2015; Vol. Volume: 5, p 123-127.
101. Chattopadhyay, S.; Raines, R. T., Review collagen-based biomaterials for wound healing. *Biopolymers* **2014,** *101* (8), 821-33.
102. Wang, L.; Wang, N.; Zhang, W.; Cheng, X.; Yan, Z.; Shao, G.; Wang, X.; Wang, R.; Fu, C., Therapeutic peptides: current applications and future directions. *Signal Transduction and Targeted Therapy* **2022,** *7* (1), 48.
103. Wang, Y.; Naleway, S. E.; Wang, B., Biological and bioinspired materials: Structure leading to functional and mechanical performance. *Bioactive Materials* **2020,** *5* (4), 745-757.
104. Hollister, S. J., Porous scaffold design for tissue engineering. *Nature Materials* **2005,** *4* (7), 518-524.
105. Wang, L.; Wang, C.; Wu, S.; Fan, Y.; Li, X., Influence of the mechanical properties of biomaterials on degradability, cell behaviors and signaling pathways: current progress and challenges. *Biomaterials Science* **2020,** *8* (10), 2714-2733.
106. O'Brien, F. J., Biomaterials & scaffolds for tissue engineering. *Materials Today* **2011,** *14* (3), 88-95.
107. Verbakel, J.; de Boer, J., Engineering stem cell metabolism using biomaterial-induced mechanotransduction. *Cell Biomaterials* **2025,** *1* (10).
108. Hersel, U.; Dahmen, C.; Kessler, H., RGD modified polymers: biomaterials for stimulated cell adhesion and beyond. *Biomaterials* **2003,** *24* (24), 4385-415.
109. Hulshof, F. F. B.; Papenburg, B.; Vasilevich, A.; Hulsman, M.; Zhao, Y.; Levers, M.; Fekete, N.; de Boer, M.; Yuan, H.; Singh, S.; Beijer, N.; Bray, M.-A.; Logan, D. J.; Reinders, M.; Carpenter, A. E.; van Blitterswijk, C.; Stamatialis, D.; de Boer, J., Mining for osteogenic surface topographies: In silico design to in vivo osseo-integration. *Biomaterials* **2017,** *137*, 49-60.
110. Hao, L.; Fu, X.; Li, T.; Zhao, N.; Shi, X.; Cui, F.; Du, C.; Wang, Y., Surface chemistry from wettability and charge for the control of mesenchymal stem cell fate through self-assembled monolayers. *Colloids and Surfaces B: Biointerfaces* **2016,** *148*, 549-556.
111. Meissner, S.; Raos, B.; Svirskis, D., Hydrogels can control the presentation of growth factors and thereby improve their efficacy in tissue engineering. *European Journal of Pharmaceutics and Biopharmaceutics* **2022,** *181*, 1-21.
112. Yang, J.; Jacobsen, M. T.; Pan, H.; Kopecek, J., Synthesis and characterization of enzymatically degradable PEG-based peptide-containing hydrogels. *Macromol Biosci* **2010,** *10* (4), 445-54.
113. Lu, Y.; Wu, Y. S.; Chen, D. S.; Wang, M. M.; Wang, W. Z.; Yuan, W. J., Microinjection of salusin-beta into the nucleus tractus solitarii inhibits cardiovascular function by suppressing presympathetic neurons in rostral ventrolateral medulla in rats. *Physiological research* **2015,** *64* (2), 161-71.
114. Annabi, N.; Rana, D.; Shirzaei Sani, E.; Portillo-Lara, R.; Gifford, J. L.; Fares, M. M.; Mithieux, S. M.; Weiss, A. S., Engineering a sprayable and elastic hydrogel adhesive with antimicrobial properties for wound healing. *Biomaterials* **2017,** *139*, 229-243.
115. Qu, J.; Zhao, X.; Liang, Y.; Zhang, T.; Ma, P. X.; Guo, B., Antibacterial adhesive injectable hydrogels with rapid self-healing, extensibility and compressibility as wound dressing for joints skin wound healing. *Biomaterials* **2018,** *183*, 185-199.

116. Matsuo, A. L.; Tanaka, A. S.; Juliano, M. A.; Rodrigues, E. G.; Travassos, L. R., A novel melanoma-targeting peptide screened by phage display exhibits antitumor activity. *Journal of molecular medicine (Berlin, Germany)* **2010,** *88* (12), 1255-64.
117. Almansour, N. M.; Pirogova, E.; Coloe, P. J.; Cosic, I.; Istivan, T. S., A bioactive peptide analogue for myxoma virus protein with a targeted cytotoxicity for human skin cancer in vitro. *Journal of biomedical science* **2012,** *19* (1), 65.
118. Hamsici, S.; Cinar, G.; Celebioglu, A.; Uyar, T.; Tekinay, A. B.; Guler, M. O., Bioactive peptide functionalized aligned cyclodextrin nanofibers for neurite outgrowth. *Journal of Materials Chemistry B* **2017,** *5* (3), 517-524.
119. Cavanaugh, M.; Silantyeva, E.; Pylypiv Koh, G.; Malekzadeh, E.; Lanzinger, W. D.; Willits, R. K.; Becker, M. L., RGD-Modified Nanofibers Enhance Outcomes in Rats after Sciatic Nerve Injury. *Journal of functional biomaterials* **2019,** *10* (2).
120. Nam, G. H.; Jo, K.-J.; Park, Y.-S.; Kawk, H. W.; Yoo, J.-G.; Jang, J. D.; Kang, S. M.; Kim, S.-Y.; Kim, Y.-M., The peptide AC 2 isolated from Bacillus-treated Trapa japonica fruit extract rescues DHT (dihydrotestosterone)-treated human dermal papilla cells and mediates mTORC1 signaling for autophagy and apoptosis suppression. *Scientific Reports* **2019,** *9* (1), 16903.
121. Wei, L.; Chen, J.; Zhao, S.; Ding, J.; Chen, X., Thermo-sensitive polypeptide hydrogel for locally sequential delivery of two-pronged antitumor drugs. *Acta biomaterialia* **2017,** *58*, 44-53.
122. Chen, C.; Su, X.; Hu, Z., Immune promotive effect of bioactive peptides may be mediated by regulating the expression of SOCS1/miR-155. *Experimental and therapeutic medicine* **2019,** *18* (3), 1850-1862.
123. Wang, L.; Cheng, N.; Wang, P.; Li, J.; Jia, A.; Li, W.; Zhang, N.; Yin, Y.; Tong, L.; Wei, Q.; Liu, G.; Li, Z.; Luo, J., A novel peptide exerts potent immunosuppression by blocking the two-site interaction of NFAT with calcineurin. *J Biol Chem* **2020,** *295* (9), 2760-2770.
124. Ross, A.; Sauce-Guevara, M. A.; Alarcon, E. I.; Mendez-Rojas, M. A., Peptide Biomaterials for Tissue Regeneration. *Frontiers in Bioengineering and Biotechnology* **2022,** *Volume 10 - 2022*.
125. Holmes, C.; Tabrizian, M., Chapter 14 - Surface Functionalization of Biomaterials. In *Stem Cell Biology and Tissue Engineering in Dental Sciences*, Vishwakarma, A.; Sharpe, P.; Shi, S.; Ramalingam, M., Eds. Academic Press: Boston, 2015; pp 187-206.
126. Shen, Z.; Ma, J.; Cai, Y.; Li, S.; Ruan, D.; Dai, S.; Sheng, Z.; Bai, J.; Yin, D.; Ping, J.; Ying, Y.; Yang, C.; Qu, S.; Jia, Z., Low-water-content polyelectrolyte hydrogels inspired by human epidermal stratum corneum. *Cell Reports Physical Science* **2023,** *4* (12), 101741.
127. Choi, H.; Choi, W. S.; Jeong, J. O., A Review of Advanced Hydrogel Applications for Tissue Engineering and Drug Delivery Systems as Biomaterials. *Gels* **2024,** *10* (11).
128. Hu, X.; Liao, M.; Gong, H.; Zhang, L.; Cox, H.; Waigh, T. A.; Lu, J. R., Recent advances in short peptide self-assembly: from rational design to novel applications. *Current Opinion in Colloid & Interface Science* **2020,** *45*, 1-13.
129. Gelain, F.; Luo, Z.; Rioult, M.; Zhang, S., Self-assembling peptide scaffolds in the clinic. *npj Regenerative Medicine* **2021,** *6* (1), 9.
130. Dodero, A.; Scarfi, S.; Mirata, S.; Sionkowska, A.; Vicini, S.; Alloisio, M.; Castellano, M., Effect of Crosslinking Type on the Physical-Chemical Properties and Biocompatibility of Chitosan-Based Electrospun Membranes. *Polymers (Basel)* **2021,** *13* (5).

131. Li, Z.; Huang, J.; Jiang, Y.; Liu, Y.; Qu, G.; Chen, K.; Zhao, Y.; Wang, P.; Wu, X.; Ren, J., Novel Temperature-Sensitive Hydrogel Promotes Wound Healing Through YAP and MEK-Mediated Mechanosensitivity. *Advanced healthcare materials* **2022,** *11* (23), e2201878.
132. Rusu, A. G.; Nita, L. E.; Simionescu, N.; Ghilan, A.; Chiriac, A. P.; Mititelu-Tartau, L., Enzymatically-Crosslinked Gelatin Hydrogels with Nanostructured Architecture and Self-Healing Performance for Potential Use as Wound Dressings. *Polymers* **2023,** *15* (3).
133. Loessner, D.; Meinert, C.; Kaemmerer, E.; Martine, L. C.; Yue, K.; Levett, P. A.; Klein, T. J.; Melchels, F. P. W.; Khademhosseini, A.; Hutmacher, D. W., Functionalization, preparation and use of cell-laden gelatin methacryloyl–based hydrogels as modular tissue culture platforms. *Nature Protocols* **2016,** *11* (4), 727-746.
134. Shirzaei Sani, E.; Kheirkhah, A.; Rana, D.; Sun, Z.; Foulsham, W.; Sheikhi, A.; Khademhosseini, A.; Dana, R.; Annabi, N., Sutureless repair of corneal injuries using naturally derived bioadhesive hydrogels. *Sci Adv* **2019,** *5* (3), eaav1281.
135. Zhao, X.; Sun, X.; Yildirimer, L.; Lang, Q.; Lin, Z. Y. W.; Zheng, R.; Zhang, Y.; Cui, W.; Annabi, N.; Khademhosseini, A., Cell infiltrative hydrogel fibrous scaffolds for accelerated wound healing. *Acta biomaterialia* **2017,** *49*, 66-77.
136. Sabnis, A.; Rahimi, M.; Chapman, C.; Nguyen, K. T., Cytocompatibility studies of an in situ photopolymerized thermoresponsive hydrogel nanoparticle system using human aortic smooth muscle cells. *Journal of biomedical materials research. Part A* **2009,** *91* (1), 52-9.
137. Cao, H.; Duan, L.; Zhang, Y.; Cao, J.; Zhang, K., Current hydrogel advances in physicochemical and biological response-driven biomedical application diversity. *Signal Transduction and Targeted Therapy* **2021,** *6* (1), 426.
138. Ansari, A.; Bhowmik, S.; Zhang, K.; Reeves, C. L.; Vahala, D.; Choi, Y. S.; Gelmi, A.; Combes, A. N.; Tuan, R. S.; Truong, V. X.; Forsythe, J. S.; Frith, J. E., A Visible Light-Responsive Hydrogel to Study the Effect of Dynamic Tissue Stiffness on Cellular Mechanosensing. *Advanced Functional Materials* **2025,** *n/a* (n/a), 2501585.
139. Kocak, F. Z.; Yar, M.; Rehman, I. U., In vitro degradation, swelling, and bioactivity performances of in situ forming injectable chitosan-matrixed hydrogels for bone regeneration and drug delivery. *Biotechnology and Bioengineering* **2024,** *121* (9), 2767-2779.
140. Mukasheva, F.; Adilova, L.; Dyussenbinov, A.; Yernaimanova, B.; Abilev, M.; Akilbekova, D., Optimizing scaffold pore size for tissue engineering: insights across various tissue types. *Front Bioeng Biotechnol* **2024,** *12*, 1444986.
141. Ebrahimi, M., Porosity parameters in biomaterial science: Definition, impact, and challenges in tissue engineering. *Frontiers of Materials Science* **2021,** *15* (3), 352-373.
142. Offeddu, G. S.; Axpe, E.; Harley, B. A. C.; Oyen, M. L., Relationship between permeability and diffusivity in polyethylene glycol hydrogels. *AIP advances* **2018,** *8* (10), 105006.
143. Ballesteros-Cillero, R.; Davison-Kotler, E.; Kohli, N.; Marshall, W. S.; García-Gareta, E., Biomimetic In Vitro Model of Cell Infiltration into Skin Scaffolds for Pre-Screening and Testing of Biomaterial-Based Therapies. *Cells* **2019,** *8* (8).
144. Ahearne, M.; Fernández-Pérez, J.; Masterton, S.; Madden, P. W.; Bhattacharjee, P., Designing Scaffolds for Corneal Regeneration. *Advanced Functional Materials* **2020,** *30* (44), 1908996.
145. Rafat, M.; Jabbarvand, M.; Sharma, N.; Xeroudaki, M.; Tabe, S.; Omrani, R.; Thangavelu, M.; Mukwaya, A.; Fagerholm, P.; Lennikov, A.; Askarizadeh, F.; Lagali, N., Bioengineered corneal tissue for minimally invasive vision restoration in advanced keratoconus in two clinical cohorts. *Nature Biotechnology* **2023,** *41* (1), 70-81.

146. Ross, A.; Nguyen, D.; MacAdam, A. J.; Salazar, G. A. M.; Gianetti, M.; Ileri, R.; Ruel, M.; Suuronen, E. J.; Alarcon, E. I., Mechanically Stable and Tunable Photoactivated Peptide-Based Hydrogels for Soft Tissue Adhesion. *Advanced Functional Materials* **2025,** *n/a* (n/a), e29084.
147. McTiernan, C. D.; Simpson, F. C.; Haagdorens, M.; Samarawickrama, C.; Hunter, D.; Buznyk, O.; Fagerholm, P.; Ljunggren, M. K.; Lewis, P.; Pintelon, I.; Olsen, D.; Edin, E.; Groleau, M.; Allan, B. D.; Griffith, M., LiQD Cornea: Pro-regeneration collagen mimetics as patches and alternatives to corneal transplantation. *Science Advances 6* (25), eaba2187.
148. Juarez, A.; Djallali, M.; Piché, M.; Thériault, M.; Groleau, M.; Beroual, S.; McTiernan, C. D.; Lin, G.; Hélie, P.; Carrier, M.; Griffith, M.; Brunette, I., A Liquid Hydrogel to Restore Long Term Corneal Integrity After Perforating and Non-Perforating Trauma in Feline Eyes. *Frontiers in Bioengineering and Biotechnology* **2021,** *Volume 9 - 2021*.
149. Simpson, F. C.; McTiernan, C. D.; Islam, M. M.; Buznyk, O.; Lewis, P. N.; Meek, K. M.; Haagdorens, M.; Audiger, C.; Lesage, S.; Gueriot, F.-X.; Brunette, I.; Robert, M.-C.; Olsen, D.; Koivusalo, L.; Liszka, A.; Fagerholm, P.; Gonzalez-Andrades, M.; Griffith, M., Collagen analogs with phosphorylcholine are inflammation-suppressing scaffolds for corneal regeneration from alkali burns in mini-pigs. *Communications Biology* **2021,** *4* (1), 608.
150. Simoliunas, E.; Ruedas-Torres, I.; Jiménez-Gómez, Y.; Edin, E.; Aghajanzadeh-Kiyaseh, M.; Zamani-Roudbaraki, M.; Asoklis, R.; Alksne, M.; Thathapudi, N. C.; Poudel, B. K.; Rinkunaite, I.; Asoklis, K.; Iesmantaite, M.; Ortega-Llamas, L.; Makselis, A.; Munoz, M.; Baltriukiene, D.; Bukelskiene, V.; Gómez-Laguna, J.; González-Andrades, M.; Griffith, M., Inflammation-suppressing cornea-in-a-syringe with anti-viral GF19 peptide promotes regeneration in HSV-1 infected rabbit corneas. *npj Regenerative Medicine* **2024,** *9* (1), 11.
151. Barroso, I. A.; Man, K.; Hall, T. J.; Robinson, T. E.; Louth, S. E. T.; Cox, S. C.; Ghag, A. K., Photocurable antimicrobial silk-based hydrogels for corneal repair. *Journal of biomedical materials research. Part A* **2022,** *110* (7), 1401-1415.
152. Fernandes-Cunha, G. M.; Brunel, L. G.; Arboleda, A.; Manche, A.; Seo, Y. A.; Logan, C.; Chen, F.; Heilshorn, S. C.; Myung, D., Collagen Gels Crosslinked by Photoactivation of Riboflavin for the Repair and Regeneration of Corneal Defects. *ACS Applied Bio Materials* **2023,** *6* (5), 1787-1797.
153. Dehli, F.; Schless, O.; Kaliske, M.; Potthof, I.; Taoum, A.; Fuest, M.; Duarte Campos, D., Biobased photocrosslinkable gelatin-methacrylate hydrogels promote the growth and phenotype maintenance of human corneal keratocytes. *Materials Advances* **2025,** *6* (12), 3805-3816.
154. Huang, J.; Jiang, T.; Qie, J.; Cheng, X.; Wang, Y.; Ye, Y.; Yang, Z.; Yan, H.; Yao, K.; Han, H., Biologically inspired bioactive hydrogels for scarless corneal repair. *Sci Adv* **2024,** *10* (51), eadt1643.
155. Gounden, V.; Singh, M., Hydrogels and Wound Healing: Current and Future Prospects. *Gels* **2024,** *10* (1).
156. Olteanu, G.; Neacșu, S. M.; Joița, F. A.; Musuc, A. M.; Lupu, E. C.; Ioniță-Mîndrican, C. B.; Lupuliasa, D.; Mititelu, M., Advancements in Regenerative Hydrogels in Skin Wound Treatment: A Comprehensive Review. *Int J Mol Sci* **2024,** *25* (7).
157. Xiao, Y.; Reis, L. A.; Feric, N.; Knee, E. J.; Gu, J.; Cao, S.; Laschinger, C.; Londono, C.; Antolovich, J.; McGuigan, A. P.; Radisic, M., Diabetic wound regeneration using peptide-modified hydrogels to target re-epithelialization. *Proceedings of the National Academy of Sciences* **2016,** *113* (40), E5792-E5801.

158. Sparks, H. D.; Mandla, S.; Vizely, K.; Rosin, N.; Radisic, M.; Biernaskie, J., Application of an instructive hydrogel accelerates re-epithelialization of xenografted human skin wounds. *Scientific Reports* **2022,** *12* (1), 14233.
159. Sparks, H. D.; Sigaeva, T.; Tarraf, S.; Mandla, S.; Pope, H.; Hee, O.; Di Martino, E. S.; Biernaskie, J.; Radisic, M.; Scott, W. M., Biomechanics of Wound Healing in an Equine Limb Model: Effect of Location and Treatment with a Peptide-Modified Collagen–Chitosan Hydrogel. *ACS Biomaterials Science & Engineering* **2021,** *7* (1), 265-278.
160. Bhatia, A.; O'Brien, K.; Chen, M.; Wong, A.; Garner, W.; Woodley, D. T.; Li, W., Dual therapeutic functions of F-5 fragment in burn wounds: preventing wound progression and promoting wound healing in pigs. *Molecular Therapy - Methods & Clinical Development* **2016,** *3*, 16041.
161. Zhu, Y.; Cankova, Z.; Iwanaszko, M.; Lichtor, S.; Mrksich, M.; Ameer, G. A., Potent laminin-inspired antioxidant regenerative dressing accelerates wound healing in diabetes. *Proceedings of the National Academy of Sciences* **2018,** *115* (26), 6816-6821.
162. John, J. V.; Sharma, N. S.; Tang, G.; Luo, Z.; Su, Y.; Weihs, S.; Shahriar, S. M. S.; Wang, G.; McCarthy, A.; Dyke, J.; Zhang, Y. S.; Khademhosseini, A.; Xie, J., Nanofiber Aerogels with Precision Macrochannels and LL-37-Mimic Peptides Synergistically Promote Diabetic Wound Healing. *Adv Funct Mater* **2023,** *33* (1).
163. Griffin, D. R.; Archang, M. M.; Kuan, C. H.; Weaver, W. M.; Weinstein, J. S.; Feng, A. C.; Ruccia, A.; Sideris, E.; Ragkousis, V.; Koh, J.; Plikus, M. V.; Di Carlo, D.; Segura, T.; Scumpia, P. O., Activating an adaptive immune response from a hydrogel scaffold imparts regenerative wound healing. *Nat Mater* **2021,** *20* (4), 560-569.
164. Lauterbach, A. L.; Wallace, R. P.; Alpar, A. T.; Refvik, K. C.; Reda, J. W.; Ishihara, A.; Beckman, T. N.; Slezak, A. J.; Mizukami, Y.; Mansurov, A.; Gomes, S.; Ishihara, J.; Hubbell, J. A., Topically-applied collagen-binding serum albumin-fused interleukin-4 modulates wound microenvironment in non-healing wounds. *npj Regenerative Medicine* **2023,** *8* (1), 49.
165. Salthouse, D.; Novakovic, K.; Hilkens, C. M. U.; Ferreira, A. M., Interplay between biomaterials and the immune system: Challenges and opportunities in regenerative medicine. *Acta biomaterialia* **2023,** *155*, 1-18.
166. Han, G.-Y.; Hwang, S.-K.; Cho, K.-H.; Kim, H.-J.; Cho, C.-S., Progress of tissue adhesives based on proteins and synthetic polymers. *Biomaterials Research* **2023,** *27* (1), 57.
167. Hu, L.; Zhou, J.; He, Z.; Zhang, L.; Du, F.; Nie, M.; Zhou, Y.; Hao, H.; Zhang, L.; Yu, S.; Zhang, J.; Chen, Y., In Situ-Formed Fibrin Hydrogel Scaffold Loaded With Human Umbilical Cord Mesenchymal Stem Cells Promotes Skin Wound Healing. *Cell transplantation* **2023,** *32*, 9636897231156215.
168. Pereira, R. V. S.; EzEldeen, M.; Ugarte-Berzal, E.; Martens, E.; Malengier-Devlies, B.; Vandooren, J.; Vranckx, J. J.; Matthys, P.; Opdenakker, G., Physiological fibrin hydrogel modulates immune cells and molecules and accelerates mouse skin wound healing. *Frontiers in immunology* **2023,** *14*, 1170153.
169. Butenko, S.; Nagalla, R. R.; Guerrero-Juarez, C. F.; Palomba, F.; David, L.-M.; Nguyen, R. Q.; Gay, D.; Almet, A. A.; Digman, M. A.; Nie, Q.; Scumpia, P. O.; Plikus, M. V.; Liu, W. F., Hydrogel crosslinking modulates macrophages, fibroblasts, and their communication, during wound healing. *Nature Communications* **2024,** *15* (1), 6820.
170. Richards, S. M.; Gubser Keller, C.; Kreutzer, R.; Greiner, G.; Ley, S.; Doelemeyer, A.; Dubost, V.; Flandre, T.; Kirkland, S.; Carbone, W.; Pandya, R.; Knehr, J.; Roma, G.; Schuierer, S.; Bouchez, L.; Seuwen, K.; Aebi, A.; Westhead, D.; Hintzen, G.; Jurisic, G.; Hossain, I.;

Neri, M.; Manevski, N.; Balavenkatraman, K. K.; Moulin, P.; Begrich, A.; Bertschi, B.; Huber, R.; Bouwmeester, T.; Driver, V. R.; von Schwabedissen, M.; Schaefer, D.; Wettstein, B.; Wettstein, R.; Ruffner, H., Molecular characterization of chronic cutaneous wounds reveals subregion- and wound type-specific differential gene expression. *International Wound Journal* **2024,** *21* (4), e14447.
171. Lemcke, H.; Voronina, N.; Steinhoff, G.; David, R., Recent Progress in Stem Cell Modification for Cardiac Regeneration. *Stem Cells Int* **2018,** *2018*, 1909346.
172. Tariq, U.; Gupta, M.; Pathak, S.; Patil, R.; Dohare, A.; Misra, S. K., Role of Biomaterials in Cardiac Repair and Regeneration: Therapeutic Intervention for Myocardial Infarction. *ACS Biomater Sci Eng* **2022,** *8* (8), 3271-3298.
173. Kaiser, N. J.; Coulombe, K. L., Physiologically inspired cardiac scaffolds for tailored in vivo function and heart regeneration. *Biomedical materials (Bristol, England)* **2015,** *10* (3), 034003.
174. Schotman, M. J. G.; Dankers, P. Y. W., Factors Influencing Retention of Injected Biomaterials to Treat Myocardial Infarction. *Advanced Materials Interfaces* **2022,** *9* (7), 2100942.
175. Chin, I. L.; Hool, L.; Choi, Y. S., Interrogating cardiac muscle cell mechanobiology on stiffness gradient hydrogels. *Biomaterials Science* **2021,** *9* (20), 6795-6806.
176. Hu, J.; Xiao, W., Effects of cardiac decellularized extracellular matrix hydrogel as a functional myocardial patch on the growth of cardiomyocytes. *Biomedical engineering online* **2025,** *24* (1), 141.
177. Zhang, Z.; Wang, X.; Fan, P.; Cheng, D.; Dang, J.; Dan, X.; Xia, Y.; Fan, H., Coupling Mitochondrial Homeostasis to Oxi-Inflamm-Aging Network Disruption via Peptide-Functionalized Nanocomposite Hydrogel for Osteoarthritis Intervention. *Advanced Materials* **2025,** *n/a* (n/a), e11804.
178. McLaughlin, S.; Sedlakova, V.; Zhang, Q.; McNeill, B.; Smyth, D.; Seymour, R.; Davis, D. R.; Ruel, M.; Brand, M.; Alarcon, E. I.; Suuronen, E. J., Recombinant Human Collagen Hydrogel Rapidly Reduces Methylglyoxal Adducts within Cardiomyocytes and Improves Borderzone Contractility after Myocardial Infarction in Mice. *Advanced Functional Materials* **2022,** *32* (32), 2204076.
179. Pooja, G.; Shweta, S.; Patel, P., Oxidative stress and free radicals in disease pathogenesis: a review. *Discover Medicine* **2025,** *2* (1), 104.
180. Liu, J.; Han, X.; Zhang, T.; Tian, K.; Li, Z.; Luo, F., Reactive oxygen species (ROS) scavenging biomaterials for anti-inflammatory diseases: from mechanism to therapy. *Journal of hematology & oncology* **2023,** *16* (1), 116.
181. Jang, W. B.; Kwon, S.-M., Bioengineering the Heart: Harnessing Biomaterials for Innovative Cardiovascular Interventions. *J Cardiovasc Interv* **2024,** *3* (3), 136-157.
182. Kim, A.; Downer, M. A.; Berry, C. E.; Valencia, C.; Fazilat, A. Z.; Griffin, M. Investigating Immunomodulatory Biomaterials for Preventing the Foreign Body Response *Bioengineering* [Online], 2023.
183. Zhang, H.; Dhalla, N. S., The Role of Pro-Inflammatory Cytokines in the Pathogenesis of Cardiovascular Disease. *Int J Mol Sci* **2024,** *25* (2).
184. Farache Trajano, L.; Smart, N., Immunomodulation for optimal cardiac regeneration: insights from comparative analyses. *NPJ Regen Med* **2021,** *6* (1), 8.
185. Yu, X., Application of Hydrogels in Cardiac Regeneration. *Cardiology and therapy* **2023,** *12* (4), 637-674.

186. Wu, T.; Liu, W., Functional hydrogels for the treatment of myocardial infarction. *NPG Asia Materials* **2022,** *14* (1), 9.
187. Esmaeili, H.; Patino-Guerrero, A.; Hasany, M.; Ansari, M. O.; Memic, A.; Dolatshahi-Pirouz, A.; Nikkhah, M., Electroconductive biomaterials for cardiac tissue engineering. *Acta biomaterialia* **2022,** *139*, 118-140.
188. Hosoyama, K.; Ahumada, M.; McTiernan, C. D.; Davis, D. R.; Variola, F.; Ruel, M.; Liang, W.; Suuronen, E. J.; Alarcon, E. I., Nanoengineered Electroconductive Collagen-Based Cardiac Patch for Infarcted Myocardium Repair. *ACS Applied Materials & Interfaces* **2018,** *10* (51), 44668-44677.
189. Muñoz, M.; Eren Cimenci, C.; Goel, K.; Comtois-Bona, M.; Hossain, M.; McTiernan, C.; Zuñiga-Bustos, M.; Ross, A.; Truong, B.; Davis, D. R.; Liang, W.; Rotstein, B.; Ruel, M.; Poblete, H.; Suuronen, E. J.; Alarcon, E. I., Nanoengineered Sprayable Therapy for Treating Myocardial Infarction. *ACS Nano* **2022,** *16* (3), 3522-3537.
190. Cristallini, C.; Rossin, D.; Vanni, R.; Barbani, N.; Bulgheresi, C.; Labardi, M.; Perveen, S.; Burchielli, S.; Terlizzi, D.; Kusmic, C.; Del Ry, S.; Cabiati, M.; Trouki, C.; Rossino, D.; Sergi, F.; Villano, A.; Aquaro, G. D.; Scarpellino, G.; Ruffinatti, F. A.; Amorim, S.; Pires, R. A.; Reis, R. L.; Rastaldo, R.; Giachino, C., A biodegradable, microstructured, electroconductive and nano-integrated drug eluting patch (MENDEP) for myocardial tissue engineering. *Bioact Mater* **2025,** *50*, 246-272.
191. Li, R.; Xu, A.; Chen, Y.; Li, Y.; Fu, R.; Jiang, W.; Li, X., Hydrogel encapsulating gold nanoparticles for targeted delivery of nitroglycerin to reduce post-cardiac dysfunction inflammation by inhibiting the Wnt/β-catenin signaling pathway. *Inflammopharmacology* **2024,** *32* (6), 3899-3911.
192. Sabarees, G.; Sam Jebaraj, Y.; Ezhilarasan, E.; Dravid Ragul, Y., Next-generation injectable hydrogels: Advanced crosslinking strategies, multi-stimuli responsiveness, and translational advances for precision regenerative medicine. *Nano TransMed* **2026,** *5*, 100109.
193. van Doorn, E. C. H.; Amesz, J. H.; Sadeghi, A. H.; de Groot, N. M. S.; Manintveld, O. C.; Taverne, Y. J. H. J., Preclinical Models of Cardiac Disease: A Comprehensive Overview for Clinical Scientists. *Cardiovascular Engineering and Technology* **2024,** *15* (2), 232-249.
194. Hennink, W. E.; van Nostrum, C. F., Novel crosslinking methods to design hydrogels. *Advanced Drug Delivery Reviews* **2002,** *54* (1), 13-36.
195. Lutolf, M. P.; Raeber, G. P.; Zisch, A. H.; Tirelli, N.; Hubbell, J. A., Cell-Responsive Synthetic Hydrogels. *Advanced Materials* **2003,** *15* (11), 888-892.
196. Diaferia, C.; Rosa, E.; Balasco, N.; Sibillano, T.; Morelli, G.; Giannini, C.; Vitagliano, L.; Accardo, A., The Introduction of a Cysteine Residue Modulates The Mechanical Properties of Aromatic-Based Solid Aggregates and Self-Supporting Hydrogels. *Chemistry – A European Journal* **2021,** *27* (60), 14886-14898.
197. Seow, W. Y.; Salgado, G.; Lane, E. B.; Hauser, C. A. E., Transparent crosslinked ultrashort peptide hydrogel dressing with high shape-fidelity accelerates healing of full-thickness excision wounds. *Scientific Reports* **2016,** *6* (1), 32670.
198. Islam, M. M.; Ravichandran, R.; Olsen, D.; Ljunggren, M. K.; Fagerholm, P.; Lee, C. J.; Griffith, M.; Phopase, J., Self-assembled collagen-like-peptide implants as alternatives to human donor corneal transplantation. *RSC Advances* **2016,** *6* (61), 55745-55749.
199. Kubyshkin, V., Stabilization of the triple helix in collagen mimicking peptides. *Organic & Biomolecular Chemistry* **2019,** *17* (35), 8031-8047.

200. Li, J.; Du, X.; Hashim, S.; Shy, A.; Xu, B., Aromatic–Aromatic Interactions Enable α-Helix to β-Sheet Transition of Peptides to Form Supramolecular Hydrogels. *J Am Chem Soc* **2017,** *139* (1), 71-74.
201. Lutolf, M. P.; Hubbell, J. A., Synthesis and Physicochemical Characterization of End-Linked Poly(ethylene glycol)-co-peptide Hydrogels Formed by Michael-Type Addition. *Biomacromolecules* **2003,** *4* (3), 713-722.
202. Depalle, B.; Qin, Z.; Shefelbine, S. J.; Buehler, M. J., Influence of cross-link structure, density and mechanical properties in the mesoscale deformation mechanisms of collagen fibrils. *J Mech Behavior Biomedical Mat* **2015,** *52*, 1-13.
203. Ishihara, S.; Kurosawa, H.; Haga, H. Stiffness-Modulation of Collagen Gels by Genipin-Crosslinking for Cell Culture *Gels* [Online], 2023, p. 148.
204. Sheu, M.-T.; Huang, J.-C.; Yeh, G.-C.; Ho, H.-O., Characterization of collagen gel solutions and collagen matrices for cell culture. *Biomaterials* **2001,** *22* (13), 1713-1719.
205. Segneanu, A.-E.; Bejenaru, L. E.; Bejenaru, C.; Blendea, A.; Mogoşanu, G. D.; Biţă, A.; Boia, E. R. Advancements in Hydrogels: A Comprehensive Review of Natural and Synthetic Innovations for Biomedical Applications *Polymers* [Online], 2025, p. 2026.
206. Hoyle, C. E.; Bowman, C. N., Thiol–Ene Click Chemistry. *Angew Chemie* **2010,** *49* (9), 1540-1573.
207. Yang, K.; Wei, K.; de Lapeyrière, M.; Maniura-Weber, K.; Rottmar, M., Amino-acid-specific thiol-ene coupling governs hydrogel crosslinking mechanism and cell behavior. *Cell Reports Physical Sci* **2024,** *5* (2), 101809.
208. Lu, H.; Carioscia, J. A.; Stansbury, J. W.; Bowman, C. N., Investigations of step-growth thiol-ene polymerizations for novel dental restoratives. *Dental Materials* **2005,** *21* (12), 1129-1136.
209. Zhang, L.; Geohagen, B. C.; Gavin, T.; LoPachin, R. M., Joint toxic effects of the type-2 alkene electrophiles. *Chem Biol Interact* **2016,** *254*, 198-206.
210. O'Brien, A. K.; Cramer, N. B.; Bowman, C. N., Oxygen inhibition in thiol–acrylate photopolymerizations. *J Polym Sci Part A: Polymer Chemistry* **2006,** *44* (6), 2007-2014.
211. Zhu, M.; Wang, Y.; Ferracci, G.; Zheng, J.; Cho, N.-J.; Lee, B. H., Gelatin methacryloyl and its hydrogels with an exceptional degree of controllability and batch-to-batch consistency. *Sci Rep* **2019,** *9* (1), 6863.
212. Moon, S. H.; Hwang, H. J.; Jeon, H. R.; Park, S. J.; Bae, I. S.; Yang, Y. J., Photocrosslinkable natural polymers in tissue engineering. *Front Bioeng Biotech* **2023,** *11*, 1127757.
213. Karimi, F.; Farbehi, N.; Ziaee, F.; Lau, K.; Monfared, M.; Kordanovski, M.; Joukhdar, H.; Molly, T. G.; Nordon, R.; Kilian, K. A.; Stenzel, M. H.; Lim, K. S.; Rnjak-Kovacina, J., Photocrosslinked Silk Fibroin Microgel Scaffolds for Biomedical Applications. *Advanced Functional Materials* **2024,** *34* (29), 2313354.
214. McAuliffe, C., Solubility in Water of Paraffin, Cycloparaffin, Olefin, Acetylene, Cycloolefin, and Aromatic Hydrocarbons1. *The Journal of Physical Chemistry* **1966,** *70* (4), 1267-1275.
215. Wilson, K. R.; Sedberry, S.; Pescatore, R.; Vinton, D.; Love, B.; Ballard, S.; Wham, B. C.; Hutchison, S. K.; Williamson, E. J., Microwave-assisted cleavage of Alloc and Allyl Ester protecting groups in solid phase peptide synthesis. *Journal of peptide science : an official publication of the European Peptide Society* **2016,** *22* (10), 622-627.

216. Mirdita, M.; Schütze, K.; Moriwaki, Y.; Heo, L.; Ovchinnikov, S.; Steinegger, M., ColabFold: making protein folding accessible to all. *Nature Methods* **2022,** *19* (6), 679-682.
217. Jumper, J.; Evans, R.; Pritzel, A.; Green, T.; Figurnov, M.; Ronneberger, O.; Tunyasuvunakool, K.; Bates, R.; Žídek, A.; Potapenko, A.; Bridgland, A.; Meyer, C.; Kohl, S. A. A.; Ballard, A. J.; Cowie, A.; Romera-Paredes, B.; Nikolov, S.; Jain, R.; Adler, J.; Back, T.; Petersen, S.; Reiman, D.; Clancy, E.; Zielinski, M.; Steinegger, M.; Pacholska, M.; Berghammer, T.; Bodenstein, S.; Silver, D.; Vinyals, O.; Senior, A. W.; Kavukcuoglu, K.; Kohli, P.; Hassabis, D., Highly accurate protein structure prediction with AlphaFold. *Nature* **2021,** *596* (7873), 583-589.
218. Eddy, S. R., Accelerated Profile HMM Searches. *PLoS computational biology* **2011,** *7* (10), e1002195.
219. Steinegger, M.; Mirdita, M.; Söding, J., Protein-level assembly increases protein sequence recovery from metagenomic samples manyfold. *Nat Methods* **2019,** *16* (7), 603-606.
220. Essmann, U.; Perera, L.; Berkowitz, M. L.; Darden, T.; Lee, H.; Pedersen, L. G., A smooth particle mesh Ewald method. *The Journal of Chemical Physics* **1995,** *103* (19), 8577-8593.
221. York, D. M.; Darden, T. A.; Pedersen, L. G., The effect of long-range electrostatic interactions in simulations of macromolecular crystals: A comparison of the Ewald and truncated list methods. *The Journal of Chemical Physics* **1993,** *99* (10), 8345-8348.
222. Bussi, G.; Donadio, D.; Parrinello, M., Canonical sampling through velocity rescaling. *J Chem Phys* **2007,** *126* (1), 014101.
223. Berendsen, H. J. C.; Postma, J. P. M.; van Gunsteren, W. F.; DiNola, A.; Haak, J. R., Molecular dynamics with coupling to an external bath. *The Journal of Chemical Physics* **1984,** *81* (8), 3684-3690.
224. Humphrey, W.; Dalke, A.; Schulten, K., VMD: Visual molecular dynamics. *Journal of Molecular Graphics* **1996,** *14* (1), 33-38.
225. Coussot, P.; Boyer, S., Determination of yield stress fluid behaviour from inclined plane test. *Rheologica Acta* **1995,** *34* (6), 534-543.
226. Moller, P.; Fall, A.; Chikkadi, V.; Derks, D.; Bonn, D., An attempt to categorize yield stress fluid behaviour. *Philosophical Transactions of the Royal Society A: Mathematical, Physical and Engineering Sciences* **2009,** *367* (1909), 5139-5155.
227. Yasuda, T.; Shimokasa, K., A proposed method of evaluating the yield stress of a thickened liquid using a simplified inclined plane test. *Journal of Texture Studies* **2022,** *53* (2), 307-314.
228. Aston, R.; Sewell, K.; Klein, T.; Lawrie, G.; Grøndahl, L., Evaluation of the impact of freezing preparation techniques on the characterisation of alginate hydrogels by cryo-SEM. *European Polymer Journal* **2016,** *82*, 1-15.
229. Lee, M.; Kim, Y. S.; Park, J.; Choe, G.; Lee, S.; Kang, B. G.; Jun, J. H.; Shin, Y.; Kim, M.; Ahn, Y.; Lee, J. Y., A paintable and adhesive hydrogel cardiac patch with sustained release of ANGPTL4 for infarcted heart repair. *Bioact Mater* **2024,** *31*, 395-407.
230. F04.05, S. Standard Test Method for Wound Closure Strength of Tissue Adhesives and Sealants; ASTM F2458 2015.
231. Standard Test Method for Compressive Properties of Rigid Plastics. ASTM International: West Conshohocken, PA, 2023; Vol. ASTM D695-23.
232. Ghosh, D.; Salinas, C. M.; Pallod, S.; Roberts, J.; Makin, I. R. S.; Yaron, J. R.; Witte, R. S.; Rege, K., Temporal evaluation of efficacy and quality of tissue repair upon laser-activated sealing. *Bioengineering & translational medicine* **2023,** *8* (2), e10412.

233. Gund, R.; Zirmire, R.; J, H.; Kansagara, G.; Jamora, C., Histological and Immunohistochemical Examination of Stem Cell Proliferation and Reepithelialization in the Wounded Skin. *Bio-protocol* **2021,** *11* (2), e3894.
234. Caetano, G. F.; Fronza, M.; Leite, M. N.; Gomes, A.; Frade, M. A., Comparison of collagen content in skin wounds evaluated by biochemical assay and by computer-aided histomorphometric analysis. *Pharmaceutical biology* **2016,** *54* (11), 2555-2559.
235. Comtois-Bona, M. E.; Chandra, A.; Hage, J. E.; Liu, B.; David Garcia-Schejtman, S.; MacAdam, A. J.; Brunette, I.; Munoz, M.; Alarcon, E. I., 3D-Printed Low-Cost Artificial Corneal Perfusion Chamber for Investigating Corneal Physiology and Diseases in Different Animal Species. *Advanced Engineering Materials* **2023,** *25* (22), 2300695.
236. McGraw, T., Safety of polyethylene glycol 3350 solution in chronic constipation: randomized, placebo-controlled trial. *Clinical and experimental gastroenterology* **2016,** *9*, 173-80.
237. Robins, S. P., Biochemistry and functional significance of collagen cross-linking. *Biochem. Soc. Trans.* **2007,** *35* (5), 849-852.
238. Nair, D. P.; Podgórski, M.; Chatani, S.; Gong, T.; Xi, W.; Fenoli, C. R.; Bowman, C. N., The Thiol-Michael Addition Click Reaction: A Powerful and Widely Used Tool in Materials Chemistry. *Chem. Mater.* **2014,** *26* (1), 724-744.
239. Fontaine, S. D.; Reid, R.; Robinson, L.; Ashley, G. W.; Santi, D. V., Long-Term Stabilization of Maleimide–Thiol Conjugates. *Bioconjug. Chem.* **2015,** *26* (1), 145-152.
240. Brodsky, B.; Persikov, A. V., Molecular structure of the collagen triple helix. *Advances in protein chemistry* **2005,** *70*, 301-39.
241. Cheng, S.; Shi, T.; Wang, X.-L.; Liang, J.; Wu, H.; Xie, L.; Li, Y.; Zhao, Y.-L., Features of S-nitrosylation based on statistical analysis and molecular dynamics simulation: cysteine acidity, surrounding basicity, steric hindrance and local flexibility. *Mol. Biosyst.* **2014,** *10* (10), 2597-2606.
242. Tsuda, S.; Masuda, S.; Yoshiya, T., Epimerization-Free Preparation of C-Terminal Cys Peptide Acid by Fmoc SPPS Using Pseudoproline-Type Protecting Group. *J. Org. Chem.* **2020,** *85* (3), 1674-1679.
243. Feng, Y.; Melacini, G.; Taulane, J. P.; Goodman, M., Acetyl-Terminated and Template-Assembled Collagen-Based Polypeptides Composed of Gly-Pro-Hyp Sequences. 2. Synthesis and Conformational Analysis by Circular Dichroism, Ultraviolet Absorbance, and Optical Rotation. *J. Am. Chem. Soc.* **1996,** *118* (43), 10351-10358.
244. O'Leary, L. E. R.; Fallas, J. A.; Bakota, E. L.; Kang, M. K.; Hartgerink, J. D., Multi-hierarchical self-assembly of a collagen mimetic peptide from triple helix to nanofibre and hydrogel. *Nature Chemistry* **2011,** *3* (10), 821-828.
245. Nagata, T.; Harada, Y.; Arai, M.; Hirose, T.; Kondo, H., Polyethylene Glycol-Based Synthetic Hydrogel Sealant for Filtration Bleb Leaks: An In Vivo and Histologic Study. *Transl. Vis. Sci. Technol.* **2020,** *9* (6), 24-24.
246. Natour, E.; Suedkamp, M.; Dapunt, O. E., Assessment of the effect on blood loss and transfusion requirements when adding a polyethylene glycol sealant to the anastomotic closure of aortic procedures: a case-control analysis of 102 patients undergoing Bentall procedures. *Journal of cardiothoracic surgery* **2012,** *7*, 105.
247. Meek, K. M.; Knupp, C., Corneal structure and transparency. *Progress in retinal and eye research* **2015,** *49*, 1-16.
248. Chang, Y. C.; Mesquita, G. M.; Williams, S.; Gregori, G.; Cabot, F.; Ho, A.; Ruggeri, M.; Yoo, S. H.; Parel, J. M.; Manns, F., In vivo measurement of the human crystalline lens

equivalent refractive index using extended-depth OCT. *Biomedical optics express* **2019,** *10* (2), 411-422.
249. Suchard, J. R., Recovery from Severe Hyperthermia (45 degrees C) and Rhabdomyolysis Induced by Methamphetamine Body-Stuffing. *The western journal of emergency medicine* **2007,** *8* (3), 93-5.
250. Mitchell, H. H.; Hamilton, T. S.; Steggerda, F. R.; Bean, H. W., THE CHEMICAL COMPOSITION OF THE ADULT HUMAN BODY AND ITS BEARING ON THE BIOCHEMISTRY OF GROWTH. *Journal of Biological Chemistry* **1945,** *158* (3), 625-637.
251. Asbell, P.; Brocks, D., Cornea Overview. In *Encyclopedia of the Eye*, Dartt, D. A., Ed. Academic Press: Oxford, 2010; pp 522-531.
252. Boll, L. B.; Raines, R. T., Context-Dependence of the Reactivity of Cysteine and Lysine Residues. *Chembiochem.* **2022,** *23* (14), e202200258.
253. Uman, S.; Dhand, A.; Burdick, J. A., Recent advances in shear-thinning and self-healing hydrogels for biomedical applications. *Journal of Applied Polymer Science* **2020,** *137* (25), 48668.
254. Salgado, G.; Ng, Y. Z.; Koh, L. F.; Goh, C. S. M.; Common, J. E., Human reconstructed skin xenografts on mice to model skin physiology. *Differentiation; research in biological diversity* **2017,** *98*, 14-24.
255. Bhamidipati, C. M.; Coselli, J. S.; LeMaire, S. A., BioGlue in 2011: what is its role in cardiac surgery? *The journal of extra-corporeal technology* **2012,** *44* (1), P6-12.
256. Yuk, H.; Varela, C. E.; Nabzdyk, C. S.; Mao, X.; Padera, R. F.; Roche, E. T.; Zhao, X., Dry double-sided tape for adhesion of wet tissues and devices. *Nature* **2019,** *575* (7781), 169-174.
257. Ma, Z.; Bourquard, C.; Gao, Q.; Jiang, S.; De Iure-Grimmel, T.; Huo, R.; Li, X.; He, Z.; Yang, Z.; Yang, G.; Wang, Y.; Lam, E.; Gao, Z. H.; Supponen, O.; Li, J., Controlled tough bioadhesion mediated by ultrasound. *Science* **2022,** *377* (6607), 751-755.
258. Wahlsten, A.; Stracuzzi, A.; Lüchtefeld, I.; Restivo, G.; Lindenblatt, N.; Giampietro, C.; Ehret, A. E.; Mazza, E., Multiscale mechanical analysis of the elastic modulus of skin. *Acta biomaterialia* **2023,** *170*, 155-168.
259. Wong, V. W.; Sorkin, M.; Glotzbach, J. P.; Longaker, M. T.; Gurtner, G. C., Surgical approaches to create murine models of human wound healing. *J Biomed Biotechnol* **2011,** *2011*, 969618.
260. van de Vyver, M.; Boodhoo, K.; Frazier, T.; Hamel, K.; Kopcewicz, M.; Levi, B.; Maartens, M.; Machcinska, S.; Nunez, J.; Pagani, C.; Rogers, E.; Walendzik, K.; Wisniewska, J.; Gawronska-Kozak, B.; Gimble, J. M., Histology Scoring System for Murine Cutaneous Wounds. *Stem cells and development* **2021,** *30* (23), 1141-1152.
261. Lazurko, C.; Khatoon, Z.; Goel, K.; Sedlakova, V.; Eren Cimenci, C.; Ahumada, M.; Zhang, L.; Mah, T. F.; Franco, W.; Suuronen, E. J.; Alarcon, E. I., Multifunctional Nano and Collagen-Based Therapeutic Materials for Skin Repair. *ACS Biomater Sci Eng* **2020,** *6* (2), 1124-1134.
262. Heichel, J.; Wilhelm, F.; Kunert, K. S.; Hammer, T., Topographic Findings of the Porcine Cornea. *Medical hypothesis, discovery & innovation ophthalmology journal* **2016,** *5* (4), 125-131.
263. Sharma, A.; Sharma, N.; Basu, S.; Sharma, R.; Aggarwal, S.; Gupta, P. C.; Ram, J.; Nirankari, V. S., Tissue Adhesives for the Management of Corneal Perforations and Challenging Corneal Conditions. *Clinical ophthalmology (Auckland, N.Z.)* **2023,** *17*, 209-223.
264. Peng, X.; Zhang, J.; Banaszak Holl, M. M.; Xiao, P., Thiol-Ene Photopolymerization under Blue, Green and Red LED Irradiation. *ChemPhotoChem* **2021,** *5* (6), 571-581.

265. Hoyle, C. E.; Lee, T. Y.; Roper, T., Thiol–enes: Chemistry of the past with promise for the future. *Journal of Polymer Science Part A: Polymer Chemistry* **2004,** *42* (21), 5301-5338.
266. Schweller, R. M.; West, J. L., Encoding Hydrogel Mechanics via Network Cross-Linking Structure. *ACS Biomaterials Science & Engineering* **2015,** *1* (5), 335-344.
267. Lutolf, M. P.; Tirelli, N.; Cerritelli, S.; Cavalli, L.; Hubbell, J. A., Systematic Modulation of Michael-Type Reactivity of Thiols through the Use of Charged Amino Acids. *Biocon Chemistry* **2001,** *12* (6), 1051-1056.
268. McGilvray, K. L.; Decan, M. R.; Wang, D.; Scaiano, J. C., Facile Photochemical Synthesis of Unprotected Aqueous Gold Nanoparticles. *J Am Chem Soc* **2006,** *128* (50), 15980-15981.
269. Coman, A. E.; Marin, M. M.; Rosca, A. M.; Tutuianu, R.; Albu Kaya, M. G.; Ionita, A.; Constantinescu, R. R.; Titorencu, I. Comparative Study of Collagen Gels Extracted from Different Sources *Gels* [Online], 2025, p. 879.
270. Koshy, S. T.; Desai, R. M.; Joly, P.; Li, J.; Bagrodia, R. K.; Lewin, S. A.; Joshi, N. S.; Mooney, D. J., Click-Crosslinked Injectable Gelatin Hydrogels. *Adv Health Mat* **2016,** *5* (5), 541-547.
271. De Smedt, S. C.; Lauwers, A.; Demeester, J.; Van Steenbergen, M. J.; Hennink, W. E.; Roefs, S. P. F. M., Characterization of the Network Structure of Dextran Glycidyl Methacrylate Hydrogels by Studying the Rheological and Swelling Behavior. *Macromolecules* **1995,** *28* (14), 5082-5088.
272. Klotz, B. J.; Gawlitta, D.; Rosenberg, A.; Malda, J.; Melchels, F. P. W., Gelatin-Methacryloyl Hydrogels: Towards Biofabrication-Based Tissue Repair. *Trends in biotechnology* **2016,** *34* (5), 394-407.
273. Matsumoto, A.; Kumagai, T.; Aota, H.; Kawasaki, H.; Arakawa, R., Reassessment of Free-Radical Polymerization Mechanism of Allyl Acetate Based on End-Group Determination of Resulting Oligomers by MALDI-TOF-MS Spectrometry. *Polymer J* **2009,** *41* (1), 26-33.
274. Yao, L.; Ling, B.; Huang, W.; Wang, Q.; Cai, X.; Xiao, J., Controllable self-assembly of tyrosine-rich triblock peptides into robust collagen mimetic bioscaffolds for aging skin rejuvenation. *Reg Biomat* **2024,** *11*, rbae085.
275. Xu, H.; Casillas, J.; Krishnamoorthy, S.; Xu, C., Effects of Irgacure 2959 and lithium phenyl-2,4,6-trimethylbenzoylphosphinate on cell viability, physical properties, and microstructure in 3D bioprinting of vascular-like constructs. *Biomedical materials (Bristol, England)* **2020,** *15* (5), 055021.
276. Cousin, M. A.; Greenberg, A. J.; Koep, T. H.; Angius, D.; Yaszemski, M. J.; Spinner, R. J.; Windebank, A. J., The Value of Systematic Reviews in Estimating the Cost and Barriers to Translation in Tissue Engineering. *Tissue engineering. Part B, Reviews* **2016,** *22* (6), 430-437.
277. Lou, P.; Liu, S.; Wang, Y.; Pan, C.; Xu, X.; Zhao, M.; Liao, G.; Yang, G.; Yuan, Y.; Li, L.; Zhang, J.; Chen, Y.; Cheng, J.; Lu, Y.; Liu, J., Injectable self-assembling peptide nanofiber hydrogel as a bioactive 3D platform to promote chronic wound tissue regeneration. *Acta Biomater.* **2021,** *135*, 100-112.
278. Nguyen, A. K.; Molley, T. G.; Kardia, E.; Ganda, S.; Chakraborty, S.; Wong, S. L.; Ruan, J.; Yee, B. E.; Mata, J.; Vijayan, A.; Kumar, N.; Tilley, R. D.; Waters, S. A.; Kilian, K. A., Hierarchical assembly of tryptophan zipper peptides into stress-relaxing bioactive hydrogels. *Nat. Commun.* **2023,** *14* (1), 6604.
279. Pugliese, R.; Gelain, F. Cross-Linked Self-Assembling Peptides and Their Post-Assembly Functionalization via One-Pot and In Situ Gelation System *Int. J. Mol. Sci.* [Online], 2020.

280. Reithofer, M. R.; Lakshmanan, A.; Ping, A. T. K.; Chin, J. M.; Hauser, C. A. E., In situ synthesis of size-controlled, stable silver nanoparticles within ultrashort peptide hydrogels and their anti-bacterial properties. *Biomaterials* **2014,** *35* (26), 7535-7542.
281. Chen, R.; Zhu, C.; Xu, L.; Gu, Y.; Ren, S.; Bai, H.; Zhou, Q.; Liu, X.; Lu, S.; Bi, X.; Li, W.; Jia, X.; Chen, Z., An injectable peptide hydrogel with excellent self-healing ability to continuously release salvianolic acid B for myocardial infarction. *Biomaterials* **2021,** *274*, 120855.
282. Fan, Z.; Fu, M.; Xu, Z.; Zhang, B.; Li, Z.; Li, H.; Zhou, X.; Liu, X.; Duan, Y.; Lin, P. H.; Duann, P.; Xie, X.; Ma, J.; Liu, Z.; Guan, J., Sustained Release of a Peptide-Based Matrix Metalloproteinase-2 Inhibitor to Attenuate Adverse Cardiac Remodeling and Improve Cardiac Function Following Myocardial Infarction. *Biomacromolecules* **2017,** *18* (9), 2820-2829.
283. Muttenthaler, M.; King, G. F.; Adams, D. J.; Alewood, P. F., Trends in peptide drug discovery. *Nat. Rev. Drug Discov.* **2021,** *20* (4), 309-325.
284. Mahapatra, M. K.; Karuppasamy, M.; Sahoo, B. M., Semaglutide, a glucagon like peptide-1 receptor agonist with cardiovascular benefits for management of type 2 diabetes. *Reviews in endocrine & metabolic disorders* **2022,** *23* (3), 521-539.
285. Zhang, T.; Chen, Z.; Tian, Y.; Han, B.; Zhang, N.; Song, W.; Liu, Z.; Zhao, J.; Liu, J., Kilogram-Scale Synthesis of Osteogenic Growth Peptide (10–14) Using a Fragment Coupling Approach. *Org. Process Res. Dev.* **2015,** *19* (9), 1257-1262.
286. Bray, B. L., Large-scale manufacture of peptide therapeutics by chemical synthesis. *Nature Reviews Drug Discovery* **2003,** *2* (7), 587-593.
287. Levi, J.; Wang, J.; Venter, F.; Hill, A., Estimated minimum prices and lowest available national prices for antiobesity medications: Improving affordability and access to treatment. *Obesity* **2023,** *31* (5), 1270-1279.
288. Takei, T.; Nakahara, H.; Ijima, H.; Kawakami, K., Synthesis of a chitosan derivative soluble at neutral pH and gellable by freeze–thawing, and its application in wound care. *Acta Biomater.* **2012,** *8* (2), 686-693.
289. Kuninaka, Y.; Ishida, Y.; Ishigami, A.; Nosaka, M.; Matsuki, J.; Yasuda, H.; Kofuna, A.; Kimura, A.; Furukawa, F.; Kondo, T., Macrophage polarity and wound age determination. *Sci. Rep.* **2022,** *12* (1), 20327.
290. Schultz, K. M.; Kyburz, K. A.; Anseth, K. S., Measuring dynamic cell-material interactions and remodeling during 3D human mesenchymal stem cell migration in hydrogels. *Proceedings of the National Academy of Sciences of the United States of America* **2015,** *112* (29), E3757-64.
291. Boopathy, A. V.; Martinez, M. D.; Smith, A. W.; Brown, M. E.; García, A. J.; Davis, M. E., Intramyocardial Delivery of Notch Ligand-Containing Hydrogels Improves Cardiac Function and Angiogenesis Following Infarction. *Tissue engineering. Part A* **2015,** *21* (17-18), 2315-22.
292. Williams, C. G.; Malik, A. N.; Kim, T. K.; Manson, P. N.; Elisseeff, J. H., Variable cytocompatibility of six cell lines with photoinitiators used for polymerizing hydrogels and cell encapsulation. *Biomaterials* **2005,** *26* (11), 1211-1218.
293. Tomal, W.; Ortyl, J. Water-Soluble Photoinitiators in Biomedical Applications *Polymers* [Online], 2020, p. 1073.
294. Zennifer, A.; Manivannan, S.; Sethuraman, S.; Kumbar, S. G.; Sundaramurthi, D., 3D bioprinting and photocrosslinking: emerging strategies & future perspectives. *Biomater Adv* **2022,** *134*, 112576.

295. Tigner, T. J.; Rajput, S.; Gaharwar, A. K.; Alge, D. L., Comparison of Photo Cross Linkable Gelatin Derivatives and Initiators for Three-Dimensional Extrusion Bioprinting. *Biomacromolecules* **2020,** *21* (2), 454-463.
296. D'Souza, A.; Yoon, J. H.; Beaman, H.; Gosavi, P.; Lengyel-Zhand, Z.; Sternisha, A.; Centola, G.; Marshall, L. R.; Wehrman, M. D.; Schultz, K. M.; Monroe, M. B.; Makhlynets, O. V., Nine-Residue Peptide Self-Assembles in the Presence of Silver to Produce a Self-Healing, Cytocompatible, Antimicrobial Hydrogel. *ACS Appl. Mater. Interfaces.* **2020,** *12* (14), 17091-17099.
297. Clarke, D. E.; Pashuck, E. T.; Bertazzo, S.; Weaver, J. V. M.; Stevens, M. M., Self-Healing, Self-Assembled β-Sheet Peptide–Poly(γ-glutamic acid) Hybrid Hydrogels. *J. Am. Chem. Soc.* **2017,** *139* (21), 7250-7255.
298. Li, R.; Zhou, C.; Chen, J.; Luo, H.; Li, R.; Chen, D.; Zou, X.; Wang, W., Synergistic osteogenic and angiogenic effects of KP and QK peptides incorporated with an injectable and self-healing hydrogel for efficient bone regeneration. *Bioact. Mater.* **2022,** *18*, 267-283.
299. Terriac, L.; Helesbeux, J.-J.; Maugars, Y.; Guicheux, J.; Tibbitt, M. W.; Delplace, V., Boronate Ester Hydrogels for Biomedical Applications: Challenges and Opportunities. *Chemistry of Materials* **2024,** *36* (14), 6674-6695.
300. Beaupre, D. M.; Weiss, R. G., Thiol- and Disulfide-Based Stimulus-Responsive Soft Materials and Self-Assembling Systems. *Molecules* **2021,** *26* (11).
301. Li, L.; Lu, C.; Wang, L.; Chen, M.; White, J.; Hao, X.; McLean, K. M.; Chen, H.; Hughes, T. C., Gelatin-Based Photocurable Hydrogels for Corneal Wound Repair. *ACS Appl. Mater. Interfaces.* **2018,** *10* (16), 13283-13292.
302. Batchelor, R. R.; Kwandou, G.; Spicer, P. T.; Stenzel, M. H., (−)-Riboflavin (vitamin B2) and flavin mononucleotide as visible light photo initiators in the thiol–ene polymerisation of PEG-based hydrogels. *Polymer Chemistry* **2017,** *8* (6), 980-984.
303. Shih, H.; Lin, C.-C., Visible-Light-Mediated Thiol-Ene Hydrogelation Using Eosin-Y as the Only Photoinitiator. *Macromolecular Rapid Communications* **2013,** *34* (3), 269-273.
304. Zhao, S.; Wang, C.; Sun, Y.; Wang, K.; Xie, G.; Zhu, H.; Zhu, H.; Zhu, S.; Liu, R., Near-Infrared Photoinitiators: Synthesis, Photophysics, and Study on the Photocuring Properties. *ACS Applied Polymer Materials* **2025,** *7* (21), 14382-14391.
305. Pattison, D. I.; Davies, M. J., Actions of ultraviolet light on cellular structures. *Exs* **2006,** (96), 131-57.
306. Weinstain, R.; Slanina, T.; Kand, D.; Klán, P., Visible-to-NIR-Light Activated Release: From Small Molecules to Nanomaterials. *Chemical Reviews* **2020,** *120* (24), 13135-13272.
307. Eftekhari, A.; de Graaf, K. R.; Takmakova, E.; Jongprasitkul, H.; Efimov, A.; Turunen, S.; Kerr, A.; Kellomäki, M.; Luxenhofer, R.; Laaksonen, T.; Durandin, N., Traceless Photopolymerization with Non-Pulsed Red Light Enables 3D-Printable Cell-Laden Hydrogels. *Advanced Materials* **2025,** *37* (30), 2502386.
308. Xu, Y.; Kirchner, M., Collagen Mimetic Peptides. *Bioengineering (Basel)* **2021,** *8* (1).
309. Huang, Y.; Lan, J.; Wu, C.; Zhang, R.; Zheng, H.; Fan, S.; Xu, F., Stability of collagen heterotrimer with same charge pattern and different charged residue identities. *Biophysical Journal* **2023,** *122* (13), 2686-2695.
310. Moran, C. J.; Ramesh, A.; Brama, P. A.; O'Byrne, J. M.; O'Brien, F. J.; Levingstone, T. J., The benefits and limitations of animal models for translational research in cartilage repair. *J Exp Orthop* **2016,** *3* (1), 1.

311. Martin, S. S.; Aday, A. W.; Allen, N. B.; Almarzooq, Z. I.; Anderson, C. A. M.; Arora, P.; Avery, C. L.; Baker-Smith, C. M.; Bansal, N.; Beaton, A. Z.; Commodore-Mensah, Y.; Currie, M. E.; Elkind, M. S. V.; Fan, W.; Generoso, G.; Gibbs, B. B.; Heard, D. G.; Hiremath, S.; Johansen, M. C.; Kazi, D. S.; Ko, D.; Leppert, M. H.; Magnani, J. W.; Michos, E. D.; Mussolino, M. E.; Parikh, N. I.; Perman, S. M.; Rezk-Hanna, M.; Roth, G. A.; Shah, N. S.; Springer, M. V.; St-Onge, M. P.; Thacker, E. L.; Urbut, S. M.; Van Spall, H. G. C.; Voeks, J. H.; Whelton, S. P.; Wong, N. D.; Wong, S. S.; Yaffe, K.; Palaniappan, L. P., 2025 Heart Disease and Stroke Statistics: A Report of US and Global Data From the American Heart Association. *Circulation* **2025,** *151* (8), e41-e660.
312. Satthenapalli, V. R.; Lamberts, R. R.; Katare, R. G., Concise Review: Challenges in Regenerating the Diabetic Heart: A Comprehensive Review. *Stem Cells* **2017,** *35* (9), 2009-2026.
313. Ballard, V. L.; Edelberg, J. M., Stem cells and the regeneration of the aging cardiovascular system. *Circ Res* **2007,** *100* (8), 1116-27.
314. Nishiguchi, M. A.; Spencer, C. A.; Leung, D. H.; Leung, T. H., Aging Suppresses Skin-Derived Circulating SDF1 to Promote Full-Thickness Tissue Regeneration. *Cell Rep* **2018,** *24* (13), 3383-3392.e5.
315. Zhao, Z.; Chen, X.; Dowbaj, A. M.; Sljukic, A.; Bratlie, K.; Lin, L.; Fong, E. L. S.; Balachander, G. M.; Chen, Z.; Soragni, A.; Huch, M.; Zeng, Y. A.; Wang, Q.; Yu, H., Organoids. *Nature Reviews Methods Primers* **2022,** *2* (1), 94.
316. Ingber, D. E., Human organs-on-chips for disease modelling, drug development and personalized medicine. *Nature Reviews Genetics* **2022,** *23* (8), 467-491.
317. Luo, J.; Tong, Y. W., Self-assembly of collagen-mimetic peptide amphiphiles into biofunctional nanofiber. *ACS Nano* **2011,** *5* (10), 7739-47.
318. Spicer, C. D.; Pashuck, E. T.; Stevens, M. M., Achieving Controlled Biomolecule–Biomaterial Conjugation. *Chemical Reviews* **2018,** *118* (16), 7702-7743.
319. Vigata, M.; Meinert, C.; Hutmacher, D. W.; Bock, N., Hydrogels as Drug Delivery Systems: A Review of Current Characterization and Evaluation Techniques. *Pharmaceutics* **2020,** *12* (12).
320. Trucillo, P., Biomaterials for Drug Delivery and Human Applications. *Materials (Basel)* **2024,** *17* (2).
321. Mitrousis, N.; Fokina, A.; Shoichet, M. S., Biomaterials for cell transplantation. *Nature Reviews Materials* **2018,** *3* (11), 441-456.
322. Hunsberger, J. G.; Shupe, T.; Atala, A., An Industry-Driven Roadmap for Manufacturing in Regenerative Medicine. *Stem Cells Transl Med* **2018,** *7* (8), 564-568.
323. Capella-Monsonís, H.; Crum, R. J.; Hussey, G. S.; Badylak, S. F., Advances, challenges, and future directions in the clinical translation of ECM biomaterials for regenerative medicine applications. *Advanced Drug Delivery Reviews* **2024,** *211*, 115347.
324. Cimenci, C. E.; Blackburn, N. J. R.; Sedlakova, V.; Pupkaite, J.; Munoz, M.; Rotstein, B. H.; Spiegel, D. A.; Alarcon, E. I.; Suuronen, E. J., Combined Methylglyoxal Scavenger and Collagen Hydrogel Therapy Prevents Adverse Remodeling and Improves Cardiac Function Post-Myocardial Infarction. *Advanced Functional Materials* **2022,** *32* (1), 2108630.
325. Kumar, V. B.; Tiwari, O. S.; Finkelstein-Zuta, G.; Rencus-Lazar, S.; Gazit, E., Design of Functional RGD Peptide-Based Biomaterials for Tissue Engineering. *Pharmaceutics* **2023,** *15* (2).
326. Güç, E.; Briquez, P. S.; Foretay, D.; Fankhauser, M. A.; Hubbell, J. A.; Kilarski, W. W.; Swartz, M. A., Local induction of lymphangiogenesis with engineered fibrin-binding VEGF-C

promotes wound healing by increasing immune cell trafficking and matrix remodeling. *Biomaterials* **2017,** *131*, 160-175.
327. Xu, J.; Nie, N.; Wu, B.; Li, Y.; Gong, L.; Yao, X.; Zou, X.; Ouyang, H., The personalized application of biomaterials based on age and sexuality specific immune responses. *Biomaterials* **2021,** *278*, 121177.
328. Chan, A. H. P.; Hu, Y.; Pardavi, B.; Xu, X.; Grant, A. J.; Wise, S. G.; Loo, L.; Tan, R. P., Developing a Single-Cell Spatial Transcriptomics Workflow for In Vivo Evaluation of Implanted Biomaterials. *Advanced Science n/a* (n/a), e13242.
329. Yang, X.; Huang, M.; Chen, H.; Dai, J.; Chen, J.; Chen, K.; Zhou, J.; Li, A.; Li, P., Biomaterial-mediated Cell Atlas: an insight from single-cell and spatial transcriptomics. *Bioact Mater* **2025,** *54*, 1-33.
330. Mesfin, J. M.; Ninh, V. K.; Diaz, M. D.; Nguyen, M. B.; Chen, A.; Wang, R. M.; Wong, E. G.; Karkanitsa, M. L.; Hunter, J. D.; Yu, J.; Bridgelal, B. D.; Pham, J.-P. A.; Taghdiri, N.; Calcagno, D. M.; Luo, C. G.; Braden, R. L.; Fu, Z.; King, K. R.; Christman, K. L., Regional and cell specific bioactivity of injectable extracellular matrix biomaterials in myocardial infarction. *Nature Communications* **2025,** *16* (1), 10387.